



**HAL**  
open science

# Toward lithium-air batteries for aircraft application: a combined experimental/modeling study

Caroline Gaya

► **To cite this version:**

Caroline Gaya. Toward lithium-air batteries for aircraft application: a combined experimental/modeling study. Other. Université de Picardie Jules Verne, 2019. English. NNT: 2019AMIE0053 . tel-03634360

**HAL Id: tel-03634360**

**<https://theses.hal.science/tel-03634360v1>**

Submitted on 7 Apr 2022

**HAL** is a multi-disciplinary open access archive for the deposit and dissemination of scientific research documents, whether they are published or not. The documents may come from teaching and research institutions in France or abroad, or from public or private research centers.

L'archive ouverte pluridisciplinaire **HAL**, est destinée au dépôt et à la diffusion de documents scientifiques de niveau recherche, publiés ou non, émanant des établissements d'enseignement et de recherche français ou étrangers, des laboratoires publics ou privés.



# Thèse de Doctorat

*Mention Chimie*

*Spécialité Génie Electrochimique*

présentée à l'Ecole Doctorale en Sciences Technologie et Santé (ED 585)

**de l'Université de Picardie Jules Verne**

par

**Caroline Gaya**

pour obtenir le grade de Docteur de l'Université de Picardie Jules Verne

**Toward lithium-air batteries for aircraft application:  
a combined experimental/modeling study**

Soutenue le 22/01/19 après avis des rapporteurs, devant le jury d'examen :

<b>M. Y. Bultel, Professeur, INP Grenoble</b>	<b>Président</b>
<b>M. P. Notten, Professeur, Université d'Eindhoven</b>	<b>Rapporteur</b>
<b>M. F. Favier, CNRS Researcher, Univ. de Montpellier II</b>	<b>Rapporteur</b>
<b>Mme N. Krins, MCF, Univ. Pierre et Marie Curie</b>	<b>Examineur</b>
<b>M. A. A. Franco, Professeur, UPJV Amiens</b>	<b>Directeur de thèse</b>
<b>M. D. Larcher, Professeur, UPJV Amiens</b>	<b>Invité</b>
<b>M. N. Chadourne, Ingénieur, IRT Saint-Exupéry</b>	<b>Invité</b>





*« Dans la vie il n'y a pas de solutions ; il y a des forces en marche : il faut les créer et les solutions suivent. »*

*- Antoine de Saint-Exupéry -*

*“Much to learn, you still have”*

*- Master Yoda -*

*“An expert is a man who has made all the mistakes which can be made, in a narrow field.”*

*- Niels Bohr -*





## Acknowledgments

Dear reader, the document you are about to read is the fulfilment of three years of thesis work. Along the winding pathways taken, this journey was enriching on both professional and personal aspects and empowered by all the people I had the chance to meet.

As all trip, an end is needed and I would like to deeply acknowledge the jury members F. Favier, P. Notten, N. Krins and Y. Bultel for giving me the chance to defend my thesis, and this way, they allowed me to close the Ph.D. student chapter to move toward new adventures. Still, prior to say goodbye, I want first to thank all the people who helped me along the expedition.

First of all, I would like to thank my supervisor A. A. Franco for giving me the chance to join the LRCS, to undertake this thesis work and to develop my skills in an enriching international team. Also, I thank him for triggering my scientific curiosity with hot topics such as virtual reality and for encouraging me to attend events to learn how to popularize science (Fête des science, Pint of Science, MT180).

In parallel, I would like to express my sincere gratitude to all my IRT supervisors. Initially, G. Gager taught me the rigorous attitude to adopt to commit the imposed project deadlines. Later, N. Chadourne was a strong pillar to achieve this thesis work. He strongly and enthusiastically supported me along the thesis journey and joined to R. Sustra-Orus they offered me the possibility to stay onboard the more electrical aircraft. For that, I would like to deeply acknowledge them.

Moreover, it is very important to me to express my sincere gratefulness to D. Larcher. Not officially involved in my thesis, he still guided me through it without asking any recognition even though he won mine fully (and an apple pie thanks to a winning bet). Dominique is for me the personification of the researcher, passionate by science and always incline to share his broad knowledge. He always enticed me to merge disciplines and to take inspiration from the surrounded nature. For all these reasons, I want to say “Merci Domi, milles fois!”.

My sincere thanks also goes to the industrial members of Safran, Zodiac Aerospace and Airbus who were involved and strongly supported the CELIA project and especially to A. Boisard, G. Cherouvrier, J. Labbé, C. Wolff, and M. Freire.

I would like also to thank B. Girard and F. Coccetti for following my work at IRT. In addition, I would like also to address special thanks to I. Calvez and N. Chadourne for helping

me to solve the several setbacks I encountered during my many (jinxed) commutations in between IRT Saint Exupéry and LRCS. In add, I would like to thank Julien Escobar for his wise manuscript corrections.

Along this three years, I had the chance to work, exchange, debate, get help from several of my colleagues and so I want to give many thanks especially to Y. Yin and A. Torayev (my Li-O<sub>2</sub> teammates), V. Thangavel, A. Jameli, C. Surcin, M. Morcrette, M. Courty, S. Laruelle, S. Grugeon, D. Hubert, N. Recham, C. Delacourt, R. Janot, C. Lenfant and V. Viallet from LRCS; M. Mammeri from LAMFA; E. Legrand from LG2A; V. Bequet from UPJV and C. Pivot, A. Durier, P. Frey, F. Lakermi, C. David, M. Morin, P. Martinez, L. Hermette, P. Zaffalon and F. Mir from IRT Saint-Exupéry (hopping to not forget anyone). More largely I would like to thank all my colleagues from both IRT Saint-Exupéry and LRCS for enlighting my days.

These three years at LRCS and IRT Saint-Exupéry would remain as a wonderful memory. Special thanks to A. Pessot who introduced me to IRT and to V. Novelli who took me under her wing since I arrived and made me discover “*the dolce vita*” in Roma. Also, many thanks to all the serious guys (and also all the folks, I let you find to which category you belong) that cross my path; M. Bazant, Y. Shao-Horn and B. Gallant for letting me discover MIT; P. Johansson and all his Chalmers team so kind with me during my stay there; M. Pouget for introducing me to acting; F. Luge who helped me to improve my MT180 speech; G. Besson for her support and for always finding the right way to captivate an audience; M. Maiza for the daily support and crazy USA trip; O. Beaujot for the energizing tea and shopping breaks; the guys from the prototyping: T. Lombard, F. Rabuel, J.-B. Chabert and special thought for R. David (for all the Justin Bieber songs I was enabled to not sing in the lab because of you); the CELIA and FUSHIA teams that always welcomed me so nicely Y. Zhang, A. Pessot, K. Mrozewski, S. Rigal and S. El Aabid; the IRT MT180 team for the funny moments shared for the sake of theatricality: B. Pawels, R. Dupuis, O. Chihani and C. Pecoste; my amazing officemates: V. Nehru Bandla, A. Thiam, L. C. Loiza Rodrigues, A. Torayev and Z. Su. Finally, many thanks to D. Leroy for helping me during the tough third year and for being a really enthusiastic intern.

I thank also all my friends from the lab and outside that I did not acknowledge yet for all the fun we had and the happy moments we shared in particular: Vianney, Simon, Charles-Antoine, Boris, Diane, Blanche, Marine, Agnes, Clément, Marlene, Ines, Clémence, Lucie,

Iryna, Damien, Ronan, Abbos, Garima, Thibault C., Thibault V., Chloé, Lucas, Nautille, Alexandre, Victor, Alice, the Delirium, the Network and the Glou Café.

As the list is too long it was hard to quote everybody one by one so please forgive for that. I want to stress that I was really pleased to meet all of you guys (PhDs, post-docs, Masters students, ice-skating fellows and Krav-maga ones).

Besides, I would like to thank my beloved family thanks to who I was able to follow my studies. I deeply acknowledge my parents for letting me do and for helping me to do whatever I felt necessary to broaden my mind (even though it implies a 6-month trip on my own without preparation at the opposite side of the earth). I also thank my sister with who I share so much, always happy to travel and to party together. Also, I acknowledge my grand-mother always joyful to tell us how much our grandfather would be proud of his grandchildren.

Last but not least, I would like to thank this guy (as Laura says) or more accurately THE guy thanks to who I have spent three delighted years. Gaspard, thanks you so much for being so supportive and for all the cheerful moments you created for us. I am so excited to discover what the future holds for us in our next adventures together!



## Preface

The work presented in this manuscript is the witness of the strong collaboration between IRT Saint-Exupéry and LRCS (Unité Mixte de Recherche CNRS 7314, Université de Picardie Jules Verne) and was developed within to the frame of the CELIA project. This project, led by IRT Saint Exupéry, gathered another academic member, IMS, as well as three of the world leading aeronautical suppliers which are Safran, Zodiac Aerospace and Airbus. The project was funded by IRT Saint-Exupéry based on the financial participations from the industrial members in parallel to an ANR funding. The thesis work was supervised by Pr. Alejandro A. Franco at LRCS. The thesis work was pioneered as it focused on lithium-air batteries development with as a target aeronautical applications. The project was initially followed at IRT Saint-Exupéry by Guillaume Gager as the Project Manager and then later by Nicolas Chadourne as the Project Manager and Aircraft Technical Referent. The gathering in this manuscript of the results obtained during these three years was proposed as the completion for the PhD degree from Université de Picardie Jules Verne.

The Chapters III and IV were presented in two different international conferences. In 2017, the modeling results were unveiled at the 68<sup>th</sup> Annual Meeting of the International Society of Electrochemistry (ISE) in Providence. Later in 2018, combination of the experimental and modeling discoveries was disclosed during the European Material Research Society (EMRS) Fall Meeting in Warsaw. Chapter III and Chapter IV were the subject of two papers. The first one, entitled “Investigation of bi-porous electrodes for lithium oxygen batteries” (*C. Gaya, Y. Yin, A. Torayev, Y. Mammeri, A. A. Franco, Electrochim. Acta, 279, 118-127, 2018*) is already published. The second one which focused on “Characterization of the porosity in highly porous carbon-loaded plastic flexible film electrodes” (*C. Gaya, A. A. Franco, C. Surcin, M. Courty, D. Larcher*) was at the time of the PhD defence still under submission. Further publications based on the last results are under consideration. Participation to two others publications as co-author enabled to broaden the approach developed in this work (“Impact of  $\text{Li}_2\text{O}_2$  Particle Size on  $\text{Li}-\text{O}_2$  Battery Charge Process: Insights from a Multiscale Modeling Perspective”, *Y. Yin, C. Gaya, A. Torayev, V. Thangavel, A. A. Franco, J. Phys. Chem. Lett., 7, 3897–3902, 2016*; “Linking the Performances of  $\text{Li}-\text{O}_2$  Batteries to Discharge Rate and Electrode and Electrolyte Properties through the Nucleation Mechanism of  $\text{Li}_2\text{O}_2$ ”, *Y. Yin, A. Torayev, C. Gaya, Y. Mammeri, A. A. Franco, J. Phys. Chem. C, 121, 19577–19585, 2017*).



## Acronyms

<b>NASA:</b>	National Aeronautics and Space Administration
<b>ACARE:</b>	Advisory Council for Aeronautics Research in Europe
<b>MEA:</b>	More Electrical Aircraft
<b>LIBs:</b>	Lithium-ion batteries
<b>LiPo:</b>	Lithium Polymer
<b>APU:</b>	Auxiliary Power Unit
<b>NTSB:</b>	National Transport Safety Board
<b>LEAPTech:</b>	Leading Edge Asynchronous Propeller Technology
<b>LISs:</b>	Lithium-sulfur batteries
<b>CIRA:</b>	Italian Aerospace Research center
<b>PEMFC:</b>	Proton Exchange Membrane Fuel Cell
<b>DLR:</b>	Deutsches Zentrum für Luft-und Raumfahrt
<b>DoD:</b>	Depth of Discharge
<b>HEV:</b>	Hybrid Electric Vehicle
<b>EV:</b>	Electric Vehicle
<b>LABs:</b>	Lithium-air batteries
<b>LOBs:</b>	Lithium-oxygen batteries
<b>BMS:</b>	Battery Management System
<b>RTIL:</b>	Room Temperature Ionic Liquids
<b>ORR:</b>	Oxygen Reduction Reaction
<b>OER:</b>	Oxygen Evolution Reaction
<b>RH:</b>	Relative Humidity
<b>PVdF:</b>	Polyvinylidene diFluoride
<b>DMSO:</b>	Dimethyl Sulfoxide
<b>PTFE:</b>	Polytetrafluoroethylene
<b>NMP:</b>	N-Methyl-2-pyrrolidone
<b>DBP:</b>	Dibutyl Phthalate
<b>DMSO:</b>	Dimethyl sulfoxide
<b>DME:</b>	Dimethoxyethane
<b>TriGDME:</b>	Triethylene glycol dimethyl ether



<b>TetraGDME:</b>	Tetraethylene glycol dimethyl ether
<b>DMA:</b>	N,N-Dimethylacetamide
<b>SSA:</b>	Specific Surface Area
<b>DSC:</b>	Differential scanning calorimetry
<b>SEM:</b>	Scanning Electron Microscopy
<b>EDX:</b>	Energy Dispersive X-Ray
<b>IR:</b>	Infrared
<b>SEI:</b>	Solid Electrolyte Interphase
<b>LiClO<sub>4</sub>:</b>	Lithium perchlorate
<b>LiTFSI:</b>	Bis(trifluoromethane)sulfonimide lithium salt
<b>LiNO<sub>3</sub>:</b>	Lithium Nitrate
<b>LiI:</b>	Lithium Iodide
<b>CNT:</b>	Classical Nucleation Theory
<b>GDL:</b>	Gas Diffusion Layer
<b>OCV:</b>	Open Circuit Voltage

## Nomenclature

$\varepsilon_i$ :	Porosity of domain $i$
$D_0$ :	Oxygen diffusion coefficient in the electrolyte
$D$ :	Effective oxygen diffusion coefficient in the electrolyte
$\tau_i$ :	Tortuosity of the domain $i$
$c^X$ :	Concentration of the X specie
$J_X^{Diff}$ :	Diffusion flux of the X specie
$S_X^{i \rightarrow j}$ :	Intraflux between domain $i$ and $j$
$R_x$ :	Source term due to reactions producing or consuming the X specie
$S_X^{i \rightarrow j}$ :	Intraflux between domain $i$ and $j$
$A_{contact}$ :	Contact surface between meso and macro domains
$V_{Li_2O_2}$ :	Volume of $Li_2O_2$ produced
$M_{Li_2O_2}$ :	$Li_2O_2$ molar mass
$\rho_{Li_2O_2}$ :	$Li_2O_2$ density
$V_m$ :	Molar volume
$I$ :	Current
$j_{Far}$ :	Overall Faradaic current
$\eta$ :	Overpotential
$n$ :	Number of electrons
$k$ :	Prefactor
$\zeta^{tunneling}$ :	Tunneling function
$U$ :	Cell potential
$U_0$ :	Thermodynamic standard cell potential
$a_{i,j}$ :	Active surface available in domain $i$ and bin $j$
$\delta_{i,j}$ :	$Li_2O_2$ thickness in domain $i$ and bin $j$
$\alpha$ :	Symmetric factor in Butler-Volmer equation
$\beta$ :	Symmetric factor in Tafel equation
$\theta$ :	Contact surface ratio
$dt$ :	Time step
$dx$ :	Bin unit

<b><i>P</i></b> :	Number of bins in the separator
<b><i>Q</i></b> :	Number of bins in the cathode
<b><i>r</i></b> :	radius
<b><i>F</i></b> :	Faraday constant
<b><i>R</i></b> :	Gas constant
<b><i>k<sub>B</sub></i></b> :	Boltzmann constant
<b><i>T</i></b> :	Temperature
<b><math>\Delta G</math></b> :	Nucleation energy barrier
<b><i>E<sub>b</sub></i></b> :	Binding energy between Li <sub>2</sub> O <sub>2</sub> and the electrode material
<b><math>\sigma</math></b> :	Specific energy between Li <sub>2</sub> O <sub>2</sub> and the electrolyte
<b><i>B</i></b> :	Geometrical parameter
<b><i>v</i></b> :	Kinetic rate

## Figures List

Figure I. 1: Schematic of the MEA concept based on fuel cells power supply compared to conventional aircraft. <sup>5</sup> .....	1
Figure I. 2: Taurus G4 conception schematic with battery packs locations spotted with numbers 1, 2 and 3. <sup>7</sup> .....	2
Figure I. 3: LEAPTech aircraft first conceptualization. <sup>9</sup> .....	2
Figure I. 4: Picture of Zephyr 7, the Airbus drone powered by photovoltaic cells and Li-sulfur cells (source: <a href="https://www.droneuniversities.com">https://www.droneuniversities.com</a> ). .....	3
Figure I. 5: Picture of Antares DLR-H2 the first aircraft powered by fuel cells (source: <a href="https://www.dlr.de">https://www.dlr.de</a> ). .....	4
Figure I. 6: Drawing of the car “La jamais contente”. <sup>29</sup> .....	8
Figure I. 7: Worldwide battery market from 1990 to 2015. <sup>49</sup> .....	10
Figure I. 8: LIBs worldwide market in volume (a) and in market share (b). (Values from 2015). <sup>48</sup> .....	11
Figure I. 9: Schematic of the different industrial cells configurations. <sup>38</sup> .....	11
Figure I. 10: Decrease of practical energy density over the battery value chain. <sup>31</sup> .....	12
Figure I. 11: The battery technology landscape as proposed by Tarascon in 2010. <sup>47</sup> ....	13
Figure I. 12: Evolution of the number of publications related to the terms “Li-air batteries” or “lithium-air batteries” or “Li-O <sub>2</sub> batteries” or “lithium-oxygen batteries” on Web of Science (data from 27/06/18). .....	14
Figure I. 13: The 10 top countries releasing the most publication on “Li-air batteries” or “lithium-air batteries” or “Li-O <sub>2</sub> batteries” or “lithium-oxygen batteries” according to Web of Science (data from 03/07/18). .....	15
Figure I. 14: Schematics of LABs discharge. ....	16
Figure I. 15: Schematics of the several kind of LABs. <sup>26</sup> .....	16
Figure I. 16: Schematic of lithium dissolution and deposition on top of lithium metal electrode. <sup>69</sup> .....	18
Figure I. 17: Schematics of oxygen transport during discharge depending on its solubility in the electrolyte. <sup>70</sup> .....	18
Figure I. 18: Description of the solution mechanism and surface mechanism occurring in Li-O <sub>2</sub> batteries. In first case, Li <sub>2</sub> O <sub>2</sub> is soluble (due to the use of high donor number) while in the second one Li <sub>2</sub> O <sub>2</sub> is insoluble (low donor number). <sup>81</sup> .....	20

Figure I. 19: Discharge and charge voltage evolution of a non-aqueous cell at $\sim 0.1 \text{ mA/cm}^2$ express in function of the charge capacity per gram of Carbon SP in the cathode. <sup>26</sup> .....	24
Figure I. 20: Schematic of LABs limitations from lab scale to aeronautical application. (Based on references <sup>53,117,118</sup> ). .....	25
Figure I. 21: Impact of the carbon used as cathode for LABs. ....	26
Figure I. 22: Variation with geologic time of Earth's atmosphere composition. <sup>154</sup> .....	29
Figure I. 23: Schematic of Earth's atmosphere structure and evolution of pressure and temperature with altitude. <sup>157</sup> .....	30
Figure I. 24: The mixing ratio of some atmospheric gases in Earth's Atmosphere as a function of altitude. <sup>11</sup> .....	30
Figure I. 25: Records of temperature, pressure, RH and ozone concentration during a commercial flight (Paris-Washington, on July 9, 1995). <sup>149</sup> .....	31
Figure I. 26: Discharge curves for an aprotic Li-O <sub>2</sub> cell (based on a Ketjen Black positive electrode) The curves give the cell output potential as a function of discharge capacity per gram of carbon in the positive electrode ( $\text{mAh.g}^{-1}$ ). $U_0$ is the thermodynamic standard cell potential. <sup>26</sup> .....	33
Figure I. 27: Discharge curves at different current densities (capacities per electrode geometric area).The vertical lines defined the mean values observed for each condition and dash lines the standard deviation. (The black curves correspond to cells used in their publication). <sup>171</sup> .....	34
Figure I. 28: Electron microscopy (FESEM) images at a magnification of 20000x of a pristine positive electrode (a) and after full discharge at (b) $5 \mu\text{A/cm}^2$ , (c) $10 \mu\text{A/cm}^2$ , (d) $25 \mu\text{A/cm}^2$ , (e) $50 \mu\text{A/cm}^2$ , and (f) $100 \mu\text{A/cm}^2$ , with the corresponding discharge curves. Scale bar 400nm. <sup>172</sup> .....	35
Figure I. 29: (a) First discharge curves of cells wetted by electrolyte composed of 0.1 M LiClO <sub>4</sub> in DME. The flow is rather water-free or water-saturated oxygen. "Leaker cell" corresponds to small leak of ambient air inside the cell and "water vapor cell" corresponds to water saturated oxygen (b) First discharge curves of cell with non-contaminated or water-contaminated electrolyte. <sup>175</sup> .....	36
Figure I. 30: LABs cycling curves obtained with different gas composition (1) dry oxygen (0 %RH), (2) oxygen with 15 %RH and (3) ambient air (50 %RH) (a) Cycling conditions: 50 $\text{mA.g}^{-1}$ applied between 2 V and 4.5 V (b) Cycling conditions: 200 $\text{mA.g}^{-1}$ with a fixed capacity of 1000 $\text{mA.g}^{-1}$ (c) Cycling at several current densities. <sup>177</sup> .....	37

Figure I. 31: SEM images of KB electrodes at different states for the $\text{Li}_2\text{O}_2$ batteries in pure/dry $\text{O}_2$ atmosphere (a, b, c), in $\text{O}_2$ atmosphere with an 15 % RH (d, e, f), and in ambient air with 50 %RH (g, h, i): before discharge (a, d, g), after discharge (b, e, h) and after recharge (c, f, i), respectively. <sup>177</sup> .....	38
Figure I. 32: $\text{Li}_2\text{O}_2$ yield versus discharge capacity of carbon paper cathodes discharged at 1 $\mu\text{A}$ and 30 $\mu\text{A}$ with different water contents in the electrolyte. The yield consists of the determined mass of $\text{Li}_2\text{O}_2$ found in the cathode related to the mass expected from the charges passed during discharge. <sup>179</sup> .....	39
Figure I. 33: Discharge curves of $\text{Li}-\text{O}_2/\text{CO}_2$ batteries with various $\text{O}_2/\text{CO}_2$ ratios at 25°C (0.2 $\text{mA}\cdot\text{cm}^{-2}$ ). <sup>181</sup> .....	39
Figure I. 34: Gas production according to charge potential applied. <sup>178</sup> .....	40
Figure I. 35: Picture of a negative electrode before cycling (a) and after 51 <sup>th</sup> cycles (cutoffs at 500 $\text{mAh g}^{-1}$ ) (b). <sup>160</sup> .....	40
Figure I. 36: Picture of a Li-air pouch cell with gas diffusion membrane (PTFE) after discharge in ambient air. <sup>186</sup> .....	41
Figure I. 37: Impact of temperature on cycling for TEGDME-based electrolyte lithium–oxygen cells Capacity limited to 1000 $\text{mAh}\cdot\text{g}^{-1}_{\text{carbon}}$ . Current: 100 $\text{mA}\cdot\text{g}^{-1}_{\text{carbon}}$ . <sup>189</sup> .....	42
Figure I. 38: Proposed mechanism to explain $\text{Li}_2\text{O}_2$ crystallites growth. <sup>169</sup> .....	43
Figure I. 39: Discharge curves at high and low discharge rate at several pressure (a) 1 atm (b) 3 atm (c) 5 atm (d) 10 atm. <sup>170</sup> .....	44
Figure I. 40: Discharge curves for diglyme-based Li-air cells discharged at 0.1 $\text{mA}\cdot\text{cm}^{-2}$ (a) and 1 or 2 $\text{mA}\cdot\text{cm}^{-2}$ (b) for several pressures (1 atm, 5 atm and 25 atm). <sup>192</sup> .....	45
Figure I. 41: LABs capacities and cycling abilities according to applied oxygen partial pressure (a) 1 <sup>st</sup> discharge, (b) Cycling with cutoff at 300 $\text{mAh}/\text{g}_{\text{electrode}}$ , (c) Cycling with cutoff at 100 $\text{mAh}/\text{g}_{\text{electrode}}$ , (d) Cycling properties versus oxygen partial pressure while applying a cutoff at 300 $\text{mAh}/\text{g}_{\text{electrode}}$ . <sup>195</sup> .....	46
Figure I. 42: Highlighting of the capacity limitation impact on cyclability overestimation. <sup>196,197</sup> .....	47
Figure I. 43: Non-exhaustive list of the several expressions of LABs capacity in the literature. <sup>26,51,55,56,198–201</sup> .....	48
Figure II. 1: Modeling of Ketjen Black based LABs discharge capacities compared to Carbon SP based ones. <sup>128</sup> .....	52
Figure II. 2: Mixing device for NMP slurries (Ultraturax).....	55

Figure II. 3: Multi-steps solvent addition process for Dip-coating electrode fabrication process. ....	55
Figure II. 4: Schematics of Dip-coated electrode fabrication process and related porosity creation. ....	56
Figure II. 5: Observation of the dip-coating process issues to overcome a) aggregates and inhomogeneous coating on top of the stainless steel grid b) cracks in the coating. ....	57
Figure II. 6: Experimental plan design to test the several parameters impacting the grid coating efficiency. The reference parameters are highlighted in dark blue. ....	57
Figure II. 7: SEM picture of a dip-coated electrode formulated with 15 wt% of binder. ....	58
Figure II. 8: SEM picture of a dip-coated electrode formulated with 15 wt% of binder and a slow drying process. ....	58
Figure II. 9: SEM pictures of a dip-coated electrode at different scale for a formulation with a dry mass of 0.28 %. ....	59
Figure II. 10: Schematics of the flexible electrodes fabrication process and related porosity creation. ....	60
Figure II. 11: Comparison of Dip-coating and Porous Flexible electrode fabrication processes pros and cons. ....	61
Figure II. 12: Pictures of disassembled and assembled Swagelok. ....	64
Figure II. 13: Pictures of (a) a dip-coated cathode (b) a porous flexible cathode (c) a GDL cathode and (d) a lithium anode. ....	64
Figure II. 14: Schematic of the several layers superposed during Swagelok assembling. In the case of dip-coated cathode, no grid is added as the cathode is already supported by a stainless steel grid. ....	65
Figure II. 15: Evolution of the atmosphere controller container for LABs called “Le Parfait” container. (a) First design at LRCS, (b) New design made for the study. ....	66
Figure II. 16: Schematic of the oxygen flow system. ....	67
Figure II. 17: Gas mixing system. ....	68
Figure II. 18: Picture of the pycnometer (AccuPyc 1330, Micromeritics). ....	69
Figure II. 19: Picture of the N <sub>2</sub> adsorption and desorption measurement device at 77 K using N <sub>2</sub> (ASAP 2020, Micromeritics). ....	70
Figure II. 20: DSC curve of PVdF-HFP carried on at 5 K/min from 25 °C to 250 °C... ..	71
Figure II. 21: Picture of VSP (Bio-Logic). ....	71
Figure II. 22: Polarization tests for DMSO + 1 M LiClO <sub>4</sub> as the electrolyte. Succession of current steps at 25 μA and -25 μA, each for 2 hours. ....	72

Figure II. 23: Pristine GDL SEM picture. ....	73
Figure II. 24: EDX mapping of the carbon element (b) in the corresponding SEM picture (a). ....	74
Figure II. 25: Pictures of the ASAP tubes after degassing containing the electrode DBP <sub>60</sub> without DBP removal (a) DBP <sub>60</sub> with DBP extracted (3 times 15 minutes in ether) (b).....	74
Figure II. 26: IR spectra of the liquid recovered after ASAP degassing, compared to pure DBP spectra.....	75
Figure II. 27: Water content results for electrolytes based on TriGDME and TetraGDME with several LiTFSI concentrations. ....	76
Figure III. 1: Structure of the bronchial tree. <sup>218</sup> .....	80
Figure III. 2: LABs electrode concept development.....	81
Figure III. 3: Schematics of the system described in the model considering coexistence of two domains in the cathode: macro-porous and meso-porous domains.....	83
Figure III. 4: Illustration of the tortuosity concept as proposed by Tjaden et al.. <sup>220</sup> .....	85
Figure III. 5: Description of the simulated system. ....	87
Figure III. 6: Calculated evolution of macro-pores active surface (b) and meso-pores one (c), of oxygen concentration in macro-pores (d) and meso-pores (e) and of porosity in macro-pores (f) and meso-pores (g) linked to the discharge curve (a) done at $I = 0.625 \text{ A/m}^2_{\text{geometric}}$ for an electrode with 50 wt% of carbon and 20 % of volume macro porosity volume ratio (initial stage was estimated after 10 s and final one corresponded to end of discharge). ....	91
Figure III. 7: a) Calculated impact of cathode thickness ( $\mu\text{m}$ ) on electrode discharge capacity ( $\text{mAh/g}_{\text{electrode}}$ ) for a current density of $62.5 \mu\text{A/cm}^2_{\text{geometric}}$ and corresponding evolution of mesoporous domain porosity for electrodes with a thickness of 75 and 200 $\mu\text{m}$ (b) and c) respectively). ....	93
Figure III. 8: Calculated impact of the current density (a) $62.5 \mu\text{A/cm}^2_{\text{geometric}}$ , b) $125 \mu\text{A/cm}^2_{\text{geometric}}$ , c) $250 \mu\text{A/cm}^2_{\text{geometric}}$ ) on the discharge capacity ( $\text{mAh/g}_{\text{carbon}}$ ) for different formulations based on Ketjen Black electrodes. ....	95
Figure III. 9: Calculated impact of the macro-porous volume ratio (from 20 to 50 %, for electrodes with different Ketjen Black ratios 50 wt%, 60 wt% and 70 wt%. Current density was estimated for each case depending on the available surface carbon and corresponded to $0.1 \mu\text{A/m}^2_{\text{carbon}}$ . ....	96



Figure III. 10: Simulation of the discharge over-potential evolution with available carbon surface decrease for an electrode with 50 wt% of carbon and 20 % of volume macro porosity volume ratio. Current density applied: $0.625 \text{ A/m}^2_{\text{geometric}}$ . .....	98
Figure III. 11: Evolution of macro-pores active surface (b) and meso-pores one (c), of oxygen concentration in macro-pores (d) and meso-pores (e) and of porosity in macro-pores (f) and meso-pores (g) linked to the discharge curve (a) done at $I = 62.5 \mu\text{A/cm}^2_{\text{geometric}}$ for an electrode with 60 wt% of Ketjen Black and 30 % of volume macro porosity volume ratio (initial stage was estimated after 10 s and final one corresponds to end of discharge). .....	99
Figure III. 12: Evolution of macro-pores active surface (b) and mesopores one (c), of oxygen concentration in macro-pores (d) and meso-pores (e) and of porosity in macro-pores (f) and meso-pores (g) linked to the discharge curve (a) done at $I = 62.5 \mu\text{A/cm}^2_{\text{geometric}}$ for an electrode with 60 wt% of carbon Super P and 30 % of volume macro porosity volume ratio (initial stage was estimated after 10 s and final one corresponds to end of discharge).....	100
Figure IV. 1: Discharge curves of several electrodes along the improvement of dip-coating process ( $I = 25 \mu\text{A}$ , electrolyte: dried DME + 0.1 M $\text{LiClO}_4$ ). .....	105
Figure IV. 2: SEM pictures of the electrodes from $\text{B}_{15}\text{D}_{2.8}\text{F}$ and $\text{B}_{15}\text{D}_{2.8}\text{S}$ formulations. ....	106
Figure IV. 3: Discharge curves of several dip-coated electrodes made with different dry mass ratio ( $I = 25 \mu\text{A}$ , electrolyte: dried DME + 0.1 M $\text{LiClO}_4$ ).....	106
Figure IV. 4: SEM pictures of an electrode made with the formulation $\text{B}_{15}\text{D}_{0.28}\text{S}$ at a magnificence of a) 40x and b) 150x.....	107
Figure IV. 5: SEM pictures of an electrode made with the formulation $\text{B}_{15}\text{D}_{0.28}\text{SM}$ at a magnificence of a) 40x and b) 130x.....	107
Figure IV. 6: Chemical formulas of a) DMSO, b) DME, c) TriGDME and d) TetraGDME. ....	109
Figure IV. 7: Polarization tests ( $\pm 25 \mu\text{A}$ for 2h) a) Comparison between DME and DMSO and b) and between TriGDME with $\text{LiClO}_4$ or LiTFSI as a salt. ....	110
Figure IV. 8: Discharge/Charge of an electrode from batch $\text{B}_{10}\text{D}_{2.8}\text{F}$ at $\pm 25 \mu\text{A}$ . ....	111
Figure IV. 9: Evolution of the electrolytes tested along the study. ....	112
Figure IV. 10: Statistical analysis of the efficiency of the DBP extraction (50 disks from $\text{DBP}_{65}$ ). .....	113
Figure IV. 11: Efficiency of DBP removal along the soaking process in ether depending on the ether cleaning steps applied to $\text{DBP}_{60}$ electrodes. ....	114

Figure IV. 12: Theoretical porosities compared to estimated porosities, calculations based on DBP mass loss. The mean values of the estimated porosities were reported in blue, while the maximum and minimum ones were shown in grey. The number of values considered for the mean values calculations were provided in the table in grey. ....	115
Figure IV. 13: Films thickness before and after DBP removal.....	117
Figure IV. 14: a) Evolution of the disks diameter (initially $\varnothing = 11$ mm) for electrodes from DBP <sub>60</sub> and DBP <sub>80</sub> and b) comparison of the shrinkage observed for the several formulations after DBP extraction. For b) electrodes were dried at the last cleaning step under a glass side to remain flat. ....	117
Figure IV. 15: Total porosity (v%) for three disks cut from DBP <sub>40</sub> , DBP <sub>60</sub> and DBP <sub>80</sub> films, measured before (blue bars) and after (gray bars) DBP extraction. The orange bars represent the volume of DBP extracted during the ether leaching step. The green bars represent the mesoporous contribution to the total volume of extracted films.....	119
Figure IV. 16: SEM pictures of (a) DBP <sub>40</sub> , (b) DBP <sub>60</sub> and (c) DBP <sub>80</sub> films before (left column) and after (right column) DBP extraction. (Magnification a) 2500x b) 2400x and c) 2500x).....	121
Figure IV. 17: Diameter evolution for disks (initially $\varnothing = 9$ mm) cut from extracted films DBP <sub>40</sub> and DBP <sub>80</sub> a) initially, b) immersed in ether and c) dried. ....	124
Figure IV. 18: DSC curves of DBP <sub>80</sub> before and after DBP extraction carried on under Argon at 5 K/min from 25 °C to 250 °C. ....	125
Figure IV. 19: Discharge curves of the Swagelok cells made using electrodes cut from a) DBP <sub>60</sub> and b) DBP <sub>80</sub> films at 50 $\mu$ A while in TriGDME + 0.5 M LiTFSI, reported in mAh.g <sup>-1</sup> <sub>electrode</sub> and mAh.cm <sup>-2</sup> <sub>electrode</sub> . Each color corresponds to the results obtained for the same cell. ....	126
Figure IV. 20: Discharge curves of the Swagelok cells made using electrodes cut from films DBP <sub>40</sub> at 200 $\mu$ A while using TriGDME + 0.5 M LiTFSI as the electrolyte reported in a) mAh.g <sup>-1</sup> <sub>electrode</sub> and b) mAh.cm <sup>-2</sup> <sub>electrode</sub> . ....	127
Figure IV. 21: SEM pictures taken from electrode DBP <sub>60</sub> previously discharged until 2 V at 50 $\mu$ A in TriGDME + 0.5 M LiTFSI. The corresponding capacities values are 2372 mAh/g <sub>electrode</sub> and 12 mAh/cm <sup>2</sup> <sub>electrode</sub> . ....	128
Figure IV. 22: a) XRD diagram of a DBP <sub>60</sub> electrode not discharge (bleu) and XRD diagram of a DBP <sub>60</sub> discharge electrode compared to b) XRD diagram of crystalline Li <sub>2</sub> O <sub>2</sub> . ....	129

Figure IV. 23: SEM pictures taken from electrode DBP <sub>80</sub> previously discharged until 2V (by consecutive repetition of ten hours of discharge, four hours of resting and EIS measurement between each cycle) at 50 $\mu$ A in TriGDME + 0.5 M LiTFSI. The corresponding capacities values are 1326 mAh/g <sub>electrode</sub> and 9 mAh/cm <sup>2</sup> <sub>electrode</sub> . .....	130
Figure IV. 24: Deformation of films a) DBP <sub>80</sub> and b) DBP <sub>60</sub> as seen in SEM pictures. ....	131
Figure V. 1: Discharge curves of the Swagelok cells made using electrodes cut from films a) DBP <sub>60</sub> & b) DBP <sub>80</sub> at 50 $\mu$ A while using TriGDME + 0.5 M LiTFSI as the electrolyte. The results are reported in percentage compared to the 3353 mAh.g <sup>-1</sup> <sub>electrode</sub> and 3420 mAh.g <sup>1</sup> <sub>electrode</sub> expected from the theoretical point of view. ....	134
Figure V. 2: Discharges curves of DBP <sub>60</sub> cells cycled at 50 $\mu$ A between 2 to 4.5 V with distinct cell preparation procedures. Capacities expressed in mAh/g <sub>electrode</sub> and mAh/cm <sup>2</sup> <sub>electrode</sub> . ....	135
Figure V. 3:a) Free energy diagram for nucleation and b) corresponding nucleation of metal nanoparticles as described by Polte. <sup>235</sup> .....	136
Figure V. 4: Zoom of the initial part of the discharges curves of DBP <sub>60</sub> cells cycled in TriGDME + 0.5 M LiTFSI at 50 $\mu$ A between 2 to 4.5 V. ....	137
Figure V. 5: Comparison of potentials at half first discharge for DBP <sub>60</sub> cells cycled in 325 $\mu$ L of TriGDME + 0.5 M LiTFSI at 50 $\mu$ A between 2 to 4.5 V after thirty minutes of precisely controlled oxygen flow. ....	138
Figure V. 6: Zoom in discharges curves in case of a DBP <sub>60</sub> cell cycled in 325 $\mu$ L of TriGDME + 0.5 M LiTFSI at 50 $\mu$ A between 2 to 4.5 V after thirty minutes of precisely controlled oxygen flow. ....	138
Figure V. 7: Room temperature evolution around the “Le Parfait” containers in the cycling room. ....	139
Figure V. 8: Removal of the discharge voltage oscillations thanks to temperature control at 25 °C. ....	139
Figure V. 9: First discharges of GDLs cells cycled in TriGDME + 0.5 M LiTFSI at 50 $\mu$ A between 2 to 4.5 V in a) not controlled conditions and b) controlled conditions (25 °C). Capacities were expressed in mAh/g <sub>electrode</sub> and mAh/cm <sup>2</sup> <sub>electrode</sub> . ....	141
Figure V. 10: First discharges of GDLs cells cycled in TriGDME + 0.5 M LiTFSI at 25 $\mu$ A between 2 to 4.5 V in not controlled conditions. Only the cell with the grey curve was exposed to air. Capacities expressed in a) mAh/g <sub>electrode</sub> and b) mAh/cm <sup>2</sup> <sub>electrode</sub> . ....	142

Figure V. 11: Discharge curves of the GDLs cells at 50 $\mu\text{A}$ in controlled conditions while using TriGDME + 0.5 M LiTFSI as the electrolyte. The results are reported in percentage compared to the $3402 \text{ mAh.g}^{-1}_{\text{electrode}}$ expected from the theoretical point of view. ....	142
Figure V. 12: SEM pictures of a) GDL electrode and TEM picture of b) Ketjen black powder. (Ketjen Black TEM results courtesy of Pr. D. Larcher).....	143
Figure V. 13: First discharges of GDLs cells cycled at 25 $^{\circ}\text{C}$ in TriGDME + 0.5 M LiTFSI at 50 $\mu\text{A}$ between 2 to 4.5 V Capacities expressed in a) $\text{mAh/g}_{\text{electrode}}$ and b) $\text{mAh/cm}^2_{\text{electrode}}$ . ....	144
Figure V. 14: First discharges of GDLs cells cycled between 2 to 4.5 V at different temperatures and currents. Only for 25 $\mu\text{A}$ and 25 $^{\circ}\text{C}$ the electrolyte was not dried, otherwise all the cells contained dried TriGDME + 0.5 M LiTFSI.....	147
Figure V. 15: Evolution of the discharges capacities mean value with temperature and discharge currents.....	148
Figure V. 16: Evolution of the standard deviation over mean capacity ratio with temperature and discharge currents.....	148
Figure V. 17: SEM picture of a toroidal particle formed on top of GDL discharge in cell containing TriGDME+ 1M $\text{LiNO}_3$ .....	150
Figure V. 18: SEM picture of red blood cell with clear toroidal shape. Image taken from Tamara et al. work. <sup>246</sup> .....	150
Figure V. 19: Schematic figured proposed by Aurbach et al. to highlight the several electrolyte properties impacting the surface and solution growth mechanisms in LABs and thus the film or toroid formation. <sup>81</sup> .....	151
Figure V. 20: Sum up of the several morphologies of LABs discharge products encountered across the literature. <sup>77,171,174,179,243,247</sup> .....	152
Figure V. 21: SEM picture of a glass fiber from separator deposited on top of a GDL fiber. ....	153
Figure V. 22: Schematic of the test implemented to define which part of the cell was responsible for capacity fading cathode versus separator/electrolyte/lithium. ....	154
Figure V. 23: Sum up of the several morphologies of LABs final discharge product observed after cycling in TriGDME + 0.5 M LiTFSI at different temperatures and currents. ....	154
Figure V. 24: SEM pictures of different discharge product morphologies deposited on the air side of cathodes operated at 27.5 $^{\circ}\text{C}$ and 25 $\mu\text{A}$ (a,b) and at 30 $^{\circ}\text{C}$ and 50 $\mu\text{A}$ (c,d). .....	155

Figure V. 25: Comparison of the SEM pictures of both sides of two cathodes operated at 27.5 °C and 50 μA.....	157
Figure V. 26: SEM pictures of a) a pristine cathode, b) the separator side of the cathode after discharge at 0.1 mA.cm <sup>-2</sup> and c) the air side of the cathode after discharge at 0.1 mA.cm <sup>-2</sup> as published in Zhang et al. work. <sup>249</sup> .....	158
Figure V. 27: SEM pictures of three different electrodes to demonstrate the variation of the discharge product morphology formed in the same side of an electrode. SEM image of Cathode D also spotted the variation within the same GDL fiber. ....	159
Figure V. 28: First discharges at 27.5 °C of cells made of GDLs pretreated at 400 °C and cycled in dried TriGDME + 0.5 M LiTFSI at 50 μA between 2 to 4.5 V. Capacities expressed in a) mAh/g <sub>electrode</sub> and b) mAh/cm <sup>2</sup> <sub>electrode</sub> .....	161
Figure V. 29: Several SEM pictures of the cathode E after cycling five times a GDL pretreated at 400 °C at 50 μA and 27 °C.....	162
Figure V. 30: Comparison of the GDLs pretreated at 400 °C a) mean capacity and b) the standard deviation ratio in opposition to previous GDLs cells. ....	162

## Table List

Table I. 1: Sum up of the most common battery technologies with detailed properties and pros and cons. ....	9
Table I. 2: List of the different redox-mediators and linked observations found by Park et al in literature. <sup>110</sup> .....	22
Table I. 3: Parameters selected for experiments simulating aircraft application of LABs. ....	31
Table II. 1: Formulations used to study porosity created along Bellcore process. ....	61
Table II. 2: Density estimations by pycnometry of the powders used for flexible electrode formulation. ....	69
Table II. 3: SSA estimations of the powders used for flexible electrode fabrication. ....	70
Table III. 1: List of the parameters used in the model. ....	90
Table IV. 1: Sum up of the formulations produced at lab scale. ....	104
Table IV. 2: Textural characterization of DBP <sub>40</sub> , DBP <sub>60</sub> and DBP <sub>80</sub> films before and after DBP leaching. ....	118
Table IV. 3: Evolutions in weight loss, porous volume and BET specific surface area (SSA) for DBP <sub>60</sub> along DBP extraction steps. ....	121



# Table of Contents

<b>General Introduction .....</b>	<b>1</b>
<b>Chapter I: State-of-the-art .....</b>	<b>7</b>
I.1. Evolution of the battery technologies .....	8
I.2. Definition of the case study: LABs .....	14
I.2.a. LABs: worldwide research status .....	14
I.2.b. LABs: working principle .....	16
I.2.c. The cathode: a key component for LABs .....	26
I.2.d. Gap between flight conditions and lab conditions.....	29
Aircraft conditions .....	29
Lab testing conditions .....	32
<i>Current density</i> .....	32
<i>Relative humidity and air composition</i> .....	35
<i>Temperature</i> .....	41
<i>Pressure</i> .....	43
I.2.e. How to define LABs capacity? .....	48
I.3. Thesis objectives .....	50
<b>Chapter II: Experimental Procedures .....</b>	<b>51</b>
II.1. Electrode fabrication process .....	52
II.1.a. Electrode materials .....	52
Carbons .....	52
Binders .....	53
Solvent for slurry preparation .....	53
Porogen agent .....	54
II.1.b. Dip-coated electrodes fabrication process.....	54
II.1.c. Porous flexible electrodes fabrication process .....	59
II.1.d. Comparison of the two electrodes fabrication processes .....	61



II.2. Battery assembling .....	63
II.2.a. Electrolyte preparation .....	63
II.2.b. Swagelok cell assembling .....	63
II.3. Experimental set-up for controlled LABs atmosphere.....	66
II.3.a. “Le Parfait” container.....	66
II.3.b. Gas flow system .....	67
II.4. Characterization techniques .....	69
II.4.a. Electrode characterization .....	69
Pycnometry measurements .....	69
Nitrogen adsorption measurements .....	69
DSC.....	70
II.4.b. Electrochemical characterization .....	71
Galvanostatic cycling.....	71
Polarization measurements .....	72
II.4.c. System characterization.....	73
SEM imaging & EDX Spectrometry .....	73
IR spectroscopy.....	74
XRD .....	75
Karl Fisher (HF).....	75
II.4.d. Continuum modeling.....	76
<b>Chapter III: Theoretical study of bi-porous electrodes .....</b>	<b>79</b>
III.1. Concept of porous electrodes with enhanced diffusion.....	80
III.2. Theoretical study.....	83
III.2.a. Model description .....	83
III.2.b. Discretization and boundary conditions.....	87
III.2.c. Parametrization .....	89
III.2.d. The reference case.....	90

III.2.e. Electrode formulation and design impacts .....	92
Effect of the electrode thickness .....	92
Macro-porous domain and carbon ratios combined effects .....	94
Effect of carbon surface .....	97
<b>Chapter IV: Experimental study of bi-porous electrodes .....</b>	<b>103</b>
IV.1. Dip-coated electrode: a first attempt toward bi-porous electrodes .....	104
IV.1.a. Formulations tested .....	104
IV.1.b. Preliminary tests .....	104
IV.2. Electrolyte modification .....	109
IV.3. Development of highly porous and flexible electrodes for LABs .....	113
IV.3.a. Efficiency of DBP removal .....	113
IV.3.b. Impact of DBP removal on porosity creation .....	115
First evaluation of the films porosity based on DBP mass loss .....	115
Volume modification along DBP extraction .....	116
Assessment of the films porosities .....	118
IV.3.c. Behavior of the films in the electrolyte solvent .....	123
IV.3.d. Thermal behavior of the films at high temperature .....	124
IV.3.e. Performances of the flexible porous carbon electrodes .....	125
IV.3.f. Discharge product formation .....	127
IV.3.g. Merging of theory with experiments .....	131
<b>Chapter V: Reproducibility issues and sensitivity to operating conditions .....</b>	<b>133</b>
V.1. Lab reproducibility issues .....	134
V.1.a Description of the reproducibility issues .....	134
V.1.b. Attempts to reduce the uncertainty .....	134
Enhanced control of the electrolyte addition step and oxygen supply .....	134
Observations of the discharge curves characteristics .....	136

Enhanced control of the operating temperature and electrode mechanical stability .....	140
Enhanced control of water contamination .....	143
V.2. LABs sensitivity toward operating conditions.....	146
V.2.a. Temperature and current effects on discharge capacity .....	146
V.2.b. Temperature and current effects on discharge product morphology .....	149
Discharge product morphologies reported in literature .....	149
Discharge product morphologies observed in several operation conditions .....	152
V.3. LABs high sensitivity toward electrode surface .....	161
V.4. Conclusions on LABs reproducibility issues .....	164
<b>Chapter VI: General conclusions and perspectives .....</b>	<b>165</b>
<b>Annex: Model contamination .....</b>	<b>193</b>
<b>Annex: Air Flushing .....</b>	<b>201</b>
<b>Annex: French Description .....</b>	<b>203</b>



# GENERAL INTRODUCTION

Worldwide connectivity is required to sustain the globalization of our societies. To promote the mobility of people all around the world, with a reduced commuting time, a strong aeronautical network has been settled. Still, the air traffic is always under improvement as it is a key parameter of societies global development, as recognized by the NASA and ACARE.<sup>1,2</sup>

Notwithstanding a positive impact on society reinforcement, air transport growth comes along with stressed environmental issues such as pollution and noise emissions. ACARE report defines two targets for 2050 in order to solve such drawbacks. The first given directive is to reduce noise and pollution thanks to new technological and design solutions. The second one, with the aim to reach long term sustainability, implies to move from current kerosene consumption toward the use of sustainable alternative fuels.<sup>2</sup>

Currently, aircraft have different supplies of energy, the propulsion is managed on one side while the onboard equipment (electronic system, light and ice protection for instance) is powered differently. Usually, this second power system is based on a mix of electrical, hydraulic/pneumatic and mechanical energies.<sup>3,4</sup> A first step toward a more environment-friendly aircraft is to move the onboard equipment energy supply into electric power. To do so, several devices could be considered, as for instance fuel cells as described in Figure I. 1.

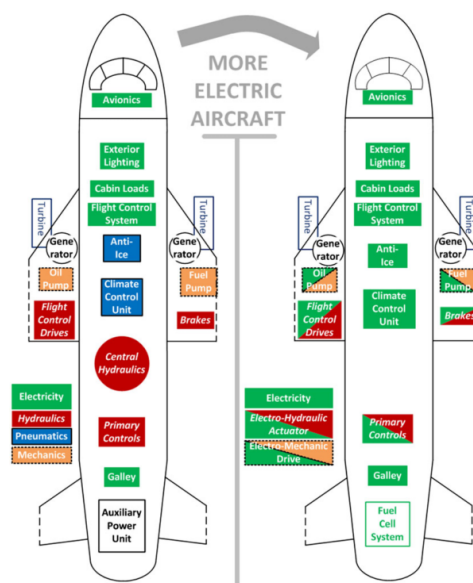


Figure I. 1: Schematic of the MEA concept based on fuel cells power supply compared to conventional aircraft.<sup>5</sup>

This aircraft development concept is known as More Electric Aircraft (MEA) and has been already studied since the 1980s.<sup>3</sup> In addition to reduced environmental impact, such hybrid systems could lead to a reduction up to 80 % of the ticket price according to Zunum Aero.<sup>6</sup>

To achieve long term sustainability, aircraft manufacturers examine development of aircrafts with electric propulsion, leading to the creation of fully electrical aircrafts. The Slovenian company Pipistrel, was pioneer as it succeeded to build the first four-seat electric aircraft and won the “Nasa Green Flight Challenge” in 2011 with their Taurus G4. To achieve an energy efficiency of 200 Passengers-Miles-per-Gallon, the aircraft was designed with a twin-fuselage and one propeller concept. Thereby, the Taurus G4 was able to host the three battery packs (88 LiPo cells in each pack) necessary to reach the energy target, as underlined in Figure I. 2.<sup>7</sup>

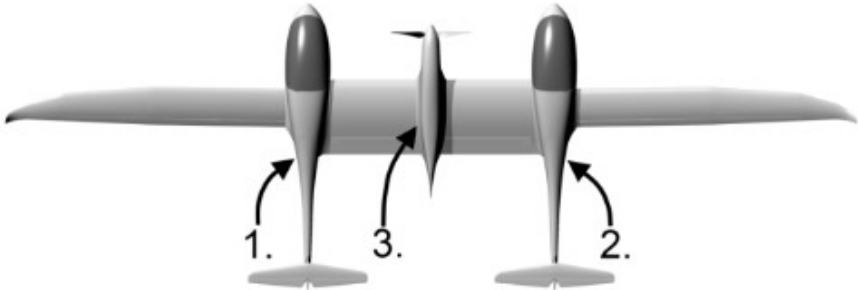


Figure I. 2: Taurus G4 conception schematic with battery packs locations spotted with numbers 1, 2 and 3.<sup>7</sup>

Moving from traditional aircraft powered by kerosene consumption to fully electric airplanes is tricky. Indeed, the energy storage devices taken onboard should be able to compete with the high gravimetric energy of kerosene ( $13000 \text{ Wh.kg}^{-1}$ )<sup>8</sup>. To welcome the new power system, complete new aircraft concepts need to be implemented, as the twin-fuselage of the Taurus G4<sup>7</sup> or the multi-propeller design of the Nasa aircraft LEAPTech, which is still under development (Figure I. 3).<sup>9,10</sup>



Figure I. 3: LEAPTech aircraft first conceptualization.<sup>9</sup>

The company Roland Berger made an inventory of the programs focusing on electrically-propelled airplanes and reached a number of seventy different projects<sup>11</sup> which underlines the diversity of the designs examined.

As previously mentioned, 100 % electrical aircraft concept is more demanding than MEA as the airplanes designs need to be revised from the scratch<sup>9</sup> while MEAs are less regarding on aircraft structure modifications. The ease of implementation, which could lead to faster validation and certification of the new MEA systems, explains the infatuation of aircraft manufacturers for MEA.

Still, prior to reach industrial level, reliable electrochemical energy storage systems, such as fuels cells and batteries, need to be improved as mentioned by NASA.<sup>1</sup> On the battery side, Airbus reached a first success thanks to their drone Zephyr 7 (Figure I. 4) powered by solar cells combined to Li-sulfur batteries (LIS). Zephyr 7 was able to flight more than ten days without any stop.<sup>12-14</sup> Lithium-Sulfur technology was selected among the new types of technologies as it offers high energy densities (theoretically: 2500 Wh .kg<sup>-1</sup> or 2800 Wh.L<sup>-1</sup>) and low costs.<sup>13,15</sup> They are still under prospect at lab scale to improve their performances and life time.



*Figure I. 4: Picture of Zephyr 7, the Airbus drone powered by photovoltaic cells and Li-sulfur cells (source: <https://www.droneuniversities.com>).*

Due to Li-ion batteries (LIBs) maturity in non-stationary energy storage (mobile, computers, automotive applications), such technology seems very promising. Boeing even started to implement some cells in their airship. Unfortunately, several problems were encountered, as for instance the trigger of a fire on board of a Boeing 787 Dreamliner.<sup>16-18</sup> The APU batteries (8 Li-ion cells) responsible for the fire were recognized to be manufactured with defects. In addition, the technology selected might not be the most suitable choice for such application (LiCoO<sub>2</sub>/Graphite). Testing and certification process lacks were also pointed out by the American NTSB.<sup>19</sup> For aircraft manufacturers, battery manufacturers and researchers, such

incidents underlined the necessity to develop rigorous batteries specifications and testing procedures to be able to certify the well-functioning of the cells in such demanding conditions.

For this reason, research to reach reliable electrochemical energy storage systems has been intensified from both academic and industrial sides. One idea to replace the conventional APU is to combine fuel cell stacks with battery packs.<sup>20</sup> For instance, the CIRA proposed to do a hybrid system based on Proton Exchange Membrane Fuel cells (PEMFC) and Li-polymer (LiPo) batteries<sup>21</sup>. On their side, the Japan Aerospace Exploration Agency in collaboration with the DLR (German Aerospace Center) evaluated the feasibility of using a hybrid system based on a PEMFC stack and LiFePO<sub>4</sub>-based battery pack in the case of the airship Antares DLR-H2 (Figure I. 5).<sup>22</sup> Finally, this aircraft developed by the DLR German Aerospace Center was the first one able to take off using a propulsion system operated thanks to fuel cells.<sup>23,24</sup>



*Figure I. 5: Picture of Antares DLR-H2 the first aircraft powered by fuel cells (source: <https://www.dlr.de>).*

On the margin of LIS batteries and fuel cells, another technology, named lithium-air battery (LAB), grasps scientists' attention due to its higher theoretical energy density. Such property is enhanced by a factor of 5 to 10 compared to current LIBs ( $5200 \text{ Wh.kg}^{-1}$ )<sup>25</sup> explains why this technology is an appealing candidate for aeronautical applications. Certainly, the loaded volume and mass are critical onboard aircrafts. Then, energy storage devices crucially need high gravimetric and volumetric energy densities.

LABs are at the bridge between batteries and fuel cells. They involve a lithium metal anode and an open porous cathode. On the cathode surface, reduced oxygen anions can react with lithium cations and form the discharge product. Oxygen supply could be ensured by the oxygen coming from ambient air or by an oxygen-supply system. In this later case, a significant reduction of the gravimetric energy would be noticed due to the oxygen supply system mass. Compared to the mature LIBs, LABs are still at the prospective stage as several technical



limitations still need to be unlocked to achieve the expectations. First, optimization of the cathode texture is required to increase practical energy while lowering the limiting phenomena such as surface passivation and pore clogging. Pore clogging is due to the formation of products inside the electrode porosity limiting further progress of the reactions as lithium and oxygen diffusion is impeded.<sup>26</sup> Secondly, most of the studies currently overlooks the impact of atmospheric conditions as most of the studies are carried out at 25 °C and atmospheric pressure. So, LABs behaviors in aeronautical atmospheric conditions should be scrutinized to evaluate the feasibility of using LABs in aircrafts.

This study was then launched, by IRT Saint-Exupéry, to understand and estimate the gap between theoretical promises of LABs and the requirements linked to their potential use in MEA. IRT Saint-Exupéry is an Institute of Technology dedicated to ease and speed up the transfer of state-of-the-art technologies from academia to industry. Thanks to a 50 - 50 public-private funding, the Celia Project was launched by IRT Saint-Exupéry in 2015. As part of the Celia Project, this study on LABs gathers both industrial partners, Zodiac Aerospace, Safran Tech and Airbus, as well as an academic laboratory, the LRCS. The experimental and theoretical studies of this thesis, entitled “Toward lithium-air batteries for aircraft application: a combined experimental/modeling study”, were conducted at the LRCS under the supervision of Prof. Alejandro A. Franco.



# CHAPTER I: STATE-OF-THE-ART

## Contents

---

I.1. Evolution of the battery technologies.....	8
I.2. Definition of the case study: LABs.....	14
I.2.a. LABs: worldwide research status.....	14
I.2.b. LABs: working principle.....	16
I.2.c. The cathode: a key component for LABs.....	26
I.2.d. Gap between flight conditions and lab conditions.....	29
I.2.e. How to define LABs capacity?.....	48
I.3. Thesis objectives.....	50

---

## I.1. Evolution of the battery technologies

The history of primary and secondary batteries development is made of successive discoveries. It is generally recognized that Volta largely spread the concept of electrochemical cell thanks to his pile. Later in 1866, another primary battery was then unveiled to the public by Leclenché.<sup>27</sup> A major historical breakthrough, was the invention by Planté in 1860 of the Lead-acid battery, the first practical rechargeable battery.<sup>28</sup> In 1899, the car called “La jamais contente”, was able to reach 100 km/h thanks to this technology. Still, such a record required to load 650 kg of Lead-acid batteries due to their low gravimetric energy density (Figure I. 6).<sup>29,30</sup> Since then, the development of batteries has as a guideline the improvement of the energy density, reduction of the safety concerns, enhanced reliability and cost decrease.



*Figure I. 6: Drawing of the car “La jamais contente”.*<sup>29</sup>

As an illustration, Ni-Cd technology, created in 1899 by Waldemar Jungner,<sup>31</sup> emerged in order to balance the low density of Lead-acid batteries<sup>30,32</sup> and progressively became the most spread secondary battery<sup>29</sup>. The Ni-MH battery, commercialized in 1989,<sup>31</sup> on their side not only improved the energy density<sup>30,31,33</sup> but also solved toxicity issues of Cobalt. In the meantime, self-discharge was more pronounced for such technology.<sup>32</sup> Finally, Ni-Cd started to disappear in favor of LIBs development.<sup>34</sup> To facilitate the understanding of the several technologies pros and cons, Table I. 1 was built based on current state-of-the-art bibliography.

Technology	Pros	Cons	Cell voltage (V)	Energy (Wh/kg)	Energy (Wh/L)	Power (W/kg)	Temperature (°C)	Cycle Life	Self-discharge /month (%)*	Developed	Sources
Lead -acid	✓ Price ✓ Robustness	✗ Low energy density ✗ Low DoD	2.1	30 - 40	50 to 70	300	- 30 - 60	200 - 300	5	Late 1800s	30,33,35
Ni-Cd	✓ DoD ✓ Cyclability ✓ Low temperature	✗ Toxic ✗ Self-discharge ✗ Low energy density	1.2	40 - 60	100- 200	200	-50 - 70	1500 - 2000	20	1899	30,31,33,35
Ni-MH	✓ Energy density ✓ Cyclability	✗ Low DoD ✗ Self-discharge ✗ Over discharge	1.2	70 - 80	200 - 300	1300-500	-20 - 50	800 - 1000	30	1988	30,32,33,35
Li-ion	✓ High energy density ✓ Price	✗ Depends on chemistry	≈ 3.6	100 - 200	> 400	3000-800	- 20 - 55	> 500	< 10	1975	33-36
Li-ion insertion chemistries	Positive electrode	Negative Electrode	Cell voltage(V)	Energy (Wh/kg)	Cycle life	Pros		Cons		Sell by**	Sources
Lithium cobalt oxide <b>LCO</b>	LiCoO <sub>2</sub>	Graphite	3.7 - 3.9	150	500 - 1000	✓ Cycling ✓ Low self-discharge	✗ Safety ✗ Cost ✗ Lifetime			Sony, Saft Sanyo, FDK	32,37-42
Lithium nickel oxide <b>LNO</b>	LiNiO <sub>2</sub>	Graphite	3.6	150	ND	✓ Cost ✓ Discharge capacity	✗ Thermal stability ✗ Cycling			ND	34,37,41
Lithium manganese oxide <b>LMO</b>	LiMn <sub>2</sub> O <sub>4</sub>	Graphite	4.0	120	1000 - 1500	✓ Fast charge/discharge ✓ Cost ✓ Thermal stability	✗ Cycling ✗ Lifetime			Nec, Samsung, Hitachi, Bosh,	30,32,34,37,41-45
Lithium nickel cobalt aluminum oxide <b>NCA</b>	Li(Ni <sub>0,8</sub> Co <sub>0,15</sub> Al <sub>0,05</sub> )O <sub>2</sub>	Graphite	3.7	190	ND	✓ Cycling ✓ Cost ✓ Calendar storage	✗ Reactivity at high temperature			Panasonic	34,37,39,40,45
Lithium nickel manganese cobalt oxide <b>NMC</b>	Li(Ni <sub>0,33</sub> Mn <sub>0,33</sub> Co <sub>0,33</sub> )O <sub>2</sub>	Graphite	3.8 – 4.0	170	ND	✓ Stability ✓ Cost	✗ Thermal stability			Sony, Sanyo, LG CHem	34,37,40,42
Lithium iron phosphate <b>LFP</b>	LiFePO <sub>4</sub>	Graphite	3.3	130	> 4000	✓ Safety ✓ Thermal stability ✓ Voltage stability ✓ Cost	✗ Low electrical conductivity and poor Li <sup>+</sup> diffusion ✗ Low volumetric capacity			UT, QH, MIT A123, Valence, BYD	32,37,42,43,45
Lithium titanate <b>LTO</b>	LCO, LFP and so on	Li <sub>4</sub> Ti <sub>5</sub> O <sub>12</sub>	2.3 – 2.5	85	> 4000	✓ Safety ✓ Lifetime	✗ Cost			Toshiba	29,32,37,43,45
Lithium rich material <b>LR-NMC</b>	xLi <sub>2</sub> MnO <sub>3</sub> · (1 - x)Li(Ni <sub>1-y-z</sub> Co <sub>y</sub> Mn <sub>z</sub> )O <sub>2</sub>	Graphite	3.75	320	< 100	✓ Higher capacity	✗ Fade of capacity ✗ Fade of voltage			ND	34,39,46

\*At 25°C \*\* Not exhaustive list  
ND: Not Defined

Table I. 1: Sum up of the most common battery technologies with detailed properties and pros and cons.

The advent of LIBs relies on lithium intrinsic properties. First of all, lithium is characterized by a low molecular weight and a low standard potential.<sup>34</sup> Using lithium permitted to design batteries with high gravimetric and volumetric energy densities and higher voltage. Moreover, it has been demonstrated by Whittingham in the 70s that lithium ion can be intercalated into various layered transition metal dichalcogenides<sup>36</sup> opening the road toward LIB development. Progressively, LIBs took the lead on portable device energy supply, previously powered by Ni-MH batteries.<sup>47</sup> Then, LIBs entered also in the market of hybrid electric vehicle (HEV) and electric vehicle (EV).<sup>31,48</sup> The battery market evolution since 1990 to 2015, underlined the overwhelming growth of LIBs market at the cost of previous technologies (Figure I. 7).<sup>49</sup>

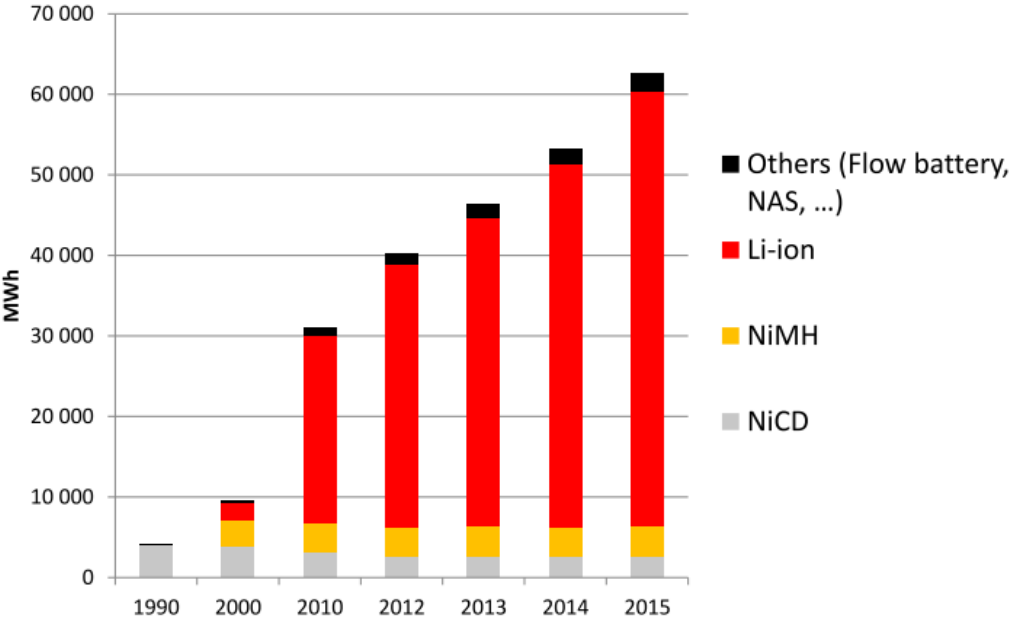


Figure I. 7: Worldwide battery market from 1990 to 2015.<sup>49</sup>

In 2015, the LIB market reached 16,7 B\$ which corresponds to 5600 M cells. Figure I. 8 highlights the major manufacturers volume production as well as their corresponding share market.<sup>48</sup> As shown, a large volume production does not imply a significant part of share values. This can be explained by the variety of chemistries and applications gathered by LIBs market (competition between some niche market and mass production).

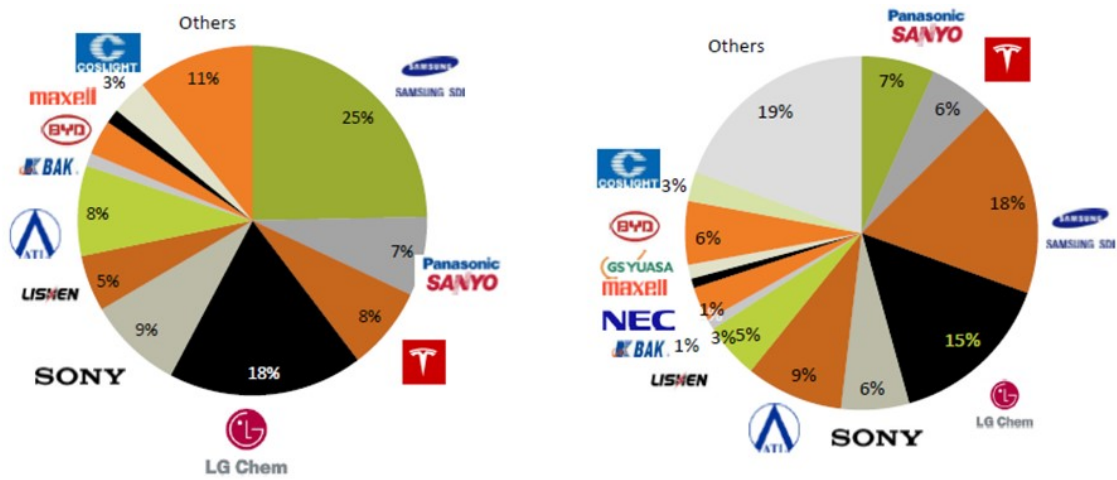


Figure I. 8: LIBs worldwide market in volume (a) and in market share (b). (Values from 2015).<sup>48</sup>

LiCoO<sub>2</sub> versus hard carbon, initially developed by Goodenough in 1980,<sup>34</sup> was one of the first chemistry of LIB commercialized (Sony 1991).<sup>31</sup> Since then, various technologies have been developed in an attempt to increase the energy density and to solve issues, such as thermal stability or toxicity depending on the selected chemistries. The main chemistry based on LCO, LNO, LMO, NMC, NCA, LFP or LR-NMC cathodes are listed and described in Table 1. The Li-ion cells are sold according three possible designs, depending on the manufacturing process (Figure I. 9). Prismatic and cylindrical cells are made with a roll-up of positive electrode, separator and negative electrode while pouch cells are made of a stack of the different layers.

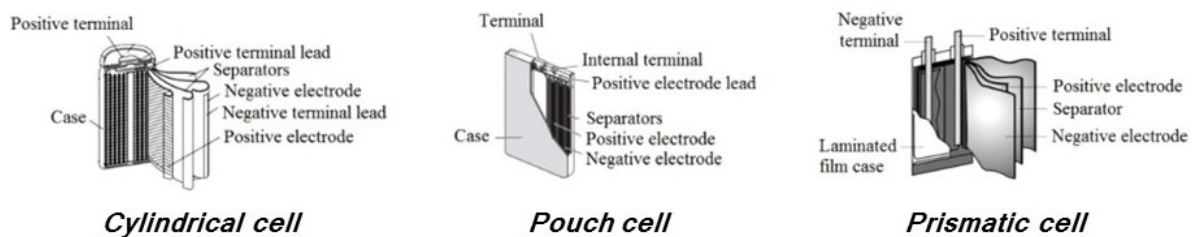


Figure I. 9: Schematic of the different industrial cells configurations.<sup>38</sup>

No matter which configuration is considered, manufacturing the cell results in a decrease of the energy density along the upscaling level as underlined in Figure I. 10.<sup>31</sup> Indeed, at lab

scale the gravimetric and volumetric energy densities are defined by the materials used. However, at industrial scale, the cells' casing, the pack assembling casing, the safety sensors and the battery management system (BMS) strongly contribute to increase the overall mass and volume without participating to the discharge or charge performances.

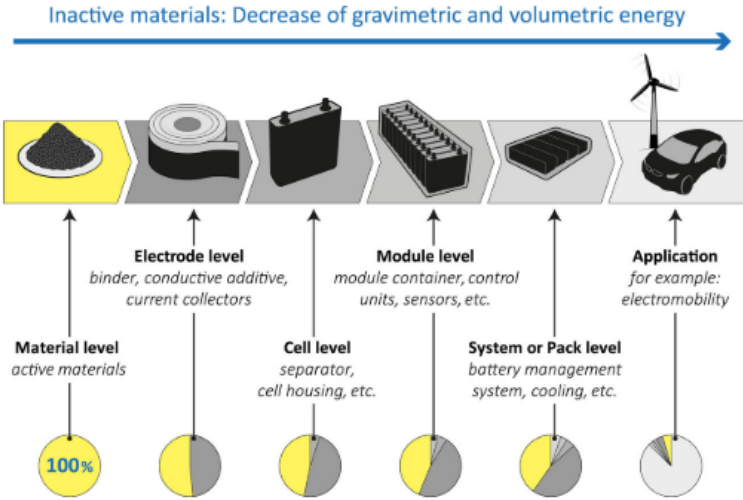


Figure I. 10: Decrease of practical energy density over the battery value chain.<sup>31</sup>

Improvement of cell engineering has permitted to significantly enhance the energy density over the years. For instance, the LCO based batteries had a volumetric capacity which was doubled in the last two decades, reaching more than 400 Wh.L<sup>-1</sup>.<sup>34</sup> Such enhancement of LIBs characteristics gives confidence of further possible improvement. Still, to develop fully electric aircrafts and vehicles, the LIBs capacity should increase by 15 to attain the gasoline one. However, LIBs capacity only increased by 5 in two centuries.<sup>47</sup> So, disruptive technologies need to be appraise to enable it.

For now, the new breakthroughs in the battery filed are the Post Li-ion technologies, which gather metal/sulfur and metal/air batteries, as well as the Post Li-ion technologies, which count among others Na-ion, Mg-ion or even Ca-ion batteries.<sup>31</sup> In 2010, Tarascon proposed a battery landscape (Figure I. 11) built on the development of three technologies with strong growth potential : Li-S, Na-ion and Li-air batteries.<sup>47</sup> While, Li-S technologies are commercialized,<sup>39</sup> some attempts to commercialize are currently launched for Na-ion (e.g the start-up TIAMAT<sup>50</sup>). On their side, LABs are still under development at lab scale.



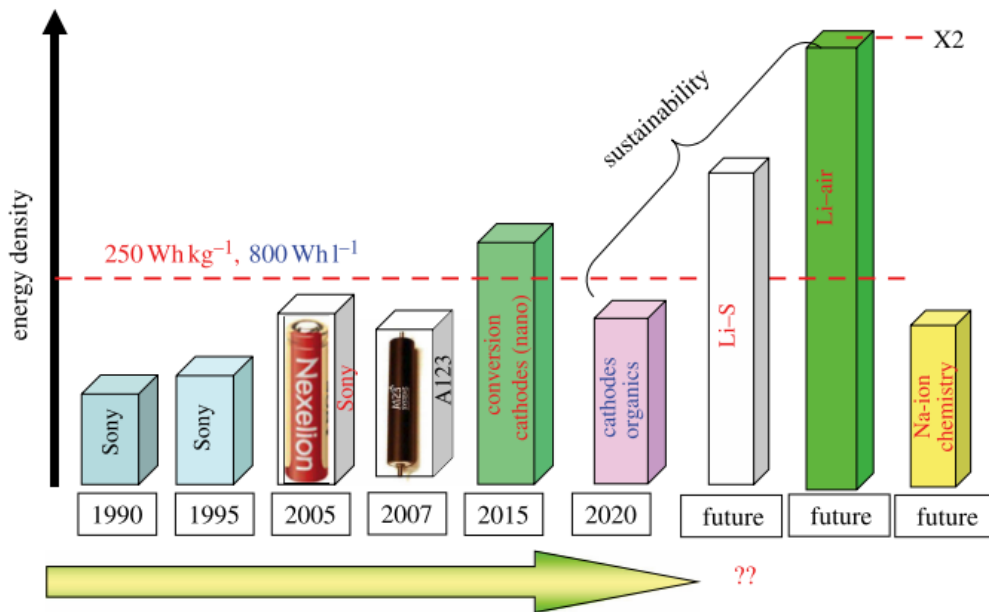


Figure I. 11: The battery technology landscape as proposed by Tarascon in 2010.<sup>47</sup>

Among all the presented technologies, IRT Saint-Exupéry launched two projects on the technologies which require more research effort but also which are the most promising in term of energy density and application. Firstly, the project FUSHIA was created to study the possibility to use fuel cells. Secondly, a more prospective project, CELIA, was elaborated to study Li-air technology and will be described here.

## I.2. Definition of the case study: LABs

### I.2.a. LABs: worldwide research status

First of all, should we discuss about Li-air or Li-oxygen batteries? The question is opened. Indeed, since the first publication of Abraham *et al.* in 1996 describing “A polymer based Electrolyte-Based Rechargeable Lithium/Oxygen Battery”,<sup>51</sup> many publications were reporting data on so-called “Li-air batteries” while, actually, there were only describing Li-oxygen ones. Making such amalgamation is yet tempting as operating such system using oxygen freely available from air would be an outstanding opportunity. Still, going from Li-oxygen to Li-air is not that trivial. First, fulfilling clear understanding of the mechanisms and limitations with oxygen is requested and then the impacts of using open cathode to air instead is necessary. As this study will focus on Li-oxygen and Li-air batteries, the second term is then an accurate meaning here and so will be used.

To get an overview of how much research is going on in this field, the number of publications per year is a relevant indicator. Taking into account all these designations, (Li-air, Li-oxygen, and so on), Web of Science found 2682 publications spread from 1996 to nowadays (Figure I. 12). While the number of publications steadily grows from 2009 and 2015, it stays almost constant since 2015 with at least 450 publications per year. Also, it appears that LABs appeal is diminishing in the last years, as the number of publications seems to stagnate, most probably due to the numerous issues still unsolved as described later.

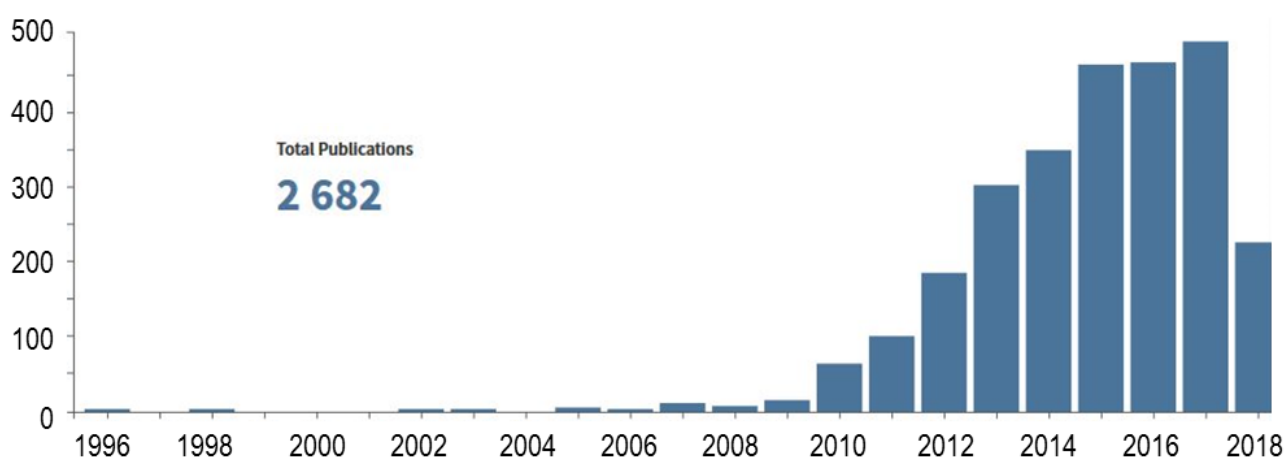


Figure I. 12: Evolution of the number of publications related to the terms “Li-air batteries” or “lithium-air batteries” or “Li-O<sub>2</sub> batteries” or “lithium-oxygen batteries” on Web of Science (data from 27/06/18).

Knowing the more active countries, based on the number of publication per country, constitutes another relevant data. As underlined in Figure I. 13, Asia counts for 70 % over the 10<sup>th</sup> first countries publishing on LABs, while North America represents 15 % and Europe 10 %. Relatively, taking into account the population of these regions, such results spotlight the sustained activity of European labs and companies on LABs.

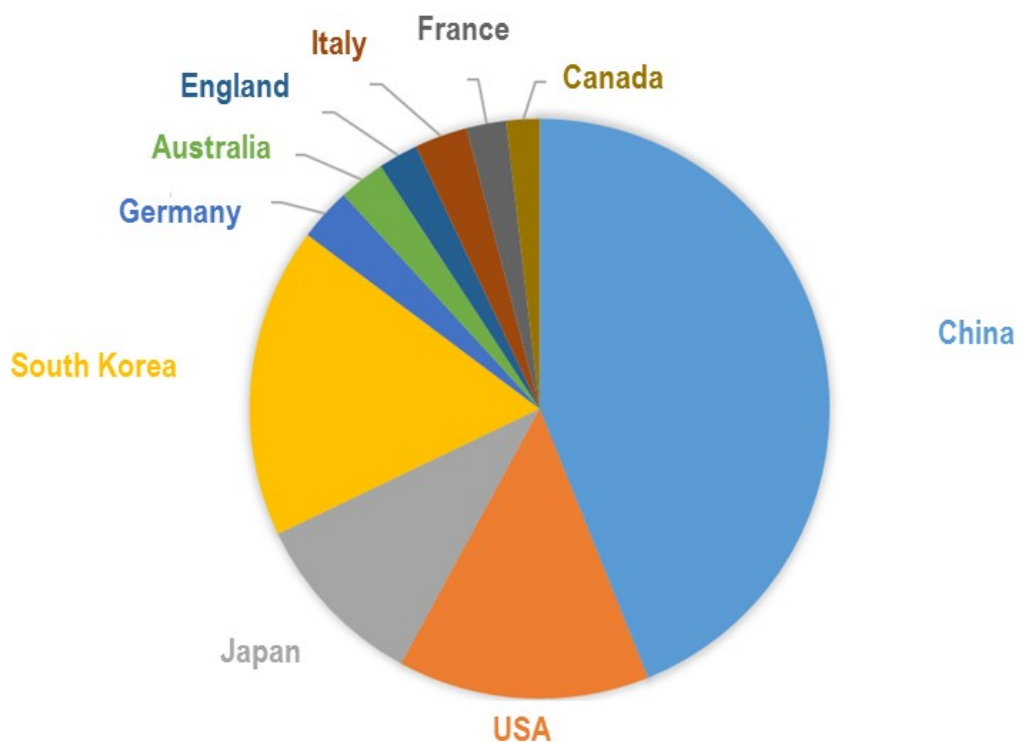


Figure I. 13: The 10 top countries releasing the most publication on “Li-air batteries” or “lithium-air batteries” or “Li-O<sub>2</sub> batteries” or “lithium-oxygen batteries” according to Web of Science (data from 03/07/18).

### I.2.b. LABs: working principle

LABs are made of four components (Figure I. 14): the two electrodes, the separator which guaranties the electronic insulation and the electrolyte, in charge mainly of ion transport and oxygen diffusion.

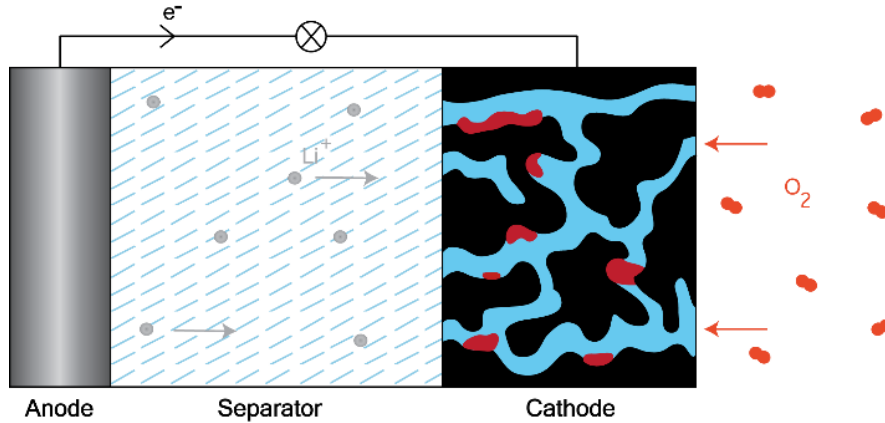


Figure I. 14: Schematics of LABs discharge.

Many kinds of LABs have been studied, with a multitude of different electrolytes and cathodes. To sum up, LABs can be divided into four groups: aprotic, aqueous, solid state and mixed aqueous/aprotic (Figure I. 15).<sup>26</sup>

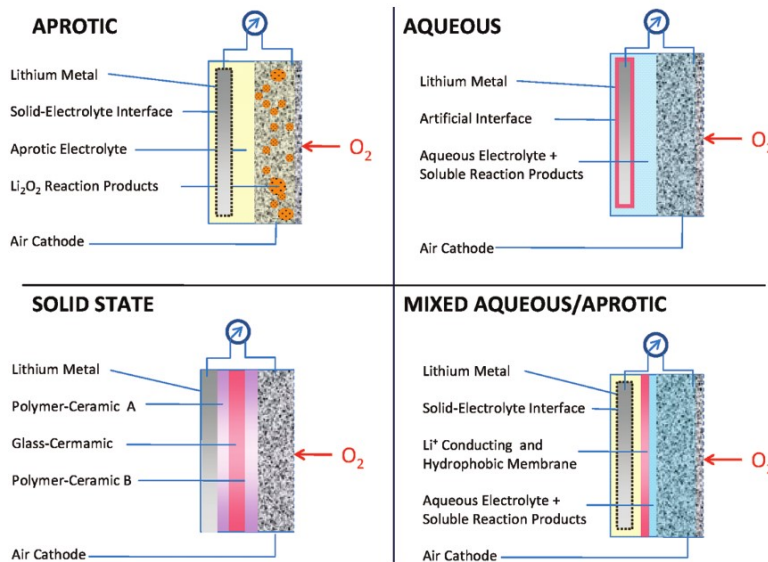
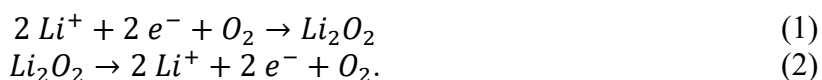


Figure I. 15: Schematics of the several kind of LABs.<sup>26</sup>

Due to lithium reactivity, aqueous systems require anode protection to avoid LiOH formation<sup>52</sup> and some membranes can also be added leading to aqueous dual electrolyte.<sup>53</sup> Thanks to an aprotic electrolyte, a solid electrolyte interphase can be formed on lithium foil and then protect it.<sup>54</sup> Solid-state batteries reduce the risk of dendrites formation at the anode side

thanks to a solid electrolyte, implying consequently lower gravimetric energy density, unlike aqueous systems, which are characterized by the highest gravimetric energy density among the LABs types. On the contrary, lower volumetric energy density is reached with aqueous system compared to aprotic LABs.<sup>54</sup> As aeronautical applications are targeted in this study, volumetric and gravimetric energy densities should both be optimized. For these reasons, only aprotic systems have been considered in this case study. The different parts of such system (cathode, anode and aprotic electrolyte) will be described below.

The most common cathode material is carbon due to its low cost, high conductivity and to the many types of carbon available. Still, other conducting materials could be used like porous gold<sup>55,56</sup> or titanium carbide.<sup>55</sup> On their surface, ORR and OER take place leading respectively to the discharge and charge of the system according to the following global reactions:



Initially, Li<sub>2</sub>O was previously considered as a possible discharge product depending on the potential frame.<sup>57,58</sup> However, Mc Closkey *et al.* spotted that Li<sub>2</sub>O production was not thermodynamically favored and only occurs during deep discharges (until 1 V). On the reverse, they highlighted that Li<sub>2</sub>O<sub>2</sub> was the main discharge product formed.<sup>59</sup>

To enhance ORR and even more OER, use of several extra catalysts was investigated. In literature, uses of several catalysts have been reported like platinum, gold, nickel as well as copper, cobalt and manganese oxides or even La<sub>0.8</sub> Sr<sub>0.2</sub>MnO<sub>3</sub>.<sup>60-62</sup> Other possibilities have been lately studied such as TiO<sub>2-x</sub> coating on top of CNT,<sup>63</sup> use of soluble FePc<sup>64</sup> or activated lithium metal oxide (Li<sub>2</sub>MnO<sub>3</sub>-LiFeO<sub>2</sub><sup>65</sup> and LiPdO<sup>66</sup>). Due to the complexity of the system and the many possible interactions induced by the use of extra catalyst, this study was built only on carbon-based electrodes.

The anode is made of a lithium foil providing the lithium cations. Besides, some studies are carried with LiFePO<sub>4</sub> as an anode to get rid of lithium metal limitation and reactivity with the electrolyte. While operating, lithium metal electrode undergoes dissolution and deposition leading to high sensitivity of the system toward the current density, as well as, risk of dendrite formation (Figure I. 16).

Also, instability of the anode is observed toward some common solvents used in LABs such as DMSO.<sup>67</sup> So to enhance stability,  $\text{LiFePO}_4$  which presents a flat potential at 3.45 V, is utilized after being previously charged, as an anode. Still,  $\text{LiFePO}_4$  is not sustainable for practical anode due to its high voltage<sup>68</sup> and subsequently is only implemented to study cathode impacts.

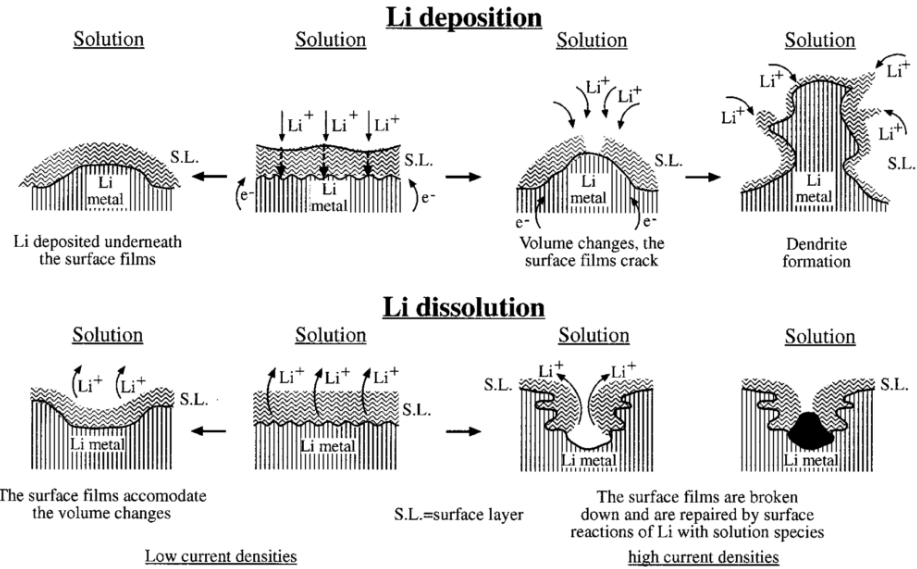


Figure I. 16: Schematic of lithium dissolution and deposition on top of lithium metal electrode.<sup>69</sup>

Several electrolytes have been studied in an attempt to stabilize the system, to promote the ionic conductivity and moreover to enhance oxygen diffusion (Figure I. 17).

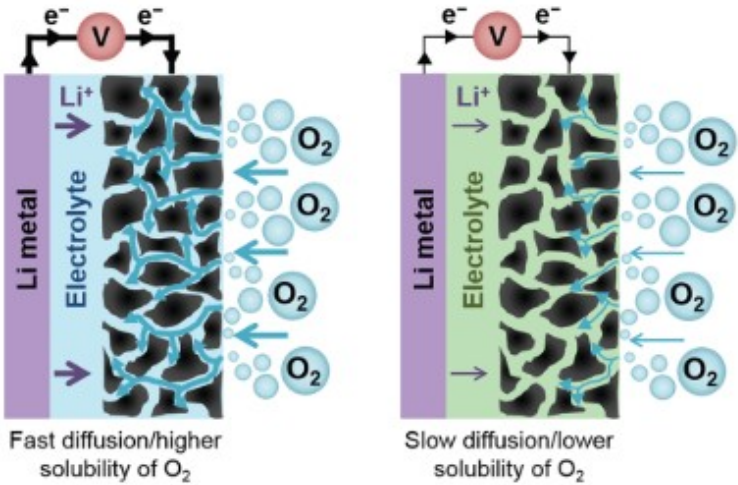


Figure I. 17: Schematics of oxygen transport during discharge depending on its solubility in the electrolyte.<sup>70</sup>

Initially, electrolytes coming from Li-ion field (*e.g.* PC) were largely used<sup>71</sup> after the demonstration of Abraham *et al.* of a Li-O<sub>2</sub> cell based on a mixture of PAN, EC and PC.<sup>51</sup> Still, instability of such alkyl carbonate electrolytes have been observed by Freunberger *et al.* in 2011.<sup>72</sup> McCloskey *et al.* also noticed carbonate electrolyte decomposition and preconized to move toward ether based electrolytes.<sup>73</sup>

Such electrolytes have been selected compared to alkyl carbonate ones for their higher stability toward O<sub>2</sub> reduced species.<sup>74</sup> Also, production of Li<sub>2</sub>O<sub>2</sub> was observed during first discharge for system using ether based electrolytes.<sup>75,76</sup> Mitchell *et al.* recognized that fading is still observed in the case of DME, even if cyclability is increased.<sup>77</sup> A major drawback of DME for LABs application is also its high vapor pressure, implying the use of ether solvents with longer chain. Still, in 2011, Freunberger *et al.* draw attention to the degradation of ether electrolytes (tetraglyme) enhanced with cycling.<sup>78</sup>

Despite previous studies, Grande *et al.* considered tetraglyme when they listed the five currently stable electrolytes. Their list promotes DMSO, CAN, TEGDME, PEGDME and PEO as safe electrolyte.<sup>53</sup> Such step back point out the difficulty to develop an electrolyte which at the same time is stable versus lithium, promotes oxygen diffusion, implies few parasitic reactions and limits passivation mechanisms. In addition, a polarity issue still need to be overcome as the electrolyte should dissolve polar species and in the meantime apolar O<sub>2</sub> too.

Another great example of such challenging research is DMSO. Besides ether-based electrolytes, Laoire *et al.* demonstrated in 2010 the reversible reduction of O<sub>2</sub> using another solvent: DMSO.<sup>79</sup> For years, DMSO has been described as adequate choice due to its high donor number properties<sup>80,81</sup> facilitating solution mechanism<sup>81-84</sup> as described in Figure I. 18 and so leading to higher capacities.<sup>85,86</sup>

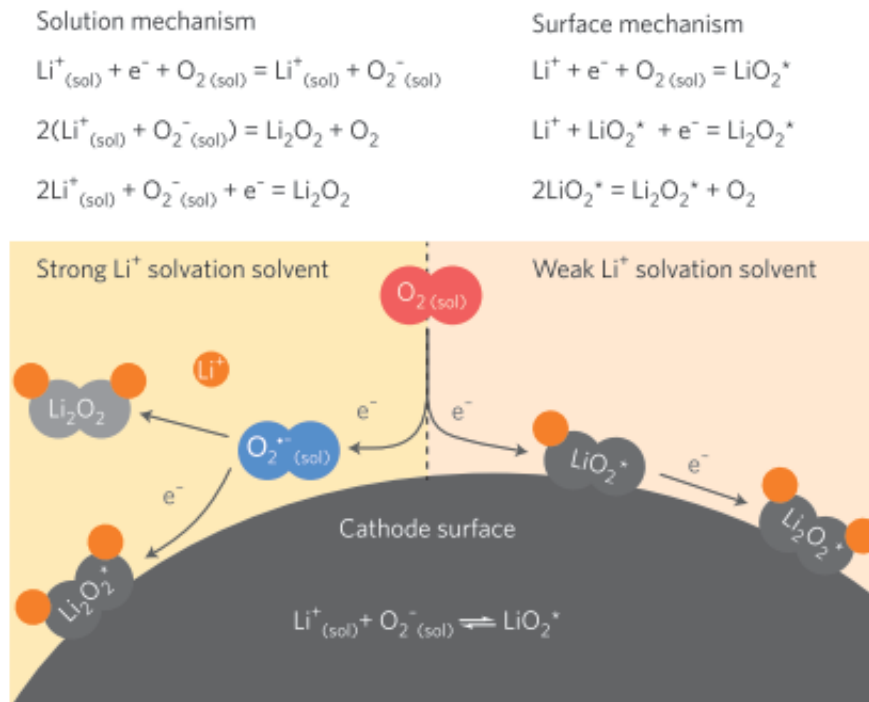


Figure I. 18: Description of the solution mechanism and surface mechanism occurring in Li-O<sub>2</sub> batteries. In first case, Li<sub>2</sub>O<sub>2</sub> is soluble (due to the use of high donor number) while in the second one Li<sub>2</sub>O<sub>2</sub> is insoluble (low donor number).<sup>81</sup>

In such case, formation of lithium superoxide occurs in the electrolyte and so enables the growth of a thick film of lithium peroxide. Such behavior is favored compared to surface mechanism which leads to faster passivation of the electrode surface and so to the cell sudden death, due to the lithium peroxide partially electronically insulating properties.<sup>87-90</sup> Even if DMSO was selected for such distinguished properties, instability versus lithium metal<sup>67,91</sup> and also versus lithium oxygen species was unveiled<sup>92-94</sup> leading to the formation of Li<sub>2</sub>CO<sub>3</sub>.<sup>95</sup> To overcome such hindrance, ionic liquids (more precisely RTIL) have also been investigated by the scientific community due to their large electrochemical stability windows as well as for their high thermal stability and non volatility.<sup>96,97,25</sup> Besides these properties, RTIL entail as consequences a low oxygen solubility and species mobility that drastically decrease the system performances. Then use of high temperature ionic liquids can be examined as suggested by Yoo *et al.*<sup>98</sup> Still, such a design should be heated leading to two possibilities: i) rather adding a heating system which will decrease the gravimetric and volumetric energy densities, ii) or rather positioning the cell next to devices producing heat continuously. As an aircraft needs to rely on high energy density batteries and due to the hazard of juxtaposing a heat source with a confined energy source, the study only sticks to aprotic LABs.



In addition to the solvent itself, salts and additives have also been scrutinized by researchers. Even if the oxygen and intermediate species solubility depends obviously on the solvent,<sup>85,99</sup> oxygen diffusion coefficient also relies on the salt selected as demonstrated by Gittleston *et al.* which used with TEGDME and DMSO several lithium salts (LiBF<sub>4</sub>, LiClO<sub>4</sub>, LiCF<sub>3</sub>SO<sub>3</sub>, LiTFSI).<sup>70</sup> Due to different ionic association strengths of the anions, which depends on the negative charge properties (size, steric effect and delocalization), the solubility will be different as the cations solvation will be changed<sup>81</sup> (in a same way that high donor number solvent impacts Li<sup>+</sup> solvation)<sup>81,100</sup>. As a consequence, the cations reactivity can be drastically modified.<sup>101</sup> Moreover, the salt concentration also affects the oxygen diffusion coefficient and so the system capabilities.<sup>70</sup> Salt stability also should be analyzed in an attempt to develop safe LABs. Thermal stability is then a crucial parameter. In this study, for instance, LiTFSI which was reported as a stable salt for LIBs, was used. Moreover, selecting a stable salt not only depends on the type of salt chosen but also on the salt purchased, as demonstrated by the several thermal stabilities observed this time for three different commercialized LiFSI salts.<sup>102</sup> To sum up, selection of a good salt is tricky, even more for LABs than LIBs due to the multitude of properties required for efficient operation.

In parallel, other additives, known as redox mediator, have been tested in an attempt to overpass the passivation impacts at the cathode side (*e.g.* LiI<sup>103–105</sup>). Easier oxidation of lithium peroxide emphasized by lower charge overpotential was claimed thanks to LiI addition.<sup>103,104,106–108</sup> Kawak *et al.* yet underlined the reactivity of LiI leading to side reactions products such as LiOH and LiOI.<sup>104</sup> Production of LiOH was confirmed and the decomposition mechanism was proposed by Liu *et al.*<sup>109</sup> Later, Park *et al.* pointed out the disparity of the results observed (Table I. 2) and reported, as a drawback, side reactions at the anode with lithium metal.<sup>110</sup> Also, interest of such an additive can be questioned as the extra-long charge plateau observed at 3 V could corresponds to degradation reactions between iodine and the electrolyte.

Table I. 2: List of the different redox-mediators and linked observations found by Park *et al* in literature.<sup>110</sup>

	RM	Concentration	Electrolyte	Redox potential (vs Li <sup>+</sup> /Li)	Note
Organic RM	TTF	10 × 10 <sup>-3</sup> M	1 M LiClO <sub>4</sub> in DMSO	3.43 V	Optimized conditions: gold electrode, DMSO solvent, LFP counter electrode
	TEMPO	10 × 10 <sup>-3</sup> M	0.1 M LiTFSI in diglyme	3.74 V	Reacts with Li metal to form soluble compounds
	Methoxy-TEMPO	50 × 10 <sup>-3</sup> M	0.5 M LiTFSI in DEME-TFSI <sup>a)</sup>	3.5 V	Modified TEMPO
	1-Me-AZADO <sup>b)</sup>	10 × 10 <sup>-3</sup> M	1 M LiTFSI in diglyme	3.6 V	Modified TEMPO
	MPT	100 × 10 <sup>-3</sup> M	1 M LiCF <sub>3</sub> SO <sub>3</sub> in tetraglyme	3.67 V	LFP counter electrode
	DMPZ	10 × 10 <sup>-3</sup> M	1 M LiTFSI in tetraglyme	3.4 V	Reacts with Li metal
	TDPA	50 × 10 <sup>-3</sup> M	0.5 M LiTfI in tetraglyme	3.4 V	Reacts with Li metal
	LiNO <sub>3</sub>	1 M	1 M LiNO <sub>3</sub> in diglyme	3.6–3.8 V	Also uses a salt, side reaction on Li metal
	DBBQ	10 × 10 <sup>-3</sup> M	1 M LiTFSI in tetraglyme or DME <sup>c)</sup>	–	For the ORR
	Organo-metallic RM	FePc	2 × 10 <sup>-3</sup> M	0.1 M LiTFSI in DMSO	3.65 V
tb-CoPc		10 × 10 <sup>-3</sup>	1 M LiTFSI in tetraglyme	3.4 V	Decomposition of tb-CoPc
Co(Terp) <sub>2</sub>		50 × 10 <sup>-3</sup> M	1 M LiTFSI in diglyme:PyT <sub>14</sub> TFSI	3.4 V	Not suitable due to a parasitic reaction
Heme		2.3 × 10 <sup>-3</sup> M	1 M LiClO <sub>4</sub> in tetraglyme	4.2 V	Biomolecule
Halide RM	LiI	50 × 10 <sup>-3</sup> M	1 M LiTFSI in tetraglyme	3.25 V	Long cycle life
		1 M	1 M LiI in tetraglyme	3 V	Li <sub>2</sub> O <sub>2</sub> main product LiOH main product Irreversible reaction
		50 × 10 <sup>-3</sup> M	0.25 M LiTFSI in DME	3 V	LiOH main product, reversible reaction with water
	LiBr	50 × 10 <sup>-3</sup> M, 1 M	0.2 M LiTFSI in diglyme	3.5 V	Li <sub>2</sub> O <sub>2</sub> main product, no side reaction
		10 × 10 <sup>-3</sup> M	1 M LiTFSI in diglyme	3.5 V	

Other additives were also proposed to stabilize the lithium metal anode surface (*e.g* LiNO<sub>3</sub>). As LiNO<sub>3</sub> has already proven remarkable efficiency in LIBs,<sup>111,112</sup> such additive/salt was later transposed to LABs. In case of LABs, LiNO<sub>3</sub> in DMA was spotlight as a stable combination leading to high efficiency and long term anode stability. Giordani *et al.* also demonstrated few side reactions in case of DMA and LiNO<sub>3</sub> mixture. Also, LiNO<sub>3</sub> acts as a redox-mediator agent helping OER and ORR.<sup>113</sup> Uddin *et al.* on their side scrutinized the SEI mechanism formation. Surprisingly, in presence of argon, polarization results were drastically reduced compared to polarization tests carried out in oxygen. They then proposed a mechanism where LiNO<sub>3</sub> regeneration is enable by oxygen leading to long life-time.<sup>114</sup> In 2015, Sharon *et al.* on their side studied the use of LiNO<sub>3</sub> in a supposedly more stable electrolyte, diglyme, and explained the formation of thicker discharge products thanks to stabilization of the radical anions thanks to the Li<sup>+</sup>/NO<sub>3</sub><sup>-</sup> strong association. Still, they acknowledge that even if diglyme is more stable than DMA, it is far from being a potential practical electrolyte due to its low stability. They finally concluded that a careful and attentive study of each key component of the system is required to reach practical system, from electrodes to solvent and salt used to make the electrolyte.<sup>115</sup> In this study, a particular focus will be made on the cathode part (see next section).

The several aforementioned electrolytes drawbacks spotlight the difficulty to determine a suitable electrolyte for LABs. Even if electrolyte impact will be partially described in the following research, developing a suitable electrolyte is still necessary to reach development of practical LABs. Due to the complexity of the systems and implied limitations, such study should be carried on its own in another project.

The tricky pathway toward performant and stable electrolyte development, as described previously, is due to the many limitations of LABs system. Satisfying oxygen diffusion inside the electrolyte through the overall electrode is not sufficient for high efficiency. Indeed, too high diffusion of oxygen through the separator until the anode will constitute an internal short-circuit. In addition to oxygen diffusion, promotion of reversible discharge product is necessary and will be impeded by the formation of a partially insulating film of discharge product  $\text{Li}_2\text{O}_2$  as well as by electrolyte degradation. Furthermore, limiting the parasitic reactions with the anode and the cathode is required. Currently, due to the high system overpotential (Figure I. 19),<sup>26</sup> high voltages are attained during the charge, promoting even more electrolyte degradation. High overpotential is a major drawback impeding development of a practical cell. It corresponds to the deviation from the standard equilibrium potential of the system (only depending on the active materials involved). On the reverse, overpotential is linked to the extra energy required in addition to thermodynamics and so take into account kinetics limitations (depends on the current density)<sup>26,60</sup> Also, the system intrinsic resistance contributes to overpotential. With time, due to the formation of the passivating discharge product<sup>54</sup> and side-reaction products,<sup>60,116</sup> overpotential rise leading to high charge plateau values. To reach practical cell, decreasing the overpotential is necessary to enable the use of electrolyte with lower voltage stability window.

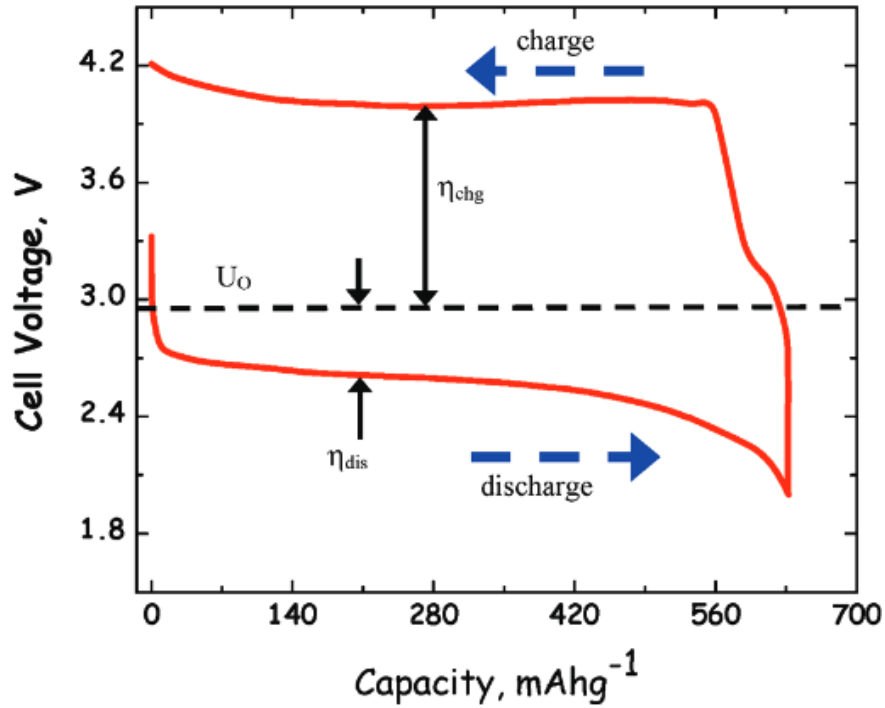


Figure I. 19: Discharge and charge voltage evolution of a non-aqueous cell at  $\sim 0.1 \text{ mA/cm}^2$  express in function of the charge capacity per gram of Carbon SP in the cathode.<sup>26</sup>

Obviously, the aforementioned limitations appeared in the case of Li-oxygen batteries. While moving to LABs, extra issues appear linked to presence of other species such as  $\text{CO}_2$ ,  $\text{N}_2$  and  $\text{H}_2\text{O}$  which could lead to additional parasitic reactions. Finally, with implementation of LABs in aircraft, new challenges emerged as the atmospheric conditions can drastically be modified (evolution of temperature and pressure). Figure I. 20 summarizes the several issues appearing at the different level of LABs maturity. Worth pointing out that the atmospheric conditions applied to LABs at lab scale are far from the application ones (see later section).

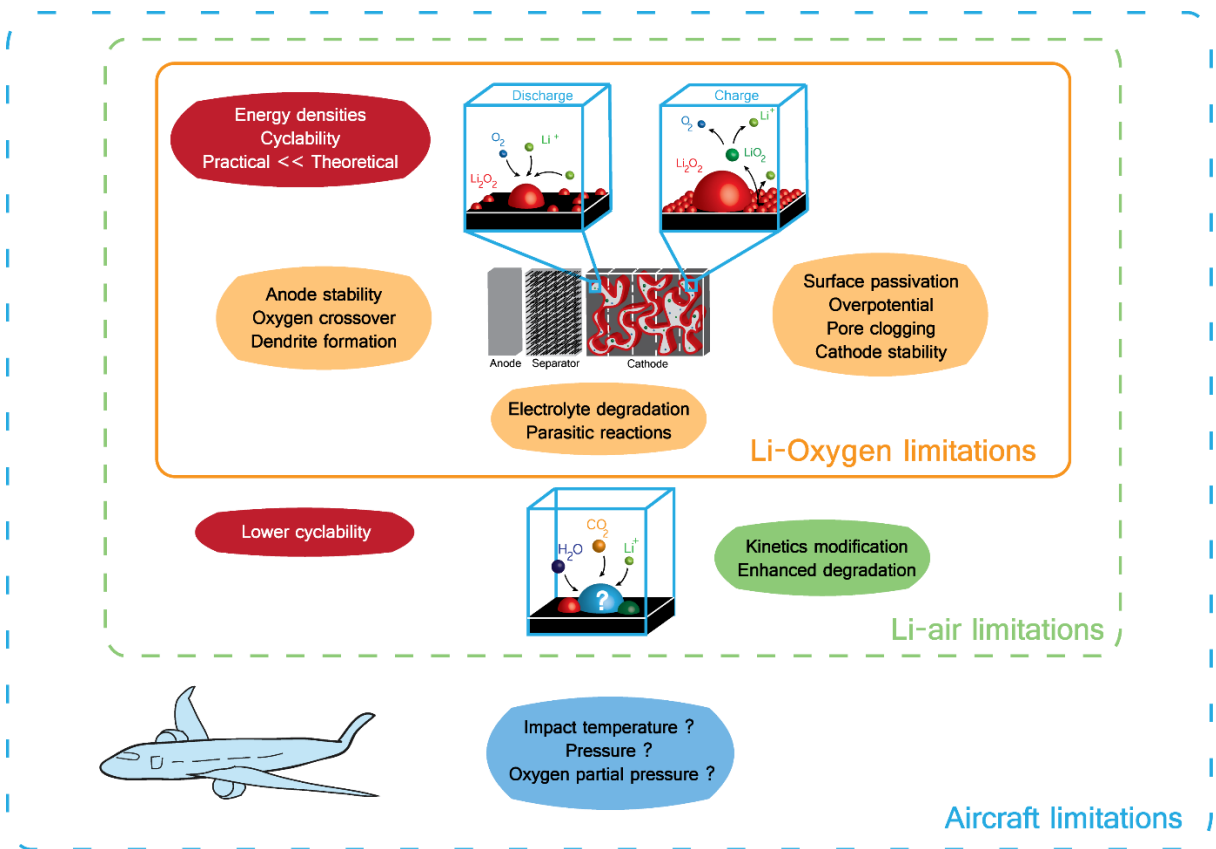


Figure I. 20: Schematic of LABs limitations from lab scale to aeronautical application. (Based on references<sup>53,117,118</sup>).

### I.2.c. The cathode: a key component for LABs

LABs practical capacity is far from theoretical expectations,<sup>52</sup> due to the many limitations previously exposed. As reactions take place at the cathode surface, this component is of prime importance. Cathode is subject of three different limitations: 1) Oxygen diffusion in the cathode is a main issue, since driving the practical capacity.<sup>119,120,121</sup> 2) Electrode passivation, resulting from the formation of insulating  $\text{Li}_2\text{O}_2$ , can lead to the sudden death of the cell.<sup>89,90</sup> 3) The clogging of the pores by the discharge product could also explain the capacity fading and the poor cyclability.<sup>122,123</sup> Pore clogging infringes lithium cations and oxygen diffusion inside the electrode and tends to limit the discharge capacity. There exist some discrepancies in the research community at defining the capacity limiting factors<sup>124</sup> as well in defining the best cathode material.

For this study, as many types of carbons are available at affordable price, only carbonaceous electrodes have been contemplated. Due to the variety of carbons available, selecting one type is not so trivial. For instance, meso-porous carbon electrodes (with pores between 3-50 nm) usually can provide larger available surface for the reactions and thus contribute to the capacity increase. But such pores are more likely to be clogged during the discharge due to their small size. On the contrary, macro-porous carbon electrodes may less suffer from pore clogging and enhance mass transport, but the surface area for electrochemical reactions is low (Figure I. 21). In the same way, cathode wettability by the electrolyte is also impacted by the kind of carbon selected. A compromise should then be found to enhance performances of LABs carbon cathodes.

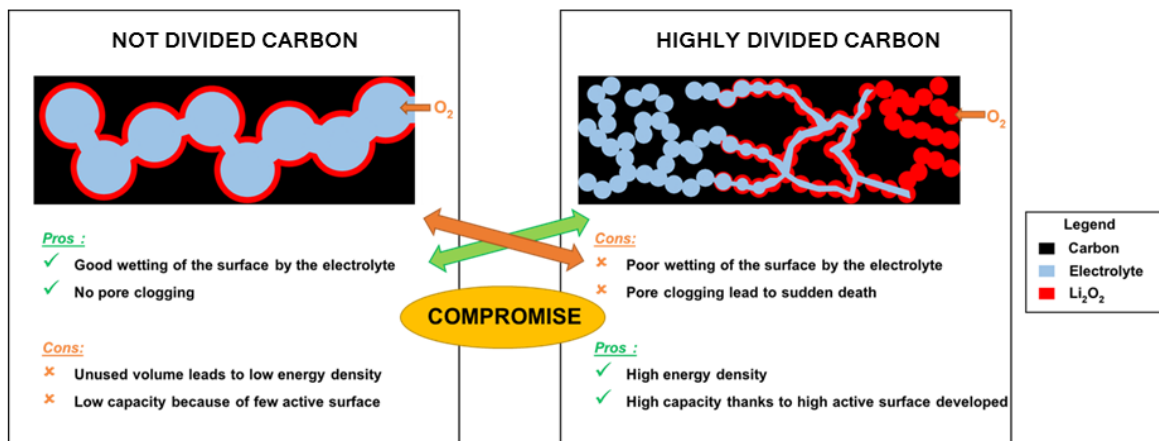


Figure I. 21: Impact of the carbon used as cathode for LABs.

Then, to define the best interplays between these limiting factors and the target of high energy density, capacity limiting factors should be first evaluated. To do so, using modeling techniques appeared for this study to be a good solution to screen the impact of each limiting factor as well as highlighting the interplays between them.

Some modeling works were already published prior to the present study. For instance, Sandhu *et al.* tracked the pore filling with  $\text{Li}_2\text{O}_2$  over discharge, using a continuum model which assumed an oversimplified electrode architecture. Oxygen diffusion limitation was underlined as the main limiting factor.<sup>125</sup> Later, Andrei *et al.* also used a similar model taking into account different ways to distribute a catalyst along the electrode thickness to enhance the ORR and study the impact of the electrolyte properties to promote the discharge capacity.<sup>126</sup> Albertus *et al.* applied an empirical fit to estimate the ohmic resistance of the discharge product. Considering flat electrode experiments and simulation results, they concluded that passivation was the main limiting parameter as pores were observed to be filled only up to 2 to 3 % of the initial volume.<sup>89</sup> In addition to the study of the passivation mechanism, the impact of the cathode texture (made of planar, cylindrical or spherical carbon particles) was also investigated by the mean of modeling by Wang.<sup>8</sup> Impact of carbon type (comparison between Ketjen Black and Carbon SP based electrode) was explored by Franco *et al.*<sup>127</sup> and Xue *et al.* who pointed out the tradeoff between surface area and pore size distributions of carbons at determining discharging cathodes overpotential and capacity.<sup>128</sup> Later, Chen *et al.* investigated the effect of carbon particle shape by comparing the calculated electrochemical response of carbon nanotubes or nanofibers based-electrodes on the discharge capacity.<sup>129</sup> Bevara *et al.* also paid attention to pore size and pore morphology as well as pore size distribution. The authors concluded that only a variance of pore size and not a change of pore shape leads to the increase of the capacity.<sup>130</sup> On their side, Xue *et al.* suggested to use electrodes with pipes favoring oxygen diffusion through the electrode thickness, from air inlet to separator side.<sup>131</sup> Sergeev *et al.* focused their research effort on pore size distribution along the electrode thickness and underlined its direct impact on the discharge curve shape.<sup>132</sup> The authors advised to use a log-uniform pore size distribution (PSD) in the cathode for improved cell performance. They concluded that a 50 % of large pores should be added in volume as an optimal value. However, such a proposed electrode texture is not easy to implement practically at lab scale. Indeed, mastering the formation of a log-uniform pore size particles is far more complicated than just a uniform distribution. Additionally, Sergeev *et al.* model did not take into account the inhibition

of electrons due to the formation of lithium peroxide and so the passivation mechanism was not taken into account leading possibly to over-estimated the values.<sup>133</sup>

In the present study it was proposed to take into account the three limitation phenomena in parallel to design efficient carbon cathode. Also, as the target application requests high energy density, the efforts were focused on thick cathodes formulated with meso-porous carbon. Still, one drawback is that large cathode thicknesses impede even more oxygen diffusion as previously discussed. To enhance diffusion inside the electrode it was proposed to add an extra-macro-porosity, on purpose, to act as a reservoir of oxygen and to facilitate oxygen diffusion throughout the electrode. While mesoporous carbon will provide high active surface for ORR and OER, the macro-porosity will enable an efficient use the overall electrode, leading to the development of bi-porous electrodes. Such bi-porous architecture presents also the advantage to be synthesized at the experimental level thanks to a uniform distribution of macro porosity inside the electrode. At lab scale, formulation of bi-porous electrodes was also investigated. Mastering the electrode texture was then of paramount importance to succeed in developing such bi-porous electrodes. Inspiration was then taken from LIB field, to help faster development of the theoretical concept.

In LIB field, the controlled removal of a volatile solvent from a liquid slurry is a common way to reproducibly produce porosity at the industrial scale, but the elimination of a porogenic substance from a solid matrix is another appealing templating option. As an example, the dissolution by water of embedded NaCl grains having controlled size leads to well-defined open porosity as applied to metallic foams<sup>134</sup> or thick binder-free composite electrodes for LIB with enhanced performances.<sup>135</sup> Worth pointing out that such dissolution-driven process potentially ensures that the created porosity is then fully accessible to liquid (electrolyte). The same approach can be applied to plastic films from which an organic porogen agent can be removed by dissolution thanks to an appropriate solvent. This is the bottom line of the so-called Bellcore technology, which led to the development of the first practical plastic electrodes<sup>136</sup> allowing the production of a full plastic (solid-liquid hybrid) LIBs (PLion)<sup>137-140</sup> with high performances.<sup>141-143</sup> This process produces light freestanding electrodes<sup>141,144</sup> with high flexibility, good mechanical properties<sup>136,140,145,146</sup>, easy to process and to upscale at the industrial level.<sup>136,140</sup> Due to this appealing ease of implementation and potential properties, such electrode process has been selected for this study. While initially, Tarascon *et al.* used graphite to formulate Li-ion electrodes,<sup>136-138</sup> here, mesoporous carbon was selected, to provide the high active surface area required for LABs. Due to the change of carbon, modification of



initial Li-ion electrodes fabrication process was necessary prior to electrode texture study. Theoretical and experimental studies are described in Chapter III and Chapter IV.

### *I.2.d. Gap between flight conditions and lab conditions*

#### *Aircraft conditions*

Aircrafts are exposed to many different atmospheric conditions along a flight as well as during their storage in a tarmac. The environment evolution is really complex as parameters like composition, pressure, hydrometric level and temperature change with altitude<sup>147-150</sup>, according to spatial position over the globe<sup>151-152</sup> and with time.<sup>153-154</sup> Earth atmosphere where aircrafts operate required then to be described.

Earth's atmosphere has evolved since the creation of Earth 4.5 billion years ago, as represented in Figure I. 23.<sup>154-155</sup> Nowadays, it is well known that at sea level the atmosphere is mainly composed of nitrogen, oxygen, water vapor and argon.<sup>156</sup> However, some traces of other gases are found as carbon dioxide, methane,<sup>154</sup> carbon monoxide,<sup>147</sup> ozone,<sup>147,149,153</sup> or even N<sub>2</sub>O.<sup>148</sup>

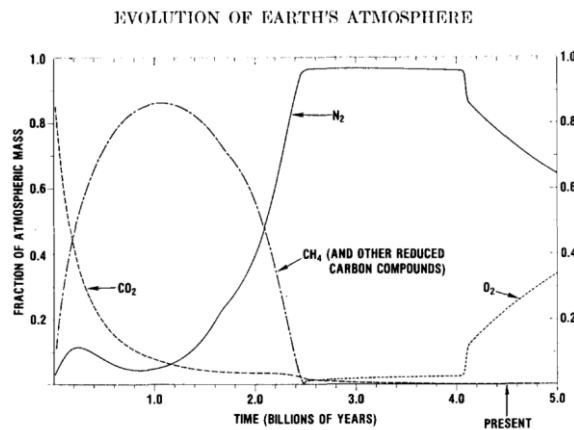


*Figure I. 22: Variation with geologic time of Earth's atmosphere composition.*<sup>154</sup>

As commercial airplanes fly between 0 to 12 km from sea level and remain mainly around 9 to 12 km from sea level, only troposphere and lower stratosphere should then be analyzed (Figure I. 23).<sup>150</sup> In these domains, both temperature and pressure tend to decrease with height. Temperature decreases almost by 80 °C from sea level to tropopause, then stays constant in stratosphere. Meanwhile, pressure decreases from 1 bar to almost 0.1 bar. These significant

variations with altitude, necessitate to take into strong consideration the impact of these two parameters onto LABs behavior.

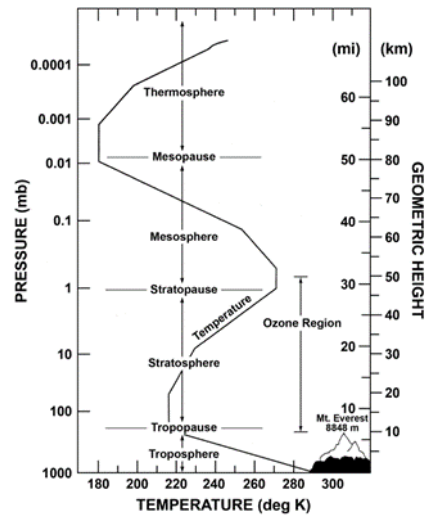


Figure I. 23: Schematic of Earth's atmosphere structure and evolution of pressure and temperature with altitude.<sup>157</sup>

Even if air composition is modified with altitude (Figure I. 24), its variations are overlooked as the gas mixing ratios remain almost constant, except for water between 0 – 20 km. Then, the relative humidity, labelled RH, is the only parameter to be taken into account in this study. RH can be defined, for a given temperature, as the percentage of the water partial pressure over its saturation vapor pressure.<sup>158</sup>

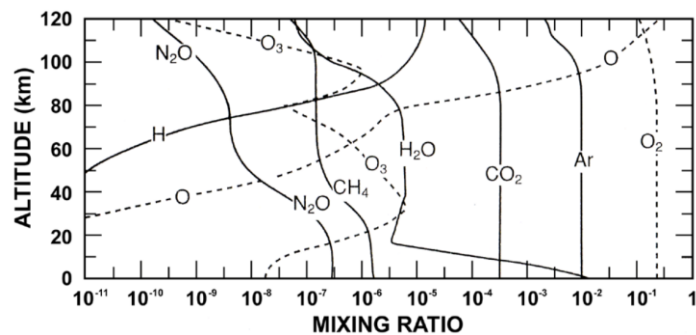


Figure I. 24: The mixing ratio of some atmospheric gases in Earth's Atmosphere as a function of altitude.<sup>11</sup>

Even though, global changes are observed with altitude, local changes also exist. Several studies provide information on parameters local evolution during flights (RH, pressure, temperature) thanks to satellites and aircraft measurements.<sup>149,150,159</sup>. Significant variations of RH, ozone content and temperature were then recorded (Figure I. 25).

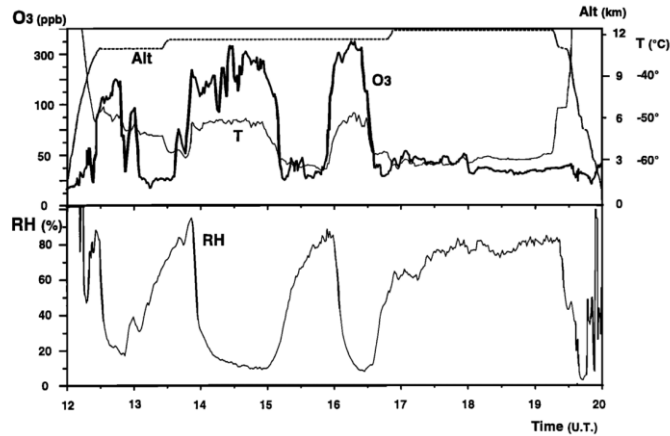


Figure I. 25: Records of temperature, pressure, RH and ozone concentration during a commercial flight (Paris-Washington, on July 9, 1995).<sup>149</sup>

Due to the variation of the parameters, even though the cruise altitude was reached, predicting the behavior of an onboard system could be tricky. To solve such issue, aircraft manufacturers used a protocol called DO-160 and entitled “Environmental Conditions and test Procedures for Airborne Equipment” to test all the equipment. To be qualified all components should bear the “extreme conditions” defined in the report (definition among other parameters of the temperature and altitude, variability of the RH, vibration and so on). Based on such document, LABs should be designed to fit the conditions exposed in Table I. 3 in order to be implemented in aeronautical conditions.

Table I. 3: Parameters selected for experiments simulating aircraft application of LABs.

Studied parameters	Scales
Temperature	-20 °C → 40 °C (use) -40 °C → 80 °C (storage)
Pressure	700 mbar → 1 bar
Oxygen partial pressure	0.14 bar → 0.2 bar
Relative humidity	100 % → 0 %

Unfortunately, the gap between the required testing conditions and the actual testing conditions at lab scale is tremendous. More than a thesis will be required to bridge them, as the numerous limitations appearing at the different levels of the system (Figure I. 20) should be first solved.

### *Lab testing conditions*

While the number of scientific papers proposing to use LABs for automotive purpose is significant,<sup>25,32,47,62,98,160–164</sup> only a few focus on LABs for aeronautical application.<sup>165–167</sup> Aside, no other applications seems to be contemplated in the state-of-the art.

In the literature, most of the theoretical values reported do not take into account the battery system weight (cooling, BMS, casing, and so on).<sup>166</sup> This lead to really optimistic development projection. For instance, Fraunhofer supposed that LAB market (quoted as Li-Luft) would be ready in 2030<sup>168</sup> while Thomson *et al.* suggest that it will occur in + 2030.<sup>11</sup> The overestimated capacities and the many limitations previously disclosed explained why nowadays LABs are still far from application, even for automotive one as illustrated by Gallagher *et al.*<sup>161</sup>

More than that, application requirements in term of temperature, pressure, gas flow and composition are overlooked by the scientific community leading to a huge gap between the performances at standard conditions (ambient temperature and pressure with pure oxygen) and those necessary to reach the testing goals described in Table I. 3. Also, in addition of atmospheric conditions, the electric power of tested lab cells should be compared to airplane power requirements. While at lab scale, the LABs power is rarely mentioned or compared, due to its meager value, current density plays an important role in cell characterization.

To precisely compare testing conditions, next part will describe the four important parameters used to study LABs at lab scale, as mentioned in scientific literature: current density, relative humidity and air composition, temperature and pressure. Later, to move from Li-oxygen to Li-air cells, descriptions of contamination mechanisms due to H<sub>2</sub>O and CO<sub>2</sub> presence will be described.

### *Current density*

Low current densities are applied to LABs due to oxygen transport limitations at the cathode and risks of dendrites formation at the anode. LABs are really sensitive to such parameter as illustrated by the increasing of overpotential and diminishing of the capacity (factor of 8) while current rises from 0.1 A to 1 mA (Figure I. 26).

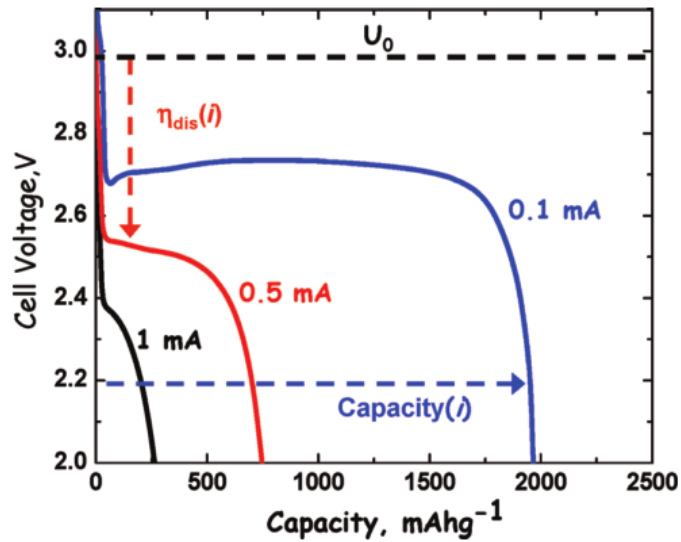


Figure I. 26: Discharge curves for an aprotic Li-O<sub>2</sub> cell (based on a Ketjen Black positive electrode) The curves give the cell output potential as a function of discharge capacity per gram of carbon in the positive electrode (mAh.g<sup>-1</sup>). U<sub>0</sub> is the thermodynamic standard cell potential.<sup>26</sup>

Other papers refer also to current density impact and highlight the same trends.<sup>169–172</sup> Still, it should be highlighted that, even if most of the time only one curve for each current density applied is shown, reproducibility issues lead to discrepancy on the observed results as shown by Griffith *et al.* in 2015 (Figure I. 27). Same trend with increase current density was observed even if some variations of the discharge capacities were noted. In 2018, Wang *et al.* also suggested to use intermittent current to extend the discharge of LABs. This way, when current was not applied, oxygen could be refilled (dissolved and transported in the electrolyte) and so oxygen transport limitations were reduced. They even proposed to reduce the value of the current at the different applying steps to maximize the capacity acquired at a given voltage cutoff.<sup>173</sup>

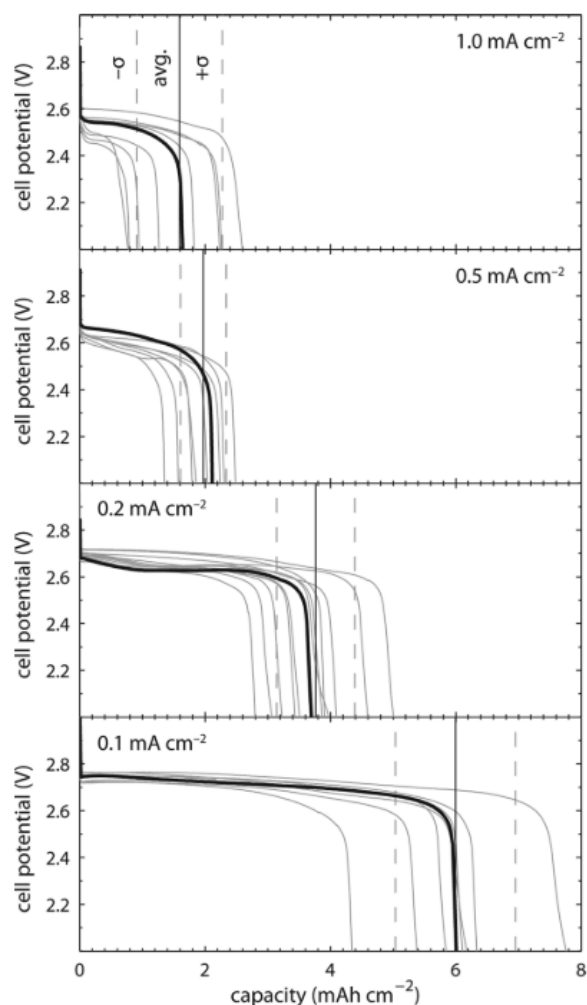


Figure I. 27: Discharge curves at different current densities (capacities per electrode geometric area). The vertical lines defined the mean values observed for each condition and dash lines the standard deviation. (The black curves correspond to cells used in their publication).<sup>171</sup>

Increase of overpotential and loss of discharge capacity were correlated by Nazar *et al.* to the change of discharge product morphology (Figure I. 28). For very low current density (e.g.  $\mu\text{A}\cdot\text{cm}^{-2}$ ),  $\text{Li}_2\text{O}_2$  toroids were observed on pristine positive electrode, while, for higher current density the carbon surface was coated by  $\text{Li}_2\text{O}_x$  small particles.<sup>172</sup> Zhai *et al.*, highlighted that higher discharge capacities were linked to large toroidal particles formation. For this reason, toroids formation should be sought.<sup>174</sup>

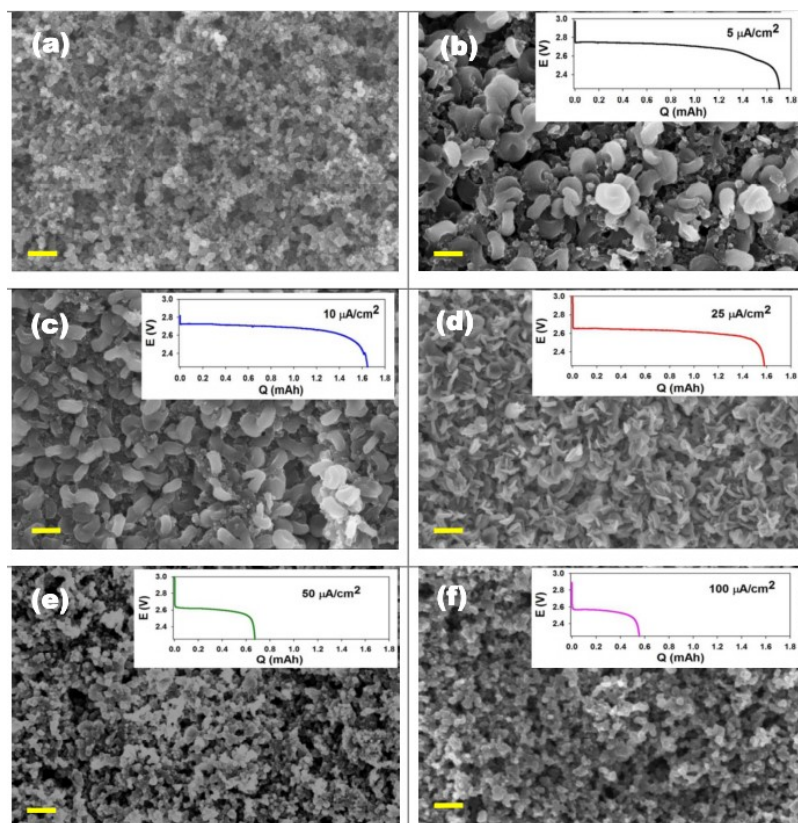


Figure I. 28: Electron microscopy (FESEM) images at a magnification of 20000x of a pristine positive electrode (a) and after full discharge at (b)  $5 \mu\text{A}/\text{cm}^2$ , (c)  $10 \mu\text{A}/\text{cm}^2$ , (d)  $25 \mu\text{A}/\text{cm}^2$ , (e)  $50 \mu\text{A}/\text{cm}^2$ , and (f)  $100 \mu\text{A}/\text{cm}^2$ , with the corresponding discharge curves. Scale bar 400nm.<sup>172</sup>

Even if, attention of researchers was mainly focused on toroidal particle formation, some of today's publications show that various morphologies can be observed as illustrated by our results (see Chapter V) even for same current density. Then, correlating morphologies such as toroids with low current density seems a bit unfair and other parameters, such as electrolyte nature, surface energy and so on, should be appraised.

#### *Relative humidity and air composition*

At first sight, it could have been easy to only target the water content of the air inlet, but it appeared that even the electrolyte moisture (in ppm) can have dramatic impacts. Both water sources will be described in the following part.

In 2011, Meini *et al.* evaluated the consequences of adding small water amount (by leak from ambient air or by water-saturated oxygen) on electrochemical performances for cells containing PC or DME electrolytes.

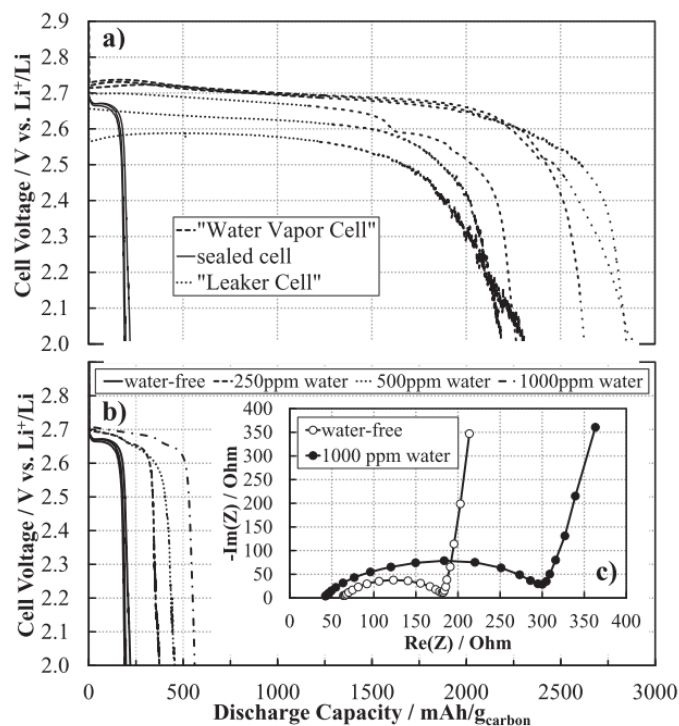


Figure I. 29: (a) First discharge curves of cells wetted by electrolyte composed of 0.1 M LiClO<sub>4</sub> in DME. The flow is rather water-free or water-saturated oxygen. "Leaker cell" corresponds to small leak of ambient air inside the cell and "water vapor cell" corresponds to water saturated oxygen (b) First discharge curves of cell with non-contaminated or water-contaminated electrolyte.<sup>175</sup>

As spotted in Figure I. 29, discharge capacity and system impedance significantly increase with rise of the water content. Even if water addition seemed appealing to enhance the capacity, the authors highlighted that its addition is not a solution as limiting reactions might take place.<sup>175</sup>

In 2014, several papers on humidity effect were released. Cho *et al.* confirmed the previous results. Cells assembled under ambient atmosphere, dry room and even glovebox and flushed under oxygen (99.995%) were compared. In the same way, water level increases discharge capacity but also system impedance and weight. The authors assumed that parasitic reactions took place explaining the destruction of lithium metal, as seen after post-mortem tests.<sup>176</sup>

Guo *et al.* decided to apply gas flows with different relative humidity: dry oxygen (0% RH), oxygen with 15% RH and also ambient air (50 %RH) to cells wetted by TetraGDME. Increase of discharge was also recorded. Nonetheless, cell cycling ability and rate were on the reverse reduced (Figure I. 30). In case of oxygen with 15 %RH and even more for ambient air,



discharge capacity faded very quickly. However, use of oxygen with 15 %RH almost doubled the first discharge capacity no matter which current density was applied. Also, the capacity fade was less critical compared to ambient air case. This difference was explained thanks to ex-situ XRD and ex-situ FTIR measurements. In each case,  $\text{Li}_2\text{O}_2$  was the main discharge product even if electrolyte decomposition occurred. Considering oxygen with 15 %RH,  $\text{LiOH}$  was also formed at the end of the discharge, as well as  $\text{Li}_2\text{CO}_3$ . For ambient air,  $\text{Li}_2\text{CO}_3$  appeared at the beginning of the discharge and was attributed to  $\text{CO}_2 - \text{H}_2\text{O}$  parasite reactions.<sup>177</sup> However, this does not explain why  $\text{Li}_2\text{CO}_3$  was observed in case of pure  $\text{O}_2$  with 15 %RH, suggesting that electrolyte or cathode material decomposition could be involved.

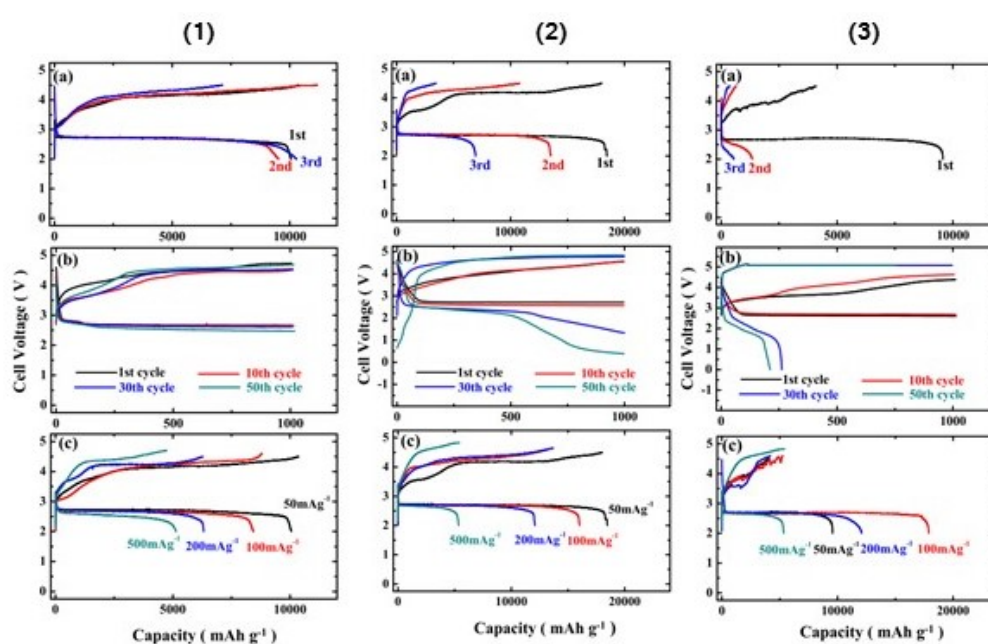


Figure I. 30: LABs cycling curves obtained with different gas composition (1) dry oxygen (0 %RH), (2) oxygen with 15 %RH and (3) ambient air (50 %RH) (a) Cycling conditions:  $50 \text{ mA.g}^{-1}$  applied between 2 V and 4.5 V (b) Cycling conditions:  $200 \text{ mA.g}^{-1}$  with a fixed capacity of  $1000 \text{ mA.g}^{-1}$  (c) Cycling at several current densities.<sup>177</sup>

Not only discharge products nature but also their morphologies were impacted. For dry oxygen, a porous film was obtained (Figure I. 31). Under ambient air, small nanosheets were noticed, irregularity of coating tends to prove partial recharge of the system. Meanwhile for oxygen with 15 %RH, toroids were obtained. The dense packing of  $\text{Li}_2\text{O}_2$  toroids might explain the increase of discharge capacity.<sup>177</sup>

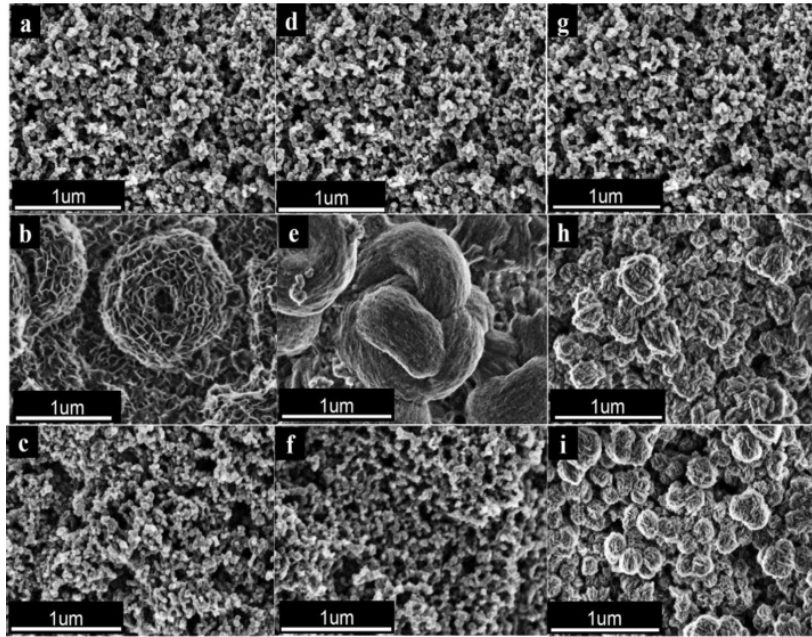


Figure I. 31: SEM images of KB electrodes at different states for the  $\text{Li}_2\text{O}_2$  batteries in pure/dry  $\text{O}_2$  atmosphere (a, b, c), in  $\text{O}_2$  atmosphere with an 15 % RH (d, e, f), and in ambient air with 50 %RH (g, h, i): before discharge (a, d, g), after discharge (b, e, h) and after recharge (c, f, i), respectively.<sup>177</sup>

Luntz *et al.* also noticed  $\text{Li}_2\text{O}_2$  toroid formation when small water content was added to anhydrous electrolyte. In addition, toroids size increased with water content which results in higher discharge capacity.<sup>178</sup>

In 2015, Schwenke *et al.* recommended to add few amount of water in the electrolyte to trigger  $\text{Li}_2\text{O}_2$  formation and prevent electrode surface from passivation. Surprisingly, contrary to previous works, no  $\text{LiOH}$  was formed on the cathode surface for electrolyte water content  $< 1\%$ . They also highlighted that water content was beneficial, as  $\text{Li}_2\text{O}_2$  yield was increased (Figure I. 32) and so parasitic reactions were not that problematic. Still, they acknowledged that avoiding compounds such as PVdF or DMSO is crucial in presence of water, as the resulting protons production could deteriorate rapidly the electrolyte.<sup>179</sup>

Such contradictory results perfectly illustrate the versatility of the conclusion made in state-of-the-art concerning the water content impact on LABs performances.

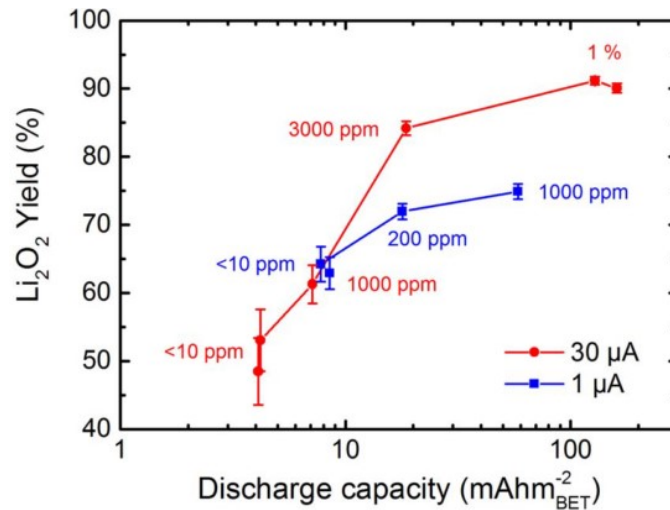


Figure I. 32:  $\text{Li}_2\text{O}_2$  yield versus discharge capacity of carbon paper cathodes discharged at  $1 \mu\text{A}$  and  $30 \mu\text{A}$  with different water contents in the electrolyte. The yield consists of the determined mass of  $\text{Li}_2\text{O}_2$  found in the cathode related to the mass expected from the charges passed during discharge.<sup>179</sup>

Water is not the only contaminant that can affect battery performances. Nitrogen and carbon dioxide from ambient air can also react in LABs. Even if it is well known that nitrogen and lithium react at room temperature<sup>180</sup> few studies were done on nitrogen impacts as they seem to be negligible.

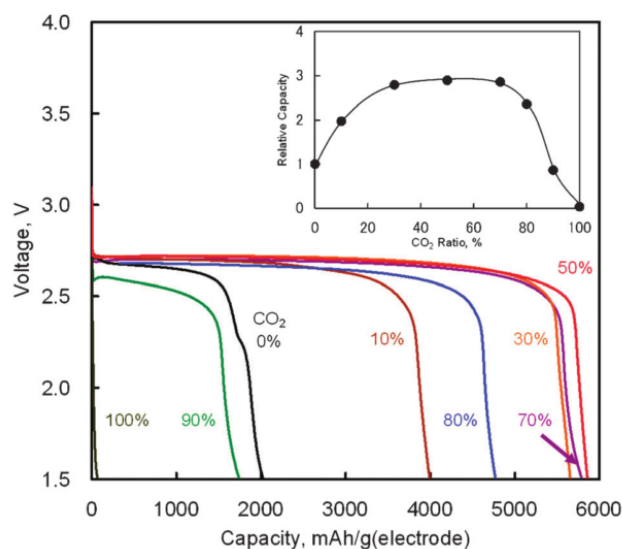


Figure I. 33: Discharge curves of  $\text{Li}-\text{O}_2/\text{CO}_2$  batteries with various  $\text{O}_2/\text{CO}_2$  ratios at  $25^\circ\text{C}$  ( $0.2 \text{ mA}\cdot\text{cm}^{-2}$ ).<sup>181</sup>

Carbon dioxide impact was studied by Takechi *et al.* (Figure I. 33).<sup>181</sup> A raise of  $\text{CO}_2$  content in  $\text{O}_2/\text{CO}_2$  mixture leads to discharge capacity rise. Still, only  $\text{O}_2/\text{CO}_2$  mixture, with 30 % to 70 % of  $\text{CO}_2$  at a discharge rate of  $0.2 \text{ mA}\cdot\text{cm}^{-2}$ , should be selected to really upgrade

performances. Takechi *et al.* emphasized that the associated mechanism still need to be explained, since proposed reaction pathways do not justify such increase in capacity.<sup>181</sup>

In literature, many publications focused on gas composition evolution upon operation, rather than gas inlet composition, in an attempt to investigate LABs mechanisms as done by Beyer *et al.*,<sup>182</sup> Black *et al.*,<sup>183</sup> Meini *et al.*<sup>184</sup> or even Thotiyl *et al.*<sup>185</sup> Following CO<sub>2</sub> and O<sub>2</sub> formations permitted to guess which discharge products were released and to assume the associated system kinetics. Indeed, the gas released would depend on which discharge product is formed (Figure I. 34).<sup>178</sup>

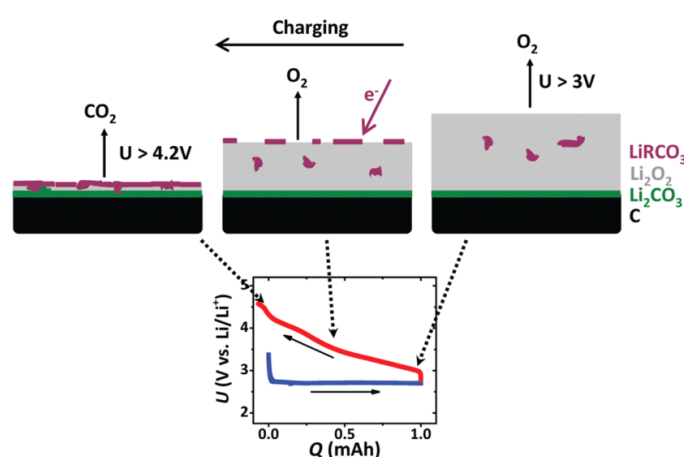


Figure I. 34: Gas production according to charge potential applied.<sup>178</sup>

Huang *et al.* explained that if oxygen is more studied than any other gas it is because of negative impact of CO<sub>2</sub> and H<sub>2</sub>O. CO<sub>2</sub> tends to passivate the positive electrode while H<sub>2</sub>O first diffuses towards negative electrode through the electrolyte and reacts with lithium foil. Then, LiOH is produced and negative electrode volume expand significantly (Figure I. 35).<sup>160</sup>

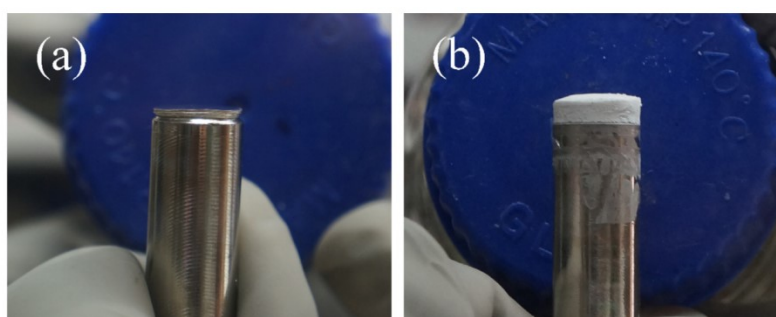


Figure I. 35: Picture of a negative electrode before cycling (a) and after 51<sup>th</sup> cycles (cutoffs at 500 mAh g<sup>-1</sup>) (b).<sup>160</sup>

Even in the case of a pouch cell made with a low permeability polymer window at the inlet side, cell volume expansion was really significant (Figure I. 36). According to the authors, the volume expansion was due to dihydrogen released after moisture infiltration inside the cell (as the system was not sealed perfectly).<sup>186</sup> Worth point out that volume expansion could be also an issue in the case of anhydrous systems. Indeed, Yoo *et al.* simulated the volumes expansion linked to anode modification and formation of discharge products at the cathode. Depending on the solubility of lithium peroxide, electrolyte leakage could be triggered as lithium peroxide filled the cathode porosity and chase the electrolyte.<sup>187</sup>



*Figure I. 36: Picture of a Li-air pouch cell with gas diffusion membrane (PTFE) after discharge in ambient air.*<sup>186</sup>

All the contradictory results highlight the lack of study at ambient air as well as the lack of information on Li-air mechanisms, stressing the existing gap between laboratory conditions and practical use of LABs.

### *Temperature*

The few available publications focusing on temperature mainly deal with improvement of ionic liquid electrolyte and all solid state batteries, since in both cases, increase of conductivity is required and could be achieved by temperature modification.<sup>98</sup> In 2011, Zhang *et al.*, alleged to develop an electrolyte (mixture of tris(2,2,2-trifluoroethyl) phosphate and PC with a  $\text{LiSO}_3\text{CF}_3$  salt) with properties allowing to work in ambient environment.<sup>188</sup> On another side, in 2013, Park *et al.* cycled a lithium oxygen cell between  $-10\text{ }^\circ\text{C}$  and  $70\text{ }^\circ\text{C}$  (Figure I. 37).<sup>189</sup>

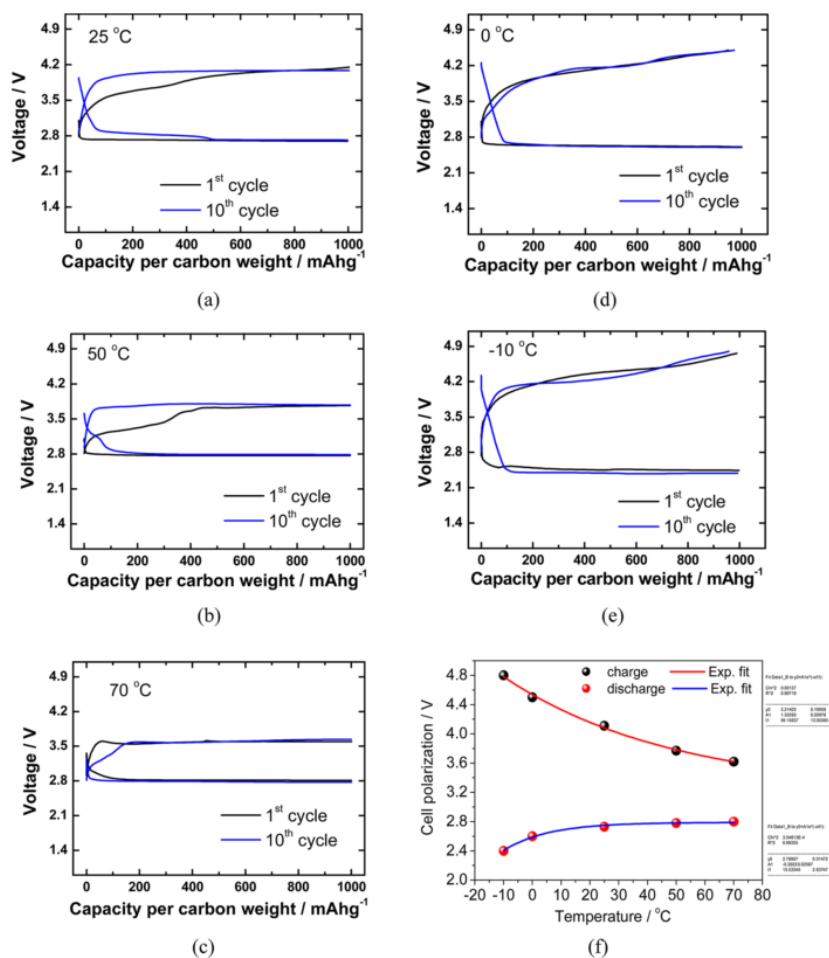


Figure I. 37: Impact of temperature on cycling for TEGDME-based electrolyte lithium-oxygen cells. Capacity limited to 1000 mAh.g<sup>-1</sup><sub>carbon</sub>. Current: 100 mA.g<sup>-1</sup><sub>carbon</sub>.<sup>189</sup>

Less polarization is reported when temperature increases. Park *et al.* attributed these reductions of polarization and charge plateau voltage to a faster kinetics. This trend is also enhanced by a diminution of electrolyte viscosity which promotes O<sub>2</sub> and Li<sup>+</sup> transport. Increasing temperature also benefits to the formation of amorphous Li<sub>2</sub>O<sub>2</sub><sup>189</sup> which leads to higher conductivity compared to crystal compounds.<sup>190</sup> Conversely, thanks to a study made between 30 °C and 70 °C on Super P electrode, Song *et al.* claimed that at high temperature more Li<sub>2</sub>O<sub>2</sub> crystal nuclei are formed and hence a thinner coating were deposited. Song *et al.* proposed to use temperature as a tool to enhance discharge ability in the non-aqueous LABs.<sup>191</sup> Tan *et al.* investigated in the same time temperature and current density and proposed a mechanism for Li<sub>2</sub>O<sub>2</sub> formation during discharge (Figure I. 38).<sup>169</sup>



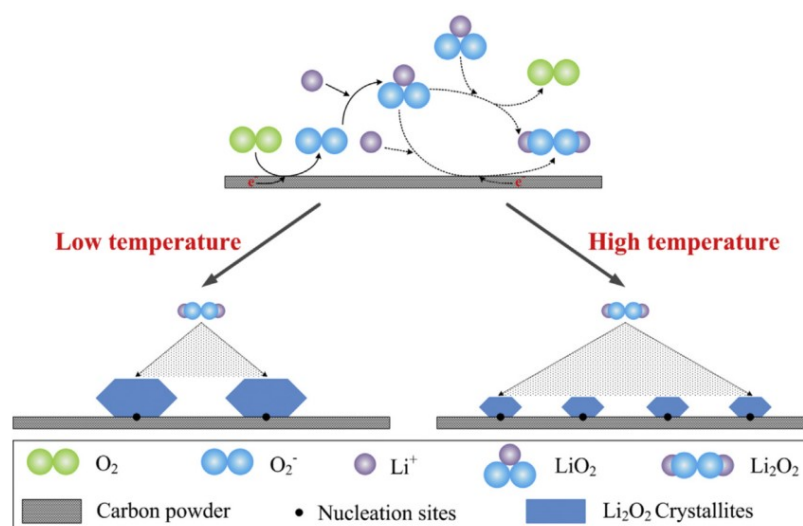


Figure I. 38: Proposed mechanism to explain  $\text{Li}_2\text{O}_2$  crystallites growth.<sup>169</sup>

At low temperature, the low number of nucleation sites leads to the growth of huge  $\text{Li}_2\text{O}_2$  crystallites on these limited nucleation sites. Raise of temperature allows an augmentation of nucleation sites and so led to thinner coating. While discharge temperature controls the number of nucleation site, product shape is controlled by current density.<sup>169</sup> Current density and temperature were then studied in parallel in this study to understand the balance between these two parameters. As spotted here, LABs are based on nucleation leading the LABs ‘community to rediscover chemistry fundamentals.

### Pressure

Pressure is a meaningful parameter to include in further investigations as it impacts oxygen availability. In 2003, Read *et al.* emphasized the importance of increasing oxygen partial pressure on discharge capacity and rate capability due to oxygen transport properties modifications.<sup>99</sup> In 2010, Yang *et al.* examined impact of discharge rate (between  $0.1 \text{ mA}\cdot\text{cm}^{-2}$  to  $1 \text{ mA}\cdot\text{cm}^{-2}$ ) and in the same time oxygen pressure (from 1 atm to 10 atm) in closed cells.<sup>170</sup> The advantage of this system is to increase oxygen availability compared to open system.<sup>170-192</sup> As shown in Figure I. 39, increasing pressure at same discharge rate provides, as expected, better discharge capacity.

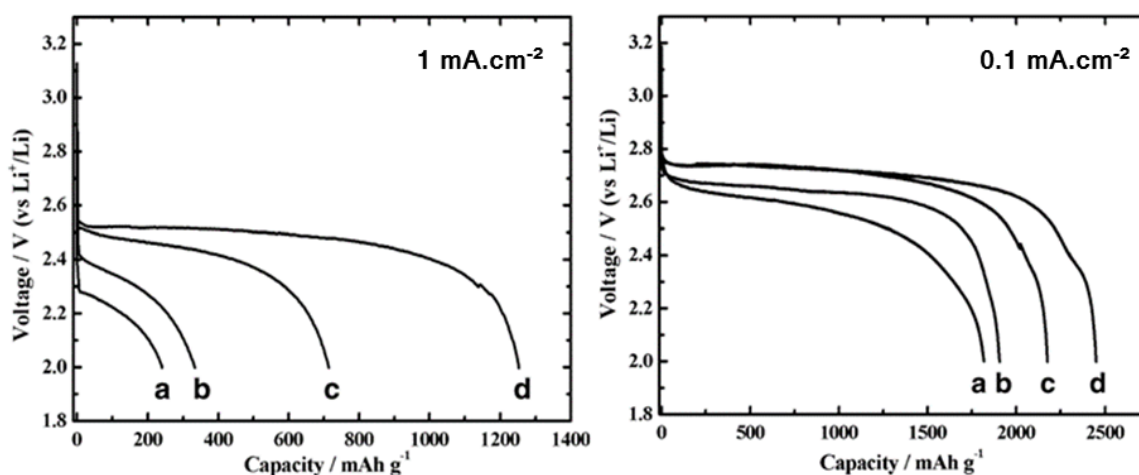


Figure I. 39: Discharge curves at high and low discharge rate at several pressure (a) 1 atm (b) 3 atm (c) 5 atm (d) 10 atm.<sup>170</sup>

Yang *et al.* emphasized that for lower rates the increase of discharge capacity is even more enhanced with higher pressure. Increase of pressure is hence a hint to reach higher discharging rate and higher capacity whereas it implies consumption of energy to reach pressure higher than atmospheric one especially in planes flying in altitude. These results are explained by the discharge product morphology. Dense films are deposited at high rates and also at low pressures and are assumed to prevent further reactions to occur.<sup>170</sup>

In 2012, Christensen *et al.* applied an external pressure to a closed cell. By pressing the sandwich cell, contact between the several parts (negative, separator and positive) is insured. As the volume of LAB changes a lot (due to new phases formation, oxygen consumption and release, dendrite formation and so on) contact is sometime lost. Applying an external pressure to the cell is then used to maintain the system cohesion as it has been proposed for LIBs.<sup>54</sup>

In 2014, Nemanick *et al.* launched the same study as Yang *et al.*, using diglyme as the solvent (previous researches were done using propylene carbonate) (Figure I. 40).<sup>192</sup> Same trend was noticed: increase of capacity with higher pressures and lower current densities. Nemanick *et al.* underlined that between 10 and 25 atm, performances are not improved because of the inefficient use of the positive electrode surface. Not complete dense film is observed on SEM picture which tends to prove that not all the surface is reacting. Two solutions to use all the surface are proposed: providing more oxygen with higher pressure or decreasing discharge rate to slowly consume oxygen. This advice were also given by Shibata *et al.* in 2015 after simulation with LBM model of  $\text{Li}^+$  and  $\text{O}_2$  transport inside positive electrode.<sup>193</sup>



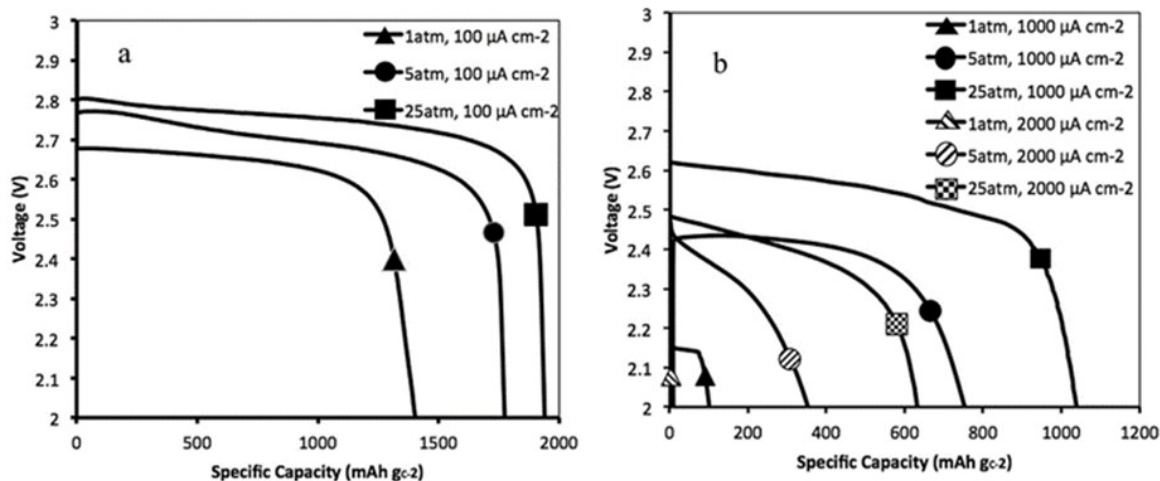


Figure I. 40: Discharge curves for diglyme-based Li-air cells discharged at  $0.1 \text{ mA cm}^{-2}$  (a) and  $1$  or  $2 \text{ mA cm}^{-2}$  (b) for several pressures ( $1 \text{ atm}$ ,  $5 \text{ atm}$  and  $25 \text{ atm}$ ).<sup>192</sup>

Pressure was not also used as an input parameter for experiments but also as a controlling parameter. In 2016, Lepoivre *et al.* reported a new device which measures pressure changes upon cycling. Combining these variations to cell potential, number of consumed electrons can be calculated and helps to understand mechanisms happening inside the cell<sup>194</sup>. These kinds of devices are powerful tools to investigate deeper LABs and particularly to focus on the gas composition impacts on performances.

In 2017, Kwon *et al.* pointed out that the oxygen partial pressure at  $1 \text{ atm}$  should be around  $0.5 \text{ atm}$  to  $0.7 \text{ atm}$  (Figure I. 41) to extend the cell stability (correlated to lower  $\text{CO}_2$  degassing) and capacity (significant evolution of oxygen upon cycling).<sup>195</sup>

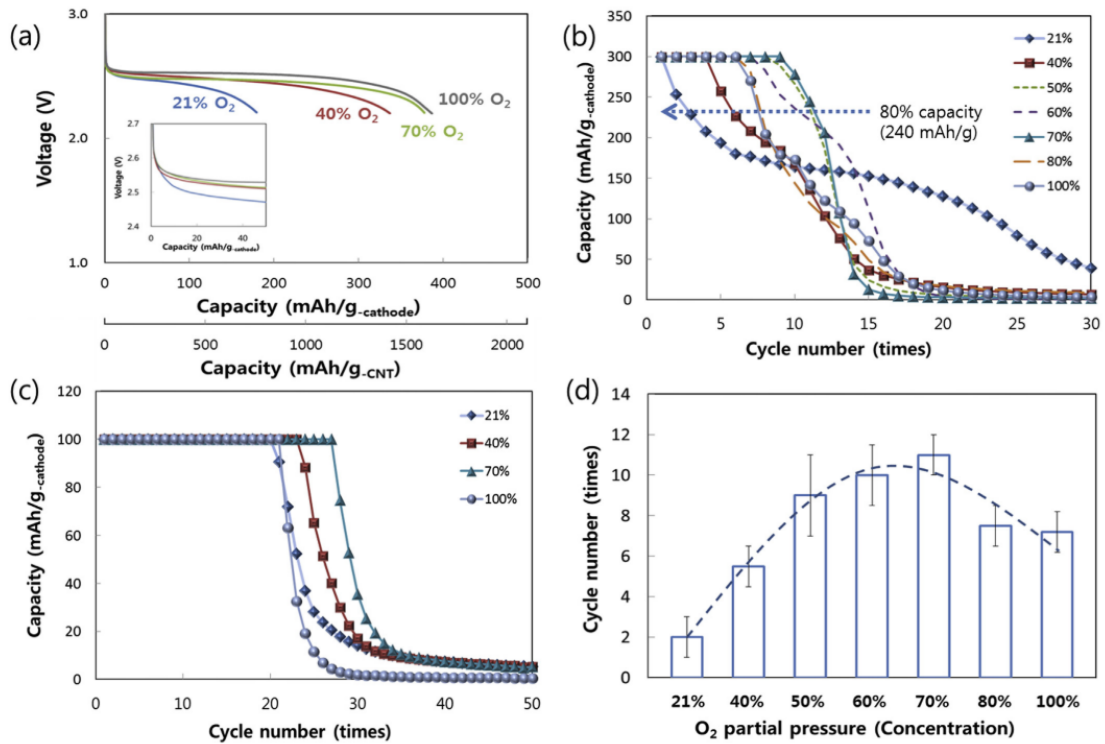
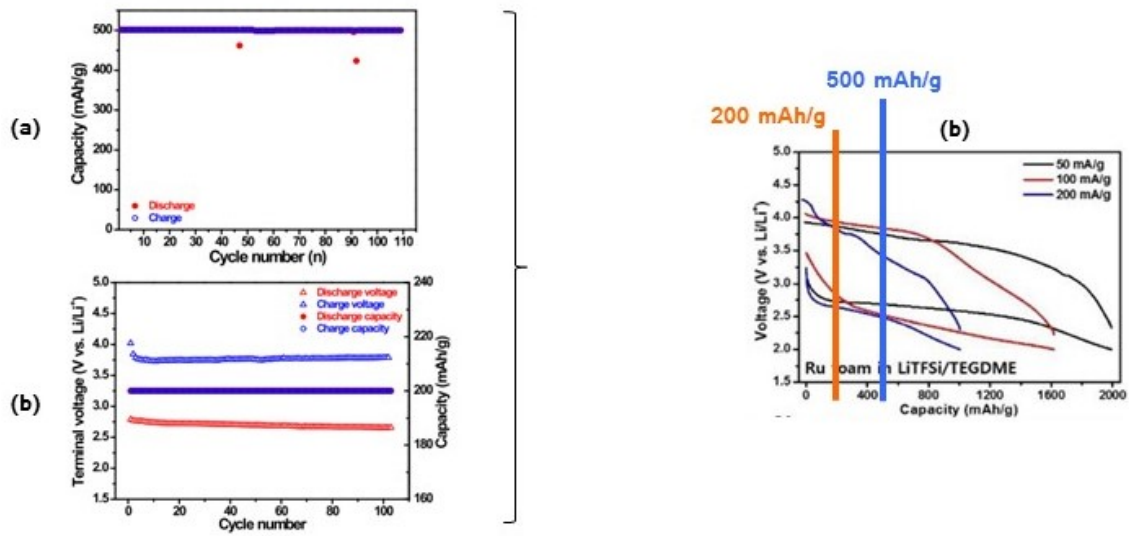


Figure I. 41: LABs capacities and cycling abilities according to applied oxygen partial pressure (a) 1<sup>st</sup> discharge, (b) Cycling with cutoff at 300 mAh/g<sub>electrode</sub>, (c) Cycling with cutoff at 100 mAh/g<sub>electrode</sub>, (d) Cycling properties versus oxygen partial pressure while applying a cutoff at 300 mAh/g<sub>electrode</sub>.<sup>195</sup>

Notwithstanding the interesting information on pressure impact, Figure I. 41 reveals the importance of the mass used to define the system capacity. Above all, comparison Figure I. 41.b and Figure I. 41.c shows how capacity retention of LABs can be easily twisted. Figure I. 41.c will tend to show that capacity retention is quite good over the cycling while Figure I. 41.b proves the opposite, meaning that cycling cutoffs should be always provided. Unfortunately, current state-of-the art, often lack of clear information on such parameter, making comparisons difficult between the several systems described in literature.

More important than the comparison of the different published results, Kwak *et al.* illustrated in their work how easily cells performances can be overestimated (Figure I. 42).<sup>196</sup> While only paying attention to Figure I. 42.a or Figure I. 42.c, performances of the system seemed pretty good. Still, while looking at Figure I. 42.b, it appeared that the cells are not at all challenged, as they are cycled in a really short range of capacity. This way, as not all electrode volume and surface is engaged, even if passivation and degradation mechanism occur, some more surface and volume will be available for the other cycles. Thus, the cycle life is just

delayed and this way, the cyclability is artificially enhanced leading to confusion and mistakes on LABs real behavior upon cycling.



**Cyclability of Li-O<sub>2</sub> batteries using Ru-foam as cathode material in LITFSI//TEGDME at a current density of (a) 50 mAh/g and (b) 200 mAh/g and with capacity limitations at (a) 500mAh/g and (b) 200 mAh/g**

**Cycle profile of Li-O<sub>2</sub> batteries using Ru-foam as cathode material (b) at a current density of 50 mAh/g 100 mAh/g and 200 mAh/g in LITFSI//TEGDME**

*Figure I. 42: Highlighting of the capacity limitation impact on cyclability overestimation.<sup>196,197</sup>*

### *I.2.e. How to define LABs capacity?*

Compared to LIBs, LABs do not rely on lithium cations intercalation. Here, lithium cations react with reduced oxygen anions on top of the cathode surface leading to higher capacities as the system is freed from intrinsic intercalation limits.

Here, the cathode acts more as a catalyst than an active material, leading to misestimated specific capacity definition ( $\text{mAh/g}_{\text{carbon}}$  or  $\text{mAh/g}_{\text{gold}}$  instead of  $\text{mAh/g}_{\text{oxygen}}$  or  $\text{mAh/g}_{\text{lithium}}$ ), lithium and oxygen being the real active materials. Also due to different electrode formulations (type of carbon use in carbon-based electrode, carbon-free electrodes, amount of binder), the final mass of the electrode can be far from the mass of catalyst, implying overestimated estimations. In addition, Choi *et al.* highlighted the impact of not standardized oxygen gas system and catalyst layers on cell volume and so on volumetric energy density estimation.<sup>198</sup> Also, in literature, several publications do not even mention the mass used to make the calculations. This clear lack of consensus leads to a jumble of results in the literature. Figure I. 43 underlines the variety of results observed in literature and compared them to the theoretical value estimated by the scientific community.



Figure I. 43: Non-exhaustive list of the several expressions of LABs capacity in the literature.<sup>26,51,55,56,198–201</sup>

Radin *et al.* proposed to follow three conventions to overcome results inhomogeneity and to facilitate comparison of the experimental results.

- First, they suggested to always provide capacity and current as function of the positive electrode mass and geometric surface area.
- Secondly, the mass of overall components of the cathode should be taken into consideration in an attempt to provide data required to implement the battery at practical level.
- Finally, they highlighted that even if a support material/current collector is used, the proof of its low contribution to the overall system is necessary.<sup>116</sup>

In this study to be conformed to this precious advices, capacities will be expressed in  $\text{mAh/g}_{\text{electrode}}$  and  $\text{mAh/cm}^2_{\text{geometric}}$  with respect to the electrode overall mass and geometric area.

Despite the precautions taken, as oxygen is consumed and incorporated to the cell while discharge product is formed, the final mass of the system will increase along discharge,<sup>52</sup> misleading the capacity estimation in  $\text{mAh/g}_{\text{electrode}}$ . Once loaded in an aircraft, it worth points out that the rise of weight will imply a change of the aircraft gravity center, impacting significantly the aerodynamic properties.<sup>165</sup>

### I.3. Thesis objectives

The initial thesis objectives were to optimize the cells developed at lab scale and to test them after in the extreme conditions defined in Table I. 3. Besides, reality of LABs development lead to a redefinition of the thesis objectives due to the many observed limitations (Figure I. 20).

As the initial requirement for LABs aeronautical application is high energy density, the first attempt was to increase the energy density of the system. To do so, a first investigation on one of the main components of the cell, the cathode, was launched. The first part of the study focused then on the cathode development, taking into account the enlargement of high active surface area, to promote ORR and OER reactions, while also taking into account the risks of passivation and pore clogging. In addition, to maximize the gravimetric energy density, thick cathodes were privileged even if it implies oxygen mass transport limitations. Then, taking into account the limitations, as well as the target of high gravimetric energy density, cathode design was studied from theoretical point of view, using multi-scale modeling, as well as from experimental point of view. At first, the several techniques implemented along experimental and theoretical investigations would be described in Chapter II. Later, the approach developed as well as the results will be described in Chapter III and Chapter IV.

Later, to move from Li-oxygen to Li-air batteries, a particular focus was made on experimental testing conditions. To study current density and temperature impacts, a reproducibility study was implemented, based on the use of GDL electrodes as a reference cathode. Variability of the results and the identified trends will be described in Chapter V. Also, in an attempt to understand the observed results, a continuum model describing potential contamination mechanisms would be also disclosed in Annex.

# CHAPTER II: EXPERIMENTAL PROCEDURES

## Contents

---

II.1. Electrode fabrication process.....	52
II.1.a. Electrode materials.....	52
II.1.b. Dip-coated electrodes fabrication process.....	54
II.1.c. Porous flexible electrodes fabrication process.....	59
II.1.d. Comparison of the two electrodes fabrication processes.....	61
II.2. Battery assembling.....	63
II.2.a. Electrolyte preparation.....	63
II.2.b. Swagelok cell assembling.....	63
II.3. Experimental set-up for controlled LABs atmosphere.....	66
II.3.a. “Le Parfait” container.....	66
II.3.b. Gas flow system.....	67
II.4. Characterization techniques.....	69
II.4.a. Electrode characterization.....	69
II.4.b. Electrochemical characterization.....	71
II.4.c. System characterization.....	73
II.4.d. Continuum modeling.....	76

---

## II.1. Electrode fabrication process

Two electrode fabrication processes have been tested to design electrodes for LABs. Initially, electrodes were produced using dip-coating process. Then, another process was scrutinized to enhance the gravimetric energy density by moving from thin toward thick electrodes fabrication. As oxygen diffusion limitation could get worse with the rise of the electrode thickness, the studied process had been chiefly selected as it allows mastering the electrode porosity. Such fabrication process is usually known in LIB field as the Bellcore process.<sup>136</sup>

In the following part, the various components of the formulations prepared will be described. Later, the aforementioned electrode fabrication processes will be reported. Once electrode fabrication will be well defined, battery assembling will be uncovered. Finally, the characterization techniques performed to evaluate the properties and performances of the different electrodes and battery cells will be disclosed.

### II.1.a. Electrode materials

#### Carbons

As previously argued, carbon-based electrodes had been selected for this study. Among the several types of carbon, Ketjen Black (EC600-JD, Akzo Nobel) was considered due to its low particle size. Also, previous continuum modeling at LRCS predicted that higher properties would be reached compared to Carbon SP, usually picked over for such application (Figure II. 1).<sup>128</sup> For comparison, Carbon SP (C.ENERGY, Imerys) and Graphite (TIMCAL SLP50, Imerys) were also chosen as electrode materials.

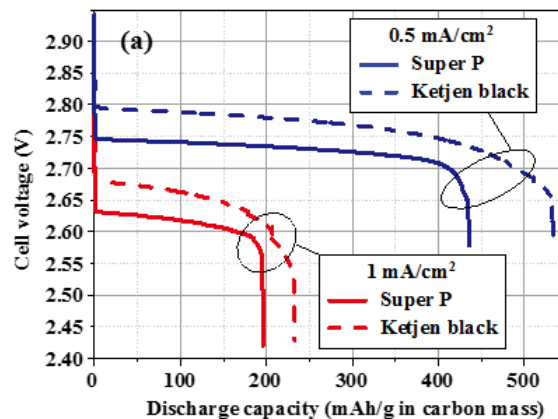


Figure II. 1: Modeling of Ketjen Black based LABs discharge capacities compared to Carbon SP based ones.<sup>128</sup>



As carbon substrate strongly influences the discharge product<sup>202</sup> and due to the high surface developed, likely to adsorb many unwanted species, Ketjen Black and Carbon SP were dried at 300°C under vacuum overnight and then stored in an oven at 50 °C until use.

### *Binders*

Different binders were used depending on the electrode fabrication process, as well as the battery components compatibility. Initially, dip-coated electrode fabrication process was implemented by previous LRCS studies for LABs electrodes fabrication. To guarantee cohesive electrodes, PVdF (Kynar, Arkema) was then chosen as the binder. Unfortunately, while electrodes were immersed in DMSO, which was at this time the electrolyte solvent, disintegration of the electrode was observed. Such behavior can be explained by the solubility of PVdF in polar solvents like DMSO or DMF,<sup>203</sup> PVdF was then solubilized in the electrolyte and the electrode cohesiveness was not ensured anymore. To overcome this issue, PVdF was replaced in dip-coated electrode fabrication process by PTFE.

Later, flexible electrodes were again based on PVdF. More precisely a copolymer of PVdF, named PVdF-HFP (Kynar Flex 2801, Arkema), was selected due to its lower crystallinity ratio and melting temperature compared to PVdF itself.<sup>204</sup> Thanks to its amorphous domain a lot of electrolyte can be stored and its crystallinity parts help formation of self-standing electrodes. According to literature, this binder is one the most stable and can be cycled at high voltage (until 5 V).<sup>136,205</sup> For all these reasons, its use was spread in LIB field to produce flexible electrode films<sup>136-140</sup> and thus was transposed in this study to LABs electrode fabrication. Compatibility of electrode binder versus electrolyte solvent was insured in this part of the study as DMSO was replaced by glymes.

Nonetheless, it worth points out that Black *et al.* highlighted the instability of PVdF toward superoxide species.<sup>202</sup> The binder could have then impacted the battery stability even if such observation was not made here. Also, along the experiments, electrodes cohesiveness seemed to be always maintained with the PVdF-HFP/glyme couple.

### *Solvent for slurry preparation*

In order to prepare the different electrodes, the powders (carbons and binders) were stirred in different solvents depending on the fabrication process taken into consideration.

While the slurry is casted by doctor blading, volatile solvents are preferred (decrease of the drying time is then achieved). Acetone, characterized by a low boiling point (56 °C) and significant vapor pressure (almost 400 mm Hg at 40 °C),<sup>206</sup> was then used as its efficiency have been already demonstrated in literature.<sup>136,140</sup> Also, acetone is economical and not toxic explaining its interest for electrode fabrication process.<sup>206</sup>

However, for dip-coating technique, less volatile solvents are required to master perfectly the slurry homogeneity and viscosity, prior to the immersion of the substrate. Formation of a homogeneous layer all along the substrate would be then facilitated. To do so, NMP, a solvent spread at the industrial scale, was selected. Its high boiling point (204.5 °C) and low vapor pressure (1 mm Hg at 40 °C)<sup>207</sup> facilitate long mixing steps and casting over a long period of time. Handling such solvent is then easier than highly volatile ones. In counterbalance, NMP is expensive and is more demanding on drying energy.<sup>207</sup> Also as NMP is a reprotoxic agent, strict safety precautions should be implemented to use it safely.

### *Porogen agent*

One additive was selected while processing fabrication of flexible electrode films. To ensure the mechanical properties of the film, DBP is usually added to Bellcore formulations and acts as a plasticizer agent. Also, DBP plays the role of a porogen agent. Once the film is prepared, DBP can be extracted thanks to low boiling solvents, here ether, creating extra porosity within the electrode.<sup>208</sup> This property was especially scrutinized in this work for mastering electrode porosity, which is of great importance in LABs.

### *II.1.b. Dip-coated electrodes fabrication process*

Dip-coating electrode fabrication process previously implemented in the lab was based on three main steps:

- First, the components are mixed together by magnetic stirring to get the slurry.  
The carbon (Carbon SP) was previously grinded at the mortar and then added to the binder (PVdF) and solvent (NMP) mixture.
- Then, a stainless steel grid (40 mesh, Ø=9 mm), was immersed in the slurry.
- Finally, the obtained grid was dried under vacuum (Buchi®).

Due to the above-mentioned reasons, PVdF was replaced in this study by PTFE and Carbon SP by Ketjen Black. To promote higher slurry homogeneity mixing, the magnetic

stirring was replaced by an Ultraturax (Figure II. 2). In parallel, the volume of NMP was raised to ensure sufficient volume for mixing.



Figure II. 2: Mixing device for NMP slurries (Ultraturax).

Also, the slurry preparation was modified by a multi-steps solvent addition as it enhances the slurry homogeneity compared to one-step solvent addition process. Finally, the optimal addition steps implemented are described in Figure II. 3 for a NMP slurry of 7 mL with a dry mass (Carbon + binder) of 3 %.

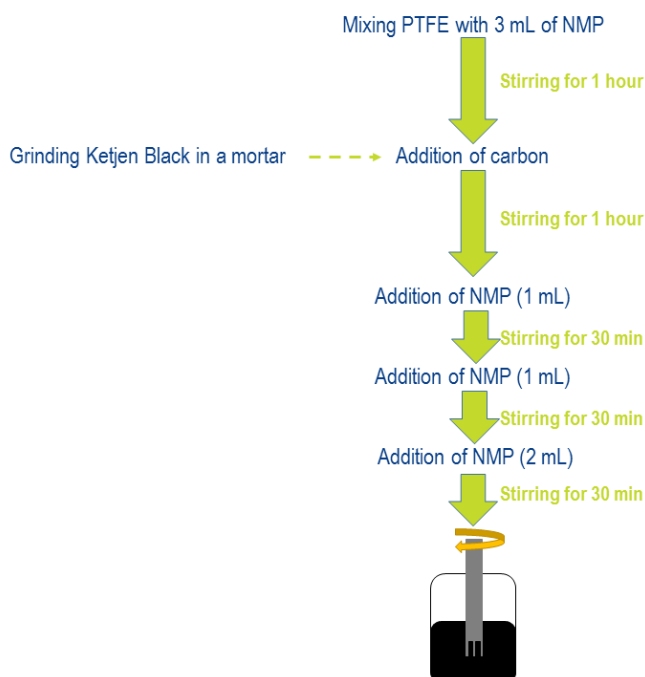


Figure II. 3: Multi-steps solvent addition process for Dip-coating electrode fabrication process.

Except the mixing steps, the rest of the process was retained to create a rough carbon surface on top of the stainless steel grid (Figure II. 4).

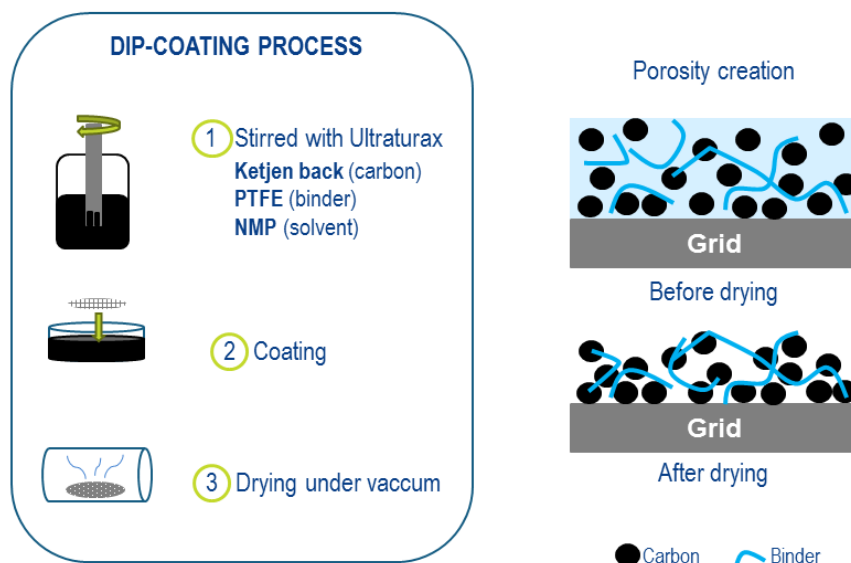


Figure II. 4: Schematics of Dip-coated electrode fabrication process and related porosity creation.

Initially, the electrodes prepared were presenting cracks and inhomogeneous coating on top the stainless steel grid (Figure II. 5). To overcome them, three parameters, possibly responsible of such observations, were explored. The first one was the binder weight ratio compared to the overall solid mass (comprising carbon and binder mass). While the binder permits to ensure the formation of a strong polymeric network maintaining the films, too high ratios were damageable. Indeed, high binder contents tend to infringe access to the carbon. As LABs performances depend on the surface of carbon available, a balance was required to have enough carbon surface developed while also keeping the film cohesiveness. Later, the second parameter modified was the dry mass ratio in the slurry: it directly impacts the slurry viscosity and so the mixing and deposition efficiencies. Finally, the drying step was also scrutinized as it could have also explained the cracks observed by SEM.

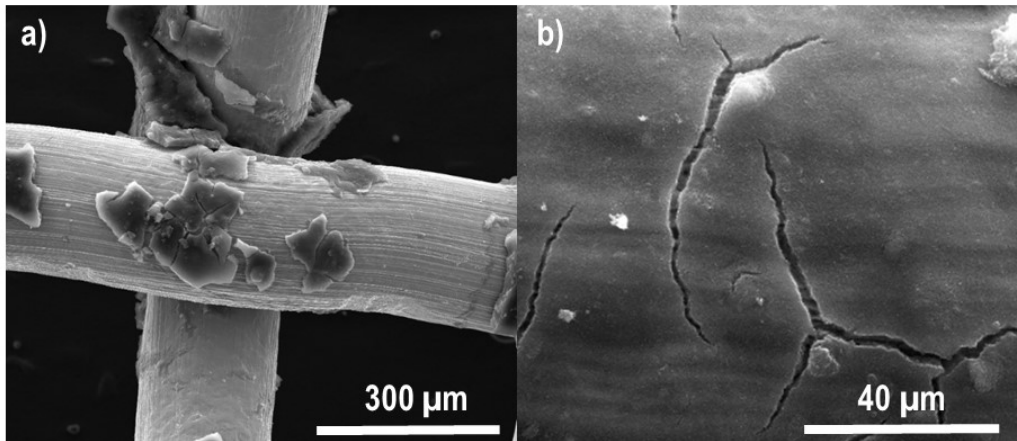


Figure II. 5: Observation of the dip-coating process issues to overcome a) aggregates and inhomogeneous coating on top of the stainless steel grid b) cracks in the coating.

To quickly test the effects of the various parameters impacting the grid coating efficiency, a reduced experimental plan was implemented. As illustrated in Figure II. 6, the plan enables to uncorrelate each parameter implication.

To create a film able to mold the grid shape and be maintained, the binder amount was adjusted. Still, as formulation with low binder amount were preferred from gravimetric energy density, lower and upper ratios were tested. In the case of 5 wt%, the coating was not improved. In the contrary, 15 wt% of binder led to higher aggregation (Figure II. 7). Then only improving the binder ratio was not sufficient.

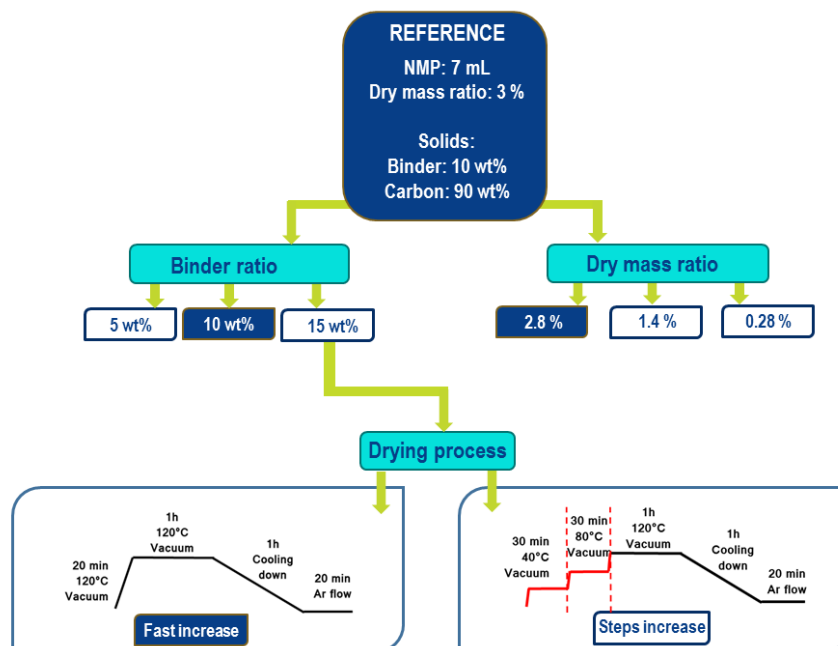
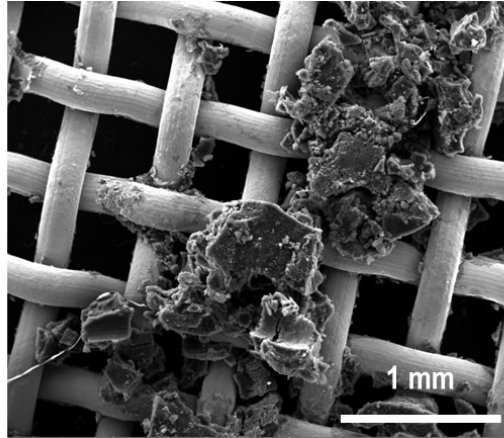
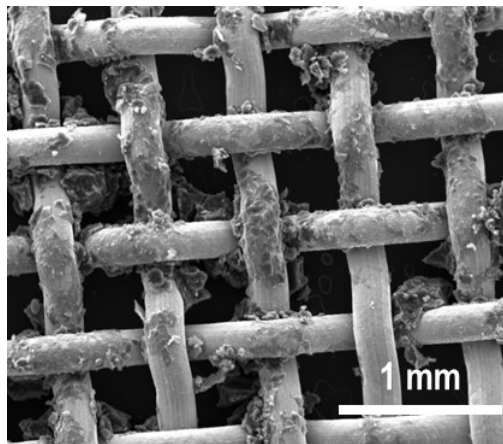


Figure II. 6: Experimental plan design to test the several parameters impacting the grid coating efficiency. The reference parameters are highlighted in dark blue.



*Figure II. 7: SEM picture of a dip-coated electrode formulated with 15 wt% of binder.*

Now let's consider the drying step, since the observed cracks suggest that the drying process is too fast to enable smooth drying, a two-steps drying procedure was enforced. The direct rise of temperature from ambient temperature to 120 °C, was replaced by two plateaus of thirty minutes each at 40 °C and 80 °C and the two drying processes were compared. Better repartition of the deposit was observed (Figure II. 8) with the slower drying process and a binder ratio of 15 wt% (*i.e.* Figure II. 7 for comparison).



*Figure II. 8: SEM picture of a dip-coated electrode formulated with 15 wt% of binder and a slow drying process.*

Finally, to uniformly deposit the slurry, this one should have a low viscosity to fit the grid shape. As the dry mass ratio in the slurry directly impacted the viscosity, two trials were done with slightly lower values than the reference case. A smooth deposit on top of the grid was then visualized while decreasing the dry mass to 0.28 % as shown in Figure II. 9.

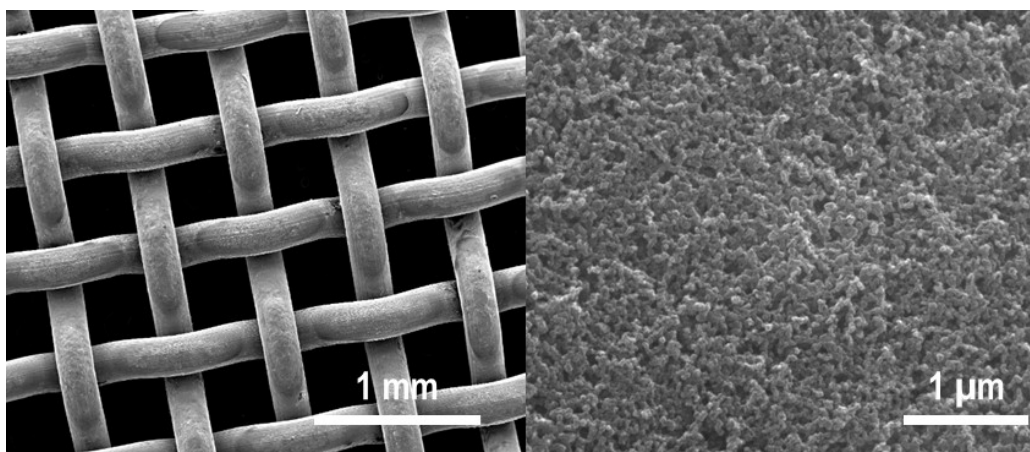


*Figure II. 9: SEM pictures of a dip-coated electrode at different scale for a formulation with a dry mass of 0.28 %.*

Further results, presented in Chapter IV, were acquired with the optimal combination of the formulation parameters, that is to say with the higher binder ratio (15 w%), the slow drying process and the lower dry mass (2.8 %).

### ***II.1.c. Porous flexible electrodes fabrication process***

Porous flexible electrode fabrication process was largely used in battery field as it enables to easily create thick and flexible porous electrodes. It is based on five main steps:

- First, the following components are mixed by magnetic stirring: active material, binder, DBP and acetone. Before stirring the components together, the powders (active material and binder) are ground in a mortar to break the aggregates.
- Later, the slurry is deposited on a Mylar foil by doctor blading.
- The film detached from the Mylar foil is then dried at ambient temperature
- The obtained film is laminated with a current collector, to ensure good contact.
- Finally, the film is soaked three times during fifteen minutes in ether, to remove the porogen agent and this way to create the porosity. As porosity formation relies on a dissolution-driven process it implies potentially the porosity created is fully accessible.



In an attempt to design porous LABs electrode, based on Ketjen Black, the formulation corresponding to negative graphite electrodes (with low BET value) was selected as a starting point and then transposed to Ketjen Black. Due to the use of highly divided carbon, the electrode formulation had to be accordingly adapted, in particular the binder content was adjusted (increased > 20 %).

For the same reasons, the amount of solvent had to be customized to fluidify the slurry which became more viscous with Ketjen Black than with graphite. If the slurry is too viscous, the magnetic stirring cannot mix properly. On the reverse, a too fluid slurry will easily spread and a thick layer cannot be achieved.

Several trials were also carried on to fix the optimal mixing time (1h30), as well as the blade gap to apply during doctor-blading casting (400 μm).

Once the modification operated, the films flued significantly during the laminating step decrease the thickness of the films. As the aim was here to explore the porosity creation inside thick self-standing films, the lamination step was not required and so not applied in the following study. The final fabrication process applied is described in Figure II. 10.

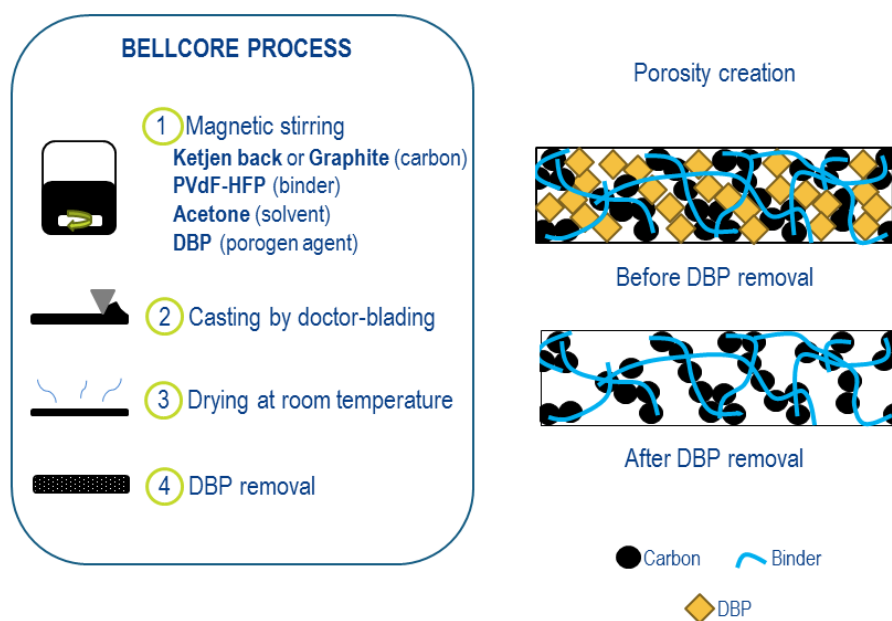


Figure II. 10: Schematics of the flexible electrodes fabrication process and related porosity creation.

Once the film was dried, the porosity creation was achieved by leaching DBP out of the film by soaking it in ether. The Bellcore process advocates the use of three consecutive



immersion steps in ether of fifteen minutes each. Some comparison tests were made a unique step of forty-five minutes.

A particular focus was made on porosity creation as the main purpose of using such electrode fabrication was to design highly porous thick electrodes. To do so, an experimental plan was implemented to study the impact of high DBP contents (from 20 w% to 80 wt%) on the final electrode porosity. Each formulation containing x weight percent of DBP was named according the following format, DBP<sub>x</sub>. The list of the several formulations tested is provided in Table II. 1. The results as well as performances of the Ketjen Black electrodes compared to the usual Bellcore graphite electrodes would be presented in Chapter IV.

*Table II. 1: Formulations used to study porosity created along Bellcore process.*

Formulation	DBP <sub>20</sub>	DBP <sub>30</sub>	DBP <sub>40</sub>	DBP <sub>50</sub>	DBP <sub>60</sub>	DBP <sub>65</sub>	DBP <sub>70</sub>	DBP <sub>75</sub>	DBP <sub>80</sub>
DBP (wt%)	20	30	40	50	61	65	70	75	80
Carbon (wt%)	17	15	13	10	8	7	6	5	4
Polymer (wt%)	63	55	47	40	31	28	24	20	16
Dry Mass (%)	19	19	16	17	14	15	14	13	1

#### ***II.1.d. Comparison of the two electrodes fabrication processes***

Figure II. 11 sums up the several drawbacks and advantages of both processes from practical application point of view, at lab and industrial level, without any concern on electrode efficiency for LABs (discussion developed in Chapter IV).

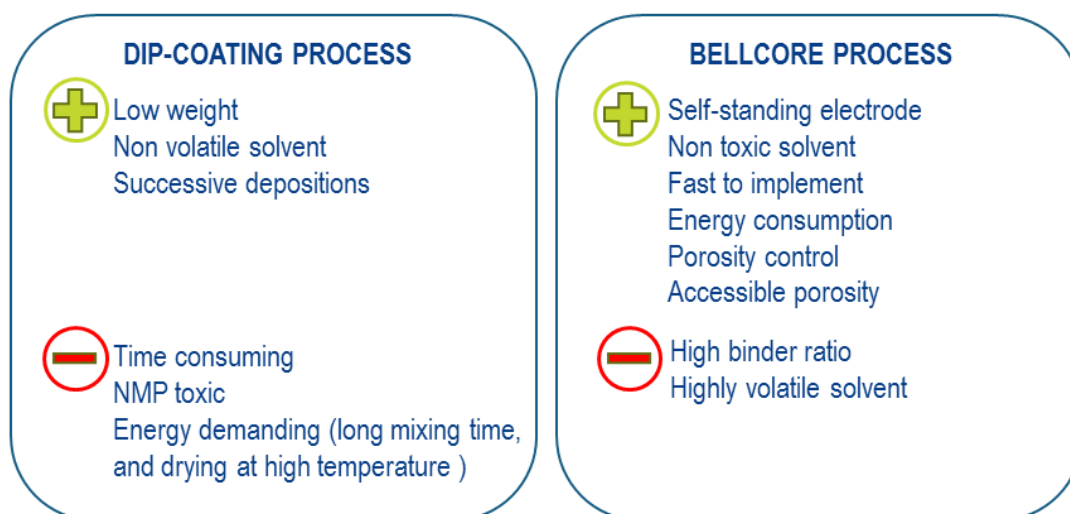


*Figure II. 11: Comparison of Dip-coating and Porous Flexible electrode fabrication processes pros and cons.*

While the dip-coating process permits to produce light electrodes with a thin carbon deposit on top of a stainless steel grid, the Bellcore process leads to thick self-standing electrodes.

To create a textured electrode, multilayers depositions can be envisaged with both processes. Still, practical application revealed difficulties to ensure that laminated films were well superposed (films with distinct porogen agent ratios flowed differently during lamination). Consequently, dip-coating process only enables multi-coatings. However, with dip-coating only thin deposits are created. To design textured thick electrodes, porous flexible electrode process was then the more suitable and easy to implement.

From industrial point of view, the difference between the two processes relies on the solvent nature. Even though dip-coating facilitates the casting steps as it is not volatile, its use is dangerous due to its chemical nature. On the reverse, porous flexible electrode process is safer. Still, solvent evaporation is a concern all along the fabrication process.

Finally, the main drawback of the dip-coating technique, absent with the Bellcore process, is the amount of energy required for mixing and drying. In parallel, in Bellcore process, higher ratio of binder is required when the electrodes are based on highly divided carbon.

## II.2. Battery assembling

### II.2.a. Electrolyte preparation

Various electrolytes had been tested to improve the system stability and performances. They were always prepared in glovebox under Argon atmosphere with an amount of water and oxygen close to zero ( $< 0.1$  ppm for each).

Each electrolyte was composed of a lithium salt and a solvent. The following salts were used:  $\text{LiClO}_4$  (Battery grade, Aldrich),  $\text{LiTFSI}$  (Sigma Aldrich),  $\text{LiI}$  (Alfa Aesar) and  $\text{LiNO}_3$  (Alfa Aesar). In parallel, five solvents were tested: DMSO (99.9 %, Sigma-Aldrich), DME (anhydrous 99.5 %, Sigma Aldrich), TriGDME (99 % stabilized, Acros Organic), TetraGDME (99 %, Acros Organic) and DMA (99.8 % anhydrous, Alfa Aesar).

Dried aluminum containers, kept for one day in an oven at  $70^\circ\text{C}$ , were used to mix both components. Once prepared, the electrolyte rested one day prior to use, to ensure proper salt dissolution. Until the end of use, prepared electrolytes remained in the glovebox.

A drying step using molecular sieve ( $4 \text{ \AA}$ , Sigma-Aldrich) was performed overnight for several electrolytes. Final water content was measured using Karl Fisher device.

### II.2.b. Swagelok cell assembling

Before assembling the cell in the glovebox, the modified Swagelok electrochemical cell parts (Figure II. 12) were cleaned in ethanol for one hour. The Swagelok cells were made of a hollow body to welcome the several cell components: electrodes, separator and electrolyte. Two pistons on top and bottom ensure current conductivity. In order to prevent electrical contact of the electrodes and separator with the hollow Swagelok body, a Mylar foil, formerly dried in an oven at  $50^\circ\text{C}$  for days, was roll on top of the inner surface. Electrical contact was then only ensured by the two pistons, each one in contact with one of the electrodes. The top piston was made of a stainless steel tube, cut at the same length of the bottom piston, to let oxygen accessing the cathode.

The Swagelok cells were preassembled out of the glovebox. The Mylar foil was added. Then, each piston was surrounded by two rings. The bottom piston was then tightened to the Swagelok body with the lower nut. Once ready, they were all placed in an oven at  $70^\circ\text{C}$  for two hours. After drying, the different parts were transferred with a dried "Le Parfait" container inside the glovebox.

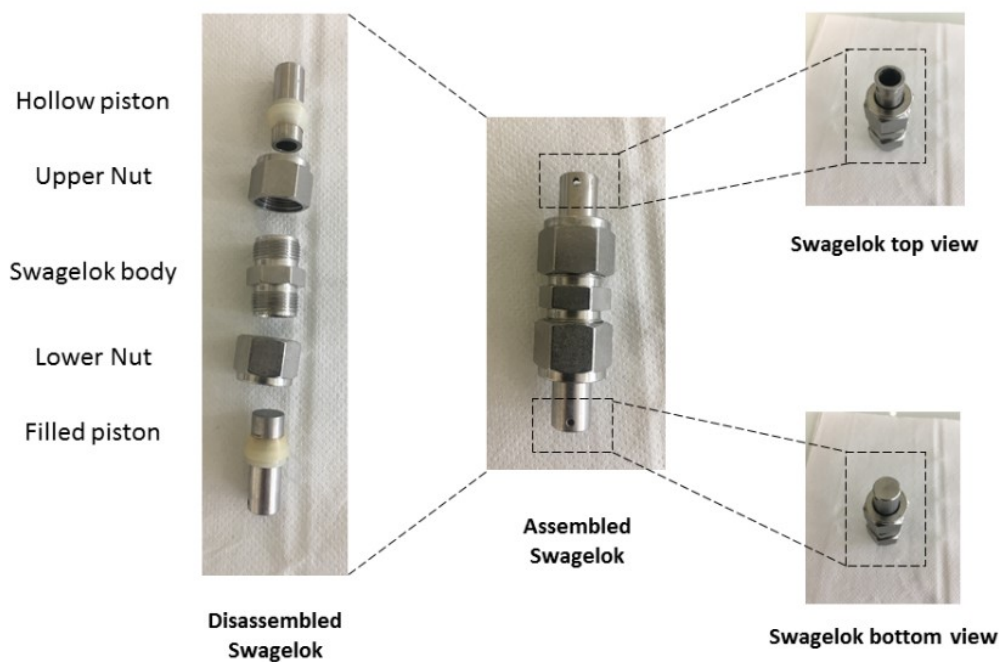


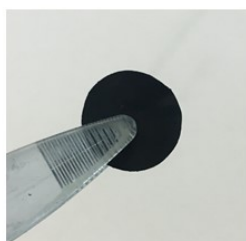
Figure II. 12: Pictures of disassembled and assembled Swagelok.

The electrochemical cell components were all kept in the glovebox. Three different cathodes were scrutinized along the study (Figure II. 13): dip-coated ( $\text{\O} = 9 \text{ mm}$ ), porous flexible electrodes ( $\text{\O} = 9 \text{ mm}$ ) or GDL electrodes ( $\text{\O} = 11 \text{ mm}$ ). GDL cathodes (H23, Freudenberg) were defined as the reference case due to their high fabrication reproducibility (industrial process).

(a) Dip-coated electrode



(b) Porous flexible electrode



(c) GDL electrode



(d) Lithium electrode



Figure II. 13: Pictures of (a) a dip-coated cathode (b) a porous flexible cathode (c) a GDL cathode and (d) a lithium anode.

In the preassemble Swagelok, the several layers of the cell are introduced as illustrated in Figure II. 14. First, the lithium disk ( $\text{Ø} = 9 \text{ mm}$ ) was inserted and then two disks of glassfibers (Whatman,  $\text{Ø} = 14 \text{ mm}$ ) to guarantee electrical isolation of the two electrodes. Later, the cathode disk was juxtaposed and finally covered by a stainless steel grid ( $\text{Ø} = 11 \text{ mm}$ ). To finish, the electrolyte was added using a micropipette ( $325 \text{ }\mu\text{L}$ ) and the upper piston tightened to close the cell.

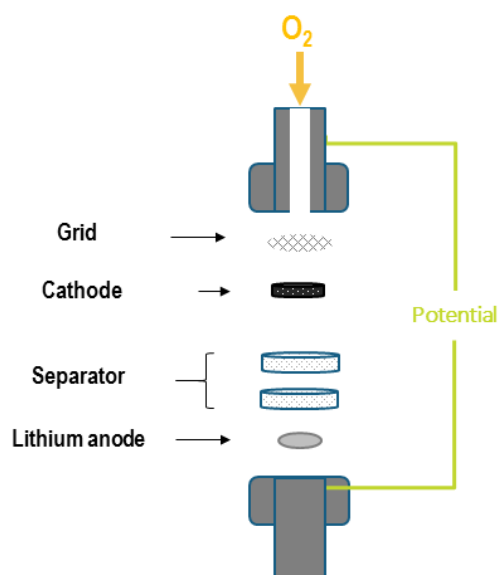


*Figure II. 14: Schematic of the several layers superposed during Swagelok assembling. In the case of dip-coated cathode, no grid is added as the cathode is already supported by a stainless steel grid.*

## II.3. Experimental set-up for controlled LABs atmosphere

### II.3.a. “Le Parfait” container

To control the atmosphere to which the Swagelok cells would be exposed, a special tight controller container was required. Initially, a first design illustrated in Figure II. 15.a. was developed at LRCS by Jean-Bernard Leriche and used by Yinghui Yin along her thesis experiments to study LABs.<sup>209</sup>

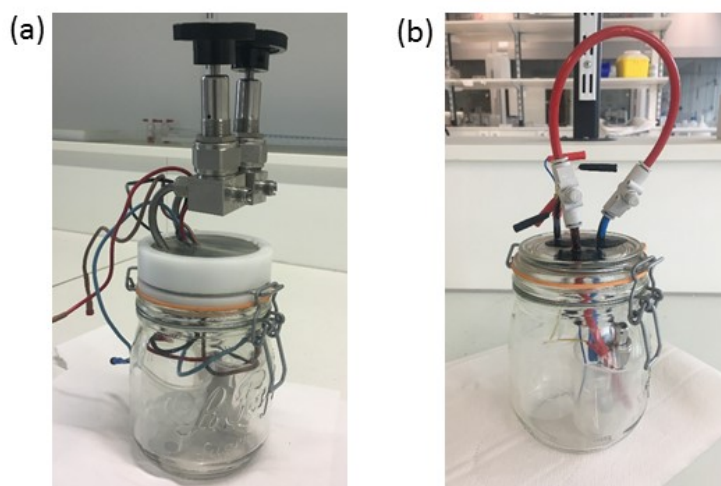


Figure II. 15: Evolution of the atmosphere controller container for LABs called “Le Parfait” container. (a) First design at LRCS, (b) New design made for the study.

As new containers were required to carry on this study and due to the high cost of the valves and the necessity to produce a new cap for each cell, a new cell design more affordable and faster to implement was developed (Figure II. 15.b.). As done previously, the starting point was a “Le Parfait” container of 0.75 L. This time the upper glass cap was kept and perforated with a drill bit (DREMEL) three times to settle air inlet and outlet tubes. The last hole permits the electrical cables to go through the cap. The cables and air tubes were fixed using an epoxy resin. Two valves were added to master the opening/closing of the air inlet and outlet. A rubber ring was then added and the modified container cap attached to the “Le Parfait” body. The airtightness of each final container was checked prior to use them in experiments. To do so, leak detector fluid was applied on the “Le Parfait” which underwent strong oxygen flow. No leak was then observed. Also, a piece of lithium foil was inserted inside a “Le Parfait” containing argon. After a week, no modifications of the lithium surface were observed.

Once the Swagelok were assembled in the glovebox, they were connected to the inner cables of the “Le Parfait” container. The valve and cap of “Le Parfait” were then closed and the system can be safely removed from the glovebox with a controlled inert atmosphere (argon).

### *II.3.b. Gas flow system*

The last part missing for controlling the atmosphere to which the cells are exposed is the gas flow system. A first simple system was then built to enable oxygen flow (Figure II. 16). A flowmeter, added to settle the pressure gauge of the oxygen lab outlet, ensured the same flow is applied. A blubber, at the end of the gas flow system, infringed gas reflux and so contaminations from the lab atmosphere.

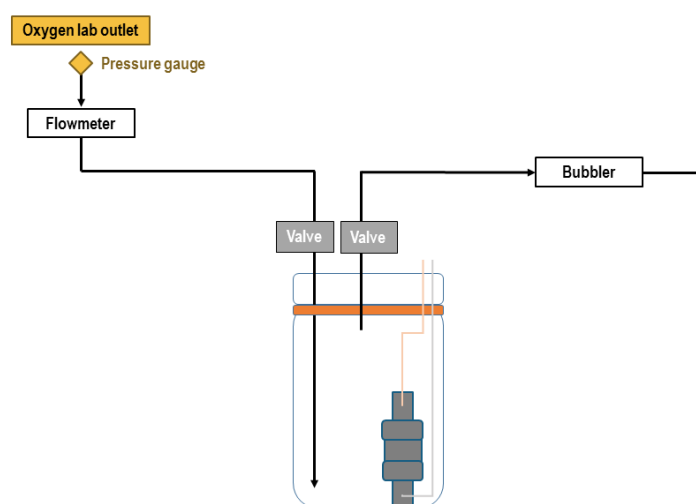


*Figure II. 16: Schematic of the oxygen flow system.*

To simulate real atmosphere and the presence of nitrogen, the gas system flow was slightly modified to facilitate oxygen/azote mixing. As only one flowmeter was available, each gas pressure gauges was fixed using the flowmeter to reach the required gas flow. Then, both gas outlets were fixed to the gas mixing system as described in Figure II. 17 .

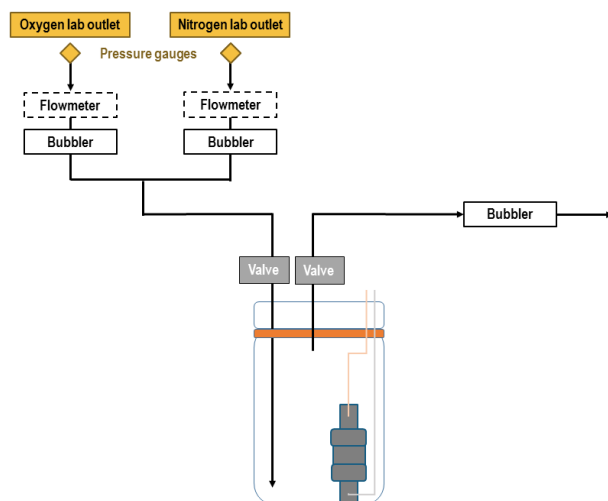


Figure II. 17: Gas mixing system.

The “Le Parfait” containers were always flushed for thirty minutes with a gas flow of  $1.5 \text{ L.h}^{-1}$  to fully remove the argon coming from the glovebox where the Swagelok cells were prepared.



## II.4. Characterization techniques

### II.4.a. Electrode characterization

#### *Pycnometry measurements*

Densities of the several powders and electrode films were estimated thanks to a pycnometer (AccuPyc 1330, Micromeritics) (Figure II. 18).



*Figure II. 18: Picture of the pycnometer (AccuPyc 1330, Micromeritics).*

To determine sample density or volume, several chambers with a well-defined volume are available depending on the volume of the sample. Once loaded with the sample, the chamber is repeatedly filled with helium. The difference in the chamber volume and the helium volume injected enables to estimate the sample volume. Thanks to the sample mass, the device consequently calculates the density of the sample. The densities of the various powders composing the flexible electrodes were measured and are listed in Table II. 2.

*Table II. 2: Density estimations by pycnometry of the powders used for flexible electrode formulation.*

<b>Components</b>	<b>Densities (g/cm<sup>3</sup>)</b>
Ketjen Black	2.23
Carbon C65	1.99
PVdF-HFP	1.79

#### *Nitrogen adsorption measurements*

To estimate powder or electrode film meso-porosity and specific surface area (SSA), gas adsorption technique based on N<sub>2</sub> adsorption at 77 K (ASAP 2020, Micromeritics) was performed (Figure II. 19).



Figure II. 19: Picture of the  $N_2$  adsorption and desorption measurement device at 77 K using  $N_2$  (ASAP 2020, Micromeritics).

Prior to analysis, each sample is degassed by heating under vacuum ( $30 \mu\text{m Hg}$ ). Nitrogen is after adsorbed on the surface, fills the porosity, to finally be desorbed. Adsorption and desorption isotherms are then acquired.

Analysis of the adsorption isotherms, using the BET formalism,<sup>210</sup> empowered the determination of the SSA of the whole sample without any restriction. Advantage of BET formalism is that a multimolecular layers treatment is taken into account compared to Langmuir's unimolecular treatment. The specific surface areas of the powders used for flexible electrode formulation were determined using such technique (Table II. 3).

Table II. 3: SSA estimations of the powders used for flexible electrode fabrication.

Components	SSA ( $\text{m}^2/\text{g}$ )
Ketjen Black	$1400 \pm 10$
Carbon C65	$93 \pm 1$
PVdF-HFP	$7 \pm 0.1$

On their side, desorption isotherms provided information on pore volume and pore size distribution, using the BJH formalism.<sup>211</sup> Worth mentioning that only pores with a size below 300 nm were accounting for such porosity estimation.

## DSC

Thermal stability of a material is easily accessible thanks to DSC. Such technique is based on the calculation of the energy required to heat a material to a set temperature, function of the temperature.

To process accurate SSA measurements on flexible electrode films, the thermal stability of the polymer during degassing step should be ensured. DSC measurements were then implemented on PVdF-HFP to be sure that the films meso-porosity was not modified by the polymer melting during the ASAP degassing step. The thermal analysis of the binder from 25 °C to 250 °C, revealed that the onset for PVdF-HFP melting is around 115 °C (Table II. 3). So, the degassing was systematically performed at 95 °C.

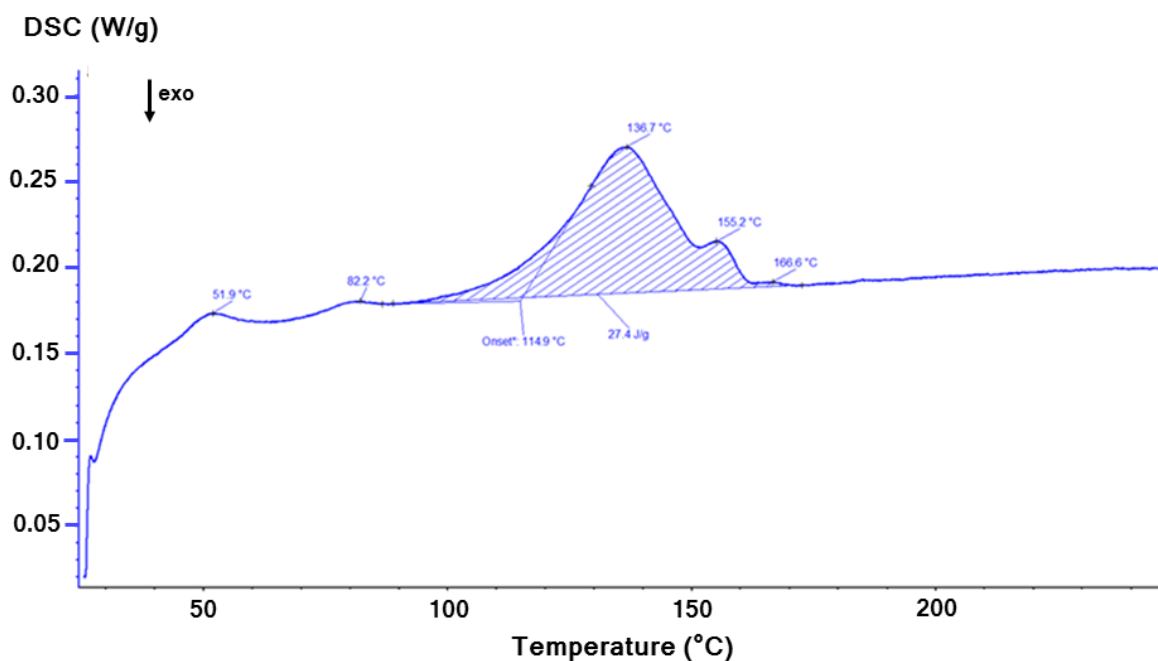


Figure II. 20: DSC curve of PVdF-HFP carried on at 5 K/min from 25 °C to 250 °C.

## II.4.b. Electrochemical characterization

### Galvanostatic cycling

To estimate the electrochemical response of the LABs cells, galvanostatic cycling were performed on a VSP (Bio-Logic) (Figure II. 21).

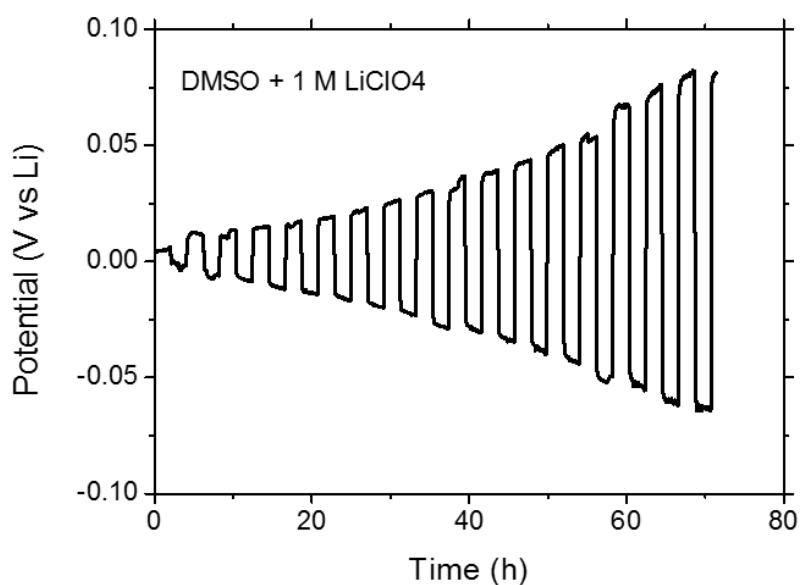


Figure II. 21: Picture of VSP (Bio-Logic).

The cycling parameters were settled using GCPL programs. Initially, cells voltages were recorded for two hours while the cells were resting. Then, discharge and later charge protocols were launched until their voltage cutoff were reached. For the first experiments, the voltage cutoffs were set at 2 V and 4.5 V respectively. Later in the study, to access the effect of temperature on performances, the VSP was coupled to an oven (Pol-Eko Aparatura Simple) to set and maintained the cell temperature.

### *Polarization measurements*

Electrolyte stability vs lithium was evaluated using polarization measurements (VSP, Bio-Logic)). Polarization is a galvanostatic technique based on the successive application of opposite current steps. Symmetric cells made of two lithium disks ( $\text{Ø} = 9 \text{ mm}$ ) separated by two separators disks ( $\text{Ø} = 14 \text{ mm}$ ) soaked in electrolyte. In the current study, repetition of current steps of  $25 \mu\text{A}$  and  $-25 \mu\text{A}$  was applied, each one lasting for two hours (e.g. Figure II. 22).



*Figure II. 22: Polarization tests for DMSO + 1 M LiClO<sub>4</sub> as the electrolyte. Succession of current steps at  $25 \mu\text{A}$  and  $-25 \mu\text{A}$ , each for 2 hours.*

SEI formation can be tracked by polarization technique, as it results in an increase of the cell resistance and so a rise of the gap between positive and negative plateaus. Once formed, the gap should remain stable except if parasitic reactions are taking place.

The constant increase of the gap between the plateaus and the non-planar shape of potential response, in the case of DMSO / 1 M LiClO<sub>4</sub>, highlighted the instability of the electrolyte with lithium. Such instability was corroborated by the literature as DMSO is not stable versus lithium, as formerly mentioned in Chapter I.

### *II.4.c. System characterization*

#### *SEM imaging & EDX Spectrometry*

To get information on the surface of the electrodes studied and after galvanostatic cycling, SEM was performed using the ETD (Everhart-Thornley Detector) in high vacuum (FEI Quanta 200F) at high voltage (20 kV for all samples). This microscopy technique is based on the projection of an electron beam on a sample. Interaction of the electrons with the sample is related to its topography and composition of the exposed sample. SEM images, as the one illustrated in Figure II. 23, are then reconstructed and analyzed. Studied surface should be conductive to get clear picture. On the opposite, nonconductive surface will lead to blurry and white contrast.

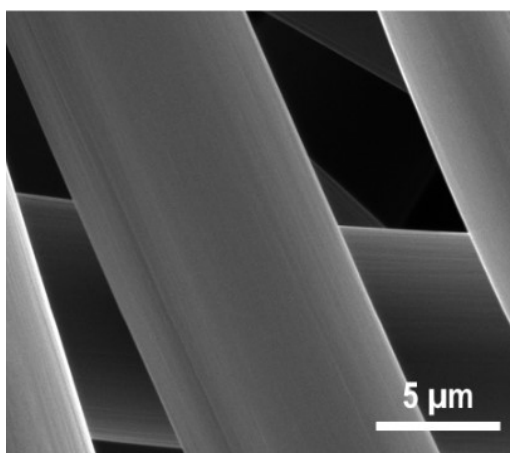


*Figure II. 23: Pristine GDL SEM picture.*

Chemical microanalysis is possibly accomplished thanks to EDX (INCA Oxford Instruments) combined to the INCA software. A mapping of the chemical components can be disclosed as the one shown in Figure II. 24. Also, all the elements with an atomic number higher than 11 can be quantified using this technique.

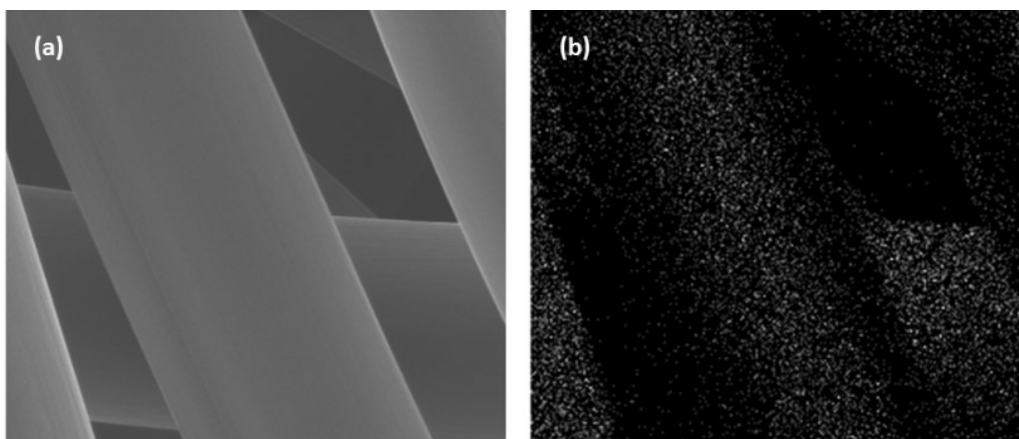


Figure II. 24: EDX mapping of the carbon element (b) in the corresponding SEM picture (a).

### IR spectroscopy

Thanks to IR Spectroscopy we could identify the liquid which appeared during the preliminary ASAP degassing step at 150 °C for non-extracted flexible films, as DBP (Figure II. 26). As illustrated in Figure II. 25, colorless droplets appeared on the surface of the ASAP tube while films still containing DBP.

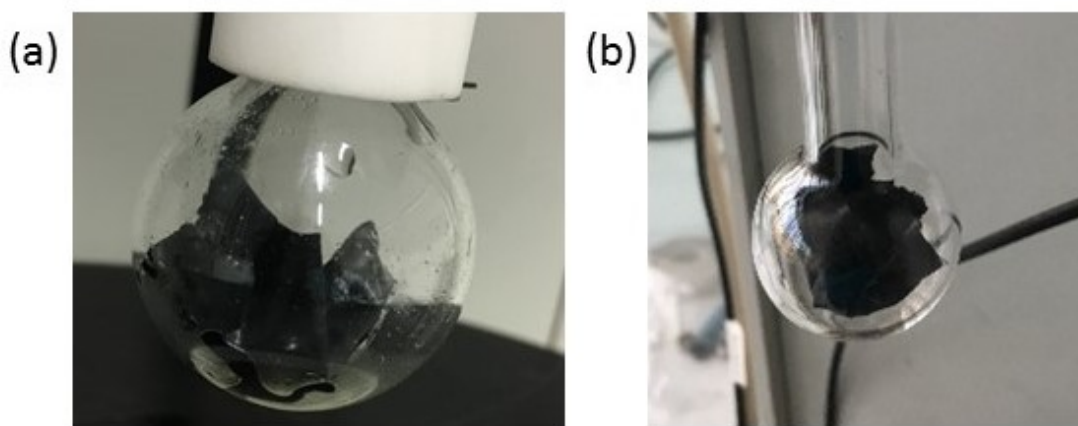


Figure II. 25: Pictures of the ASAP tubes after degassing containing the electrode  $DBP_{60}$  without DBP removal (a)  $DBP_{60}$  with DBP extracted (3 times 15 minutes in ether) (b).

This observation is in agreement with the DBP vapor pressure ( $\sim 1$  mm Hg) largely overpassing the applied pressure (30 mm Hg) at this temperature (150 °C).<sup>212,213</sup>

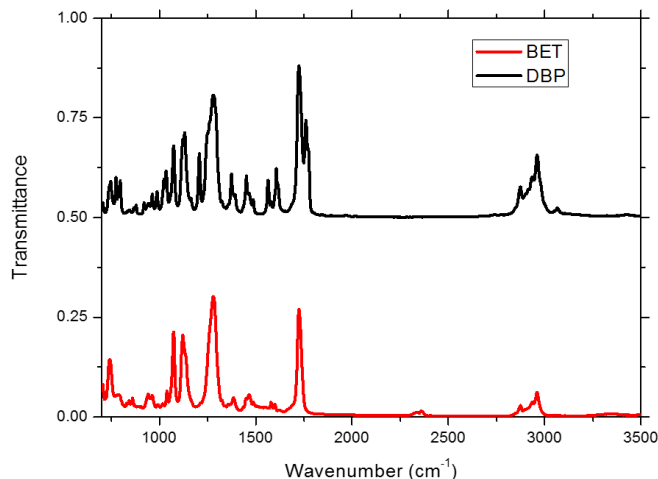


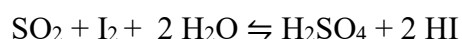
Figure II. 26: IR spectra of the liquid recovered after ASAP degassing, compared to pure DBP spectra.

## XRD

The XRD, known as X-ray diffraction was developed in order to analyze crystalline materials. Thanks to it, the nature of the material phase could be determined. To do so, the sample studied is exposed to an X-ray beam according to several angles of exposition. Due to the atoms repetition in the crystal, the X-ray beam is then diffracted. While Bragg's law is satisfied (constructive interference), the diffraction could be observed and a pattern, intensity function of the exposition angle, could be plotted. Thanks to comparison to the patterns of pure phase, the crystalline solids in the sample could be determined.<sup>214</sup>

## Karl Fisher (HF)

Karl Fisher technique is used to determine the water content in ppm of a solution, thanks to coulometric titration (756 KF Coulometer). The titration is based on sulfur dioxide oxidation with water according to the following reaction:



A KF solution made of iodine, sulfur dioxide and imidazole dissolved in Diethylene glycol monoethyl ether filled the titration cell. A base (imidazole) is added to entice the reaction toward acids production and so water consumption. The iodide formed by the oxidation of HI in  $\text{I}_2$  is quantified by coulometric titration and then the water content directly estimated using Faraday's law.

The water content was estimated for different electrolytes, all composed of a salt and a solvent (Figure II. 27). As the water content raised with the amount of salt for both solvents, water contamination was attributed to the highly hygroscopic salt used (LiTFSI)

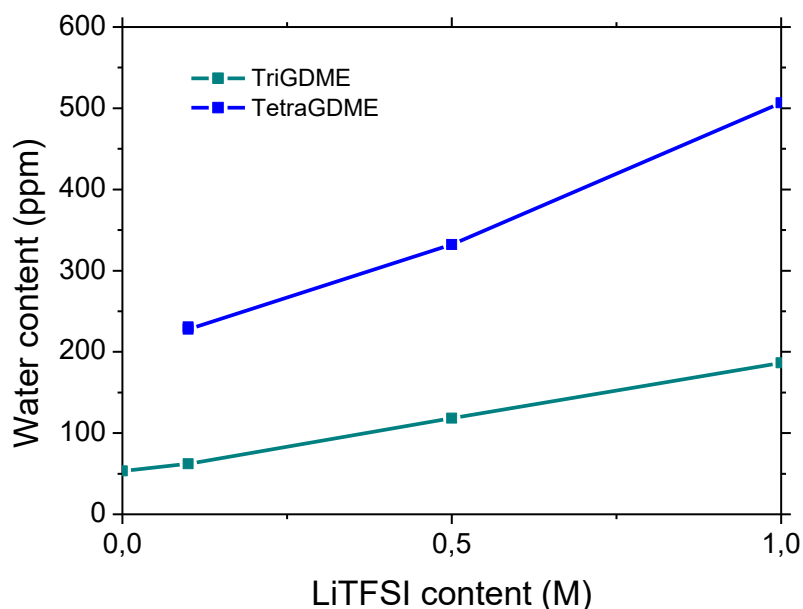


Figure II. 27: Water content results for electrolytes based on TriGDME and TetraGDME with several LiTFSI concentrations.

Worth mentioning that 500 ppm of water in TetraGMDE is equivalent to  $2.8 \cdot 10^{-2} \text{ mol.L}^{-1}$  of water. Calculations based on the dioxygen Bunsen coefficient in TetraGMDE provided by Read et al.,<sup>120</sup> led to a dioxygen concentration of  $4.2 \cdot 10^{-3} \text{ mol.L}^{-1}$ . Water content can then easily overpass dioxygen content and so can strongly impact the cell performances even if few amounts (ppm) are found in the electrolyte.

To solve this issue, electrolytes were then always dried with molecular sieve to limit at most their water contents. After drying, values as lower than 3 ppm were achieved.

#### II.4.d. Continuum modeling

The system was also investigated and each parameter scrutinized using another technique, continuum modeling, which in this sense completely entered in the experimental procedure implemented along the study.

As mentioned in literature, the LABs are complex systems with many technical barriers to overpass, requesting the help of modeling to assess improved understanding.<sup>215-217</sup> Among the several papers published, many were dealing with continuum modeling of non-aqueous



LABs.<sup>216,217</sup> Such trend finds its root in the efficiency and flexibility of such models, which are powerful tools, privileged to access the mechanisms taking place in the system. As transport, passivation and pore blocking, are well defined using continuum modeling technique, it had been selected to study here the electrode texture impacts. Worth point out that atomistic models are also presented in the literature to provide insight on the reaction mechanisms. Still, study of the possible contamination mechanisms was also enabled here thanks to the use of multiscale modeling (cf. Annex).

In the present study the multi-scale models were developed using the Finite Volume Method. The several models built were coded using the software Matlab (R2014b).



# CHAPTER III: THEORETICAL STUDY OF BI-POROUS ELECTRODES

## Contents

---

III.1. Concept of porous electrodes with enhanced diffusion.....	80
III.2. Theoretical study.....	83
III.2.a. Model description.....	83
III.2.b. Discretization and boundary conditions.....	87
III.2.c. Parametrization.....	89
III.2.d. The reference case.....	90
III.2.e. Electrode formulation and design impacts.....	92

---

### III.1. Concept of porous electrodes with enhanced diffusion

In the context of carbonaceous porous electrode design, two parameters should be balanced to reach efficient LABs electrodes. The tricky development of LABs is due to the requirement of high surface available while also satisfying efficient oxygen diffusion inside the electrode. While the first parameter favors utilization of highly divided carbon leading supposedly to meso-porosity creation, it also tends to decrease oxygen diffusion. Pore clogging, which is in this case more likely to occur, will then prevents further diffusion. On the reverse, to enhance oxygen diffusion, larger pores creating macro-porosity are preferred. Still, in such case lower surface is created, stressing even more surface passivation.

So, how to merge these two requirements to design optimal electrodes? A first look to the nature can help to identify a solution. Dealing with oxygen diffusion and highly developed surface, attention should be drawn to the lung (Figure III. 1). A clear ramification emerges. While the initial bronchi only serve oxygen supply by slowing down the flow thanks the sections subdivisions, the last ones also enable to multiply the exchange surface between the gas flow and the blood while breathing.<sup>218</sup> Even if in LABs case, oxygen is not provided directly by a gas flow but thanks to the electrolyte in which the oxygen is dissolved, some inspiration should be taken from this efficient structure.

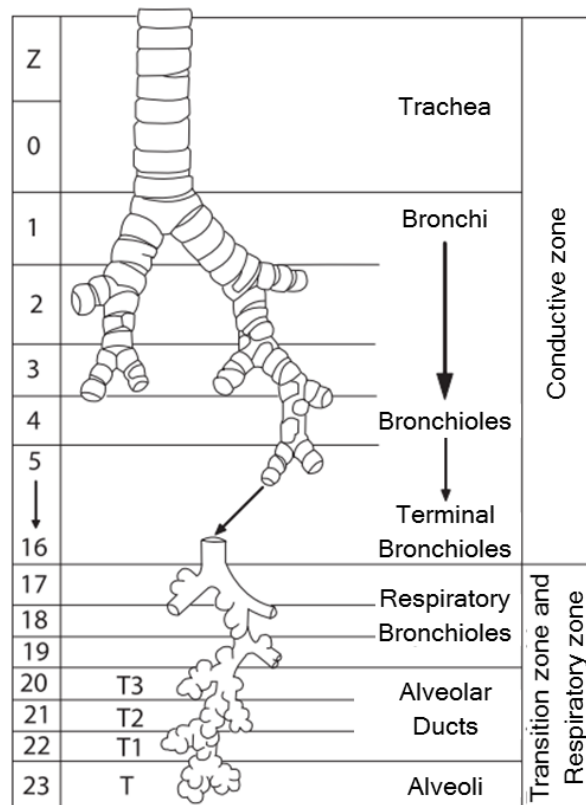


Figure III. 1: Structure of the bronchial tree.<sup>218</sup>

While exactly reproducing such structure seems too complex and not needed, the idea of successive domains with different porosities seemed relevant. As an analogy, macro-porosity could be used to provide oxygen, acting like the first part of bronchi. Secondly, meso-porosity could be added to promote higher developed surface as ensured by the acini directly connected to the alveoli.

Two potential distributions of these domains were foresighted. Rather these domains could be distributed in a way they form multilayers with the macro-porosity close to the oxygen inlet. Rather these domains can be mixed along the depth of the electrode to form a lung-like simplified structure, called “bi-porous electrode” to differentiate it from previous “multilayers electrode”. Figure III. 2 highlights the approach implemented to develop LABs electrodes.

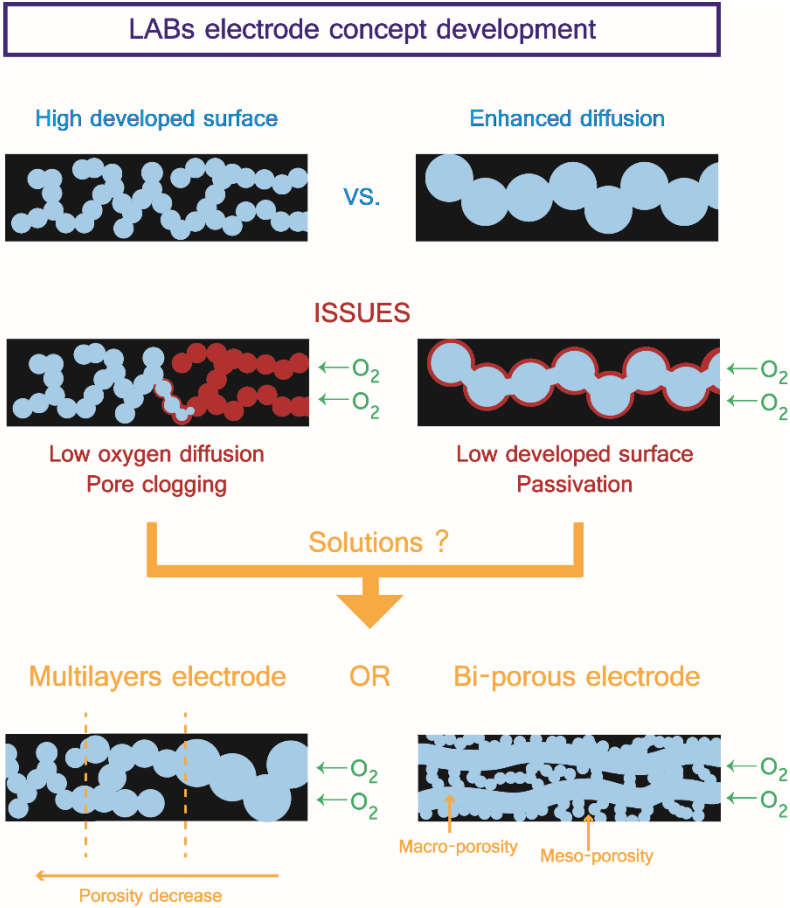


Figure III. 2: LABs electrode concept development.

At lab scale, to design such electrodes, two electrode fabrication processes, previously described in Chapter II, were implemented. Initially the multilayers electrode was supposedly achieved by the two processes: rather thanks to multiple coating on top of a grid, rather using lamination of several flexible films. Still, due to the deformation of the flexible films while

laminating them together, such process was finally dedicated only to bi-porous electrode fabrication. The results experimentally observed would be the subject of Chapter IV.

To evaluate the interest of the bi-porous electrodes and to facilitate the definition of the macro-porosity ratio needed, prior to launched the experiments, a bi-porous electrode model was implemented. The theoretical study was not implemented on the multilayer electrodes as the experimental process was less tunable than the one of flexible porous electrode. Bi-porous electrodes design seemed also more appealing, as well as, more interesting in terms of energy density as thick electrodes can be produced.

Indeed, to enhance the gravimetric energy density of the cell, utilization of a thick electrode is favored. Diffusion limitation is then triggered in such condition. Though, porosity creation has to be well mastered to reduce its impacts. To do so, the Bellcore process (nowadays Telcordia<sup>140</sup>) was considered as explained. Such fabrication procedure enables to form two domains inside the electrode. The first one is made of carbon and binder. In the case of Ketjen Black (highly divided carbon), this domain is then assumed to be meso-porous. The second one is a macro-porous domain created by leaching out the porogen agent during the fabrication. The electrodes were thereby complex bi-porous systems which needed to be initially studied from theoretical point of view. As formerly demonstrated, identifying the failure mode of a battery depending on the electrode texture is problematic. Fortunately, modeling is a powerful tool helping to identify which limiting factor took the lead, as well as enabling to understanding the correlations existing between the several parameters described. Along this study, three main failure modes had been identified while focusing only on the electrode: the surface passivation, the pore clogging and obviously the oxygen diffusion limitation. To clearly identify them and thus examined which electrode bi-porosity should be selected, a modeling study taking into account these three limiting phenomena was implemented.

## III.2. Theoretical study

### III.2.a. Model description

The model was built considering the combination of two 1D models, one for each porous domain inside the electrode. Also, isothermal conditions were assumed ( $T = 298 \text{ K}$ ) while describing electrochemistry, transport and passivation mechanisms. In order to understand which limitations are impacting the performance according to the tested electrode formulation and configuration, passivation, pore clogging and diffusion limitations were analyzed at the same time. Then, the model only described a simplified discharge kinetic mechanism (Eq. 1):



Other hypotheses were made. Firstly, a thin layer deposition mechanism was assumed for  $\text{Li}_2\text{O}_2$  deposition on the electrode surface. Thin film formation is based on the creation of a passivation film on top of the carbon surface until a thickness of 10 nm as underlined by DFT calculations.<sup>219</sup> Besides, for the sake of simplicity, side reactions such as electrolyte decomposition were neglected. The electrolyte was TetraGDME as properties of TriGDME were hardly accessible in the literature.

Electrode based on Ketjen black and PVdF-HFP were simulated for the aforesaid reasons. Due to the small carbon particles size and reinforced by experimental trials, only high binder ratios were implemented as they are required for producing thick electrodes leading to formulations with 50 w% to 70 wt% of carbon.

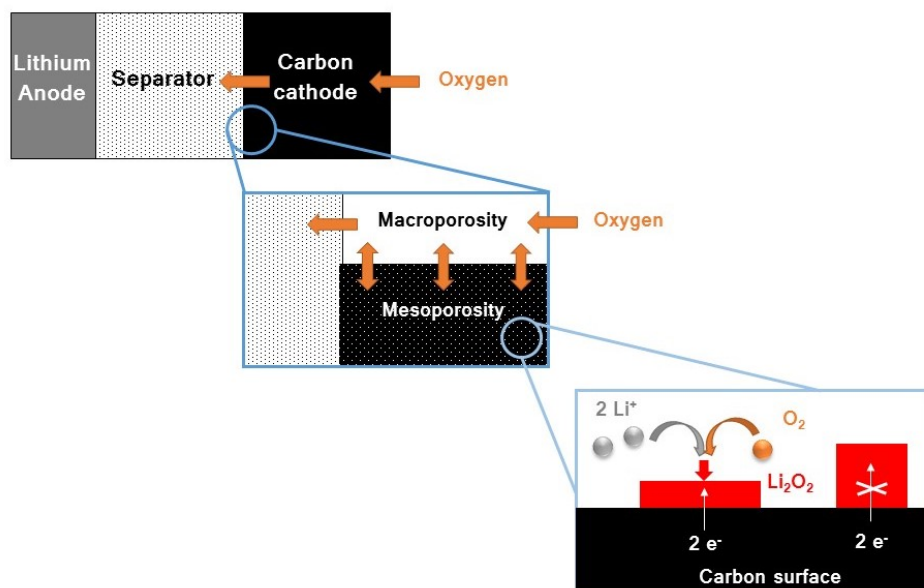


Figure III. 3: Schematics of the system described in the model considering coexistence of two domains in the cathode: macro-porous and meso-porous domains.

As illustrated in Figure III. 3, the two previously described porous domains were assumed to be coexisting in the cathode and were exchanging oxygen (mathematically described via an intraflux). The volume ratio of the macro-porosity was set from 20 % to 50 % with respect to the electrode volume.

To describe the meso-porous domain, carbon surface was calculated with respect to the carbon weight volume in the formulation, its density and its active surface area. The active surface value inserted in the model ( $7.68 \cdot 10^9 \text{ m}^2 \cdot \text{m}^{-3}$ ) was confirmed to be in the same range as the experimental one ( $3.12 \cdot 10^9 \text{ m}^2 \cdot \text{m}^{-3}$ ) thanks to BET ( $1417 \text{ m}^2 \cdot \text{g}^{-1}$ ) and pycnometry ( $2.23 \text{ g} \cdot \text{cm}^{-3}$ ) measurements carried on Ketjen Black. The model then tended to overestimate the carbon active surface. This trend could also be intensified by electrode surface wettability as electrolyte do not perfectly wet the electrode surface. Still, as the range was respected, the trend on discharges performances remained relevant while comparing the performances of several formulations.

The macro-porous domain was initially fully filled by electrolyte, leading to a porosity  $\varepsilon_{macro}$  of 1. As the macro-porous volume was significant, it was approximated that even though  $\text{Li}_2\text{O}_2$  was produced, the availability of the macro-porous domain will persist. Thus, porosity evolution was not tracked over time for macro-porous domain but only for meso-porous one. The diffusion coefficient of the macro-porous domain corresponded to the oxygen diffusion coefficient  $D_0$ .  $D_0$  was assumed to be equal to the oxygen diffusion coefficient in the electrolyte solvent (value for TetraGDME taken from work of Laoire *et al.*)<sup>79</sup>.

Inside the meso-porous domain, the porosity decreased along the simulation in function of the volume of  $\text{Li}_2\text{O}_2$  produced. The porosity regression influenced the ease for diffusion to take place. Its impact was thus inspected in the model using Bruggeman relation:<sup>220,221</sup>

$$D_{meso} = D_0 \cdot \left( \frac{\varepsilon_{meso}}{\tau_{meso}} \right) = D_0 \cdot \varepsilon_{meso}^{1.5} \quad \text{Eq. 2}$$

where  $D_{meso}$  corresponded to the effective diffusion coefficient of the meso-porous domain. The tortuosity factor  $\tau_{meso}$  traduced the gap between ideal pathway ( $L_{cv}$ ) from non-ideal one ( $L_p$ ) as represented in Figure III. 4. As carbon black particles are spherical, the Bruggeman relation was valid in the meso-porous domain.<sup>127</sup> Though, it should be kept in mind that such relation described only simple diffusion<sup>220</sup> and thus did not precisely traduced the transport occurring inside experimental electrodes. Still, in an attempt to compare different electrode compositions and structures, such approximation seemed appropriated. The initial value of the



meso-porous domain was set at 60 % according to the pycnometry measurements carried on Ketjen Black.

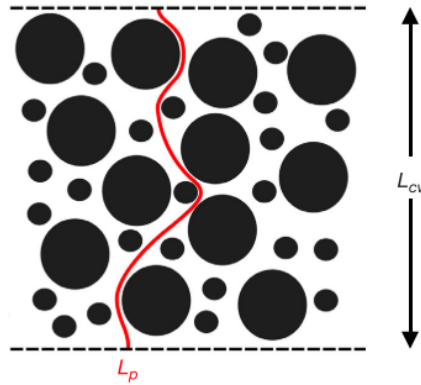


Figure III. 4: Illustration of the tortuosity concept as proposed by Tjaden et al.<sup>220</sup>

As a first estimation and as lithium availability was not often questioned in literature, lithium concentration was assumed to be sufficient (assumed to be always equal to 1 M), to remain almost constant and hence lithium cations transport was neglected. Finally, only oxygen diffusion was solved considering two diffusion equations, one for each porous domain. Diffusion was then described, taking into account porosity evolution, according to Fick's law:

$$\frac{\partial(\varepsilon_i \cdot c_i^{O_2})}{\partial t} = -\nabla J_{O_2}^{Diff,i} - S_{O_2}^{i \rightarrow j} - R_{O_2}^{electro\chi,i} \quad Eq. 3$$

where  $\varepsilon_i$  was the porosity of the domain  $i$ ,  $c_i^{O_2}$  the oxygen concentration in domain  $i$ ,  $J_{O_2}^{Diff,i}$  the diffusion flux in domain  $i$ ,  $S_{O_2}^{i \rightarrow j}$  the intraflux between the domain  $i$  and  $j$ ,  $R_{O_2}^{electro\chi,i}$  the source term due to electrochemical reaction, with  $i, j$  setting for macro or meso porous domain.

The diffusion flux was described in each domain  $i$  by the following equation:

$$J_{O_2}^{Diff,i} = -D_i \frac{\partial c_i^{O_2}}{\partial x}. \quad Eq. 4$$

The exchange of oxygen between the two domains was not numerically described. To do so, an extra term was introduced to characterize the oxygen flow. This term  $S_{O_2}^{i \rightarrow j}$  was named as the intraflux term and depends on the contact surface between the domains. Also, as diffusion is due to the balance of concentrations between two medias, the intraflux was directly proportional to the difference of concentration between the macro and meso porous domains. The intraflux term was then calculated by

$$S_{O_2}^{i \rightarrow j} = k' \cdot A_{Contact} (c_i^{O_2} - c_j^{O_2}) \quad Eq. 5$$

where  $A_{Contact}$  denoted the contact surface between the two domains estimated from experimental electrode. Such surface was roughly estimated based on the number and diameter of macro-pores observed on an electrode via SEM. Accessing the value of the exchange coefficient  $k'$  was on the reverse difficult to access, for this reason a parameter sensitivity analysis was implemented to define its value.

At each time step, the volume of  $Li_2O_2$  in bin  $j$  and domain  $i$  was calculated according to Eq. 6:

$$\frac{\partial V_{Li_2O_2}^{i,j}}{\partial t} = \frac{j_{Far,j}^i \cdot A \cdot M_{Li_2O_2}}{n \cdot F \cdot \rho_{Li_2O_2}} \quad Eq. 6$$

Thanks to the volume of  $Li_2O_2$  produced, the porosity was recalculated at each time step to take into account the decrease of free space due to production of the discharge product.

From the volume of  $Li_2O_2$ , the growth of  $Li_2O_2$  thickness  $\delta$  was computed in each part of the electrode and limited by the following  $\zeta^{tunnelling}$  function, capturing the phenomenon of hole tunneling<sup>219</sup> through the discharge product. Once the thickness  $\delta$  reached the hole tunneling distance,  $a_{j,n}$  the active surface of carbon in bin  $j$  and domain went to zero due to Eq. 7:

$$a_{i,j} = \zeta_{i,j}^{tunnelling} \cdot a_0 \quad \text{with} \quad \zeta_{i,j}^{tunnelling} = \frac{1 - \text{erf}(\delta_{i,j} - 7)}{2} \quad Eq. 7$$

The surface was then inactivated for further reactions and further  $Li_2O_2$  growth was infringed.

The total faradic current  $j_{Far,j}$  in bin  $j$  depended on the current density applied to the system  $I$  (expressed in  $[A/m^2_{\text{geometric}}]$ ). As two domains coexisted in each bin ( $i$  and  $i'$ ), the total current density applied to the system was linked to the faradic current  $j_{Far,j}^i$  or  $j_{Far,j}^{i'}$  of each domain  $n$  and  $n'$  in bin  $j$  with respect to the total surface of carbon via Eq. 8:

$$I = \sum_j \left[ j_{Far,j}^i \cdot \frac{a_{i,j}}{a_{i,j} + a_{i',j}} + j_{Far,j}^{i'} \cdot \frac{a_{i',j}}{a_{i,j} + a_{i',j}} \right] \quad Eq. 8$$

where  $a_{i,j}$  referred to the carbon surface in bin  $j$  and domain  $i$ .

By using the overall faradic current, access to the overpotential  $\eta$  was given at each time step using the Tafel equation

$$j_{Far,j}^i = n.F.k.c^{1-\beta}.e^{\left(-\frac{\beta n F \eta}{RT}\right)} \quad \text{Eq. 9}$$

with  $n$  the number of exchange electrons,  $F$  the faradic constant,  $k$  the kinetic rate,  $\beta$  the charge transfer,  $R$  the gas constant and  $T$  the temperature. The electrode potential was afterwards defined by

$$U = U_0 - \eta . \quad \text{Eq. 10}$$

Knowing  $j_{Far,j}^i$  permitted to evaluate the number of oxygen consumed at each time step and in each bin. So, the correct number of mole of oxygen, available inside the volume of electrode still accessible, was assessed after removing the amount of oxygen involved in electrochemistry via  $R_{O_2}^{electro\chi,i}$ .

### III.2.b. Discretization and boundary conditions

Once the mass transport equation and all its parts were mathematically defined, Eq. 3 was discretized in order to be implemented inside a code. To do so, the system simulated was divided in P+Q bins, respectively number of bin for the separator and for the cathode (Figure III. 5).

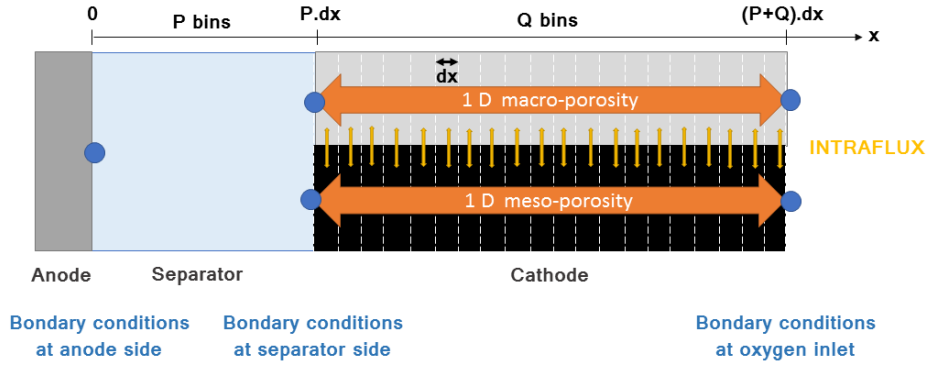


Figure III. 5: Description of the simulated system.

As  $S_{O_2}^{i \rightarrow j}$  and  $R_{O_2}^{electro\chi,i}$  were actually calculated in each bin of the electrode, only the proper diffusion part was discretized, leading to the expression of  $\varepsilon_{j,n}^t \cdot c_{j,n}^t$  approximation in bin  $j$  and domain  $n$  (meso-porous or macro-porous domain) at time  $t$  according to following equations:

$$\varepsilon_{j,n}^{t+1} \cdot c_{j,n}^{t+1} = \varepsilon_{j,n}^t \cdot c_{j,n}^t + \frac{dt}{dx^2} \left( \kappa_{j-\frac{1}{2},n}^t \cdot c_{j-1,n}^t - \left( \kappa_{j-\frac{1}{2},n}^t + \kappa_{j+\frac{1}{2},n}^t \right) c_{j,n}^t + \right. \\ \left. \kappa_{j+\frac{1}{2},n}^t \cdot c_{j+1,n}^t \right) - dt \cdot (S_{O_2}^{n \rightarrow m,t} + R_{O_2}^{electro\chi,n,t}) \quad \text{Eq. 11}$$

$$\text{with } \kappa_{j+\frac{1}{2},n}^t = \frac{\kappa_{j,n}^t + \kappa_{j+1,n}^t}{2} \quad \text{Eq. 12}$$

$$\text{And } \kappa_{j,n}^t = D_0 \cdot (\varepsilon_{j,n}^t)^{1.5}. \quad \text{Eq. 13}$$

The discretization was valid only in the cases where the condition  $\frac{D \cdot dx^2}{dt} \leq \frac{1}{2}$  was respected.<sup>222</sup>

Boundary conditions were required to solve Eq. 3 at the interfaces oxygen inlet/ cathode, cathode/separator and separator/anode. As the cathode was assumed to be completely flooded with electrolyte, the last cathode bin  $M$  was assumed to be in contact with a bin  $M + 1$  fully filled with an electrolyte saturated with oxygen. Then, at the oxygen inlet side, oxygen concentration in bin  $P + Q + 1$  was then defined by:

$$c_{P+Q+1}^{O_2} = c_{sat}^{O_2}. \quad \text{Eq. 14}$$

At the interface cathode/separator, actually two interfaces should be considered as the macro-porous and the meso-porous domains were both in contact with the separator. To solve this, the oxygen flow was assumed to be separated between the two domains depending on the contact surface between each domain and the separator, respectively named  $\theta_{macro}$  and  $\theta_{meso}$ . These surfaces were defined as following:

$$\theta_{macro} = \frac{A_{macro}}{A} \quad \text{Eq. 15}$$

$$\theta_{meso} = \frac{A - A_{macro}}{A} \quad \text{Eq. 16}$$

with  $A_{macro}$  the surface of contact between the macro-porous domain and the oxygen inlet side.  $A_{macro}$  was estimated thanks to the radius of macropores  $r_{macro}$  and the volume of macro-porous domain observed in experiments.  $A$  corresponded here to the cathode geometric area.

Also, to ensure a smooth gap at the edge between cathode domain and separator, while estimating the diffusion at last bin of the separator  $M$ , the mean value between of  $\kappa_M^t$  and

$\kappa_{M+1,n}^t$  was implemented instead of  $\kappa_{M+1,n}^t$  only. Same way, the mean value of  $\kappa_{M+1,n}^t$  and  $\kappa_M^t$  was applied at bin  $M + 1$  as a substitute of  $\kappa_M^t$  due to porosity evolution.

At the anode side, oxygen flux was set to zero, to express that oxygen diffusion stopped at the anode contact. Then, while calculating the diffusion in the first cathode bin  $M$ , the concentration of bin  $M - 1$  was fixed likewise:

$$c_{M-1}^{O_2} = c_M^{O_2}. \quad \text{Eq. 17}$$

### ***III.2.c. Parametrization***

One tricky step while developing a code is the definition of the parameters. The aim here was to study which type of bi-porous electrodes should be developed at lab scale (volume of macro-pore necessary and understanding impact of formulation on limiting parameters). Still, in an attempt to simulate meaningful information, data from the parallel experimental study were required to develop the code.

A batch of flexible porous electrode was examined and its mean thickness measured with a digital Vernier caliper was implemented, as well as the radius and number of macro-pores observed in SEM picture. Even though such approach could overlook the effect of some parameters, like the modification of the number and diameter of macro-pores obtained with the several formulations tested, it appeared that the system was already complex enough. Thus, all codes were launched with the same macro-pore diameter. Depending on the volume of macro-pores inserted, only the number of macro-pores and contact surface between the two domains were recalculated assuming formation of cylindrical channels with a length equal to the cathode thickness.

To clearly identify the impact of the several computed parameters, a sensitivity study was implemented. Effects of intraflux prefactor, contact area between the porous domains, diffusion coefficient (applying  $\pm 10\%$  and  $\pm 20\%$  to each parameter) and carbon surface availability (50%, 70% or 90% available compared to fully available) were studied. Finally, it ends up that oxygen diffusion coefficient and carbon surface were the more impacting as expected, due to their large impact on diffusion efficiency and electrochemistry. The code was then built using the parameter values given in Table III. 1.

Table III. 1: List of the parameters used in the model.

Parameters	Values	Units	Source
Faradic constant $F$	96 485	C.mol <sup>-1</sup>	Universal constant
Gas constant $R$	8.314	J.mol <sup>-1</sup> .K <sup>-1</sup>	Universal constant
Temperature $T$	298	K	Assumed
Cathode length	100	μm	From experimental data
Cathode geometric area $A$	1	m <sup>2</sup>	Assumed
Pore radius in macroporosity $r_{macro}$	1.6	μm	From experimental data
Number of bin	30	/	Assumed
Time step $dt$	0.01	s	Assumed
Oxygen concentration $c_{sat}^{O_2}$	4.43	mol.m <sup>-3</sup>	Reference <sup>79</sup>
Diffusion coefficient $D_0$	$2.17 \cdot 10^{-10}$	m <sup>2</sup> .s <sup>-1</sup>	Reference <sup>79</sup>
Intraflux prefactor $k'$	$1.10^{-6} \cdot D_0$	s <sup>-1</sup> .m <sup>-2</sup>	Assumed
Li <sub>2</sub> O <sub>2</sub> Molar Mass	45.881	g.mol <sup>-1</sup>	Reference <sup>128</sup>
Li <sub>2</sub> O <sub>2</sub> density	$2.3 \cdot 10^6$	g.m <sup>-3</sup>	Reference <sup>128</sup>
Ketjen Black specific surface area	$7.68 \cdot 10^9$	m <sup>2</sup> .m <sup>-3</sup>	Reference <sup>117</sup>
Super P specific surface area	$6.87 \cdot 10^7$	m <sup>2</sup> /m <sup>3</sup>	Reference <sup>128</sup>
Equilibrium potential ORR $E_0$	2.96	V	Reference <sup>223</sup>
Symmetric coefficient $\beta$	0.5	/	Assumed
Tafel prefactor $k$	$1.10^{-12}$	mol <sup>1/2</sup> .m.s <sup>-1</sup>	Assumed

### III.2.d. The reference case

To carry a survey, an initial reference case need to be defined. In this study, in order to match the experimental study, a Ketjen Black electrode with a carbon ratio of 50 wt%, a macroporous ratio of 20 % was simulated using the parameters defined in Table III. 1 and will correspond to the reference case. Figure III. 6 revealed the relevance of the model which gave new insights on the limiting parameters.

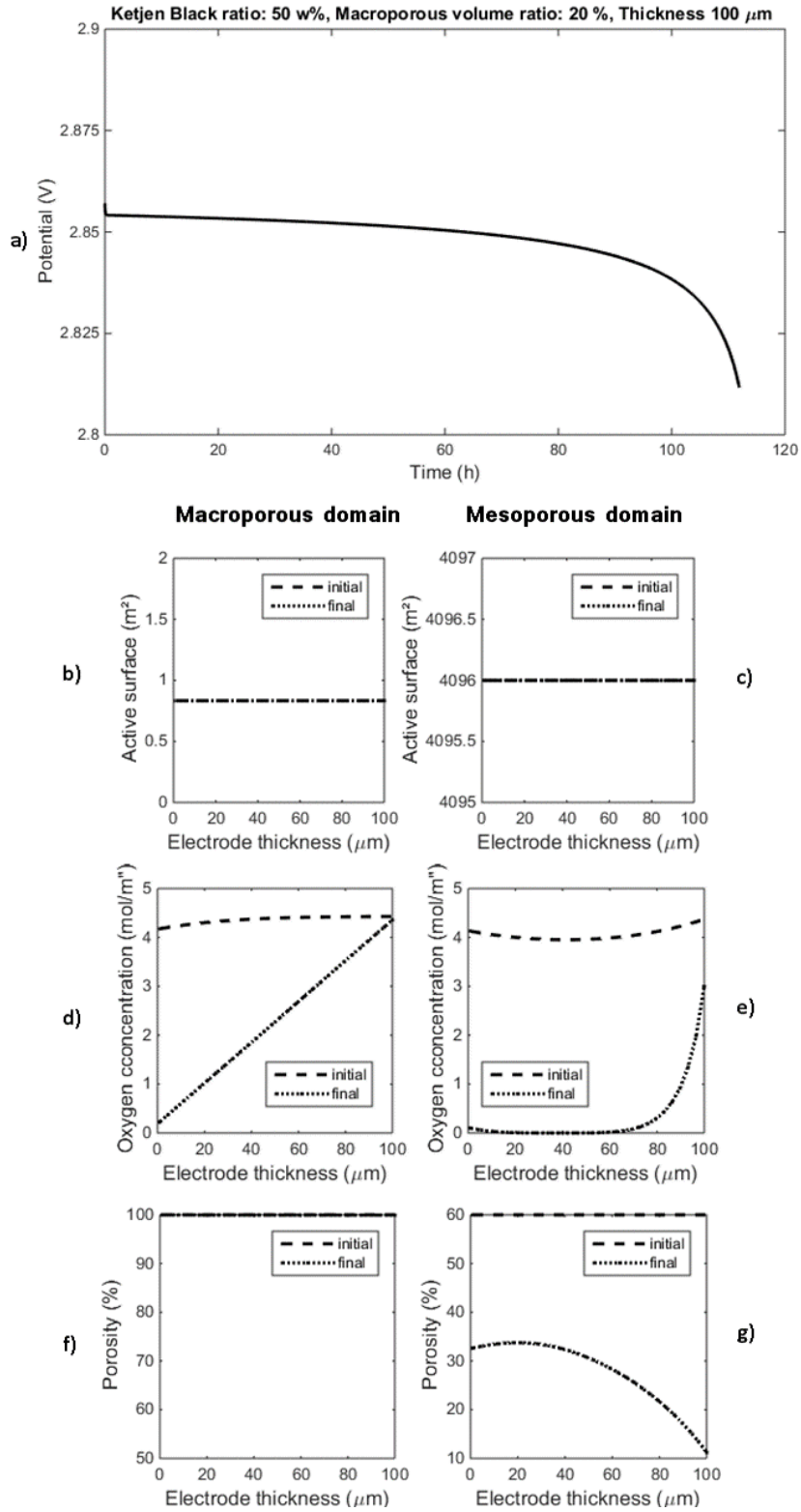


Figure III. 6: Calculated evolution of macro-pores active surface (b) and meso-pores one (c), of oxygen concentration in macro-pores (d) and meso-pores (e) and of porosity in macro-pores (f) and meso-pores (g) linked to the discharge curve (a) done at  $I = 0.625 \text{ A}/\text{m}^2_{\text{geometric}}$  for an electrode with 50 wt% of carbon and 20 % of volume macro porosity volume ratio (initial stage was estimated after 10 s and final one corresponded to end of discharge).

The calculated evolution of the carbon active surface shown in Figure III. 6.b and Figure III. 6.c emphasized that the electrode surface passivation was not the limiting factor of capacity since active surface was still available in both domains at the end of the discharge. Figure III. 6.d and Figure III. 6.e, on the other side, described the evolution of the oxygen concentration and underscored the impact of the oxygen diffusion limitation. At the end of discharge in the macro-porous domain, some oxygen was still available, especially at the oxygen inlet. Still, concentration decreased fast at the separator side. In addition, Figure III. 6.e and Figure III. 6.f provided data on the porosity evolution as the filling of pores was tracked over time. Porosity at the end of discharge presented a bending shape with lower porosity at the separator side compared to the one at the middle of the electrode domain (Figure III. 6.f). This porosity gradient could be explained by the oxygen diffusion process. On the oxygen inlet side, oxygen was consumed and refueled quickly allowing further reactions. Thanks to the macro-porous domain, diffusion was also fast enough from the oxygen inlet side to the separator side. On the way, oxygen was also supplied to the meso-porous domain (Figure III. 5) leading to a higher production of discharge product and then to a lower porosity. In the middle of the electrode, diffusion was slowed down due to the meso-porous domain properties (tortuosity and porosity). So, discharge products were produced slowly as oxygen needed to diffuse first. Finally, evolutions of all these limiting parameters were correlated to the discharge capacity and overpotential as illustrated in Figure III. 6.a.

In all the cases described, Ketjen Black electrodes were characterized with parameters provided in Table III. 1, with a carbon ratio between 50 wt% to 70 wt% and a macro-porous volume ratio ranging from 20 % to 50 %, the limiting impact of oxygen diffusion had not been contested. All potential fades were linked to the decrease of oxygen diffusion in the meso-porosity, even if free space was still available and  $\text{Li}_2\text{O}_2$  thickness was inferior to the hole tunneling distance.

### ***III.2.e. Electrode formulation and design impacts***

#### ***Effect of the electrode thickness***

The most evident parameter to inspect while analyzing diffusion through thick electrodes was the electrode thickness. Different thicknesses were then tested and the corresponding discharge curves were reported in Figure III. 7.



Low value of thickness led to enhanced capacities (in  $\text{mAh/g}_{\text{electrode}}$ ) with in return higher overpotential. This trend could be explained by the oxygen consumption. In a thick electrode, oxygen reacted and speedily went toward zero concentration. Diffusion did not have time to happen and the sudden death of the cell popped up. For electrodes with lower thicknesses, oxygen was consumed by reaction and supplied back thanks to diffusion. The overpotential rise came from the increase of the local current density. In the case of thinner electrodes, there was less carbon and so the current density experienced by carbon surface was more significant.

The increase of capacity was clearly linked to a more efficient utilization of the electrode as shown by the evolution of porosity inside the electrodes in Figure III. 7.b and Figure III. 7.c. In the case of an electrode with  $75 \mu\text{m}$  compared to a  $200 \mu\text{m}$  one, the porosity was far more reduced at the end of discharge, meaning that more lithium peroxide was formed. For the  $200 \mu\text{m}$  electrode, a significant amount of the porosity was still available which corresponded to a large amount of carbon surface still free for reaction. The use of such thick electrode was then not efficient and the specific capacity ( $\text{mAh/g}_{\text{electrode}}$ ) reduced.

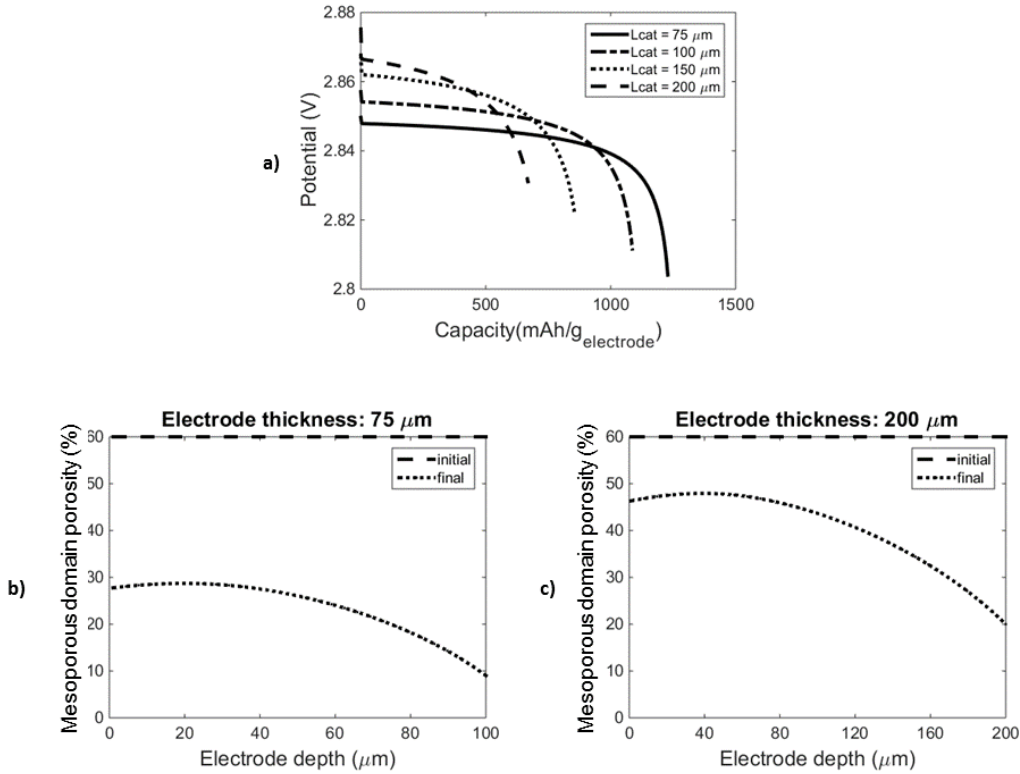


Figure III. 7: a) Calculated impact of cathode thickness ( $\mu\text{m}$ ) on electrode discharge capacity ( $\text{mAh/g}_{\text{electrode}}$ ) for a current density of  $62.5 \mu\text{A/cm}^2_{\text{geometric}}$  and corresponding evolution of mesoporous domain porosity for electrodes with a thickness of  $75$  and  $200 \mu\text{m}$  (b) and c) respectively).

### *Macro-porous domain and carbon ratios combined effects*

As here efficient formulation of electrodes for LABs was at stake, a comprehensive study was launched to identify clearly the intrinsic links between the several involved parameters. Initially, macro-porous volume ratio and carbon weight ratio were considered in parallel.

Two different ways of comparing the performances of electrodes with different parameters were possible. Rather a constant current could be applied to each electrode ( $\mu\text{A}/\text{cm}^2_{\text{geometric}}$ ), rather a current density depending on the electrode developed surface ( $\mu\text{A}/\text{m}^2_{\text{carbon}}$ ) could be applied. While the initial case was close to the application target, the second one facilitated the evaluation of the efficiency of the electrode. Indeed, with large carbon amount variation, the final current densities applied to the electrodes could be drastically different and thus the electrochemical responses completely different. Undeniably, such system were really sensitive to the current density as illustrated in Figure III. 8 and expected from literature.<sup>26</sup> Then, to plainly understand what occurred at electrode level, both approaches were implemented consecutively.

Sensitivity of such systems toward current density was due to the fast consumption of oxygen while applying high current density. While concentration dropped quickly, oxygen diffusion could not counterbalance the consumption and thus led to capacity fade.

Regardless of the current density, the simulation results shown that an increase of carbon content always led to the decrease of capacity. As mentioned previously in case of Ketjen black based electrode with a thickness of 100 nm, oxygen diffusion was always the limiting factor while carbon surface was still available. Here, when the carbon content was increased, more surface was available for the reaction, oxygen was consumed rapidly and its concentration drop appeared sooner. Diffusion limitation was then emphasized and capacity fading occurred earlier. At the end, the mass of carbon unused or still available was more significant leading to a lower discharge capacity ( $\text{mAh}/\text{g}_{\text{carbon}}$ ).

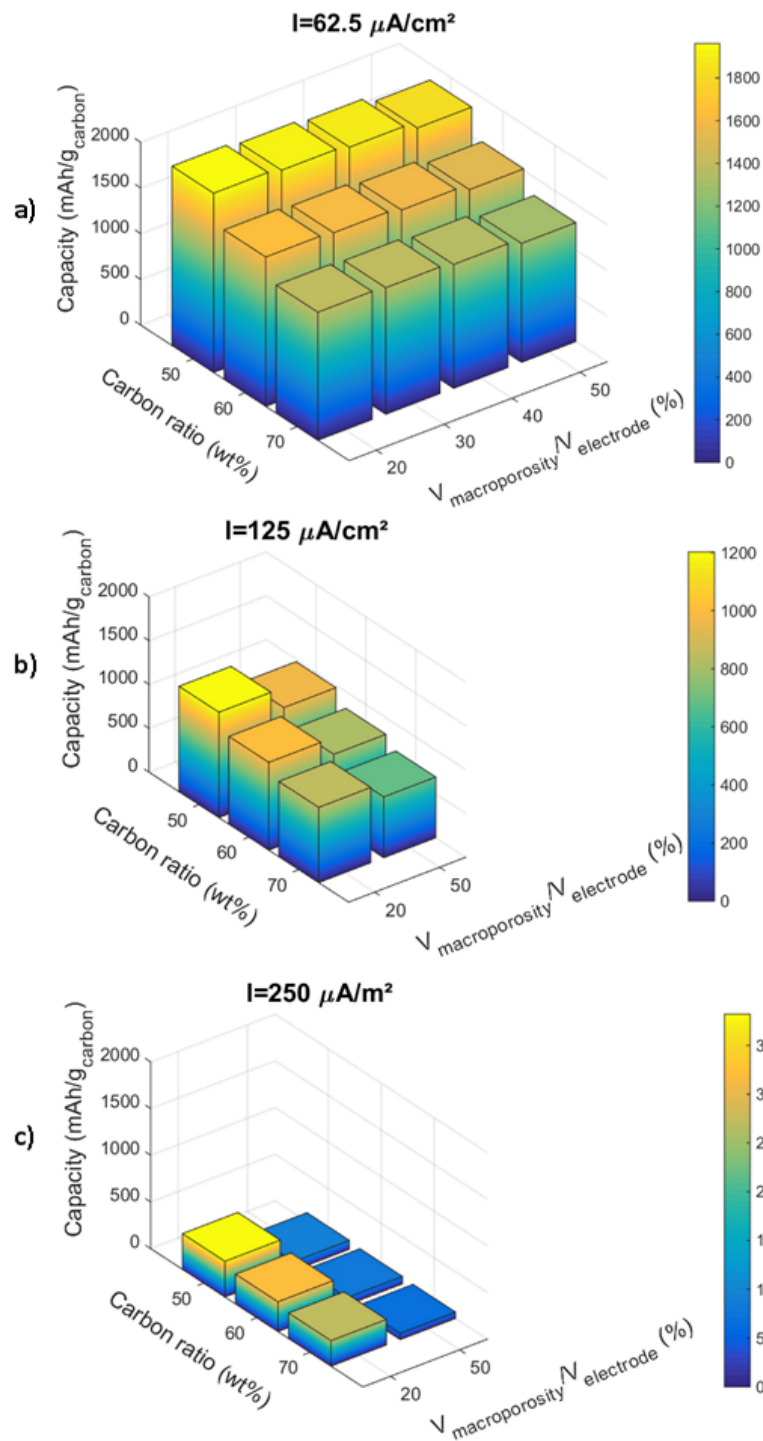


Figure III. 8: Calculated impact of the current density (a)  $62.5 \mu\text{A}/\text{cm}^2_{\text{geometric}}$ , b)  $125 \mu\text{A}/\text{cm}^2_{\text{geometric}}$ , c)  $250 \mu\text{A}/\text{cm}^2_{\text{geometric}}$  on the discharge capacity (mAh/g<sub>carbon</sub>) for different formulations based on Ketjen Back electrodes.

From the previous study, it would be easy to conclude that with lower carbon contents and, above all, with lower macro-porous volume ratios the discharge capacity of the cell would be improved. Still, this was biased by the comparison of the results at same current density ( $\mu\text{A}/\text{cm}^2_{\text{geometric}}$ ) and also as capacity was only expressed in function of mAh/g<sub>carbon</sub>. Another

batch of models were then run, this time at the same current density. The applied current was calculated according to the carbon developed surface estimated for each formulation (calculated based on  $62.5 \mu\text{A}/\text{cm}^2_{\text{electrode}}$  applied in the case of electrode with 50 wt% of Ketjen Black and 20 % of macro-porous volume ratio which leads to a  $0.1 \mu\text{A}/\text{m}^2_{\text{carbon}}$ ). The results were reported in Figure III. 9.

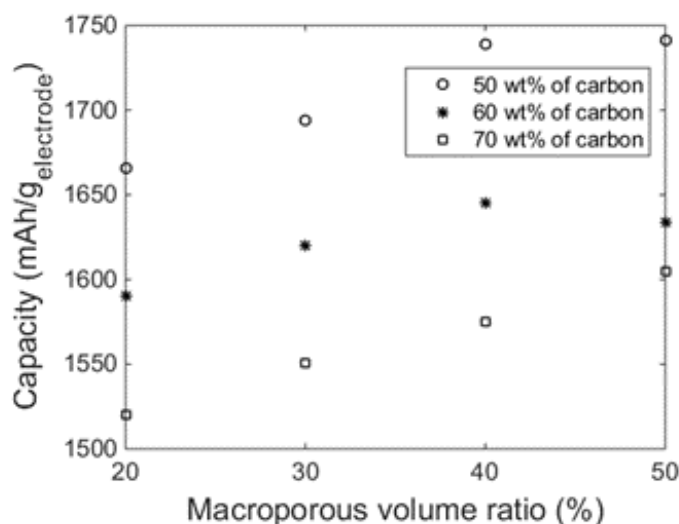


Figure III. 9: Calculated impact of the macro-porous volume ratio (from 20 to 50 %, for electrodes with different Ketjen Black ratios 50 wt%, 60 wt% and 70 wt%. Current density was estimated for each case depending on the available surface carbon and corresponded to  $0.1 \mu\text{A}/\text{m}^2_{\text{carbon}}$ .

Contrary to the previous study,<sup>132</sup> capacity was not multiplied by a factor of 5 while introducing 50 % of porous volume, most probably due to the fact that in the current study, electron-tunneling was taken into account and thus precipitate capacity fading. In fact, for all carbon ratios from 50 wt% to 70 w%, the capacity increased with addition of macro-porous volume. Still, depending on this amount added, capacity gain was not that significant. Indeed, while for 50 wt% of carbon the capacity significantly evolved until adjunction of 40 % of macro-porous volume, value stagnated after. For 60 wt% of carbon, a decline was even observed for higher ratio than 40 % of macro-porous volume. Only in case of 70 wt% of carbon, the capacity always raised in the range of macro-porous volume from 20 % to 50 %.

The increase of capacity with higher volume dedicated to macro-porous domain could be easily explained. In case of high carbon loadings, oxygen reacted on top of the carbon and was consumed fastly. As diffusion was not fast enough and oxygen available for reactions decreased promptly inside the electrode. Also, not all the carbon surface was reacting as oxygen was not able to properly diffuse inside the overall meso-porous media. Then, some carbon loaded in the

electrode only participated to the electrode weight and was not used for reactions. That is why the highest capacities were acquired for 50 wt% of carbon.

Diffusion in meso-porous domain was slower compared to the macro-porous one, due to the porosity and tortuosity of the media. Adding macro-porous domain allowed to the oxygen to first diffuse quickly along the electrode thickness. Also, oxygen could in the same way directly access to the meso-porous domain in each bin. So, the distance of diffusion across macro and then meso-porous domains was smaller compared to a diffusion pathway using only the meso-porous media (Figure III. 5). Thereby, more carbon could react, promoting higher capacity as seen for the 50 wt% and 70 wt% of carbon cases. After a point, adding macro-porous domain could not improve the performance anymore as diffusion inside the electrolyte itself became the only limiting factor (carbon surface already accessible). Even more, with too high volume of macro-pores compared to carbon loaded, capacity was significantly limited as underlined with 60 wt% of carbon.

To conclude, definition of the optimal formulation from theoretical point of view was not obvious as carbon and macro-porous domain volume ratios did not impact linearly the capacity. From this theoretical study, it was observed that the best formulation to test experimentally should be based on 50 wt% of carbon with 40 % of macro-porous volume. Worth point out that for only 50 wt% of carbon, 50 wt% of binder should be used in parallel. Such high binder intake would clearly impact the carbon surface accessibility and thus such results should be treated carefully. So, the safer conclusion to extract from these results was that more than 40 % of macro-porous volume was not required. This value should then be defined as the target of macro-porous volume to introduce inside the electrode.

### *Effect of carbon surface*

As an echo of the last consideration, carbon surface availability was then scrutinized introducing a parameter  $\alpha$  to convey the coverage of carbon surface by the binder as well as the inaccessibility of carbon surface due to the pore connectivity. Three values of coverage were tested and compared to zero coverage case (Figure III. 10).

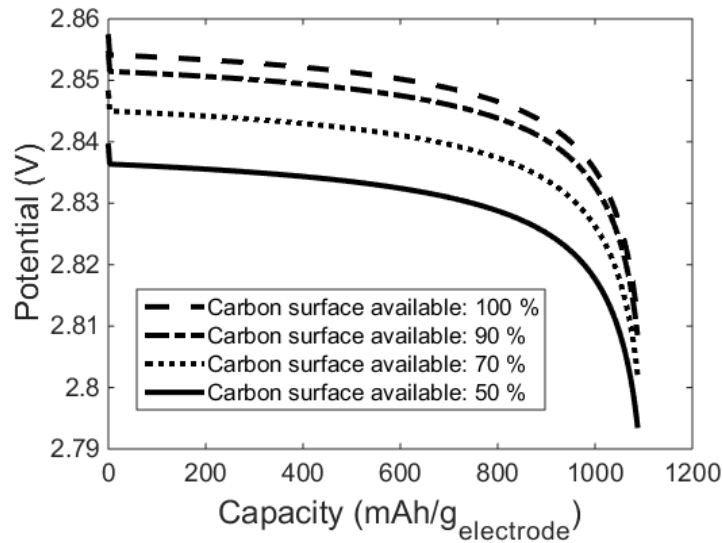


Figure III. 10: Simulation of the discharge over-potential evolution with available carbon surface decrease for an electrode with 50 wt% of carbon and 20 % of volume macro porosity volume ratio. Current density applied:  $0.625 \text{ A/m}^2_{\text{geometric}}$ .

As expected, while reducing the carbon surface availability at constant current, overpotential raised due to higher current density experienced by the carbon surface left available. Here, as oxygen diffusion remained the limiting parameter, capacity fading always occurred at same discharge capacity. Still, as overpotential lead to lower system performances as described in literature, even if an efficient electrode for oxygen diffusion was designed, its performances would be minimized by the overpotential boost.

Use of another type of carbon, Carbon Super P, was also investigated. Even though, Carbon Super P is a highly divided carbon, its specific surface is completely different from Ketjen Black. While for Ketjen Black electrodes, the limitation clearly came from the rarefication of the oxygen inside the electrode (Figure III. 11), another trend was experienced due to this diminished carbon surface (Figure III. 12).

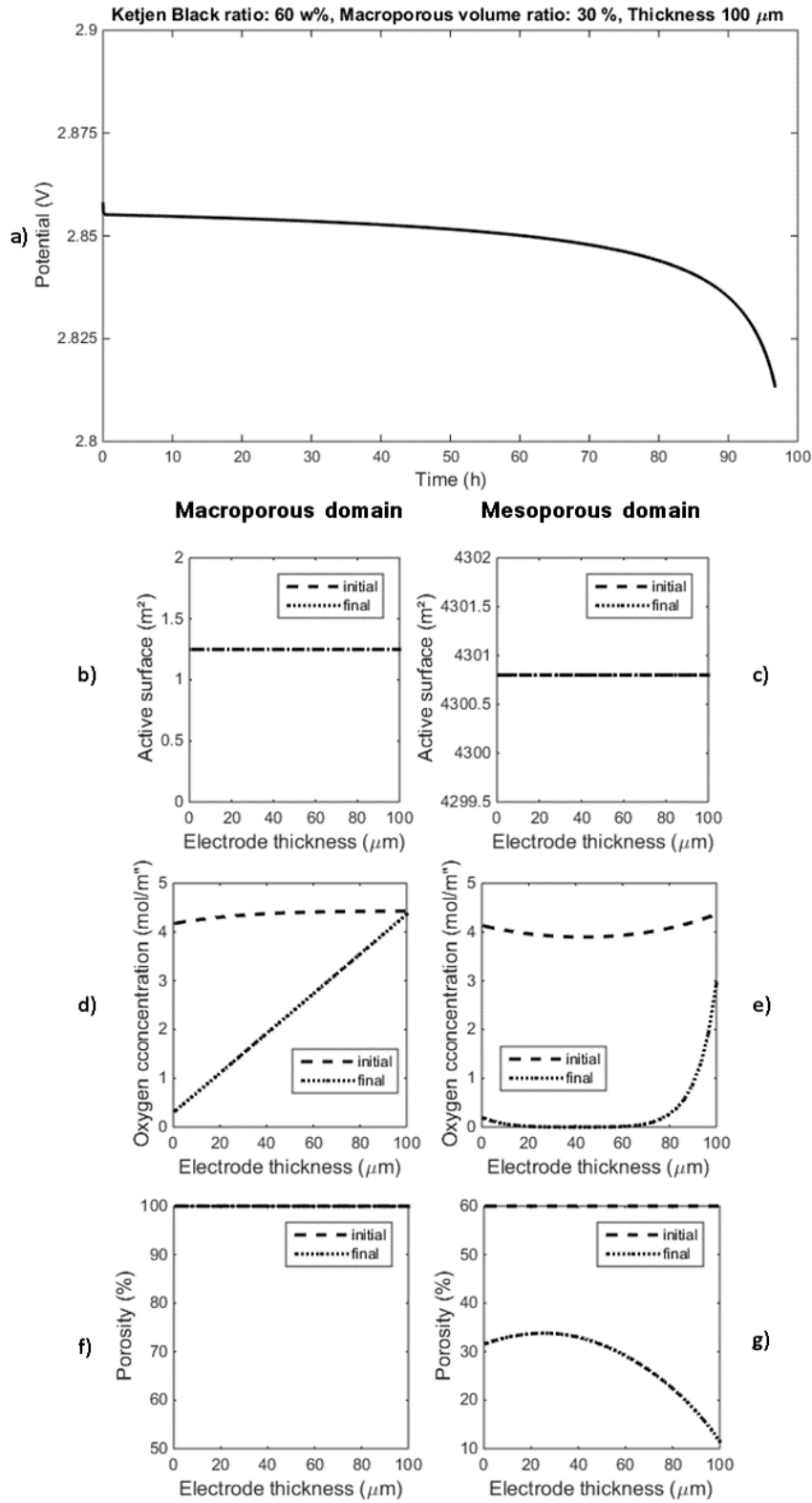


Figure III. 11: Evolution of macro-pores active surface (b) and meso-pores one (c), of oxygen concentration in macro-pores (d) and meso-pores (e) and of porosity in macro-pores (f) and meso-pores (g) linked to the discharge curve (a) done at  $I = 62.5 \mu\text{A}/\text{cm}^2_{\text{geometric}}$  for an electrode with 60 wt% of Ketjen Black and 30 % of volume macro porosity volume ratio (initial stage was estimated after 10 s and final one corresponds to end of discharge).

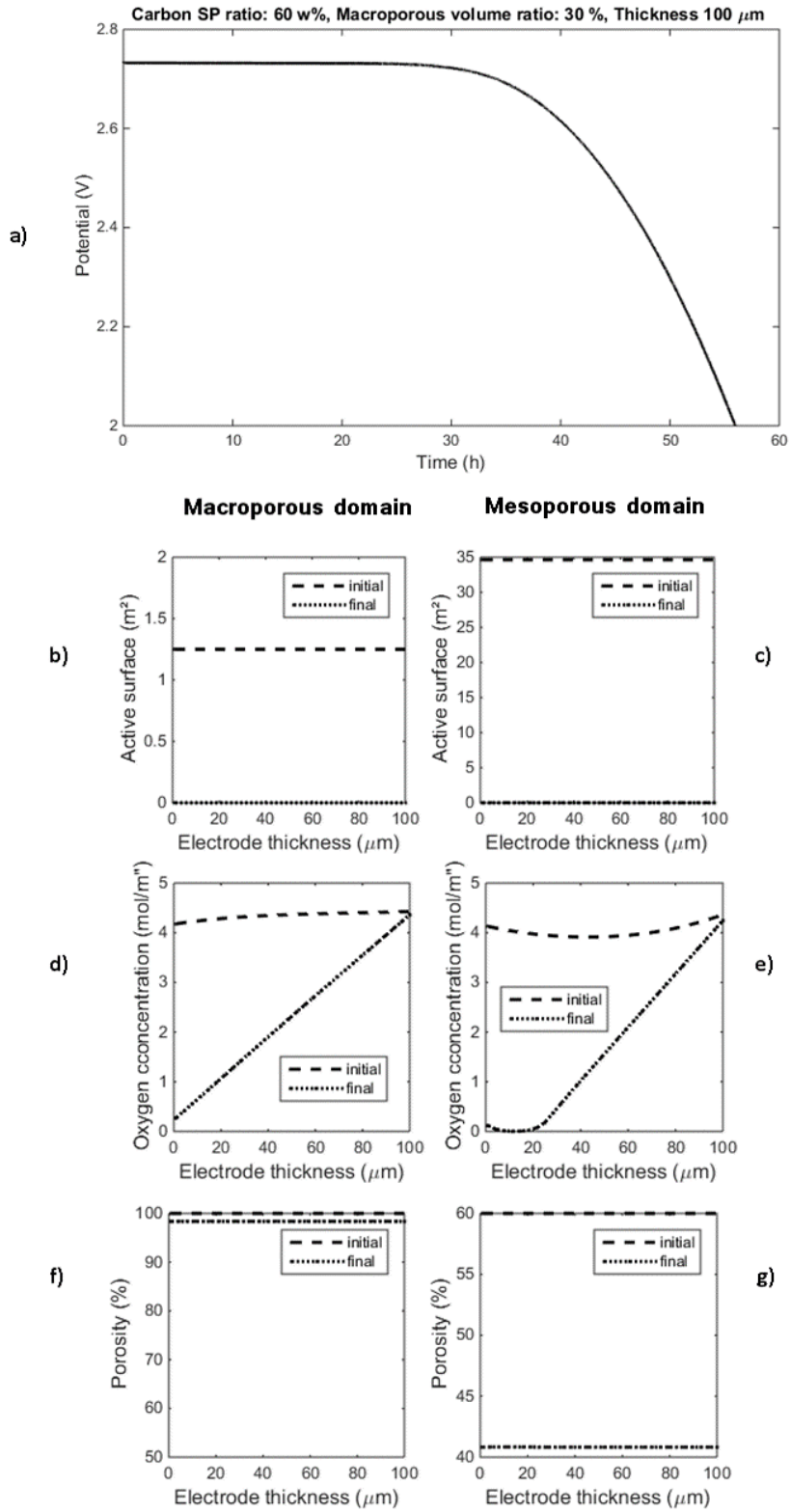


Figure III. 12: Evolution of macro-pores active surface (b) and mesopores one (c), of oxygen concentration in macro-pores (d) and meso-pores (e) and of porosity in macro-pores (f) and meso-pores (g) linked to the discharge curve (a) done at  $I = 62.5 \mu\text{A}/\text{cm}^2_{\text{geometric}}$  for an electrode with 60 wt% of carbon Super P and 30 % of volume macro porosity volume ratio (initial stage was estimated after 10 s and final one corresponds to end of discharge).



For Carbon Super P, the limiting factor was the passivation of the active surface due to the  $\text{Li}_2\text{O}_2$  deposition until a thickness equal to the hole tunneling distance. Active surface in each porous domain was then equivalent to zero (Figure III. 12.a. and Figure III. 12.b.). As passivation phenomena occurred faster than oxygen concentration reduction, oxygen was still available but no free carbon surface was remaining in the system. These considerations highlighted the necessity to carefully select the carbon used to formulate LABs electrodes. Moreover, it also spotlighted the high sensitivity of the system toward carbon surface.



# CHAPTER IV: EXPERIMENTAL STUDY OF BI-POROUS ELECTRODES

## Contents

---

IV.1. Dip-coated electrode: a first attempt toward bi-porous electrodes.....	104
IV.1.a. Formulations tested.....	104
IV.1.b. Preliminary tests.....	104
IV.2. Electrolyte modification.....	109
IV.3. Development of highly porous and flexible electrodes for LABs.....	113
IV.3.a. Efficiency of DBP removal.....	113
IV.3.b. Impact of DBP removal on porosity creation.....	115
IV.3.c. Behavior of the films in the electrolyte solvent.....	123
IV.3.d. Thermal behavior of the films at high temperature.....	124
IV.3.e. Performances of the flexible porous carbon electrodes.....	125
IV.3.f. Discharge product formation.....	127
IV.3.g. Merging of theory and experiments.....	131

---

## IV.1. Dip-coated electrode: a first attempt toward bi-porous electrodes

Prior to develop multilayers electrode, the formulation of monolayer electrode was revised as previously summed up in Chapter II. In addition to SEM observations, the several electrodes produced were tested by applying discharge and charge currents  $\pm 25 \mu\text{A}$  with voltage cutoffs of 2.2 V and 4.2 V respectively.

### IV.1.a. Formulations tested

Various formulations were tested using the dip coating process. For ease of understanding, the several formulations would be described according the following format:  $B_xD_yZ$  with Z replaced by F to describe the drying process with fast increase of temperature or by S, in case of temperature step increase. X and Y stand for the ratios of binder ( $B_x$ ) and dry mass ( $D_y$ ) respectively. In case of multiple coating (double coating steps), M is added to the end of the formulation format to highlight the change.

Table IV. 1 summarizes the main formulations tested along the study. The versatile trials made to modify the slurry viscosity, permitting smooth deposition on the grid, as well as the ones dedicated to the study of multiple-step solvent addition would not be reported here. In the following study,  $B_{10}D_{2.8}F$  was defined by convention as the reference as it was the first formulation tested after viscosity and solvent addition tests.

Table IV. 1: Sum up of the formulations produced at lab scale.

		Dry mass (%)		
		2.8	1.4	0.28
Binder ratio (wt%)	5	$B_5D_{2.8}F$	X	X
	10	$B_{10}D_{2.8}F$ (reference)	$B_{10}D_{1.4}F$	$B_{10}D_{0.28}F$
	15	$B_{15}D_{2.8}F$ , $B_{15}D_{2.8}S$	X	$B_{15}D_{0.28}S$

### IV.1.b. Preliminary tests

Due to the early stage of the study, only few experiments were carried out on the several formulations. Then, a strong comparative study could not be made on their electrochemical responses. The main inputs to choose which formulation was the more suitable were the visual observations of the slurry as well as SEM images of the deposit after drying. Still, some

electrochemical tests were applied to the electrodes (Figure IV. 1) and some hypothesis could be formulated to explain those results.

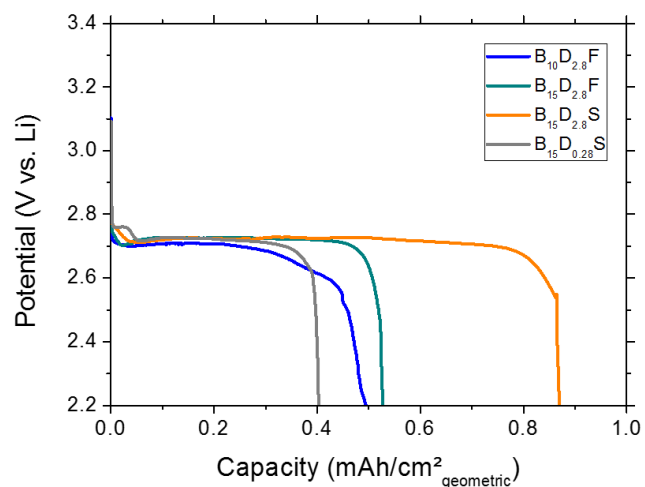


Figure IV. 1: Discharge curves of several electrodes along the improvement of dip-coating process ( $I = 25 \mu A$ , electrolyte: dried DME + 0.1 M LiClO<sub>4</sub>).

As highlighted in Figure IV. 1, the discharge capacity looked like to increase with the improvement of the dip-coated electrode formulation.

While only increasing the binder ratio from 10 to 15 wt%, discharge capacity was slightly enhanced (only 0.03 mAh/cm<sup>2</sup><sub>geometric</sub>). More significantly, a smoother and stable plateau was registered. These two trends could be respectively related to the rise of carbon deposited on top of the grid due to the higher stability of the deposit (stronger polymeric network) achieved thanks to the binder ratio increment. This seemed valid in the light of the images recorded by SEM (Figure IV. 2) and so was assumed to be accurate.

With also the slowing down of the drying step, an amelioration of the capacity was recorded (extra 0.34 mAh/cm<sup>2</sup><sub>geometric</sub>). Such observation was supposed to be linked to a higher carbon deposit on top of the grid. Still, while analyzing SEM pictures, less carbon seemed accumulated (Figure IV. 2). However, repartition of the carbon looked more homogeneous. Actually, with dense aggregates as spotlighted in Figure IV. 2.b, electron collection was less effective and most probably lower surface was created for ORR (as some significant part of the grid was uncovered). On the reverse, thin deposit as seen in Figure IV. 2.c must enhance electron collection and provide more reaction surface.

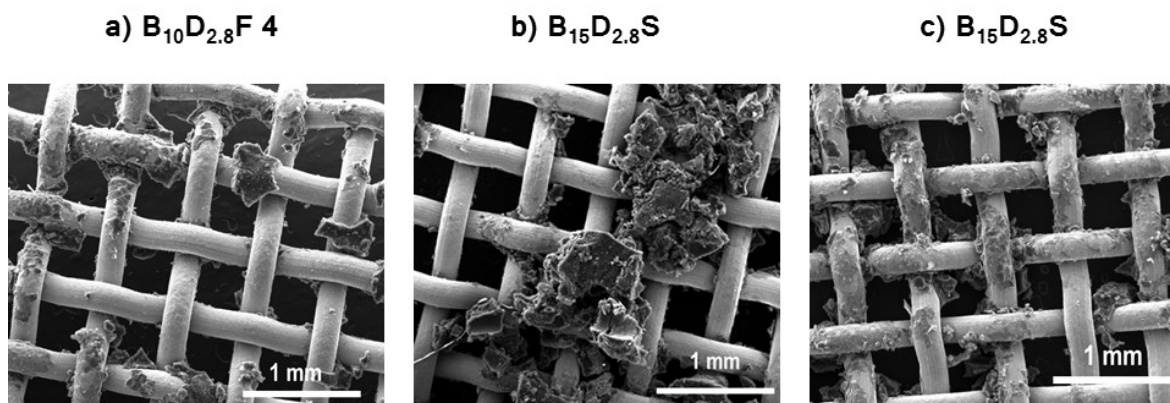


Figure IV. 2: SEM pictures of the electrodes from  $B_{15}D_{2.8}F$  and  $B_{15}D_{2.8}S$  formulations.

In parallel, effect of the dry mass ratio was examined and led to smoother deposit as demonstrated in Chapter II. Despite coating visual aspect improvement, moving from 2.8 % to 1.4 % of dry mass in the slurry did not affect the discharge capacity even so a flatter plateau was observed (Figure IV. 3).

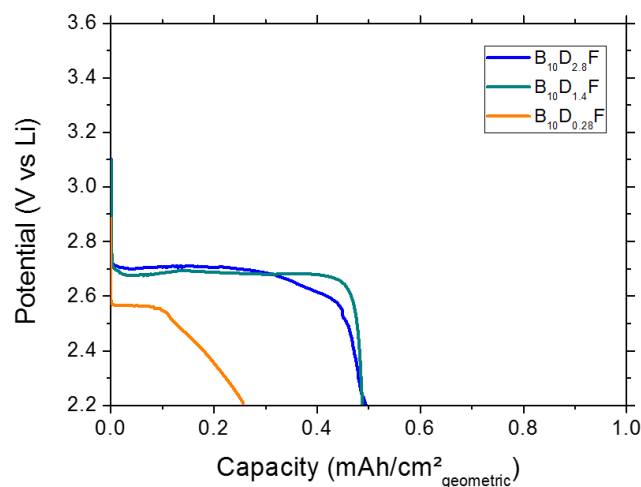
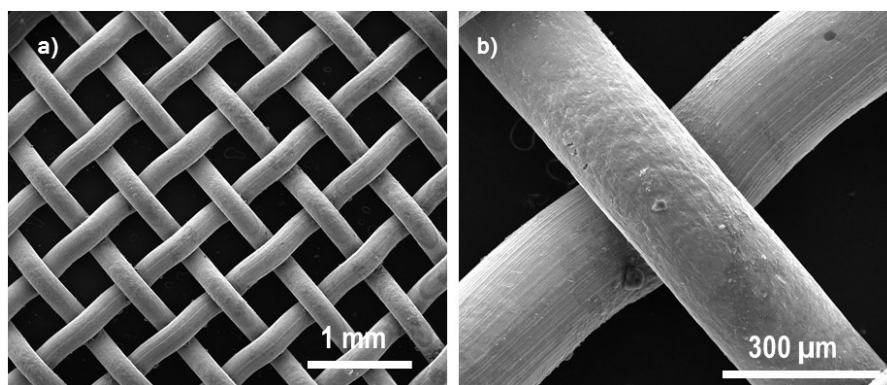


Figure IV. 3: Discharge curves of several dip-coated electrodes made with different dry mass ratio ( $I = 25 \mu A$ , electrolyte: dried DME + 0.1 M  $LiClO_4$ ).

While transposing the dry mass ratio reduction to the previous improved formulation ( $B_{15}D_{2.8}S$ ), results also did not reach the expectations. Indeed,  $B_{15}D_{0.28}S$  capacity was divided by a factor of 2 compared to  $B_{15}D_{2.8}S$  one (Figure IV. 1). As revealed by Figure IV. 4, only few carbon was deposited which could explain the capacity drop.



*Figure IV. 4: SEM pictures of an electrode made with the formulation  $B_{15}D_{0.28}S$  at a magnificence of a) 40x and b) 150x.*

Trying to enhance the capacity and to design multilayered electrode, a batch of electrodes was dipped twice and entitled  $B_{15}D_{0.28}SM$ . Significant improvement of the carbon ratio coated on top of the grid was then achieved (Figure IV. 5).

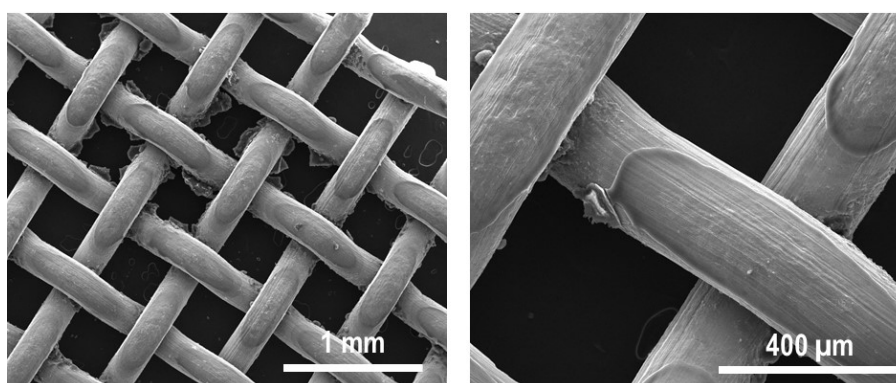


*Figure IV. 5: SEM pictures of an electrode made with the formulation  $B_{15}D_{0.28}SM$  at a magnificence of a) 40x and b) 130x.*

The appearance of the double coating, thin and almost translucent, called for a deeper optimization study on such a fabrication process. Even though, a smooth coating was obtained, it did not mold the grid shape and was then not homogeneous. It seemed that the slurry was not viscous enough to stick to the grid and just flowed through it. One hint that could be followed for further studies would be to test  $B_{15}D_{1.4}S$  and  $B_{15}D_{0.56}S$  to see if a dry mass in between 1.4 % and 0.28 % would improve the film deposition. A slight increase of the viscosity could help the slurry to be maintained on top of the grid prior to drying.

Due to the resulting low capacity ( $0.86 \text{ mAh/cm}^2_{\text{geometric}}$  and  $6.12 \text{ mAh/g}_{\text{electrode}}$ ) with this electrode fabrication process, a different formulation procedure was later contemplated based

on the well-known Bellcore process. Still, across the development of dip-coated electrodes two major improvements on cell operation and stability were performed.

First, as exhibited in Figure IV. 5, B<sub>10</sub>D<sub>0.28</sub>S had a stronger overpotential than other cases, as well as, lower discharge capacity. Such behavior was correlated with the longer flushing time applied for this only case (one hour against thirty minutes). Also, it was observed post-mortem that after cycling all the electrodes and separator used were dry when DME + 0.1 M LiClO<sub>4</sub> was used as the electrolyte. As DME is extremely volatile (48 mmHg @ 20 °C according to the supplier datasheet) long flushing step or operation times aggravated the evaporation of the solvent in the container (some μL of electrolyte for 0.75 L in the container). Then, electrolytes and flushing time were revised to enhance the system stability and operation.



## IV.2. Electrolyte modification

As aforementioned announced, selecting a suitable electrolyte for LABs is not that trivial. Previous studies carried out at LRCS were using DMSO as the electrolyte solvent.<sup>209</sup> Still, DMSO is unstable versus lithium metal<sup>67,91</sup> and lithium oxygen species.<sup>92-94</sup> In literature, the use of ether based solvents was presented as a good candidate for LABs application.<sup>224</sup> As Laoire *et al.* spotlighted the lower impediment of ORR while using DME compared to DMSO,<sup>79</sup> such solvent was initially tested. Still, as illustrated above, use of DME was problematic due to its tendency to evaporate quickly. The few amount of electrolyte was evaporated in the “Le Parfait” large volume, leading to the cell drying and fading. Then, as literature claimed better stability with glyme, TriGDME was used instead. Also, some tests were made with TetraGDME. Interest of TriGDME compared to TetraGDME is its lower viscosity due to shorter chains (Figure IV. 6). Electrode wettability by TriGDME was then supposed to be higher. Though, literature mainly mentioned the use of TetraGDME rather than TriGDME one.

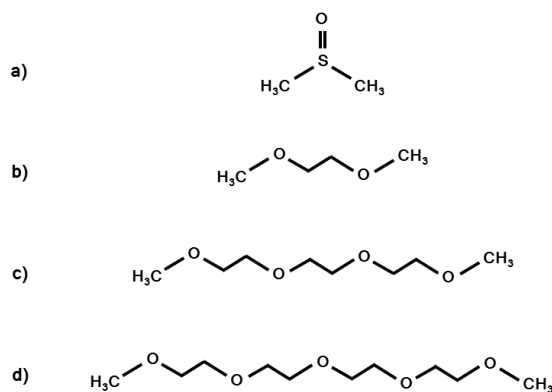


Figure IV. 6: Chemical formulas of a) DMSO, b) DME, c) TriGDME and d) TetraGDME.

In parallel, LiClO<sub>4</sub> was initially selected with DME as it presents a strong advantage for LABs application: its stability toward moisture exposition.<sup>225</sup> Unfortunately, its explosive nature<sup>226,227</sup> is a strong negative counterbalance for its use at industrial scale, even though it is commonly spread in laboratories studies.

While DME/LiClO<sub>4</sub> mixture was efficient, changing only DME was not suitable. Indeed, only changing the electrolyte solvent with no regard to the salt could lead to incompatibility issues such the one encountered while mixing TriGDME with LiClO<sub>4</sub>. In perchlorate, chlorine is at a high oxidation state and so is a strong oxidizer which can react and create glycol perchlorate esters after the break down of ether chains under the attack of ClO<sub>4</sub><sup>-</sup>.<sup>228,229</sup> For this reason, LiTFSI was considered as an alternative. Unfortunately, such selection came along with

a significant cons, LiTFSI is highly hygroscopic<sup>230</sup> and so the cell would be highly sensitive to moisture.

Stability of the several electrolytes was evaluated using polarization tests (Figure IV. 7).

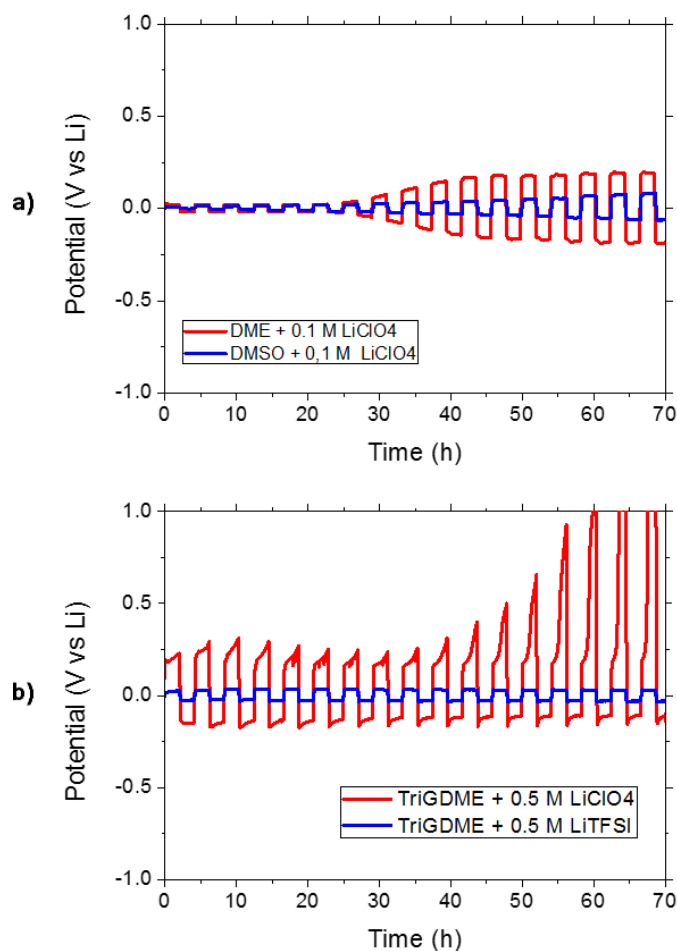


Figure IV. 7: Polarization tests ( $\pm 25 \mu A$  for 2h) a) Comparison between DME and DMSO and b) and between TriGDME with LiClO<sub>4</sub> or LiTFSI as a salt.

Figure IV. 7 emphasizes several occurring phenomena. First of all, instability of DMSO toward lithium metal can be observed thanks to the constant increase of the distance between the two plateaus (Figure IV. 7.a). The gap between the two plateau can be correlated to the system resistance. If the system is stable, the gap should be maintained. If a resistive SEI is formed, an increment of the gap should be noticed. If a stable SEI is formed, the gap should finally reach a constant value. Also, if the plateau does not remain flat, reaction occurring under current application are spotlighted.

At the light of such behavior, it was clearly shown that DME is not stable overtime against lithium. Indeed, after twenty-five hours of polarization test, the resistance was significantly amplified and during application of current step no flat plateau was recorded (Figure IV. 7a).

Though, interest of DME could be questioned. While testing the dip-coated electrode, the capacity fade (Figure IV. 8) was initially attributed to cell drying due to DME evaporation in the “Le Parfait” container. Still, from these polarization results, capacity fade during cycling could be also explained by DME instability versus lithium.

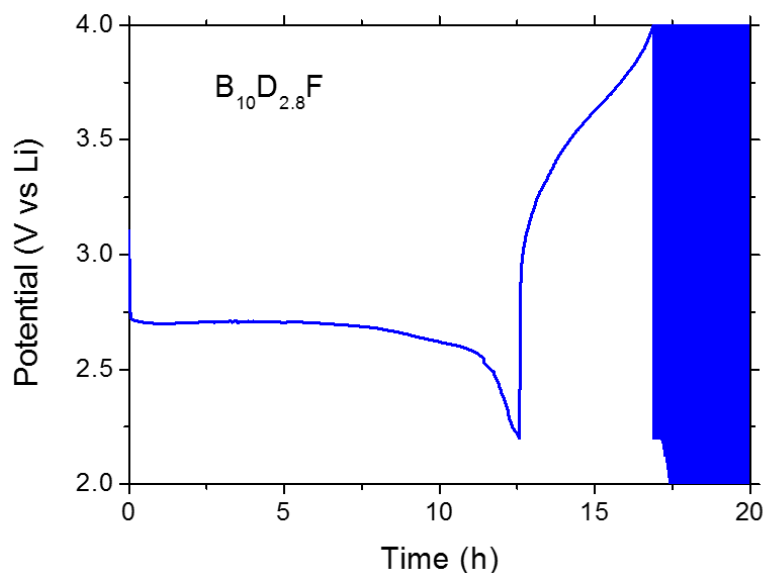


Figure IV. 8: Discharge/Charge of an electrode from batch  $B_{10}D_{2.8}F$  at  $\pm 25 \mu A$ .

On another side, TriGDME stability was tested under polarization condition. Worth point out that in the TriGDME case, the salt concentration was modified to compensate the solvent high viscosity as it could hinder ionic conduction. For such reason, salt concentration was slightly enhanced from 0.1 M to 0.5 M. It appeared that, at one lithium electrode, reactions started to occur as exposed by the asymmetric rise of one of the polarization plateau (Figure IV. 7.b). Such reaction was attributed to the degradation of the electrolyte (attack of the salt on the solvent). In fact, once the salt was changed, dissymmetric behavior was removed and a stable gap was displayed along the polarization test (Figure IV. 7.b). Then, stability of TriGDME + 0.5 M LiTFSI toward lithium was demonstrated.

Later, few tests were carried on using other salts or electrolytes supposedly helping to protect the lithium metal foil (TriGDME/LiNO<sub>3</sub>, DMA/LiNO<sub>3</sub>) or to act as a redox mediator (TriGDME/LiI).

As demonstrated here, the evolution of the electrolyte retained was cautiously thought (Figure IV. 9). Despite a careful questioning, final use of ether based solvent was not the optimal choice as instability of ether-based solvents was also reported in literature.<sup>78,224</sup> Nevertheless, development of suitable electrolytes for LABs is still lacking (ionic liquid seem

promising<sup>231</sup> still request too high operating temperature). Taking into account that, in the current study a strong focus was made on electrode texture development, TriGDME/0.5 M LiTFSI was then kept along the overall cathode study, to ensure comparison in between the several results.

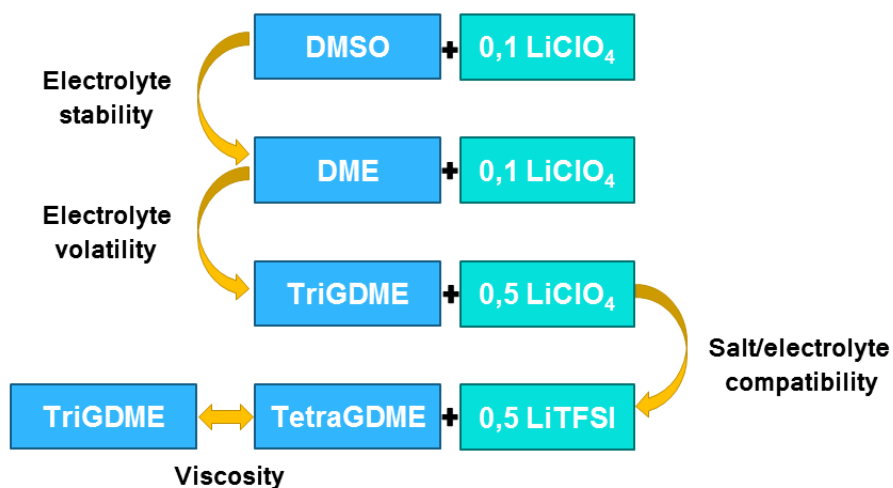


Figure IV. 9: Evolution of the electrolytes tested along the study.

### IV.3. Development of highly porous and flexible electrodes for LABs

From theoretical point of view, it was defined that the addition until 40 % of macro-porosity would enhance diffusion. In parallel, at experimental level, the creation of bi-porous electrode was achieved thanks to flexible porous electrodes. To corroborate the theoretical findings with experiments results, the electrode porosity should be precisely determined prior to make further comparisons. Then, characterization of the self-standing flexible porous electrodes was implemented.

Initially, as porosity was created by leaching out a porogen agent, here DBP, its removal efficiency was firstly checked. Later, the nature and amount of created porosity (macro or meso porosity) were probed all along the electrode fabrication process. Due to the multitude of formulation tested, a particular focus was made from DBP<sub>40</sub> to DBP<sub>80</sub> (films respectively with 40 w% and 60 w% of DBP in their formulation) as they covered most of the experimental framework. Finally, assessment of Li<sub>2</sub>O<sub>2</sub> formation and electrochemical responses would be described.

#### IV.3.a. Efficiency of DBP removal

The efficiency of the DBP removal was estimated by a statistical study carried out on 50 disks cut from DBP<sub>65</sub>. Each disk was weighted before and after full leaching process (3 consecutive soakings in pure ether) and the resulting weight loss was compared to the initial mass of DBP in the disk, leading to the efficiency of the removal (%) (Figure IV. 10).

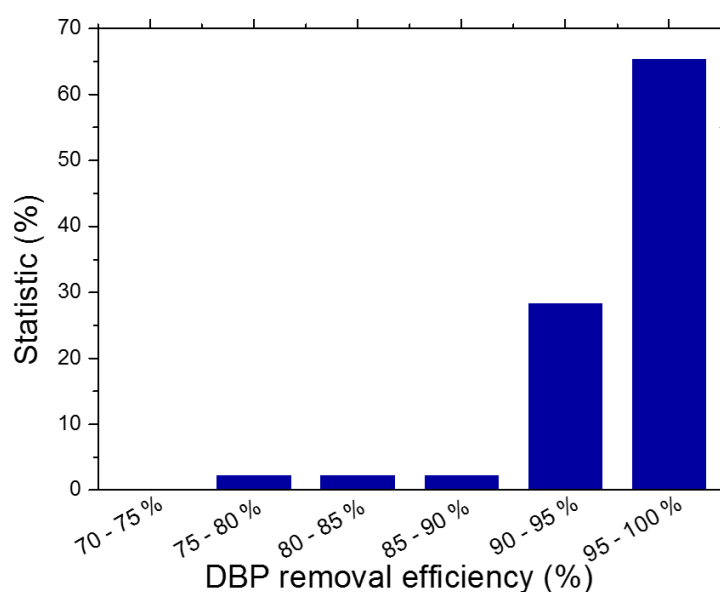


Figure IV. 10: Statistical analysis of the efficiency of the DBP extraction (50 disks from DBP<sub>65</sub>).

The mean leaching efficiency was found equal to 94.4 %. DBP extraction was in the 90 – 100 % efficiency range for 94 % of the disks, and there was no disk with an extraction efficiency lower than 75 %. Although these results could mean that the DBP removal was, statistically, almost fully accomplished for electrode films with such high DBP contents, their punctual slight deviation from full (100 % efficient) leaching could also enlighten some inhomogeneity in the DBP content through the entire films from which the disks were cut. This was of paramount importance since the initial chemical inhomogeneity straightly impacts the texture of the DBP-extracted electrode films. Same slight deviation from 100 % efficiency was observed for three electrodes from DBP<sub>40</sub> (91, 92 and 95 %) and three from DBP<sub>80</sub> (80, 93 and 94 %). More homogeneous results were achieved with DBP<sub>40</sub>.

To understand deeper the cleaning process, efficiency of DBP extraction in DBP<sub>60</sub>, at each leaching step, was evaluated (each fifteen minutes in clean ether) and compared to a one-leaching step (forty five minutes in same ether bath) (Figure IV. 11).

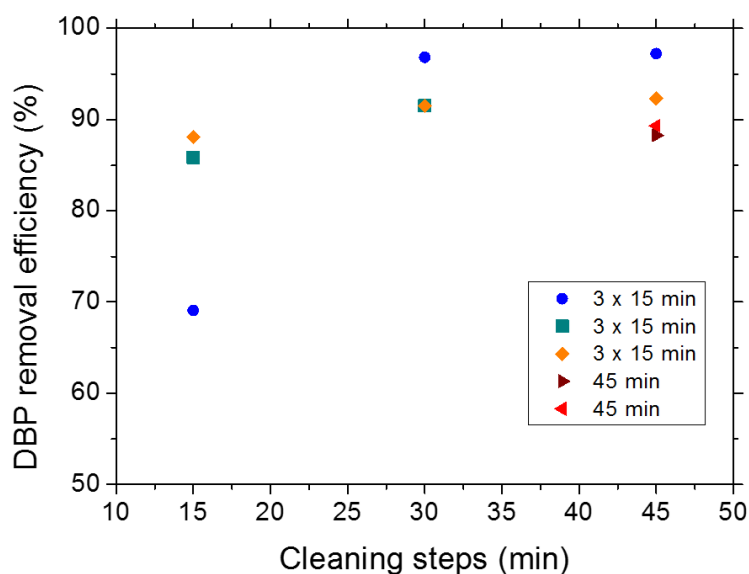


Figure IV. 11: Efficiency of DBP removal along the soaking process in ether depending on the ether cleaning steps applied to DBP<sub>60</sub> electrodes.

In each case with three cleaning steps, the first step allowed to remove more than 65 % of the initial DBP content. The second soaking in ether, then helped to pull out between 3 % to 26 % more. The impact of the last soaking was less significant but still led to extract a last extra 1 %. Only one step of 45 min, was clearly damageable as lower DBP amounts were withdraw. The difference of results between three consecutives steps and the equivalent one could be explained by some kinetics and/or saturation issues in DBP-containing ether. To sum up,

efficient DBP removal was fulfilled using three consecutive cleaning steps in ether and was used all along the study.

### *IV.3.b. Impact of DBP removal on porosity creation*

#### *First evaluation of the films porosity based on DBP mass loss*

Each film porosity was quickly estimated based on the mass loss measured during the leaching process. The mass loss was directly attributed to DBP extraction and so to porosity creation. The results were compared to theoretical porosities, evaluated this time taking into account that full initial DBP content was extracted (Figure IV. 12).

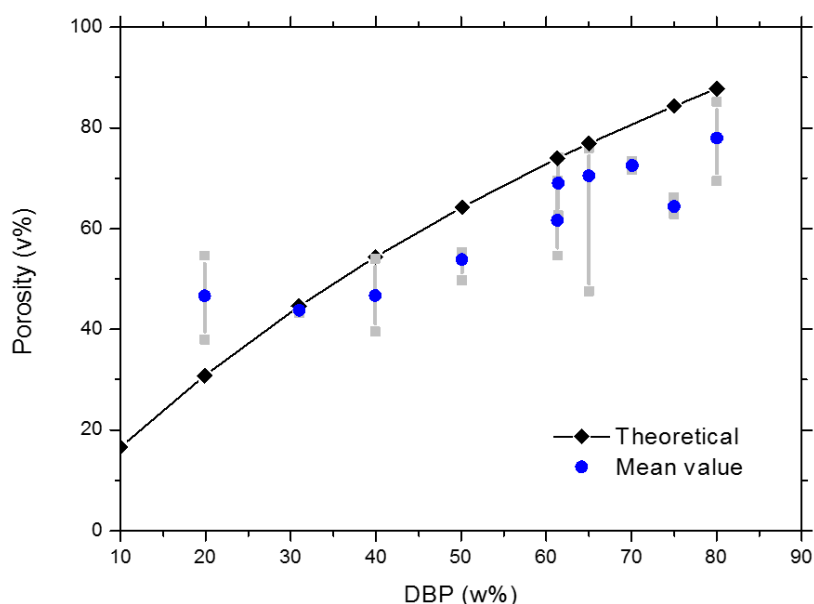


*Figure IV. 12: Theoretical porosities compared to estimated porosities, calculations based on DBP mass loss. The mean values of the estimated porosities were reported in blue, while the maximum and minimum ones were shown in grey. The number of values considered for the mean values calculations were provided in the table in grey.*

Surprisingly, not all the values were lower than the theoretical porosity (case of DBP<sub>20</sub>). Indeed, as theoretical porosities were calculated estimating that all the DBP initially present in the electrode was removed, experimental porosities were expected to be lower, due to the not fully efficient DBP removal formerly demonstrated. Still, results for DBP<sub>20</sub> could be explained while observing the electrodes. Actually, the formulations were developed to create electrodes with high DBP ratios (to reach 20 – 50 % of macro-porosity as deduced from the theoretical study), lowering in these adjusted formulations the amount of DBP to 20 w% tended to lead to high brittleness. Most probably, due to the electrode fragility, some electrode parts must have

fell apart leading to higher mass loss compared to the mass of DBP initially inserted in the electrodes.

Another relevant information appeared also while analyzing the case of DBP<sub>60</sub>. Two different batches had been prepared for such formulation leading to two values of mean porosity separated by additional 7 %. The only difference between these two films was the grinding time of the powders in the mortar. The first one was blended during five minutes while the second one was mixed between ten to fifteen minutes. With less aggregation of solid particles, the film was better blended and so DBP was certainly more homogeneously distributed along the electrode, explaining an estimated porosity closer the theoretical value.

Such observation highlighted the strong impact of the grinding step, together with chemical homogeneity effect, in developing homogeneous films. Actually, even in case of DBP<sub>65</sub> which has been demonstrated to be well extracted by a statistical study, chemical inhomogeneity was revealed by the range of estimated porosities. Still, as spotlighted by the high mean value, most of the electrodes were well extracted and homogeneous.

Even though some conclusions were drawn from previous calculations, they remained based on theoretical calculations without taking into account the films volume. A clear estimation of the porosities was then required using the films volume (thickness x surface). Prior to any further investigations, the volume modifications of the films along DBP extraction were analyzed in priority.

### *Volume modification along DBP extraction*

Firstly, evolution of thicknesses for the several films was studied (Figure IV. 13). For films with a DBP ratio ranging from 20 wt% to 40 wt%, thickness evolution was negligible. However, for higher DBP ratios, a clear increase of the thicknesses was notified and seemed to increase after DBP extraction.



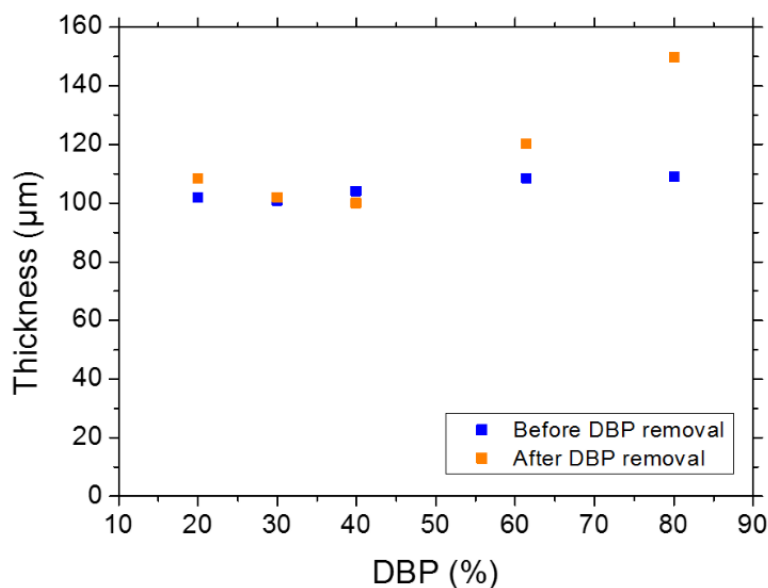


Figure IV. 13: Films thickness before and after DBP removal.

As illustrated in Figure IV. 14.a, the leaching process induced volume changes. Films with high initial DBP content tended to curl and shrink after extraction. Shrinkage also seemed proportional to the DBP amount. This trend was easily understood by the stronger modification occurring while removing 80 w% of DBP compared to only 40 w%. This was certainly more impacting the electrode texture as it corresponded in theory to the formation of 88 % of porosity, more significant than the 45 % expected for DBP<sub>40</sub> (Figure IV. 12).

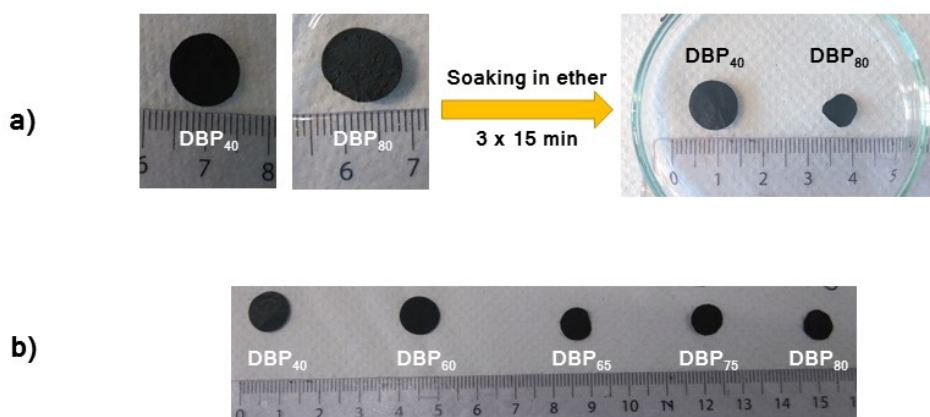


Figure IV. 14: a) Evolution of the disks diameter (initially  $\varnothing = 11$  mm) for electrodes from DBP<sub>60</sub> and DBP<sub>80</sub> and b) comparison of the shrinkage observed for the several formulations after DBP extraction. For b) electrodes were dried at the last cleaning step under a glass side to remain flat.

After measurement, decrease of DBP<sub>80</sub> disk diameter was assessed to be equal to 0.1 cm. The shrinkage observed was compensated by the expansion of the film thickness. Verification

of the volume evolution was proceeded on DBP<sub>80</sub> and same volume was calculated before and after DBP removal (0.01 cm<sup>3</sup>). At the light of such observation the porosity of the electrode could be estimated using the initial volume calculated for each formulation as overall volume was still unchanged even though films thickness and surface were modified.

### Assessment of the films porosities

Based on the weight composition (Table II. 1) and individual density of the components (Table II. 2), the expected initial (carbon-polymer-DBP) and final (carbon-polymer) densities of the films were predicted. While the initial density was bound to the DBP films content, the one of the extracted films was theoretically constant ( $\rho = 1.88 \text{ g/cm}^3$ ) since they were only made of polymer and carbon in the same weight ratio (4/1). Pycnometry measurements performed on DBP<sub>40</sub> and DBP<sub>60</sub> large stripes (tens of cm<sup>2</sup>), before DBP extraction, led to density values in very good agreement with the expected ones (Table IV. 2).

Table IV. 2: Textural characterization of DBP<sub>40</sub>, DBP<sub>60</sub> and DBP<sub>80</sub> films before and after DBP leaching.

	With DBP			DBP extracted	
	Initial density (g.cm <sup>-3</sup> ) Calcul. / Meas.	Mesoporous volume (ASAP, v%)	BET SSA (m <sup>2</sup> .g <sup>-1</sup> )	Mesoporous volume (ASAP, v%)	BET SSA (m <sup>2</sup> .g <sup>-1</sup> )
DBP <sub>40</sub>	1.42 / 1.38	X	X	10	31.7
DBP <sub>60</sub>	1.27 / 1.32	0	2.5	14	56.2
DBP <sub>80</sub>	1.15 / X	X	X	12	33.0

The chemical composition of the films and the juxtaposition of their components was then confirmed. More importantly, the absence of significant closed porosity was demonstrated. If significant amount of porosity was closed, then helium could not access to the pore and thus pycnometry measurement will be distorted. Actually, such closed porosity could have been produced due to fast acetone evaporation.

Once discarded the possibility of an initial close porosity, porosity estimation was implemented for three disks from each formulation DBP<sub>40</sub>, DBP<sub>60</sub> and DBP<sub>80</sub>. Firstly, the total initial porosities of the films were assessed (porous v%, blue bars Figure IV. 15) by comparing their apparent volumes (thickness x surface area) to the sum of their components volumes. Values ranging from 44 v% to 49 v% were observed for DBP<sub>40</sub>, clueing the very good homogeneity of the film. Also, values from 33 % to 42 % were found for DBP<sub>60</sub>, and from 0 % to 42 % for DBP<sub>80</sub>, highlighting again the decrease of film homogeneity with DBP content. As demonstrated by pycnometry measurements, the film initial porosities were open.

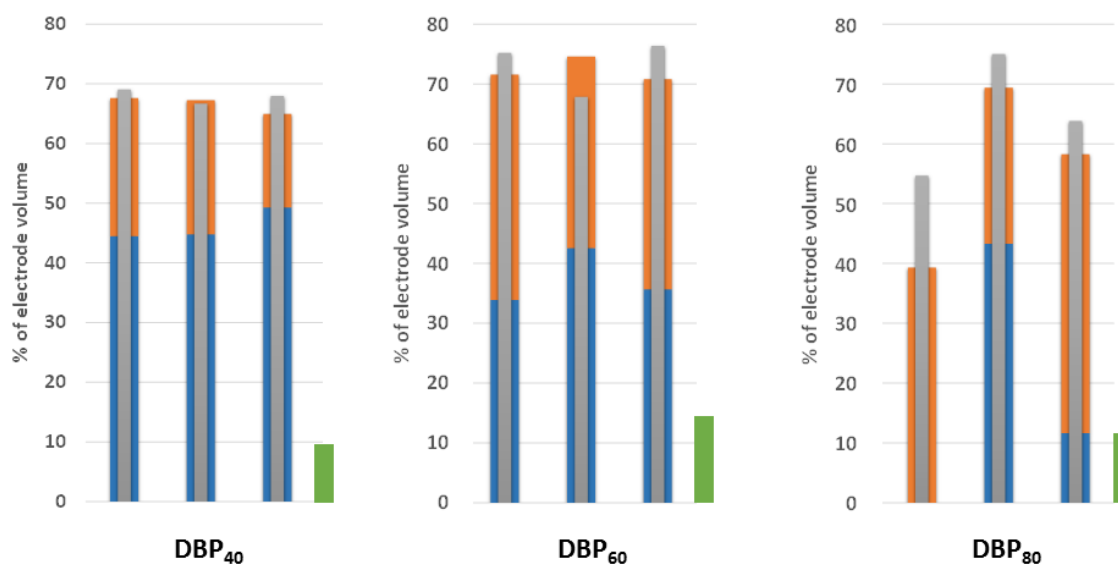


Figure IV. 15: Total porosity (v%) for three disks cut from DBP<sub>40</sub>, DBP<sub>60</sub> and DBP<sub>80</sub> films, measured before (blue bars) and after (gray bars) DBP extraction. The orange bars represent the volume of DBP extracted during the ether leaching step. The green bars represent the mesoporous contribution to the total volume of extracted films.

Also, nitrogen adsorption analyses indicated that the porosities were due to macro-pores as only negligible meso-porous contribution ( $0.002 \text{ cm}^3 \cdot \text{g}^{-1}$ ) and very low SSA ( $2.5 \text{ m}^2 \cdot \text{g}^{-1}$ ) were recorded for DBP<sub>60</sub> even though significant amount of porosity was estimated.

Then, the total porosities of the disks were similarly evaluated after DBP extraction, taking into account the disks volume modification (gray bars on Figure IV. 15). As expected, the global porosity was found systematically increased by the DBP extraction, but the heterogeneity trend previously spotted for the initial porous volumes was here similarly observed for the final porosities (67 – 69 v% for DBP<sub>40</sub>, 68 – 77 v% for DBP<sub>60</sub>, and 54 – 74 v% for DBP<sub>80</sub>). Discrepancies of the initial and final porous volumes increased with the rise of DBP initial content.

Again, knowing the density of DBP ( $1.05 \text{ g/cc}$ ) and assuming that the evolution in the film weight during ether extraction was only due to the DBP dissolution, the porous volume left behind was calculated based on the experimental film mass loss and compared to the initial electrode volume. These v% values were shown as orange bars in Figure IV. 15. For the three disks cut from DBP<sub>40</sub>, the calculated DBP-related porous volume satisfyingly matched the gap between the initial and final global porosity. This match was slightly less pronounced for DBP<sub>60</sub>

and even worst for DBP<sub>80</sub>, illustrating again the large heterogeneity in the films composition and texture for the highest initial DBP contents.

To use these electrodes in LABs applications, knowing quantitatively their global porosity was insufficient. As already demonstrated, the nature of the porosity would drastically impact the behavior and performances of LABs. In order to get more insight, BET SSA and meso-porous volume were determined by N<sub>2</sub> isotherm adsorption (Table IV. 2). It worth reminds that only pores with a size below 300 nm were taking into account for the porous volume measurement while using such technique.

As exemplified by DBP<sub>60</sub>, DBP extraction clearly triggered the creation of open and accessible meso-pores which were totally absent in the precursor films. Still, the meso-porosity formation was not proportional to the initial DBP content (Table IV. 2, green bars on Figure IV. 15). Since meso-pores had high surface/volume ratio, this logically came with a large increase in SSA (Table IV. 2). Whatever the initial DBP content was, meso-porous volume (green bars on Figure IV. 15) was always lower than the volume of extracted DBP, meaning that this extraction also created some macro-porosity.

Pycnometry analyses of extracted films revealed density values spreading from 1.37 g/cm<sup>3</sup> (DBP<sub>40</sub>) to 1.65 g/cm<sup>3</sup> (DBP<sub>60</sub>), which was very much lower than expected (1.88 g/cm<sup>3</sup>). The only way to explain this surprising result was a significant evolution of the internal film texture during DBP leaching and/or drying step, resulting in the closing (*i.e.* not any more accessible to He) of a part of the initial or created porosity. As a quantitative example, the difference between expected and measured density for extracted DBP<sub>40</sub> film corresponded to a final electrode having 26 % of its volume made of not accessible porosity. This internal reorganization was probably at the origin of the shape evolution and curling of the disks observed during the DBP extraction and drying steps (Figure IV. 14).

SEM pictures of films before and after DBP extraction (Figure IV. 16) confirmed a textural effect of the DBP content before and after the leaching steps. Clearly, with DBP extraction surface roughness was enlarged and larger micrometric voids/cracks were noticed. Extracted films exhibited further voids and pores, delimiting carbon/polymer agglomerates, especially for DBP<sub>60</sub>, and DBP<sub>80</sub>.

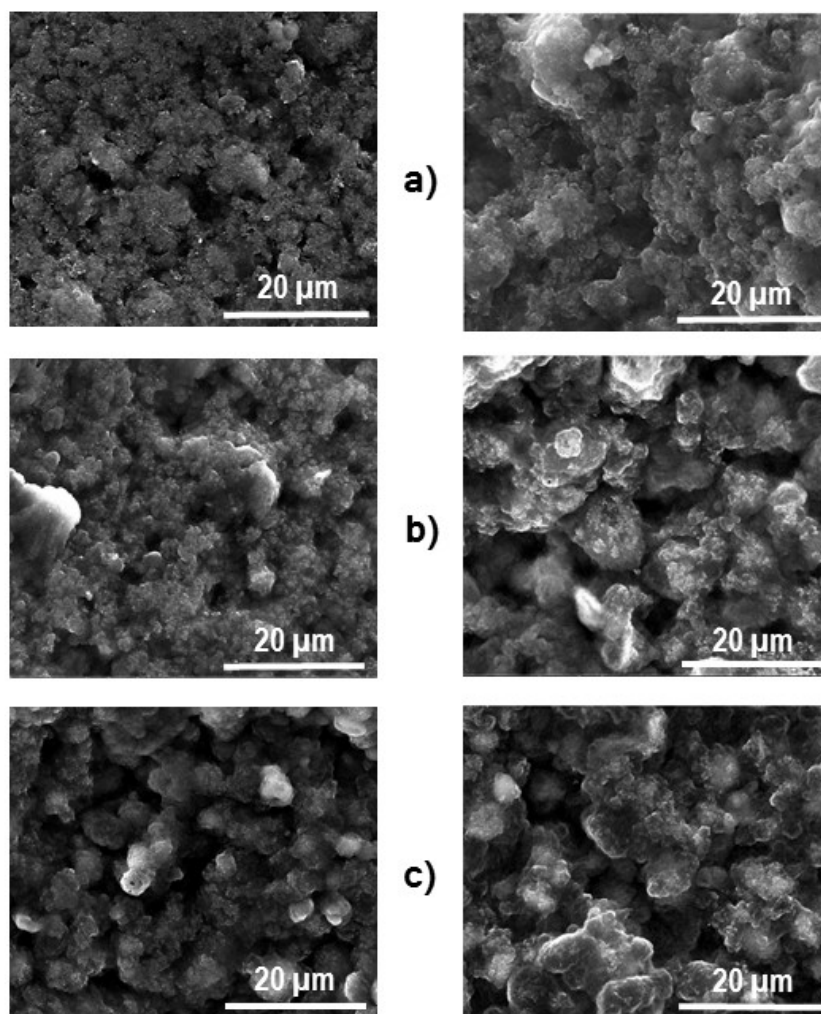


Figure IV. 16: SEM pictures of (a) DBP<sub>40</sub>, (b) DBP<sub>60</sub> and (c) DBP<sub>80</sub> films before (left column) and after (right column) DBP extraction. (Magnification a) 2500x b) 2400x and c) 2500x).

To better understand the evolution occurring at the several leaching steps, individual impact of ether treatment was scrutinized. Both the porous volume and SSA neatly increased during each leaching step while DBP was progressively extracted (Table IV. 3).

Table IV. 3: Evolutions in weight loss, porous volume and BET specific surface area (SSA) for DBP<sub>60</sub> along DBP extraction steps.

Cleaning step	Total DBP loss (%)	Porous volume (cm <sup>3</sup> /g)	BET Specific surface area (SSA, m <sup>2</sup> .g <sup>-1</sup> )
#0	-	0.002	2.5
#1	69.0	0.053	7.2
#2	97.0	0.133	25.7
#3	97.4	0.243	56.2

Even though resulting in a very slim DBP loss (0.4 %), step#3 was associated with the largest porous volume and SSA increases, clearly confirming the need of the three steps. The slight amount (< 3 %) of remaining non-dissolved DBP was likely located in isolated inner parts of the film, non-accessible to ether percolation. Note that the maximum films SSA remained lower ( $56 \text{ m}^2.\text{g}^{-1}$ ) than the Ketjen Black expected contribution ( $280 \text{ m}^2.\text{g}^{-1}$  for DBP<sub>60</sub>), confirming that carbon particles were embedded in the polymeric film, hindering a part of its surface. Still, a significant amount of the carbon surface was accessible and measured. As large pores have small surface/volume ratio, the slight increase in SSA spotted during step #1 ( $2.5 \rightarrow 7.2 \text{ m}^2.\text{g}^{-1}$ ), while more than two third (69 %) of the DBP was gone, indicated the formation of large pores from easily accessible large DBP-rich zones of the films, therefore firstly and quickly extracted. Thereafter, smaller and less accessible DBP clusters were then progressively accessed and leached out along the subsequent two steps (#2 and #3). This explained the much larger gains in SSA, especially during step #3. It was assumed that such phenomenon was taking place within the micrometric carbon/binder agglomerates clearly visible on the SEM images, and between which, large micrometric macro-pores were also clearly observed (Figure IV. 16). The ratio between the gain in porous volume and the gain in SSA gave a first evaluation of the related pore size, and was founded to be lying below 10 nm during steps #2 and #3.

To sum up, the texture of the several porous-carbon loaded plastic film prepared for the study was identify. Initially, the films already exhibited open and accessible macro-porosity, as high as 40 v%, and no meso-porosity as demonstrated in Table IV. 2 and Table IV. 3. Still, DBP extraction enabled to enhance the formation of macro-porosity as well as forming meso-pores. Still, formation of extra-porosity came with a cost as electrodes suffered from internal reorganization leading to close porosity (e.g. 26 v% for DBP<sub>40</sub>). Such close porosity was a significant drawback for LABs application. Indeed, high amount of open porosity was required for LABs. So, the closed pores will just decrease the energy density as they will not participate to the discharge/charge mechanisms.

Another relevant information was the homogeneity of the films. Even though statistically it was demonstrated that DBP extraction was really efficient (e.g. 94 % of the disks cut from DBP<sub>65</sub> films reached between 90 % to 100 % of extraction efficiency), it clearly appeared that the chemical homogeneity of the film decreased with increment of the DBP ratio. This would then also be a disadvantage as the local properties of the films would be radically different, introducing uncertainty in the real value of porosity of the films. As the electrochemical responses of the films will depend on the porosity created (volume of porosity = space to

produce  $\text{Li}_2\text{O}_2$ ), inhomogeneity could lead to variations of the performances for the electrodes coming from the same batch. For this reason,  $\text{DBP}_{40}$  would be preferred as it displayed an initial homogeneous macro-porosity and composition, resulting in a similar homogeneity after extraction.

So, due to films inhomogeneity and closed porosity, the use of high DBP initial contents ( $> 60 \text{ w}\%$ ) did not appear as a relevant choice to reach homogeneous high porosity in carbon-based flexible electrodes. However, homogeneous films having high porosity (ca.  $50 \text{ v}\%$ ), bimodal meso/macro porosity, and high accessible carbon surface area (ca.  $50 \text{ m}^2 \cdot \text{g}_{\text{electrode}}^{-1}$ ) were fabricated while using moderate DBP content (e.g.  $\text{DBP}_{40}$ ).

Still, mastering the ratio between meso and macro porosities stroke as being difficult. Surely, initially the electrodes were macro-porous highlighting that the carbon did not define the carbon-polymer-DBP domain porosity. Also, as shown, the cleaning steps led to first creation of macro-porosity and then of meso-porosity. Finally, bi-modal structure was guaranteed, DBP removal giving access to the carbon surface. Still, the macro-pores/meso-pores ratio was not easily tuned, as spotlighted by the similar volume of meso-pores founded in the films though they had different initial DBP ratio (green bars in Figure IV. 15).

In the light of prior observations, it was then concluded that, as such electrode fabrication process enabled to produce homogeneous bi-modal electrodes while cautiously preparing them and when considering lower DBP ratios, their use could be transposed to LABs as well as other metal-air batteries. Still, it worth underscores that the process would not permit to achieve exactly the ratios predicted from the previous theoretical study. For that, another fabrication should be then developed as for instance using templating.

### ***IV.3.c. Behavior of the films in the electrolyte solvent***

As formerly shown, films had a tendency to shrink after DBP extraction. Then, prior to further test in electrochemical cell in presence of electrolyte (ether based solvent as TriGDME and TetraGDME were used), evolution of the film while immersed in ether was inspected.

Expansion was noticed while soaking the films  $\text{DBP}_{40}$  and  $\text{DBP}_{60}$  in ether (Figure IV. 17). An expansion of  $0.1 \text{ cm}$  was noticed for both formulations. Such swelling attested that the ether filled the electrode porosity and so will the electrolyte do.



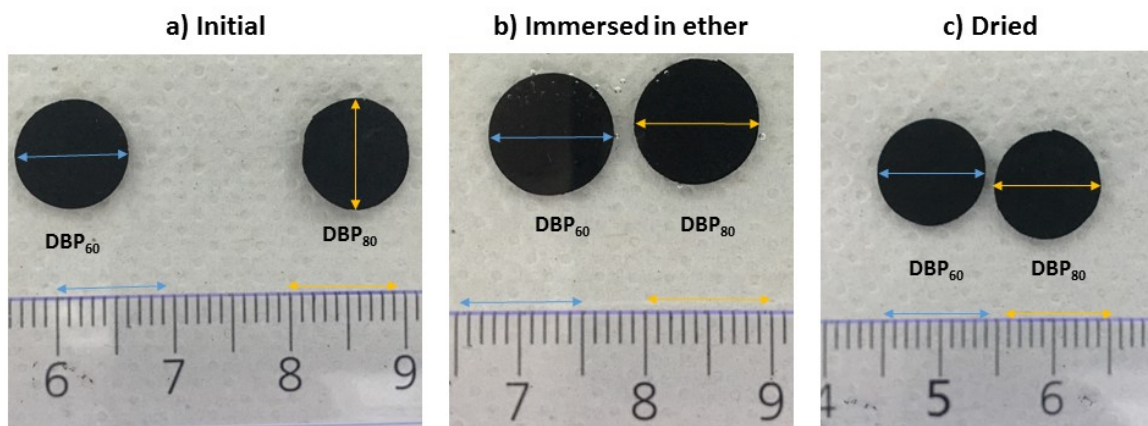


Figure IV. 17: Diameter evolution for disks (initially  $\varnothing=9$  mm) cut from extracted films  $DBP_{40}$  and  $DBP_{80}$  a) initially, b) immersed in ether and c) dried.

Still, a concern on binder swelling appeared, as this spread could be irreversible. To check it, the electrodes were dried. The final diameters (Figure IV. 17.c) of the disks were equal to the one of extracted films (Figure IV. 17.a). This meant that binder swelling should not be a concern. Indeed, same diameter expansion was demonstrated even though disk  $DBP_{60}$  contained more binder. For these reasons, volume expansion was linked only to the penetration of the ether inside the disk.

#### ***IV.3.d. Thermal behavior of the films at high temperature***

Due to the targeted application, thermal stability of the electrode was a highly prized characteristic. Actually, this property was emphasized by Du Pasquier *et al.* for this type electrode.<sup>140</sup> To certify it and to give idea of the range of stability, DSC measurements were applied to  $DBP_{80}$  film, before and after DBP removal, as shown in Figure IV. 18.



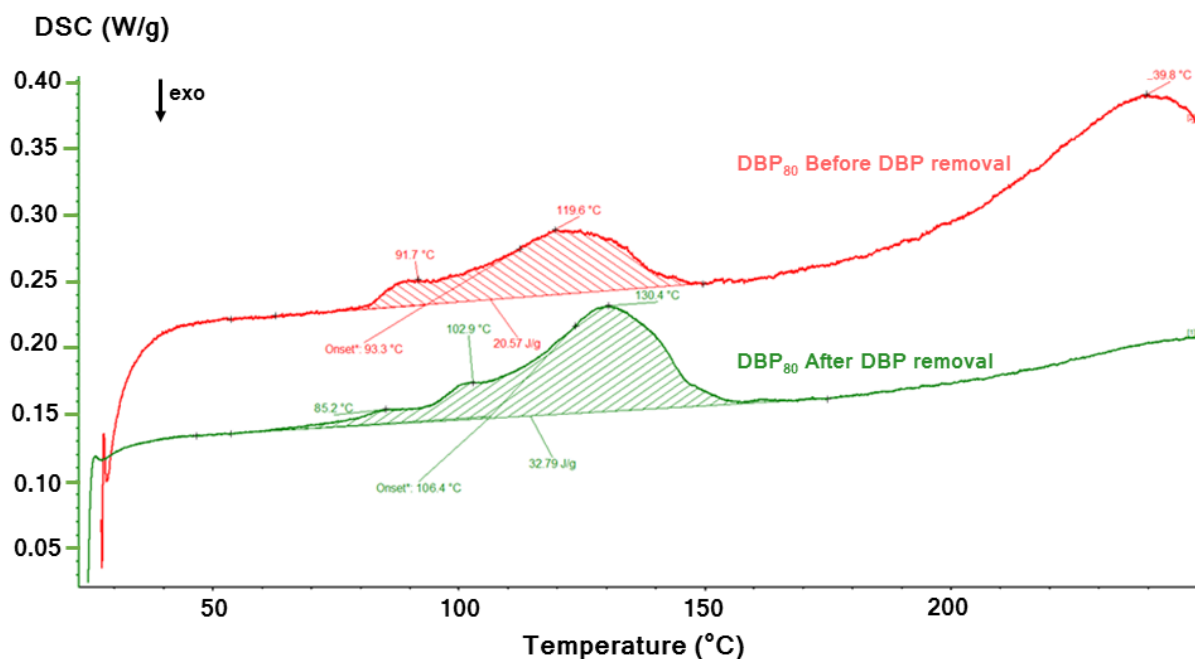


Figure IV. 18: DSC curves of DBP<sub>80</sub> before and after DBP extraction carried on under Argon at 5 K/min from 25 °C to 250 °C.

While PVdF-HFP melts at 115 °C, slightly lower temperatures were required in both exposed cases. The diminution of the stability was more probably due to the interactions existing between the carbon and polymer in the extracted films. Still, the temperature range achieved for the extracted films (until 85.2 °C) was of interest for aircraft application as the battery should support 80 °C during storage.

#### IV.3.e. Performances of the flexible porous carbon electrodes

As the goal of the study was to develop electrodes for LABs, the films were tested electrochemically. To clearly evaluate the performances and improvements required, the results were reported in Figure IV. 19 according to  $\text{mAh.g}^{-1}_{\text{electrode}}$  and  $\text{mAh.cm}^{-2}_{\text{electrode}}$ .

To analyze, the efficiency of the electrode utilization, the theoretical capacity of the electrodes was initially calculated assuming that all the porous volume of the electrode (70 % of porosity assumed for all films) could be filled by  $\text{Li}_2\text{O}_2$ . Obviously these values were overestimated as existence of some closed porosity was disclosed. Still, it provided a first estimation of the gap between practical (Figure IV. 19) and theoretical capacities. It was estimated that  $2699 \text{ mAh/cm}^3_{\text{void}}$  could be achieved by the  $\text{Li}_2\text{O}_2$  production in the porous volume over discharge. Once applying it to the volume and mass of practical electrodes the

theoretical capacities were 3265 mAh/electrode for DBP<sub>40</sub>, 3353 mAh/electrode for DBP<sub>60</sub> and 3420 mAh/electrode for DBP<sub>80</sub>.

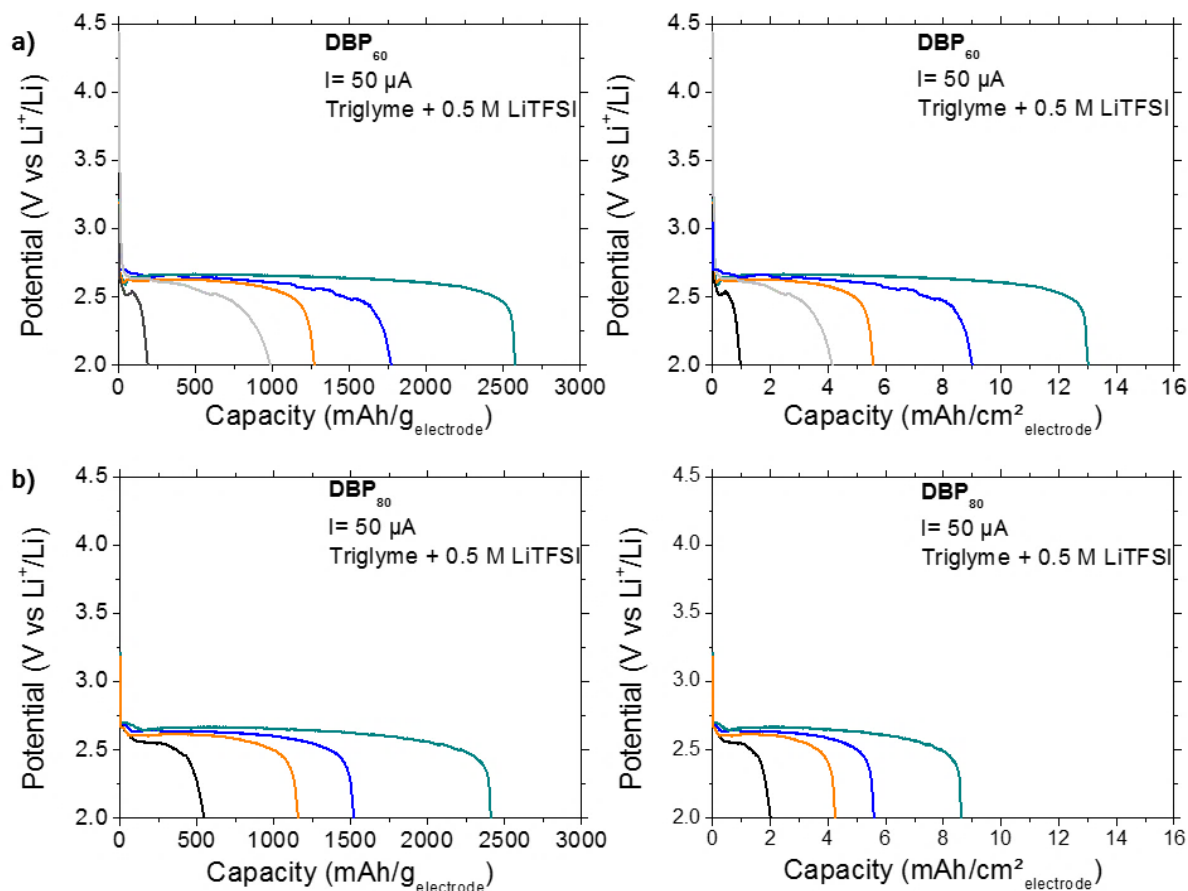


Figure IV. 19: Discharge curves of the Swagelok cells made using electrodes cut from a) DBP<sub>60</sub> and b) DBP<sub>80</sub> films at 50  $\mu$ A while in TriGDME + 0.5 M LiTFSI, reported in  $\text{mAh.g}^{-1}_{\text{electrode}}$  and  $\text{mAh.cm}^{-2}_{\text{electrode}}$ . Each color corresponds to the results obtained for the same cell.

Actually, the best performances of DBP<sub>60</sub> and DBP<sub>80</sub> electrodes finally corresponded to 80 % and 70 % of the respective theoretical capacities. This meant that the flexible electrodes produced are efficient electrodes for LABs.

However, in parallel, 6 % and 16 % of the predicted capacities were reached in the worst cases (cases corresponding to the lowest capacities in mAh/g and mAh/cm<sup>2</sup><sub>electrode</sub>). At first sight, the lack of reproducibility was overwhelming. Certainly, the capacities, initial curve shapes and overpotentials of the several curves were strikingly different.

At higher current, DBP<sub>40</sub> was tested and as expected it led to lower capacities (Figure IV. 20). Indeed, the gap between recorded and theoretical capacities was noteworthy. This highlighted the strong sensitivity of LABs toward the current density and oxygen diffusion

limitation. Same as for the other films, reproducibility issues were also noticed (here capacities were doubled from one experiment to another).

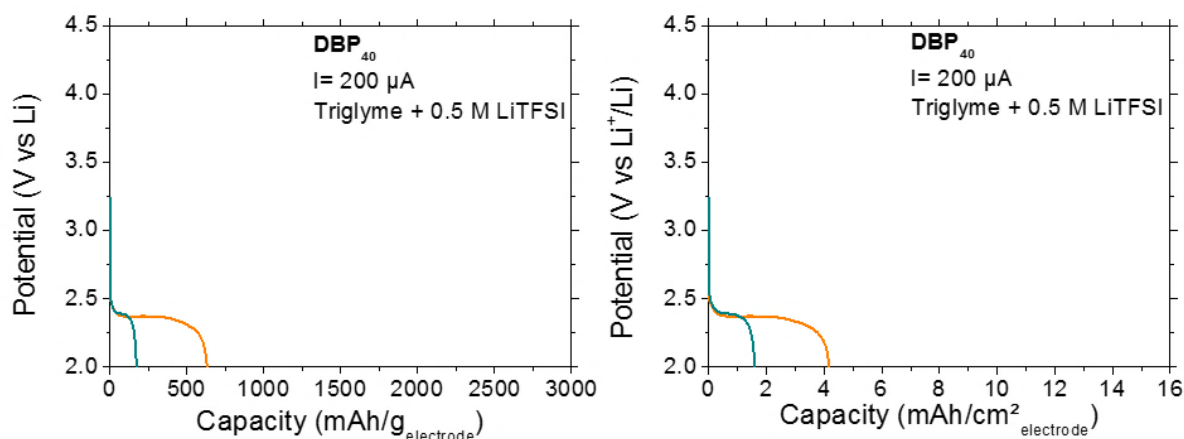
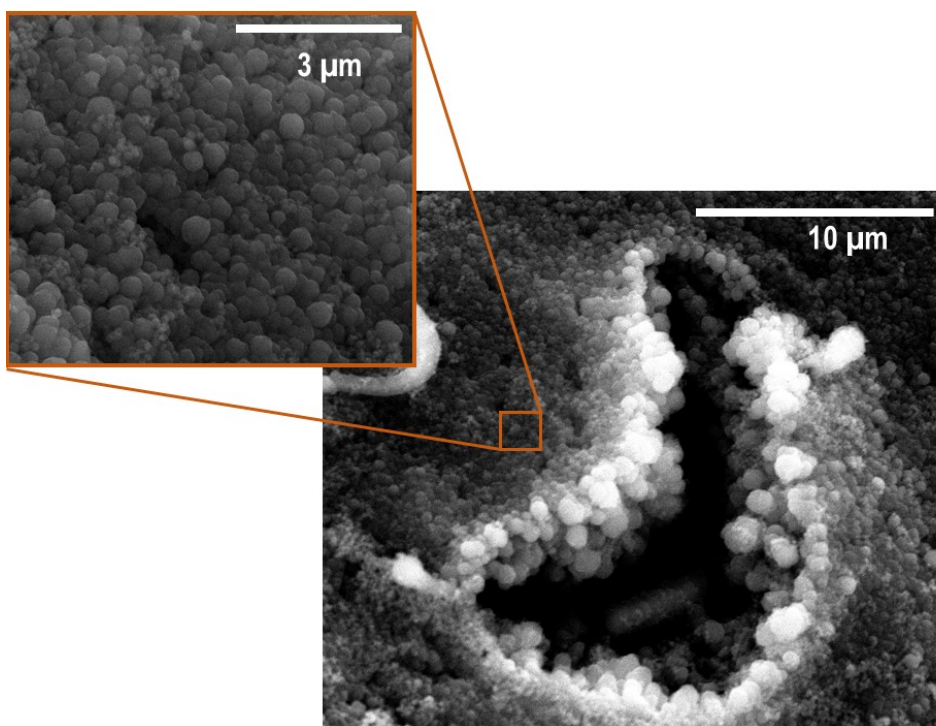


Figure IV. 20: Discharge curves of the Swagelok cells made using electrodes cut from films  $DBP_{40}$  at  $200 \mu A$  while using TriGDME + 0.5 M LiTFSI as the electrolyte reported in a)  $mAh.g^{-1}_{electrode}$  and b)  $mAh.cm^{-2}_{electrode}$ .

The lack of repetitive results impeded then to reach any further conclusion. Actually, few papers in literature mentioned the lack of reproducibility from which LABs are suffering, even though, sensitivity of LABs toward discharge product morphology was quoted many times.<sup>54,81,169,171,172,179,190</sup> Thankfully, Griffith *et al.* nicely illustrated the “inherent random variability of  $Li_2O_2$  cells” and correlated it to the discharge product morphology.<sup>171</sup> Then, to continue the study, morphology of the discharge electrodes was examined to see if in this case it could explain the large gaps observed between the same experiments.

### IV.3.f. Discharge product formation

Discharge product was firstly studied in case of  $DBP_{60}$ . One electrode was observed by SEM to check formation of the discharge product at its surface (Figure IV. 21). Creation of spherical particles, with various sizes depending on the position on the electrode surface, was notified on all the electrode surface. It undoubtedly stroke in Figure IV. 21 that larger spheres were produced at the edges and inside the electrode macro-pores. On the contrary, on the meso-porous part a dense film made of smaller spheres were discerned. From these observations, it was clearly seemed that macro-porosity helped to enhance the efficiency of discharge reaction as anticipated from the theoretical study.



*Figure IV. 21: SEM pictures taken from electrode DBP<sub>60</sub> previously discharged until 2 V at 50 μA in TriGDME + 0.5 M LiTFSI. The corresponding capacities values are 2372 mAh/g<sub>electrode</sub> and 12 mAh/cm<sup>2</sup><sub>electrode</sub>.*

Since, formation of a product was noticed on the electrode surface, determination of its nature was required to clearly affirmed that it was the discharge product. Therefore, XRD tests were launched to determine if crystalline Li<sub>2</sub>O<sub>2</sub> was formed on the surface (Figure IV. 22).

XRD diagram of the DBP<sub>60</sub> electrode after full discharge was compared to the diagram of the hardware (XRD holder with a beryllium window containing a non-discharge electrode). Two pics seemed to correspond to Li<sub>2</sub>O<sub>2</sub> (around 32 and 35 °2θ) even if their intensity seemed overwhelming by the other pics intensity. This difference of intensities could be explained by the few amount of Li<sub>2</sub>O<sub>2</sub> formed compared to the other components of the electrode and even more compared to the beryllium sample holder.

Even though Li<sub>2</sub>O<sub>2</sub> was detected in its crystalline form, it could also have been formed in its amorphous phase too. Actually, literature report formation of both phases in LABs.<sup>190,232</sup> Formation of both phases could give an explanation of the small intensity of the pics observed. At least, production of Li<sub>2</sub>O<sub>2</sub> was certified. Thus, the observed particles formed on the electrode surface (Figure IV. 21) were attributed to discharge product formation.

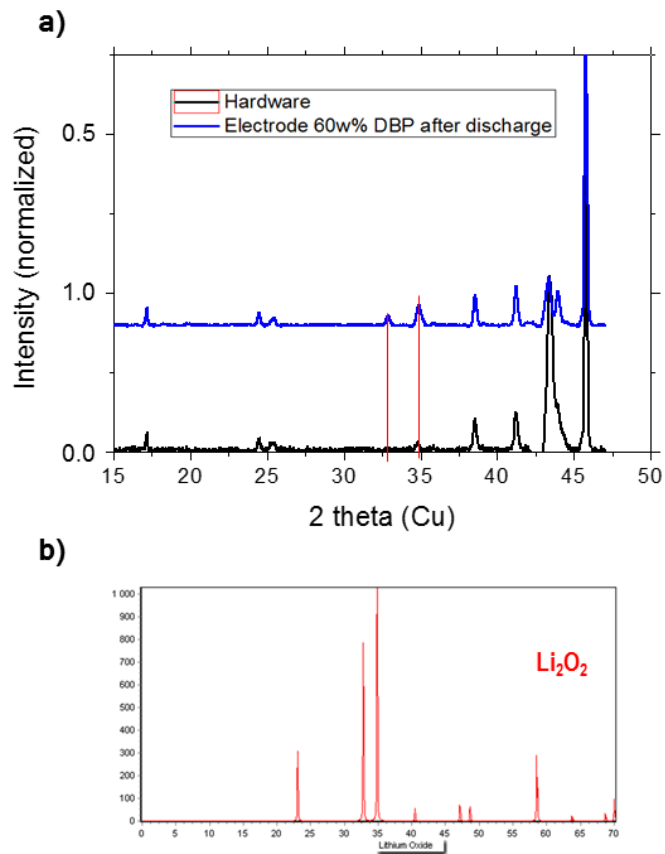
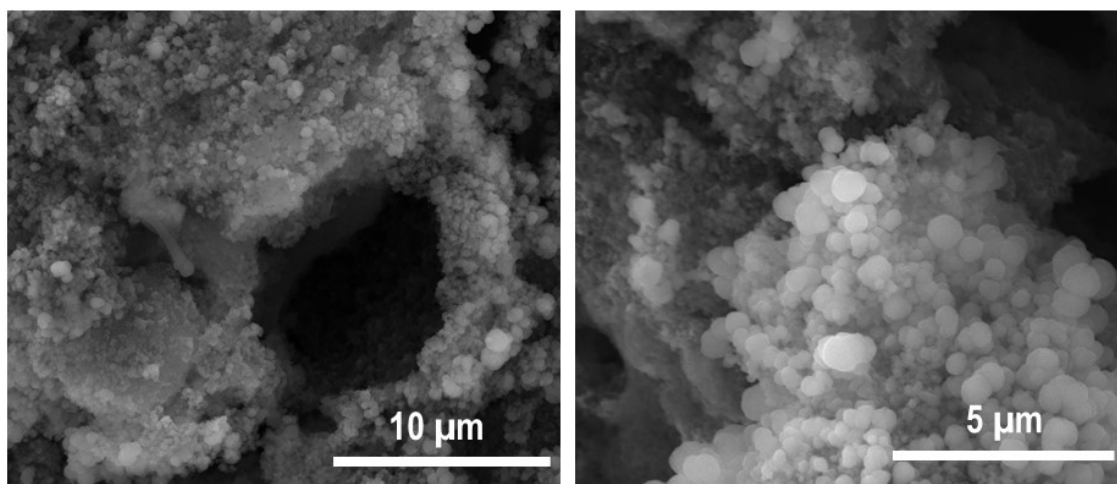


Figure IV. 22: a) XRD diagram of a  $\text{DBP}_{60}$  electrode not discharge (bleu) and XRD diagram of a  $\text{DBP}_{60}$  discharge electrode compared to b) XRD diagram of crystalline  $\text{Li}_2\text{O}_2$ .

An electrode from  $\text{DBP}_{80}$  was also analyzed by SEM trying to see if noticeable results were found compared to the  $\text{DBP}_{60}$  case (Figure IV. 23) which was discharge at once until 2 V.  $\text{DBP}_{80}$  on the reverse was discharged by repetitive sequences of ten hours of discharge and four hours of resting to enable evaluation of the impedance spectra evolution over discharge. The EIS results clearly shown an increase of charge transfer over discharge, which could corroborate the deposition of a passivating product as  $\text{Li}_2\text{O}_2$ .



*Figure IV. 23: SEM pictures taken from electrode DBP<sub>80</sub> previously discharged until 2V (by consecutive repetition of ten hours of discharge, four hours of resting and EIS measurement between each cycle) at 50  $\mu$ A in TriGDME + 0.5 M LiTFSI. The corresponding capacities values are 1326 mAh/g<sub>electrode</sub> and 9 mAh/cm<sup>2</sup><sub>electrode</sub>.*

While SEM pictures for DBP<sub>60</sub> demonstrated the formation of densely packed particles with large spheres in particular at the macro-pores edges, more homogeneous repartition of the particles sizes was noted for DBP<sub>80</sub>. Forsooth, this might come from the lower discharge capacity achieved with this electrode and thus to the lower Li<sub>2</sub>O<sub>2</sub> production and growth.

Also, this particular DBP<sub>80</sub> electrode suffered significantly from deformations as illustrated in Figure IV. 24. Even though the electrode thickness was preserved (while comparing to the thickness in Figure IV. 24 to the one after DBP removal in Figure IV. 13), the flexible electrodes clearly suffered from compression. The other electrode from DBP<sub>60</sub> was also distorted but to a lesser extent. As the DBP<sub>80</sub> thickness was preserved, the compression sensibility was not attributed to the electrode expansion and thus to the electrode formulation. These alterations must occur during the celling of the Swagelok as the grid seemed to pierce the electrodes with different intensity. As the celling was manually done in Swagelok, the pressure applied to the cell were modified from one to another experiment.

Due to the large deformation of the films, the electrochemical results should be revised. The distinct deformation of the films compressed by the grid could also explained the discrepancy of the discharge curves as the surface developed at the oxygen inlet side, as well as, the electron collection would be totally different depending on the compression applied.



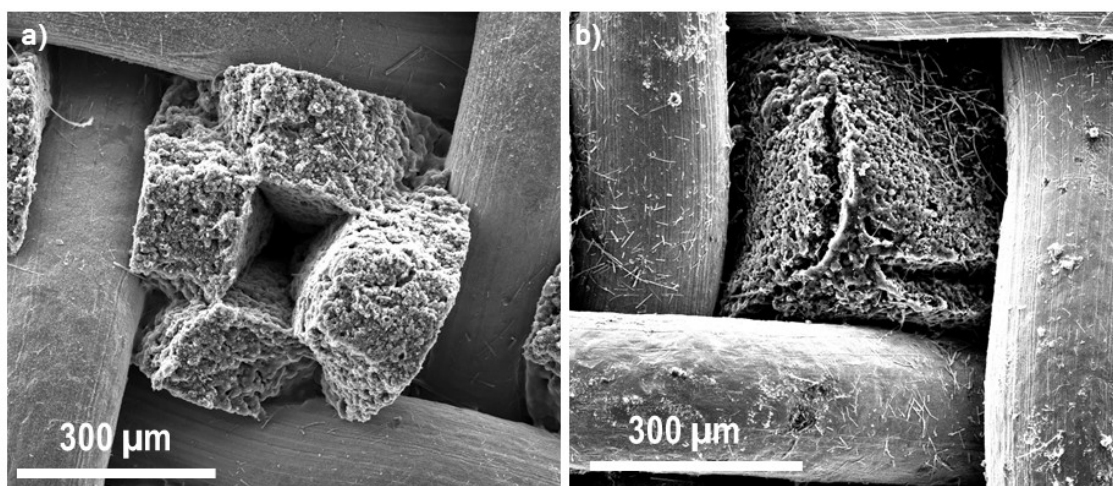


Figure IV. 24: Deformation of films a)  $DBP_{80}$  and b)  $DBP_{60}$  as seen in SEM pictures.

### *IV.3.g. Merging of theory with experiments*

Along the two last chapters, two main axes were followed: modeling study and experimental implementation of electrode fabrication for LABs. Still, worth spotlight that these two approaches were indivisible as they feed each other. Indeed, while the model need experimental parameters to be built it gave advice on electrode formulation like the macro-porous volume ratio to target (from 20 % to 50 %) for enhanced results.

Achievement of practical bimodal electrode was then demonstrated using the so-called Bellcore process. Both meso-porosity and macro-porosity were noticed in the films produced and porosity could be tuned using the DBP ratio. High efficiency of the electrode porosity utilization was proven in several cases. Still, high DBP ratios demonstrated their limits due to some chemical inhomogeneity. Also, decorrelation of the meso/macro porosity creation was not straight forward using this fabrication process. To finish, the electrode performances were shown to be linked to the compression applied to the electrodes.

In addition, at the light of the discharge product formed on top of the electrodes, one assumption used in the model could be questioned. Actually, utilization of thin film formation hypothesis could be criticized, as in experiments two sizes of discharge product were witnessed in  $DBP_{60}$ . Still, the choice to overlook the particle size distribution was made in the theoretical study due to the complexity of the model to settle in order to achieve it. Impact of particle sizes distribution was studied with coworkers thanks to two models (one for charge and one for discharge).<sup>117,233</sup> This part of the work was attached to Y. Yin thesis.<sup>209</sup>

Unfortunately, reproducibility issues did not permit to precisely determine the electrochemical performances of the designed electrodes. In an attempt to improve the repeatability of the experiments, several trials were implemented to have an enhanced control of the operating conditions.



# CHAPTER V: REPRODUCIBILITY ISSUES AND SENSITIVITY TO OPERATING CONDITIONS

## Contents

---

V.1. Lab reproducibility issues.....	134
V.1.a Description of the reproducibility issues.....	134
V.1.b. Attempts to reduce the uncertainty.....	134
V.2. LABs sensitivity toward operating conditions.....	146
V.2.a. Temperature and current effects on discharge capacity.....	146
V.2.b. Temperature and current effects on discharge product morphology.	149
V.3. LABs high sensitivity toward electrode surface.....	161
V.4. Conclusions on LABs reproducibility issues.....	164

---

## V.1. Lab reproducibility issues

### V.1.a Description of the reproducibility issues

Formerly, discrepancy of the discharges curves shapes and capacities was observed for self-standing electrodes (Figure V. 1).

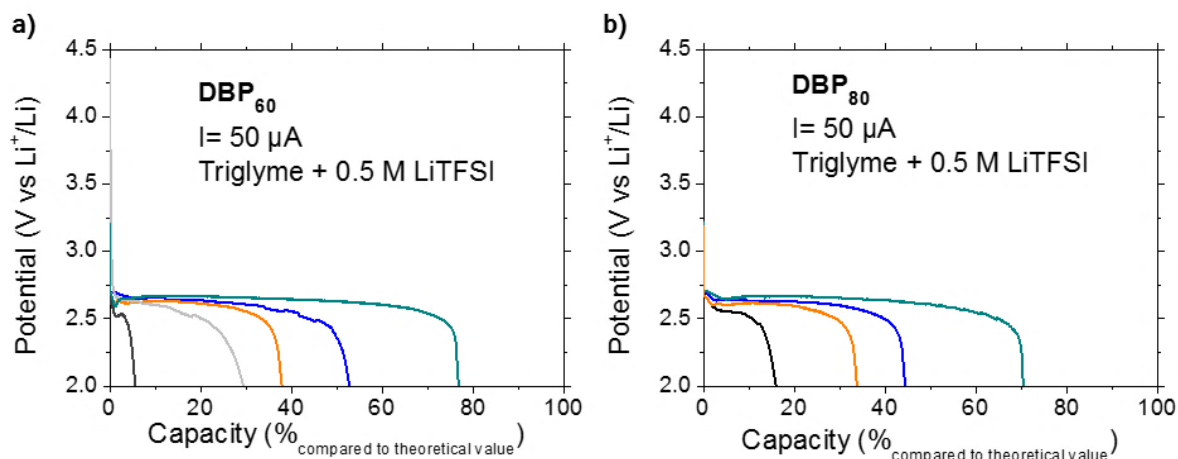


Figure V. 1: Discharge curves of the Swagelok cells made using electrodes cut from films a) DBP<sub>60</sub> & b) DBP<sub>80</sub> at 50 μA while using TriGDME + 0.5 M LiTFSI as the electrolyte. The results are reported in percentage compared to the 3353 mAh.g<sup>-1</sup><sub>electrode</sub> and 3420 mAh.g<sup>-1</sup><sub>electrode</sub> expected from the theoretical point of view.

Some local inhomogeneities of the films induced by the home-made process, in addition to deformation/compression occurring while assembling the Swagelok could explain the dispersion of the results. Still, to ensure that the variability of the results was not also due to other parameters, a progressive enhanced control of the operating conditions was settled.

### V.1.b. Attempts to reduce the uncertainty

#### Enhanced control of the electrolyte addition step and oxygen supply

The first change operated was to precisely measure the volume of added solvent. While initially twenty drops of solvent were counted using a glass Pasteur pipet, after the results were get after adding precisely 325 μL of electrolyte thanks to a micro-pipette. Moreover, while initially a pressure gauge positioned at the oxygen delivery was controlling the oxygen flow, a flowmeter was added to strengthen the oxygen flow management. For the DBP<sub>60</sub> film prepared with longer grinding step, some experiments were repeatedly implemented to follow the effects

of such changes on results variance. The resulting discharge curves were plotted in Figure V. 2 and compared to previous experiments less controlled.

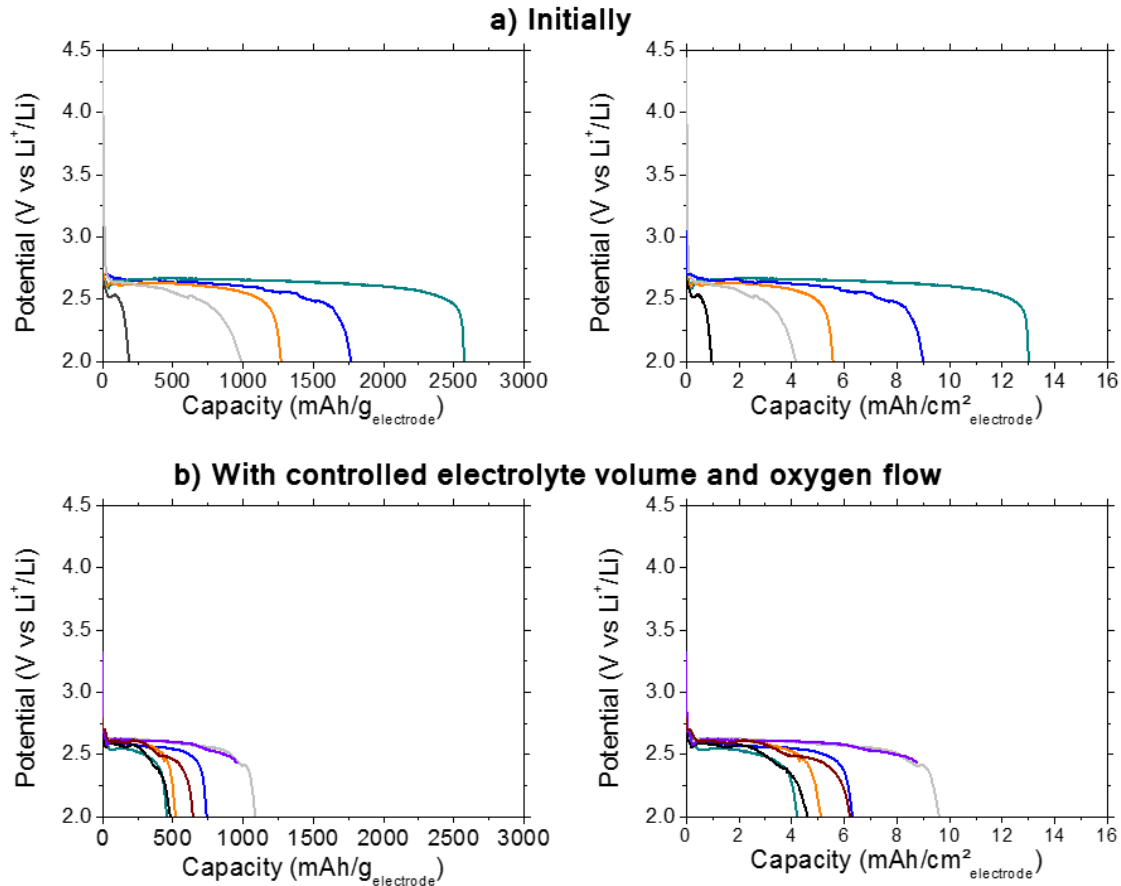


Figure V. 2: Discharges curves of DBP<sub>60</sub> cells cycled at 50  $\mu$ A between 2 to 4.5 V with distinct cell preparation procedures. Capacities expressed in mAh/g<sub>electrode</sub> and mAh/cm<sup>2</sup><sub>electrode</sub>.

The new parameters led to lower mean capacities values (696 mAh/g<sub>electrode</sub> and 6.40 mAh/cm<sup>2</sup><sub>electrode</sub> compared to 1359 mAh/g<sub>electrode</sub> and 6.54 mAh/cm<sup>2</sup><sub>electrode</sub> previously). Still, a beneficial impact was observed on the standard variation value as it was divided by 3 and 2 (respectively for capacities in mAh/g<sub>electrode</sub> and mAh/cm<sup>2</sup><sub>electrode</sub>).

For this reason, from now all the results presented were obtained using cells that have:

- been flushed in exact same conditions (thirty minutes of oxygen flow at 1.5 L.h<sup>-1</sup>),
- exactly the same amount of electrolyte (325  $\mu$ L).

Still, this spare progress came along with complex and various initial discharge shapes which would be inspected in next part to see if correlation exists between them and the discharge capacities.

### Observations of the discharge curves characteristics

Prior to modify the experimental conditions, the already obtained discharge plots were compared to determine if the curves characteristics could point out possible trends. While scrutinizing more specifically the initial part, some clear dips were observed. In a previous study implemented at the LRCS, the dips noticed were clearly linked to the  $\text{Li}_2\text{O}_2$  nucleation.<sup>233</sup> As initially highlighted by Köhler's theory,<sup>234</sup> the nucleation step requires a certain quantity of energy to accumulate enough reactant to trigger the precipitation and thus the nuclei formation. Once nuclei are formed, particles growth could start as predicted by the classical nucleation theory (CNT) (Figure V. 3).<sup>235</sup>

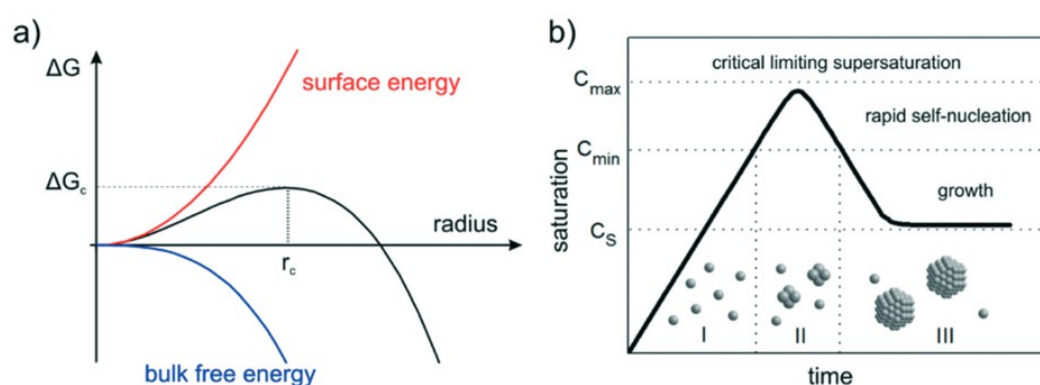


Figure V. 3: a) Free energy diagram for nucleation and b) corresponding nucleation of metal nanoparticles as described by Polte.<sup>235</sup>

To see if nucleation mechanisms could explain the discrepancy, the dips were compared (Figure V. 4). Two different patterns were identified while analyzing the plots before the main discharge plateau. In some cases, two consecutive plateaus were observed (Figure V. 4.a.). In others, apparition of a first plateau tailed by a dip was noticed (Figure V. 4.b.). Unfortunately, no obvious correlations between the discharge efficiency and the plot shape was evidently identified. At least, it was noticed that nucleation likely took place.

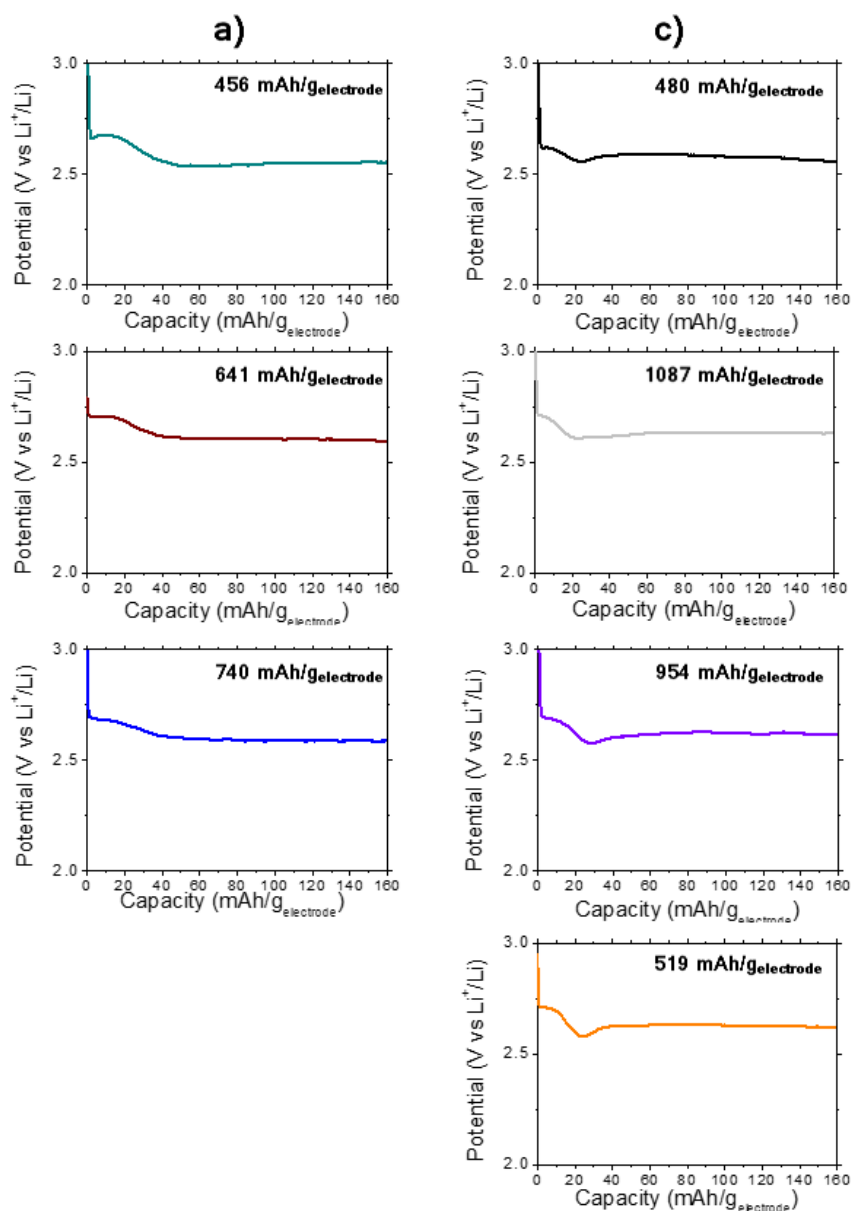


Figure V. 4: Zoom of the initial part of the discharge curves of  $DBP_{60}$  cells cycled in  $TriGDME + 0.5 M LiTFSI$  at  $50 \mu A$  between 2 to 4.5 V.

Then, other possible correspondences were searched. As the discharge plateau overpotential was evolving depending on the case, discharge capacities were compared to the potential at half first discharge, to see if the lower performances were due to higher system overpotential (Figure V. 5). Higher overpotential traduced higher system resistance and so some variations could be founded depending on the electrode itself, the electronic percolation and contact resistance and even on the cell assembling. No straight links appeared while comparing these two parameters. Then the cell overall resistance was not responsible for the difference of performances.

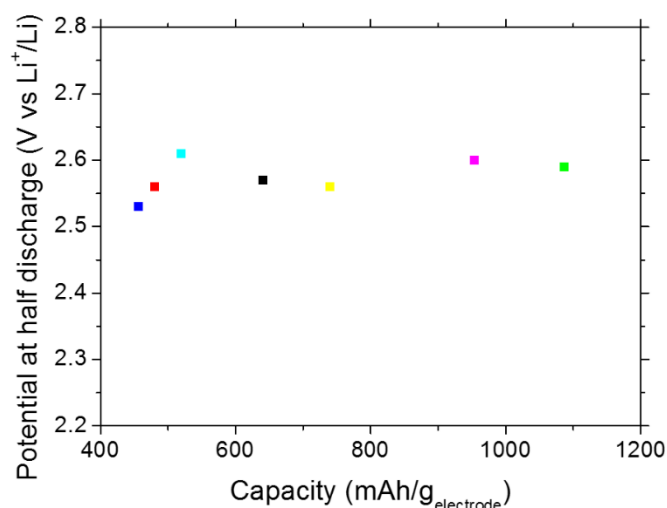


Figure V. 5: Comparison of potentials at half first discharge for DBP<sub>60</sub> cells cycled in 325  $\mu$ L of TriGDME + 0.5 M LiTFSI at 50  $\mu$ A between 2 to 4.5 V after thirty minutes of precisely controlled oxygen flow.

Finally, no clear pattern linked the discharge capacity to the overpotential. This infringed to make more advanced conclusions. Still, while scrutinizing the curve at smaller scale, two-hour period oscillations were perceived as highlighted in Figure V. 6.

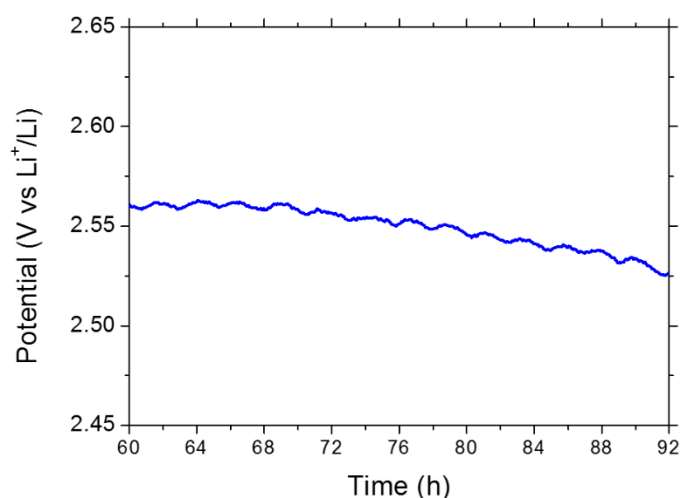


Figure V. 6: Zoom in discharges curves in case of a DBP<sub>60</sub> cell cycled in 325  $\mu$ L of TriGDME + 0.5 M LiTFSI at 50  $\mu$ A between 2 to 4.5 V after thirty minutes of precisely controlled oxygen flow.

After recording the temperature evolution in the cycling room, similar oscillations (same period) in temperature were recorded and attributed to the air cooling system (Figure V. 7) as oscillations variations were spread from 18.4 to 20.2  $^{\circ}$ C.

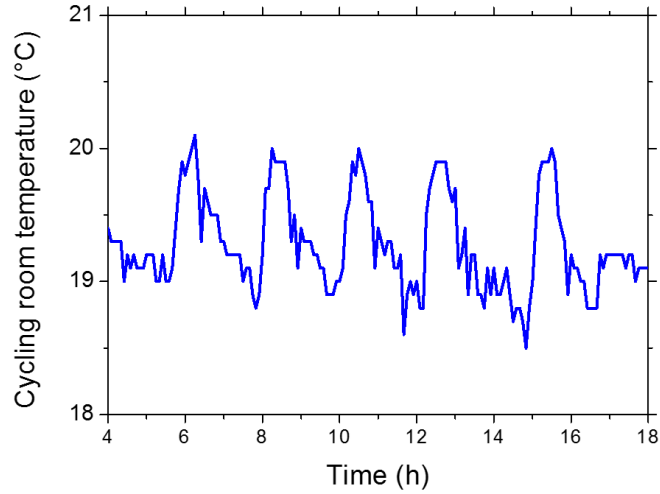


Figure V. 7: Room temperature evolution around the “Le Parfait” containers in the cycling room.

The control of the operating temperature at 25 °C enabled to suppress the oscillations as pointed out in Figure V. 8.

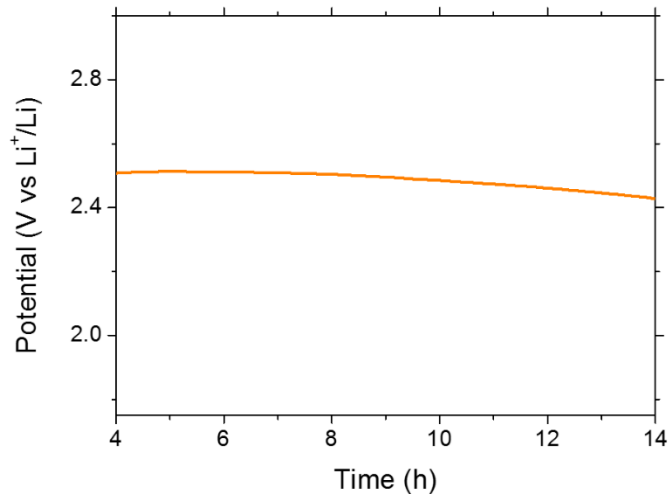


Figure V. 8: Removal of the discharge voltage oscillations thanks to temperature control at 25 °C.

For these reason, mastering the temperature to which the cells were exposed was of paramount importance as significant oscillations in voltage were induced with only 2 °C of difference. This spotted the strong sensitivity of LABs toward temperature and suggested strong kinetics limitations.

### *Enhanced control of the operating temperature and electrode mechanical stability*

In an attempt to reduce the uncertainty of the cells operation, the first measure was then to control the temperature. The operation temperature control was managed using a stove in which the VSP cables were inserted. As the stove did not possess cooling system, the temperature set should be higher than the cycling room one, explaining why 25 °C was selected at first as the operating temperature. Later, only higher temperatures were applied to the cell for the same reason. Prior to launch the electrochemical tests, two hours of resting time in the stove were always assigned to the cells for the sake of temperature homogenization. Along this step, the OCV was stabilized, implying that enough resting time was applied.

In parallel, the second measure taken was the modification of the electrodes. As previously spotted, bi-porous electrodes suffered from compression. During post-mortem analysis, the deformed electrodes stuck to the grid due to strong deformations. Then, Bellcore-like electrodes were replaced by electrodes, named GDLs, that could undergo the compression step. Made of carbon fibers interlaced, GDLs promote good electronic conductivity and were homogeneously produced thanks to an industrial process. Even though GDL could be compressed as spotted in the fuel-cell field,<sup>236-238</sup> GDL electrodes were reversibly deformed which facilitated their observation at SEM once pulling them out from the stainless steel grid. A significant advantage of GDLs was also their porosity (66 %) comparable to bi-porous electrodes overall porosity. Thanks to their properties GDLs were then good candidate to make comparisons with previous electrodes.

In opposition to what was supposed, using GDLs (more homogenous and bearing compression) in the more controlled conditions did not solved the reproducibility issues (Figure V. 9).



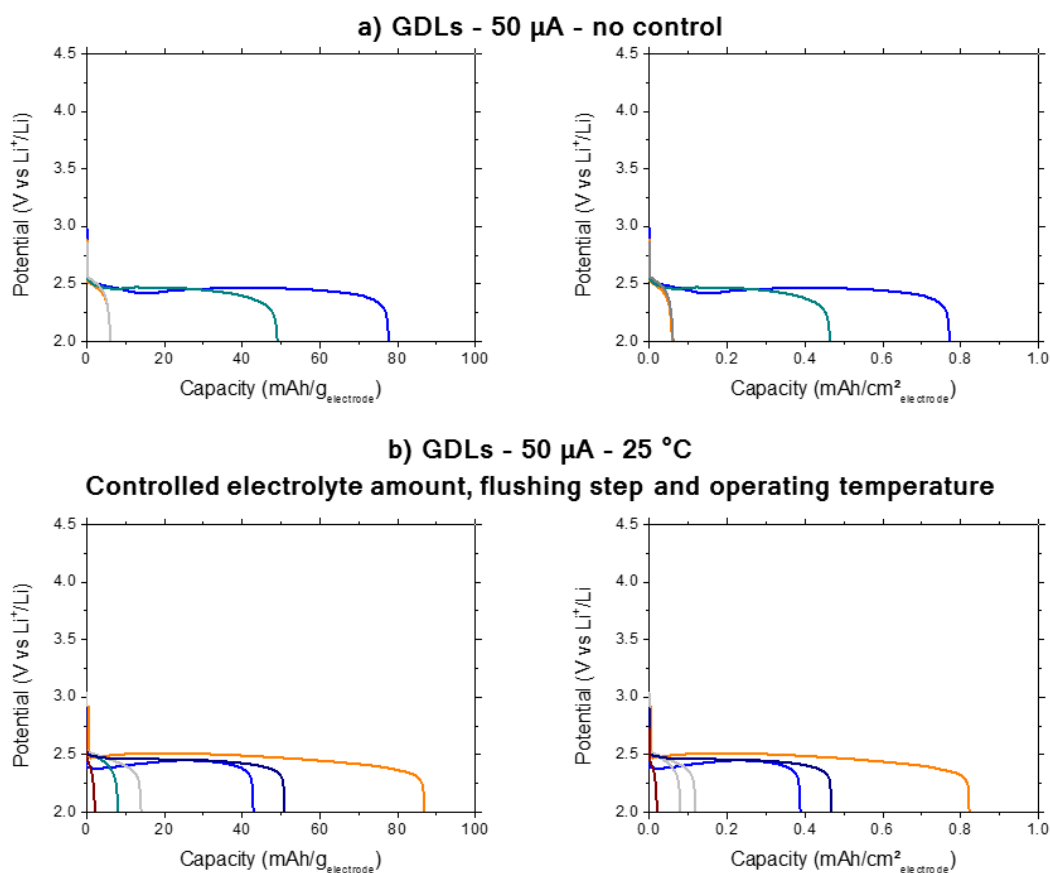


*Figure V. 9: First discharges of GDLs cells cycled in TriGDME + 0.5 M LiTFSI at 50  $\mu$ A between 2 to 4.5 V in a) not controlled conditions and b) controlled conditions (25 °C). Capacities were expressed in mAh/g<sub>electrode</sub> and mAh/cm<sup>2</sup><sub>electrode</sub>.*

Indeed, with or without controlled conditions, reproducibility issues remained, leading to two types of discharges responses. Either the cells were able to discharge for some time or they suffered from fast capacity fading. Air leak was rejected as a potential explanation for the capacity drop, as after a trial similar to Figure V. 9.a. but at 25  $\mu$ A, one cell was on purpose exposed to air (corresponding to the grey curve in Figure V. 10). The cell exposed was characterized by an approximate “middle” value of capacity, as well as, a lower and less stable plateau. Thus, if discharge was due to air leak, same curve shape should have been observed. This led to the conclusion that another phenomenon was taking place.

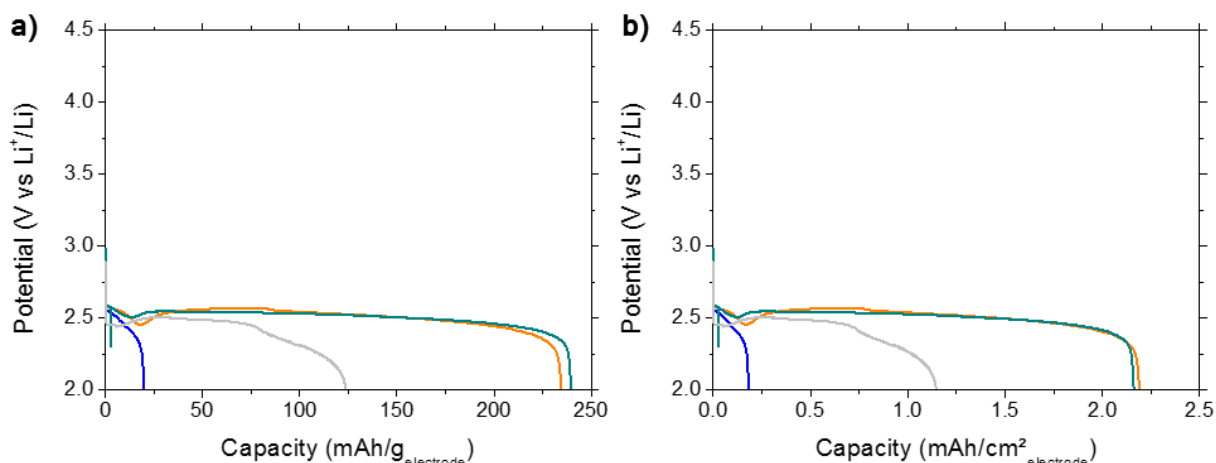


Figure V. 10: First discharges of GDLs cells cycled in TriGDME + 0.5 M LiTFSI at  $25 \mu\text{A}$  between 2 to 4.5 V in not controlled conditions. Only the cell with the grey curve was exposed to air. Capacities expressed in a)  $\text{mAh/g}_{\text{electrode}}$  and b)  $\text{mAh/cm}^2_{\text{electrode}}$ .

Results with GDLs appeared to be even worse than home-made electrodes (mean value of  $34.8 \text{ mAh/g}_{\text{electrode}}$  for a standard deviation of  $28.6 \text{ mAh/g}_{\text{electrode}}$ ). Indeed, this time, while comparing the achieved gravimetric capacities to theoretical value, less than 5 % was attained (Figure V. 11). Besides, GDLs had approximately the same porosity than the flexible bi-porous electrodes and thus similar theoretical capacity based on the volume available for  $\text{Li}_2\text{O}_2$  production. Still, this value should be nuanced for GDL as low carbon surface was developed and thus lower discharge capacity could be attained compared to electrode design with enhanced porous volume utilization. This comforted the idea that special texture of the electrode such as the described bi-porous electrodes is required to develop efficient LABs electrodes.

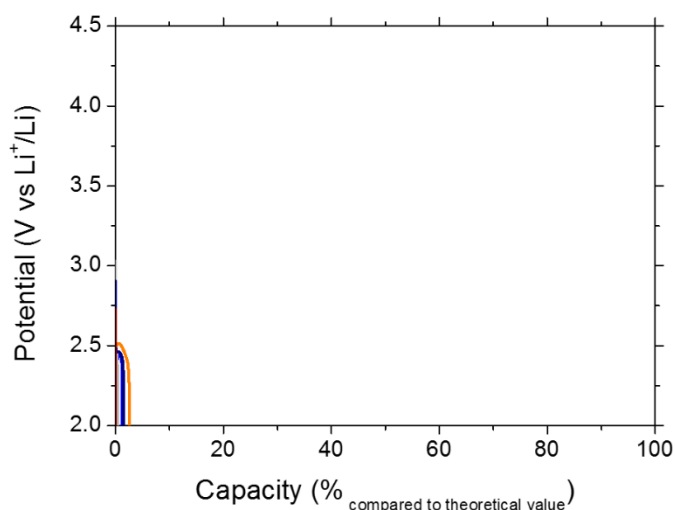


Figure V. 11: Discharge curves of the GDLs cells at  $50 \mu\text{A}$  in controlled conditions while using TriGDME + 0.5 M LiTFSI as the electrolyte. The results are reported in percentage compared to the  $3402 \text{ mAh.g}^{-1}_{\text{electrode}}$  expected from the theoretical point of view.

Moreover, another parameter could have explained the lower GDLs performances compared to flexible bi-porous electrodes and the larger gap between the several curves: the electronic conduction. Indeed, in GDLs few contact points existed between the fibers limiting the overall electronic conduction and the electron collection at the grid level (Figure V. 12). On reverse, the flexible bi-porous electrodes were made of a highly divided carbon (Figure V. 12) which ensured the electronic percolation, even if the electrode was deformed. This way, GDLs performed not as well as flexible bi-porous electrodes.

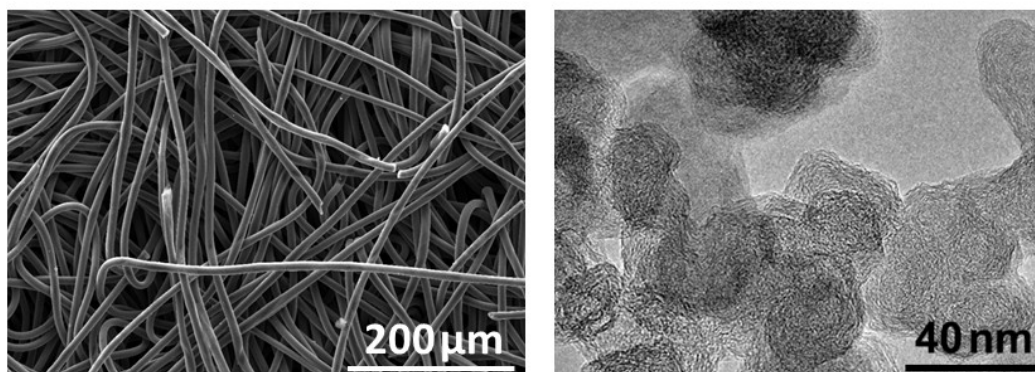


Figure V. 12: SEM pictures of a) GDL electrode and TEM picture of b) Ketjen black powder. (Ketjen Black TEM results courtesy of Pr. D. Larcher).

To sum-up, the lower capacities of GDLs could be easily understood from surface developed and electronic conduction point of view. Still, they clearly suffered from significant reproducibility issues and so other parameters such as water contamination could also lead to non-reproducibility.

### *Enhanced control of water contamination*

Effect of water contamination can affect the cells functioning as illustrated in literature. Meini *et al.* nicely showed that water contamination (ppm) influenced considerably the first cell discharge. Surprisingly, even if the cell was only in presence of 250 ppm of water, the capacity was strongly enhanced.<sup>175</sup> Same drift was later recovered by Cho *et al.* with water traces.<sup>176</sup> Schwenke *et al.* initially attributed this improvement to the direct formation of LiOH, while finally moving toward the assumption that Li<sub>2</sub>O<sub>2</sub> was actually reacting with water leading to LiOH formation.<sup>179</sup> Guo *et al.* observed that until 15 %RH, the first discharge was enhanced compared to dry oxygen and confirmed the formation of LiOH in addition to Li<sub>2</sub>CO<sub>3</sub> and Li<sub>2</sub>O<sub>2</sub> by combining XRD and FTIR techniques.<sup>177</sup>

Based on such findings, the results captured earlier (Figure V. 9) could be revised. Indeed, the separation of the discharge in two types: either long or short first discharges could be attributed to water contamination. Still, as shown previously, the water contamination was not coming from air leak. Then, the most probable source of water was the electrolyte. In reality, even if all the salt and solvent were only opened in glovebox with controlled atmosphere, they could have been contaminated by exposure to scarce water traces in the glovebox.

Then, to identify if water was responsible of such results, the electrolyte (TriGDME + 0.5 M LiTFSI) was dried overnight using molecular sieve. Its water content evolved from 118 ppm to less than 3 ppm. Significant decrease of the discharge capacity was then reached, confirming the water impact as described in literature (Figure V. 13).

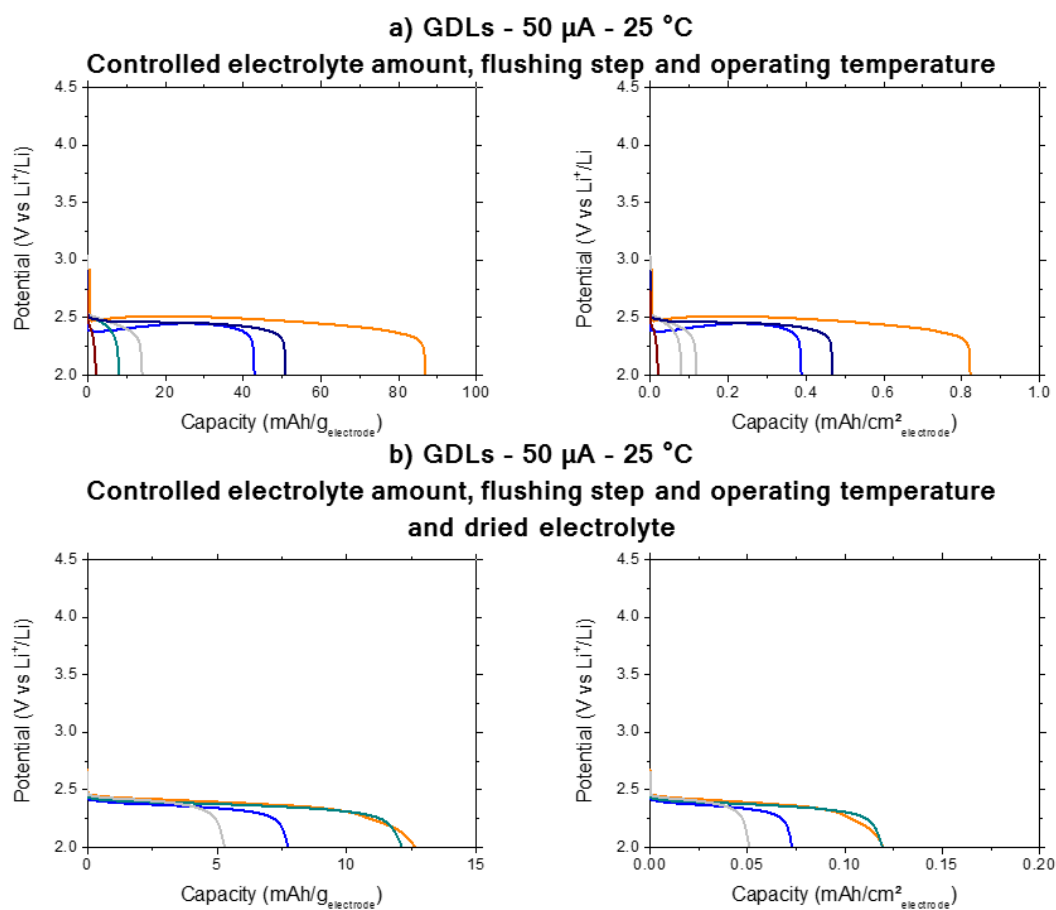


*Figure V. 13: First discharges of GDLs cells cycled at 25  $^{\circ}$ C in TriGDME + 0.5 M LiTFSI at 50  $\mu$ A between 2 to 4.5 V Capacities expressed in a) mAh/g<sub>electrode</sub> and b) mAh/cm<sup>2</sup><sub>electrode</sub>.*

The mean discharge value was reduced to 9.4 mAh/g<sub>electrode</sub> and standard deviation was estimated at 2.9. As standard deviation expressed the disparity of the results, it was concluded that reproducibility of the experiments was improved by removing the water traces. Starting

from there, and due to the LABs sensitivity toward the described parameters, all further experiments were always executing with:

- Perfectly controlled electrolyte addition,
- Precisely fixed oxygen flushing step,
- Controlled operating temperature,
- Strict water removal.

Behaviors of the cells and discharge product morphology get at several temperatures and currents values were accurately studied. GDLs electrodes were used for the rest of the study due to their mechanical resistance and reproducibility from one sample to another. Also, GDLs enabled to clearly see the formation of discharge product depending on the conditions applied.

## V.2. LABs sensitivity toward operating conditions

Application of LABs in aeronautical conditions required a certain stability of the system toward temperature changes. Still, it was demonstrated that LABs were impacted by slight temperature evolution (only 2 °C were sufficient to affect their behavior as shown in Figure V. 6). Besides temperature, another important parameter to study was the current applied to the system as it traduced the power that could be delivered by the cells. Same way as temperature, the current influenced considerably the electrochemical performances as shown when comparing Figure V. 9. These was easily explained by the correlation existing between current and oxygen diffusion. With too high current values, oxygen diffusion rapidity was insufficient to refill back the electrode leading to fast shortage of the cells performances.

As temperature and current were two parameters of tremendous importance and due to the complex analyze of the graphs owing to the lack of reproducibility, the different conditions were studied by always comparing 4 different discharges. In addition, SEM examination of the GDL electrodes was also always implemented for each bench of conditions. Finally, repeated observations of the SEM pictures from several GDLs discharged in the same conditions were executed, and the noticed morphologies were then compared.

### *V.2.a. Temperature and current effects on discharge capacity*

As aforementioned explained, only temperatures higher than 25 °C were explored (25 °C to 40 °C). On this frame, the electrolyte was thermally stable.<sup>239</sup> Going to higher temperature was not relevant due the limitations already revealed. In parallel, two currents were applied (25  $\mu$ A and 50  $\mu$ A). The first discharges resulting from the operating conditions were summarized in Figure V. 14.

First it appeared at 25 °C and 25  $\mu$ A that significant higher capacities were achieved. This was nicely explained by the utilization of a not dry electrolyte and thus a modification of the kinetics with LiOH production as explained earlier. For this reason, these results were discarded from others to enable comparison.

Once results due to water contamination were put aside, two opposite trends were noticed even though some discrepancies like the extra-long and not stable discharges at 50  $\mu$ A and 27.5 °C were observed. While at 25  $\mu$ A the rise of temperature corresponded to a diminution of the discharge capacity mean value, the reverse tendency was spotted at 50  $\mu$ A as illustrated

in Figure V. 14. It is well known that temperature and current both impact the kinetics. While temperature facilitates reaction kinetics and/or enhances the species mobility, a current increase tends to have the reverse effects. Indeed, it was largely demonstrated for LABs that high current lead to lower discharge capacity because of oxygen limitation. Thus, predicting combined effect of temperature and current was delicate as they push in opposite ways. Then, their combined effects were clearly highlighted and divided in two trends as shown in Figure V. 14.

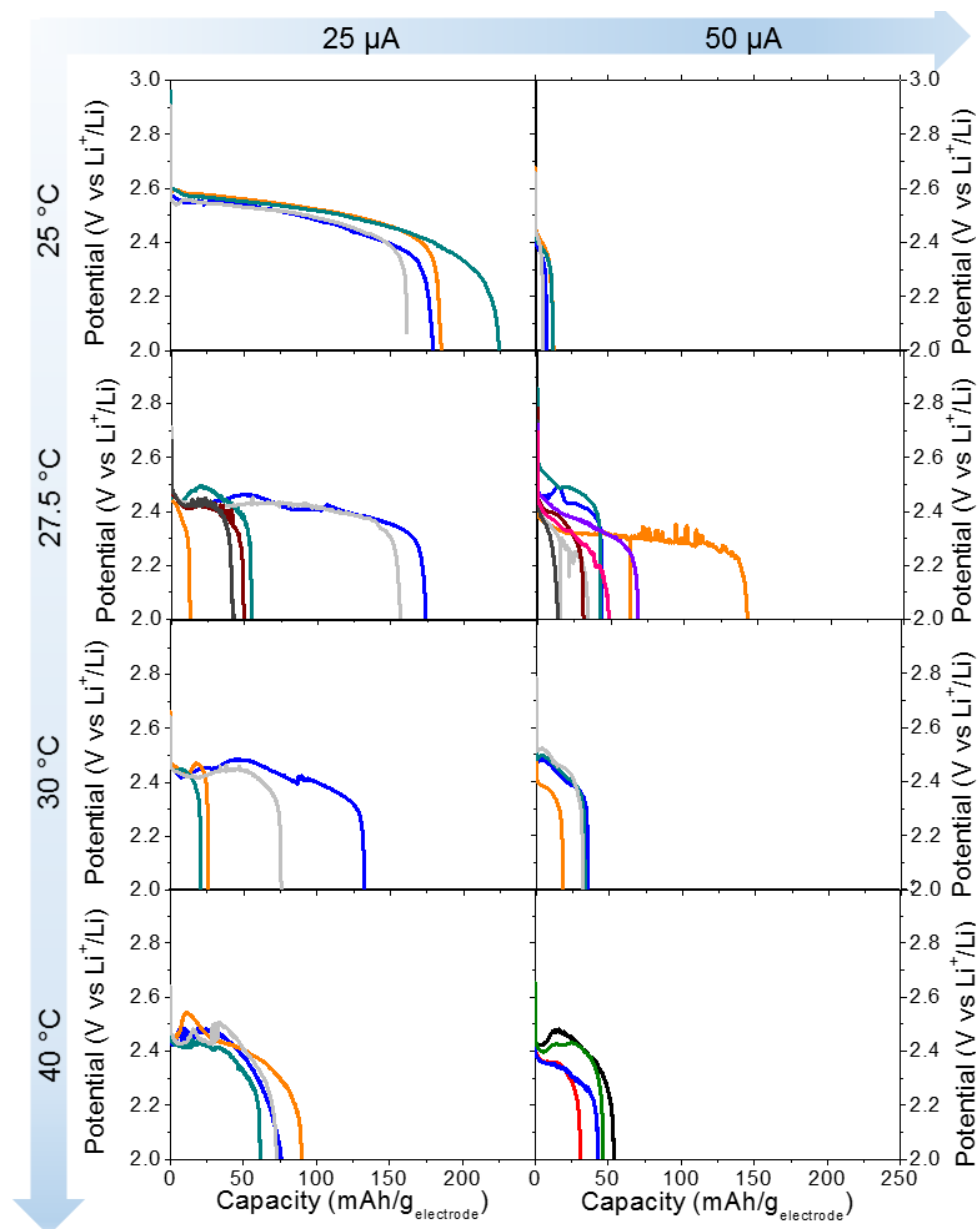


Figure V. 14: First discharges of GDLs cells cycled between 2 to 4.5 V at different temperatures and currents. Only for 25  $\mu$ A and 25  $^{\circ}$ C the electrolyte was not dried, otherwise all the cells contained dried TriGDME + 0.5 M LiTFSI.

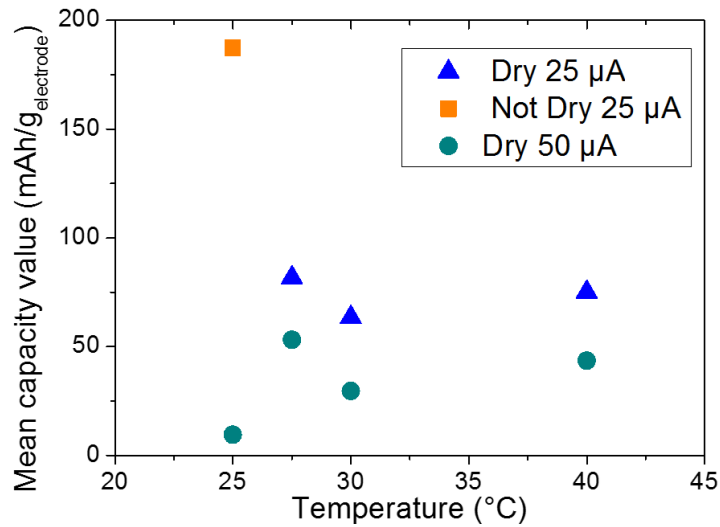


Figure V. 15: Evolution of the discharges capacities mean value with temperature and discharge currents.

Also, it was remarked that reproducibility issues were partially reduced thanks to temperature increase, as spotlighted by the variation of the standard deviation ratio for both currents applied. To quantify the evolution of reproducibility, standard deviations noted in each conditions were calculated. As actually the mean capacity significantly changed from one case to another one, the results of the percentages represented by the standard deviations compared to the respective mean capacity were plotted in Figure V. 16.

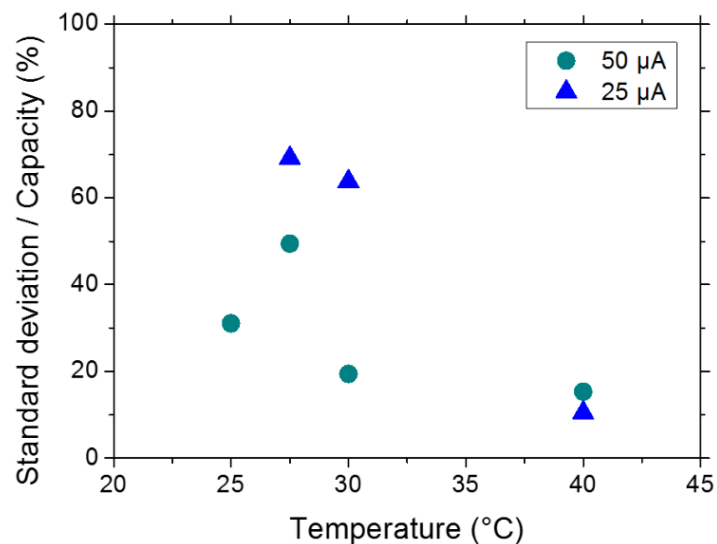


Figure V. 16: Evolution of the standard deviation over mean capacity ratio with temperature and discharge currents.

As illustrated, reproducibility clearly improved while temperature was increased even if for 50  $\mu\text{A}$  and 27.5  $^{\circ}\text{C}$  an unexpected rise was observed compared to other results get at 50  $\mu\text{A}$ . Such astonishing results were correlated to the mean discharge capacity value. Indeed, while



for duo of conditions, twin measurements were always noticed for high values (as for instance at 25 °C and 50  $\mu$ A: 12.1 - 12.7 mAh/g<sub>electrode</sub> and 5.29 - 7.74 mAh/g<sub>electrode</sub>) here more tests were done but only one value was significantly higher than the other ones (unstable orange curve in Figure V. 14). This led to higher standard deviation and mean value calculations. Actually after removing this unforeseen value, mean value dropped until 40.3 mAh/g<sub>electrode</sub> and the ratio of standard deviation over mean capacity until 29.7 mAh/g<sub>electrode</sub> leading to smooth evolution of the values with temperature. Other relevant observation was that at 40 °C a higher reproducibility was recorded for the highest current value, underlining the beneficial impact of rise temperature in LABs. Even if it was already demonstrated in literature that higher current density could be damageable, its impact was not clearly correlated to the temperature.

To sum up, it was clearly identified that temperature impacted the kinetics and thus the discharge capacity. Temperature also helped to enhance the experiments reproducibility. Impact of current density on discharge capacity was nuanced as such parameter should studied aside from temperature. Still, at such point, understanding the improvements was not allowed from previous results. Necessity to go deeper into the study was still required to understand the origin of reproducibility issues. As LABs are based on reaction surface, analyze by SEM of the electrode after discharge seemed relevant to observed qualitatively the efficiency of the discharge, as well as, the repetitively of the discharge product morphologies observed.

### *V.2.b. Temperature and current effects on discharge product morphology*

#### *Discharge product morphologies reported in literature*

A clear trend popped up while analyzing the LABs discharge product morphologies as many papers published by the scientific community reported formation of “toroids”. Actually, while selecting the key-words “lithium-air batteries” OR “lithium-oxygen batteries” AND “toroids” in Web of Science browser 1083 papers were found over the 2682 counted for LABs (c.f. Chapter 1). This significant number of papers mentioning such particle shape highlighted the large tendency consisting in looking for toroids while occulting formation of other shapes. Many serious work focused on “toroids”, “toroidal” or even “toroid-like” particles formation,<sup>77,81,171,174,178,179,202,240–243</sup> most probably due to their characteristic and easily identified shape as illustrated in Figure V. 17.

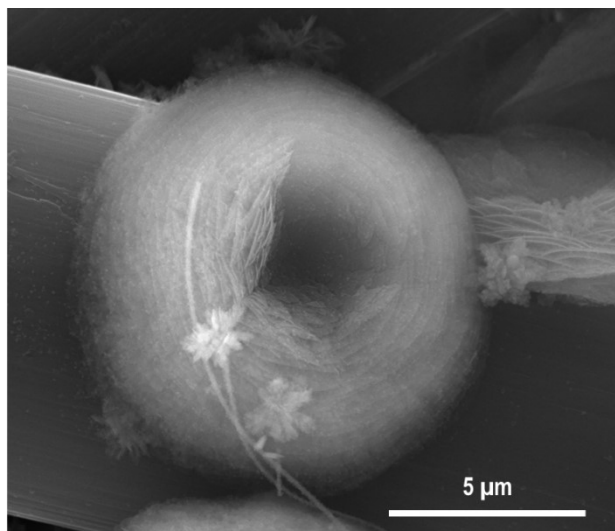


Figure V. 17: SEM picture of a toroidal particle formed on top of GDL discharge in cell containing TriGDME+ 1M LiNO<sub>3</sub>.

Astonishingly, their shape reminds the red blood cell (Figure V. 18), in charge to transport the oxygen to the several organs of the human body. Even if the red blood cell shape could be supposedly linked to oxygen, some works, such as the ones of Canham or Deuling *et al.*, attributed it to a minimum of membrane bending energy and to the membrane elasticity properties respectively.<sup>244,245</sup> Then, the toroidal form is more linked to the cell properties than the optimal contact surface for oxygen adsorption as it could easily be initially supposed. Perhaps the visual likeness of some LABs discharge particles to human red blood cell was responsible for the undeserved fame of toroids among the several discharge product morphologies witnessed at lab scale.

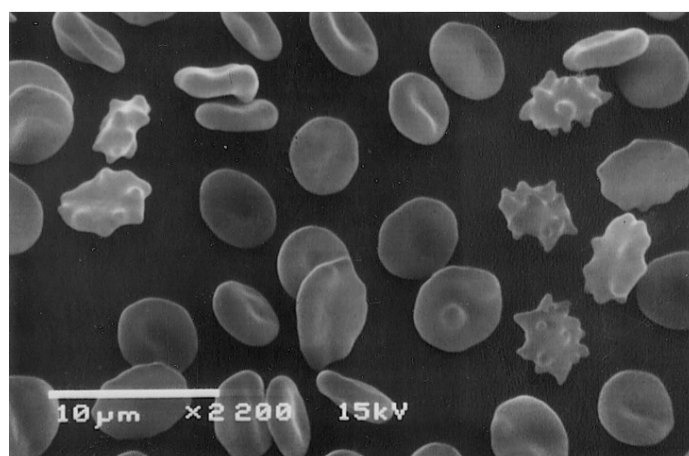


Figure V. 18: SEM picture of red blood cell with clear toroidal shape. Image taken from Tamara *et al.* work.<sup>246</sup>

Once that the too strong focus on toroid formation was exposed, other type of discharge product morphologies should be disclosed as well as their origins. Usually, formation of toroids was opposed to film-formation, each of them impacting the limitation mechanisms which could take place. With film formation, passivation is more likely to occur while for large toroids electron transport could be hindered.<sup>81</sup>

Triggering of one type of particle, toroids or film, were directly linked to the electrolyte used to perform the discharge as the formation mechanism solution-pathway or surface-pathway were possible depending on the solvent donor number, the ionic association strength and the water content. Thus, Aurbach *et al.* nicely summed up the several properties of the electrolyte influencing the discharge product formation (Figure V. 19).<sup>81</sup>

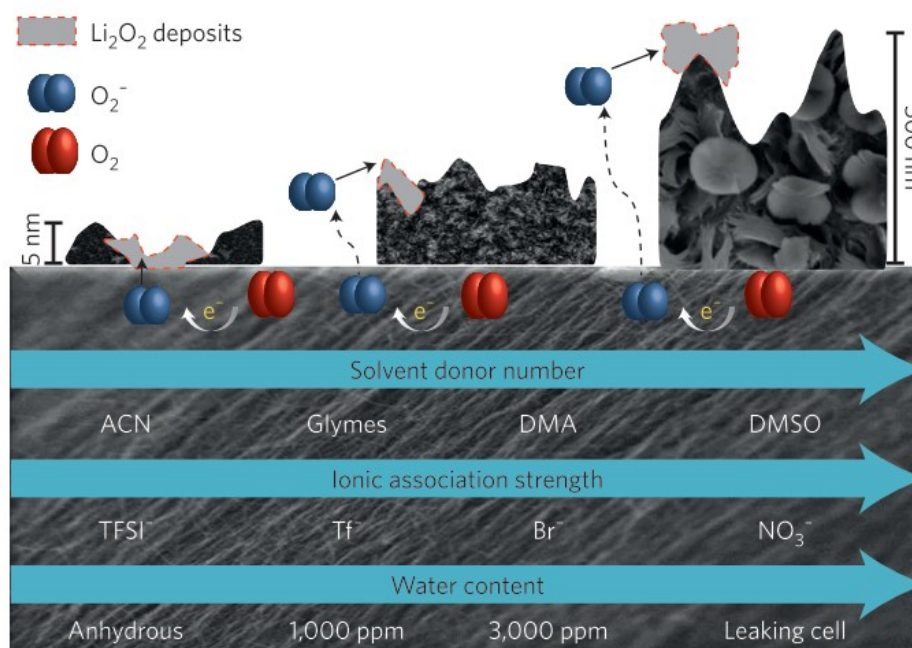


Figure V. 19: Schematic figured proposed by Aurbach *et al.* to highlight the several electrolyte properties impacting the surface and solution growth mechanisms in LABs and thus the film or toroid formation.<sup>81</sup>

However, as seen in literature and in our experiments, not only two types of particles (toroid versus film) were formed after discharge of LABs. Figure V. 20 was built in an attempt to sum up all the morphologies observed in literature and the corresponding cathodes and electrolytes.

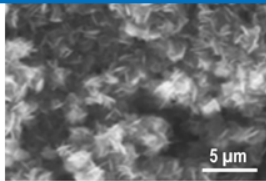
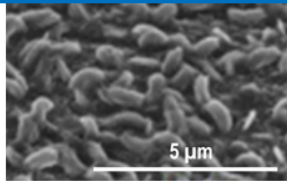
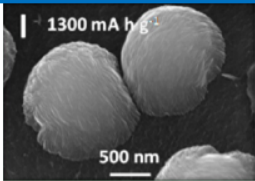
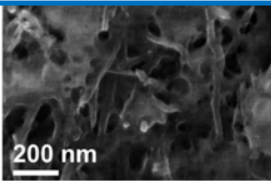
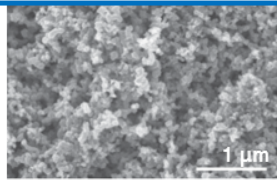
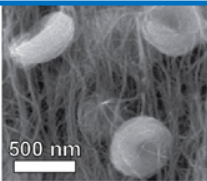
Needle	Crescent	Ball-like
 <p><b>Griffith <i>et al.</i>, ACS AMI, 2015</b>  <b>Electrolyte:</b>  DME + 1 M LiTFSI  <b>Cathode:</b>  GDL</p>	 <p><b>Schwenke <i>et al.</i>, JES, 2015</b>  <b>Electrolyte:</b>  DiGME + 0.5 M LiTFSI  <b>Cathode:</b>  Carbon paper</p>	 <p><b>Zhai <i>et al.</i>, JACS, 2013</b>  <b>Electrolyte:</b>  TEGDME + 1 M LiCF<sub>3</sub>SO<sub>3</sub>  <b>Cathode:</b>  Activated carbon</p>
Film	Small spheres	Toroid
 <p><b>Mitchell <i>et al.</i>, EES, 2011</b>  <b>Electrolyte:</b>  EC:DMC + 1 M LiPF<sub>6</sub>  <b>Cathode:</b>  CNF</p>	 <p><b>Aetukiri <i>et al.</i>, Nat. Chem, 2015</b>  <b>Electrolyte:</b>  DME + 1 M LiTFSI  <b>Cathode:</b>  Vulcan XC72 carbon cathode</p>	 <p><b>Mitchell <i>et al.</i>, JPCL, 2015</b>  <b>Electrolyte:</b>  DME + 0.1 M LiClO<sub>4</sub>  <b>Cathode:</b>  CNT</p>

Figure V. 20: Sum up of the several morphologies of LABs discharge products encountered across the literature.<sup>77,171,174,179,243,247</sup>

While reduction of the particle size with the application of higher current density was often mentioned,<sup>171,172,240,247</sup> only few papers really compared the impact of the electrolyte. Hopefully, Johnson *et al.* nicely compared the impact of several common solvents for LABs and proposed to explain particle formation not because of two competitive mechanisms but due to a unique one, strongly influenced by the solvent. Solvent impact was explained at the light of the modification of the Li<sub>2</sub>O<sub>2</sub> solubility or “more precisely, the free energy of the reaction  $\text{LiO}_2^* \rightleftharpoons \text{Li}^+_{(\text{sol})} + \text{O}_2^-_{(\text{sol})} + \text{ion pairs} + \text{higher aggregates (clusters)}$ ”.<sup>85</sup> Still, as disclosed in next part, such approach did not explain or even mentioned the variation of the morphologies noticed in the same configuration (cathode, electrolyte and current density). Then, other significant parameter not taken into account yet should be unveiled and studied.

### *Discharge product morphologies observed in several operation conditions*

As seen along the electrochemical tests, none of the cell succeed to overpassed twenty-five cycles for this reason all the cells underwent the same treatment. The particles finally deposited on top of the GDL surface corresponded then to the discharge product formed that

could not be reversibly decomposed. Here, it was decided to compare the discharge product at the end of the cycling due to the variety of behaviors.

All the cells confronted were first cycled prior to be disassembled in glovebox where they were cleaned with TriGDME. After, they were transferred to the SEM chamber. It worth point out that even if a cleaning step was applied, some fibers were noticed on top of the GDLs discharged (Figure V. 21). The fibers were analyzed by EDX and later compared to the EDX carried on the separator. It was then validated that the fibers came from the separator and must have been detached and deposited on each side of the GDL during the cleaning step in TriGDME.

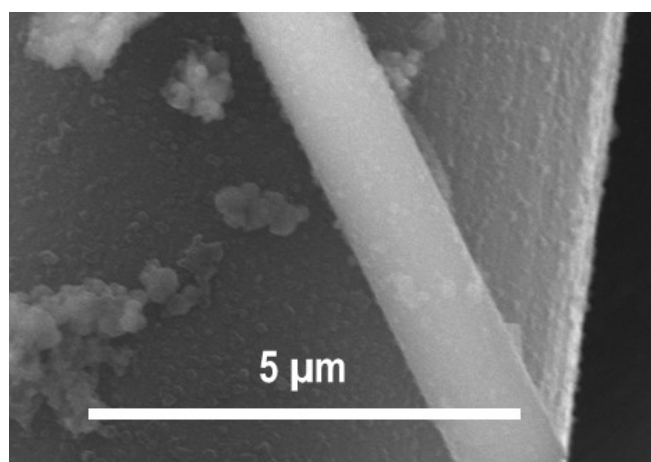


*Figure V. 21: SEM picture of a glass fiber from separator deposited on top of a GDL fiber.*

As for some combination of the operating conditions (temperature and current density), it happened randomly that some cells performed nicely while others failed more quickly (Figure V. 14), at least one from each performance-type were observed by SEM. Later, to go deeper into the study, morphologies were also inspected for cells characterized by almost the same electrochemical behavior.

To certify that the cells failure was linked to the cathode limitations (passivation, formation of irreversible products, pore clogging or even too low active surface) and not to electrolyte or lithium foil degradation, a simple experiment was settled. As explained in Figure V. 22, a first cell was cycled and then disassembled in glovebox to form two descendant cells, one containing the previous lithium foil + separator + electrolyte with a new cathode, the second one containing fresh lithium foil + separator + electrolyte with the cathode already discharge. Finally, only the cell with the novel cathode was able to discharge again, highlighting that the capacity fading was clearly induced by cathode limitations.



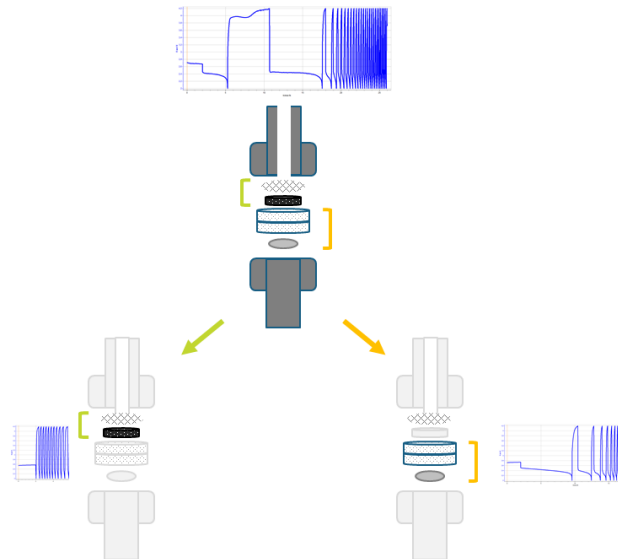


Figure V. 22: Schematic of the test implemented to define which part of the cell was responsible for capacity fading cathode versus separator/electrolyte/lithium.

After assessing that the origin of capacity fading was due to the cathode, looking at the final cathode stage was necessary. After varying the temperature from 25 °C to 40 °C and the current from 25  $\mu$ A and 50  $\mu$ A, a large range of morphologies was encountered. Figure V. 23 spotted this variety of shapes and thus stressed the complexity of LABs operation.

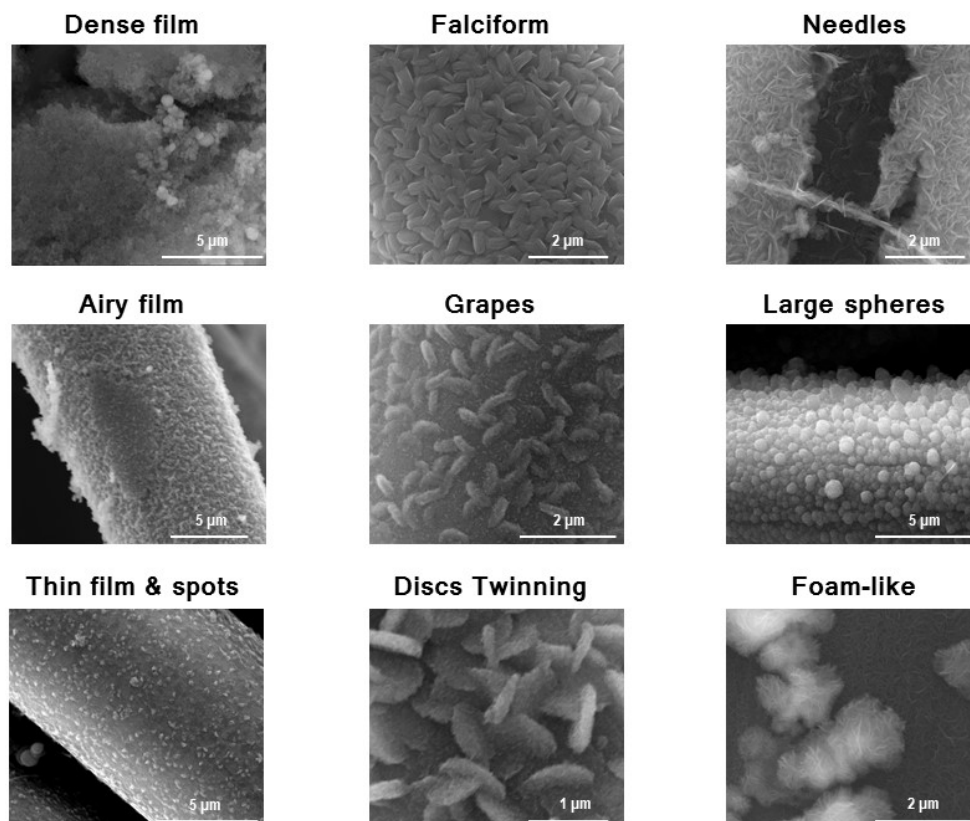


Figure V. 23: Sum up of the several morphologies of LABs final discharge product observed after cycling in TriGDME + 0.5 M LiTFSI at different temperatures and currents.

Even though all the morphologies presented in Figure V. 23 were not operated in the same conditions, it was of major importance to underscore that the different morphologies were produced for same cells (cathode-electrolyte-anode).

More precisely, comparisons of the final product morphologies were settled for two different combinations of the operating conditions (Figure V. 24). At 27.5 °C and 25  $\mu$ A, two different films, a dense one (Figure V. 24.a) and an airy one (Figure V. 24.b), were produced even if same conditions were applied. While comparing the electrochemical behavior of the two cells it appeared that the first one discharged initially for long time and then starting from the second discharge the discharge capacity decreased. In contrast, for the other cell the second discharge was longer than the first one. Even though explaining the different formations of the two films was difficult, it seemed from the results that density of the film formed strongly depended on the discharge depth as well as on the charge step. Indeed, while the cell a) followed a two-step charge, the cell b) was characterized only by one charge plateau.

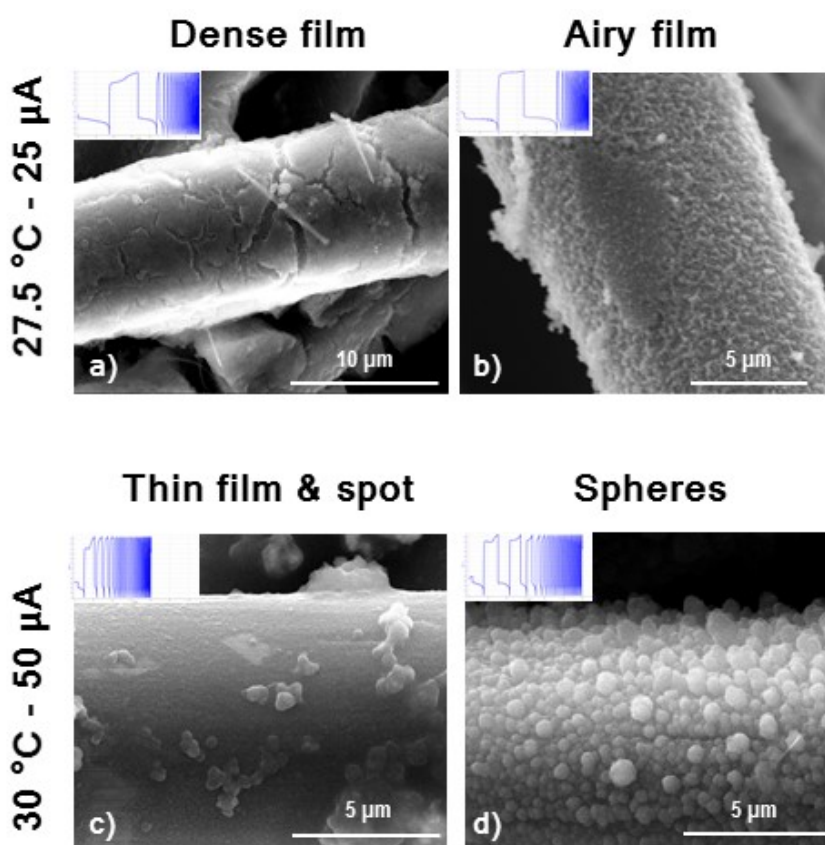


Figure V. 24: SEM pictures of different discharge product morphologies deposited on the air side of cathodes operated at 27.5 °C and 25  $\mu$ A (a,b) and at 30 °C and 50  $\mu$ A (c,d).

These different performances of the cells during the charge pointed out that the conclusions made in our previous work<sup>117</sup> should be reassessed. Initially, we attributed the two charge plateaus to the successive decomposition of, first, the  $\text{Li}_2\text{O}_2$  film and then the  $\text{Li}_2\text{O}_2$  large particles. Still, here obviously two films were formed and only their respective densities were different, invalidating then the first hypothesis made in the modeling study that only one dense thin film can be produced. Obviously from the present experiments, charge process was not only sensitive to the particle size. Ganapathy *et al.* took another approach to understand the mechanism occurring over charge using X-ray diffraction.<sup>248</sup> They demonstrated in their case (using an activated carbon based cathode and TetraGDME + 0.1 M LiTFSI) that the first plateau existing between 2.8 V and 3.4 V corresponded to transformation of amorphous  $\text{Li}_2\text{O}_2$  as no modification of XRD patterns were noticed. Then, they attributed the second plateau existing around 3.4 V to 3.9 V to a solid solution process leading to  $\text{Li}_{2-x}\text{O}_2$  formation and then decomposition back to lithium cations and oxygen. Unfortunately, here the overpotentials observed were not corresponding to the one announced, making interpretations complicated. Also, their study starting with the postulate that toroids were formed over discharge. Still, no SEM proof was presented either in the paper or in the supporting information. Then, estimating that the difference of the overpotential values was due to a more resistive system (GDL electrode) and that actually not toroids but films were formed, conclusions made by Ganapathy *et al.* could be transposed to the results of Figure V. 24.a and Figure V. 24.b. Then, while more amorphous  $\text{Li}_2\text{O}_2$  was produced over the first discharge, an airy film was formed. While crystalline  $\text{Li}_2\text{O}_2$  was formed, a denser film was formed. Still, the triggering of one or another type of  $\text{Li}_2\text{O}_2$  was not discerned.

While now comparing Figure V. 24.c and Figure V. 24.d, two dissimilar morphologies were developed, even though the charge mechanisms were the same (two plateaus). This time, except the initial discharge which evolved from one sample to another one, the same profile with reduction of the discharge capacity over the cycles was recorded. Still, in the light of the SEM pictures, the particles sizes were drastically distinct. These results just reaffirmed that formation of dense film was more damageable to the cell performances than the formation of large particles, must probably due to passivation limitation as previously described.

Finally making conclusive links between the morphologies and the operating conditions appeared to be too deceitful and tricky. Diverse morphologies were perceived in same conditions but, even more seriously, within the same electrode. Differences were noticed while



comparing the two sides of a same electrode (side exposed to air or side next to the separator) as illustrated Figure V. 25.

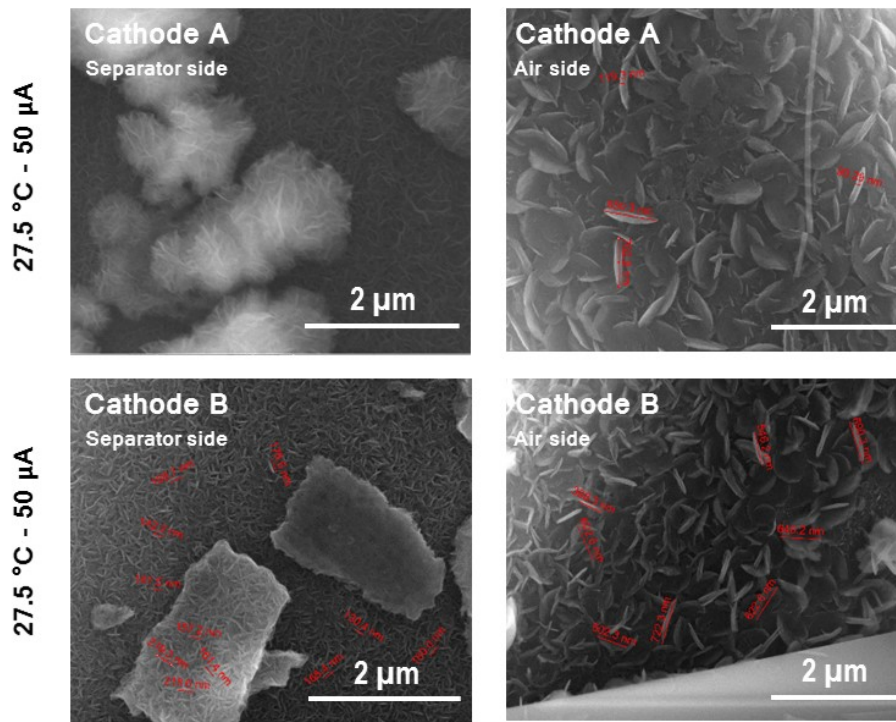


Figure V. 25: Comparison of the SEM pictures of both sides of two cathodes operated at 27.5 °C and 50  $\mu$ A.

Surprisingly, in case of Cathode A, two distinct morphologies were formed: discs on air side and foam-like on the separator side. Less significant changes between the two sides were noticed for Cathode B. This time, same morphology was observed in both sides, yet, the particles sizes were multiplied by at least three while opposing the ones on the separator side to the ones at the air inlet. Actually, such results nicely fitted the observations from the literature. Several papers, reported non-uniform distribution of the discharge products. In 2010, Zhang *et al.* published SEM pictures of their LABs cathode with a substantial production of the discharge product at the air side compared to separator one (Figure V. 26).<sup>249</sup>

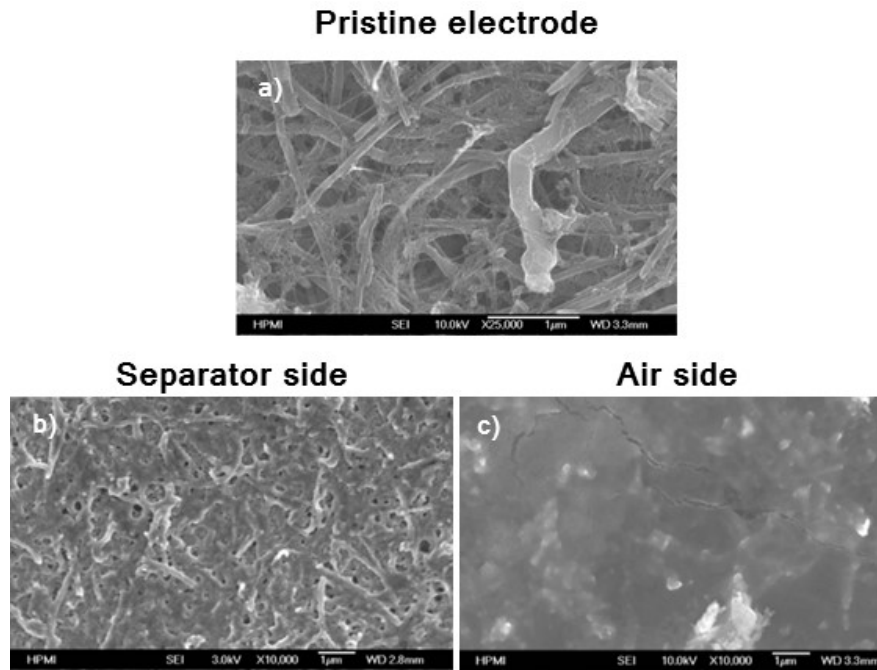


Figure V. 26: SEM pictures of a) a pristine cathode, b) the separator side of the cathode after discharge at  $0.1 \text{ mA.cm}^{-2}$  and c) the air side of the cathode after discharge at  $0.1 \text{ mA.cm}^{-2}$  as published in Zhang *et al.* work.<sup>249</sup>

One year later, they attributed the location of discharge product according to electrolyte-filling.<sup>57</sup> The electrodes fully flooded led to production at the air side mainly, due to the slow oxygen diffusion within the electrolyte. Not enough electrolyte on the reverse facilitated and enhanced the production at the separator side. In their paper they suggested then to manage the electrolyte-filling to perfectly wet the electrode without lack or excess of electrolyte to evenly form discharge product. Based on such observations, as in our experiments all the cells were containing identical volume of electrolyte (in excess), intensified production of the discharge products was expected at the air side. Previous SEM pictures (Figure V. 25) confirmed the accuracy of these expectations.

Later in 2012, Nanda *et al.* demonstrated and quantified the non-uniform distribution of the discharge product by tomography. Using modeling they highlighted the responsibility of oxygen diffusion and the LABs kinetics in the irregular deposition. Finally, they also affirmed that more homogeneous distribution was observed at the center of the electrode compared to the edges.<sup>250</sup> In the current study such variations from the edges to the center were not noticed, most probably due to the utilization of extremely porous GDLs and not dense electrodes.

Later on, Ren *et al.* went even further as they highlighted that the distribution was dependent on the current density applied (higher current density  $\rightarrow$  higher production at air side)<sup>251</sup> which matched the previous explanations. Still, this did not allowed to understand why

even in same conditions and especially same current density, more discrepancy was noticed for cathode A compared to B (Figure V. 25). Furthermore, even while inspected the same side of an electrode, several particles shapes were detected on the same side of the GDL (Figure V. 27). Additionally, within the same GDL fiber, several morphologies were also noticed.

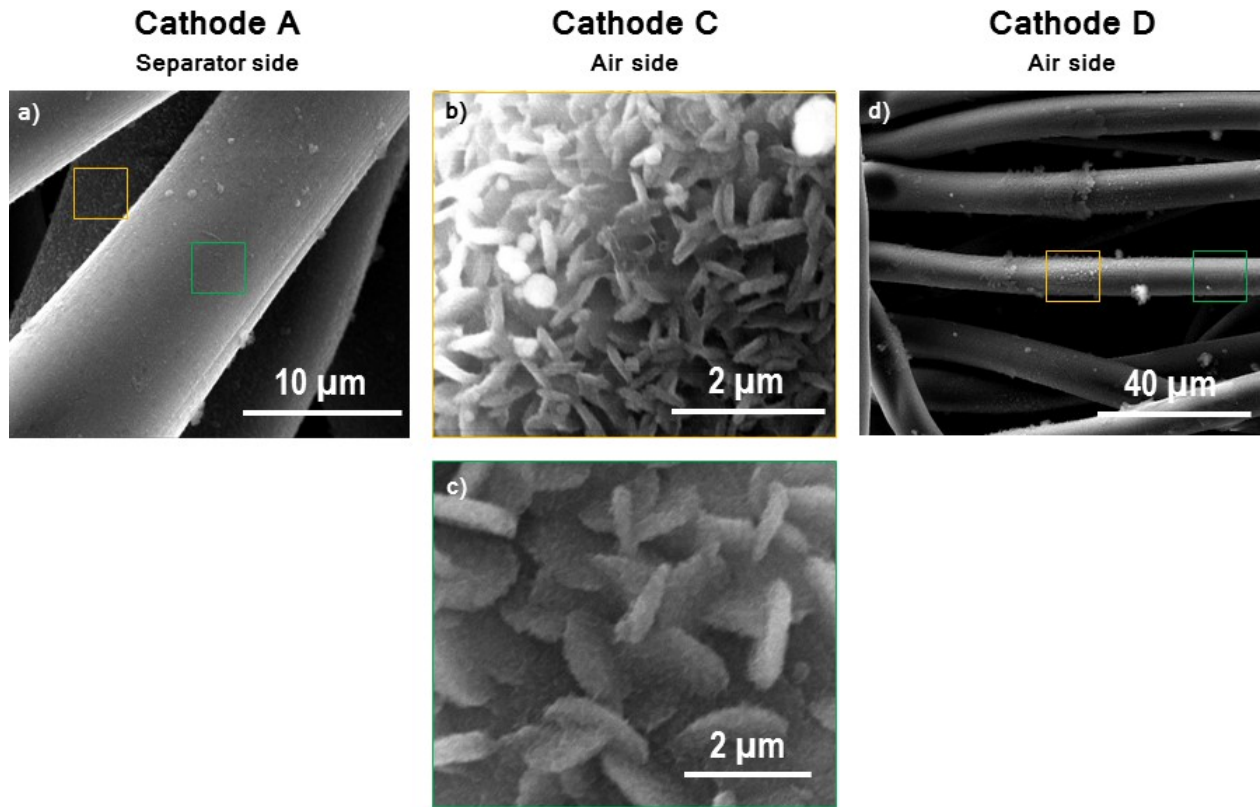


*Figure V. 27: SEM pictures of three different electrodes to demonstrate the variation of the discharge product morphology formed in the same side of an electrode. SEM image of Cathode D also spotted the variation within the same GDL fiber.*

As displayed, variations of the discharge product morphology and size were distinguished, depending on the position on the electrode (Cathode C) or in function of the depth of the electrode (Cathode A). These observations for Cathode A could match the explanations given in literature, as in Cathode A the GDL fibers closer to the inner part of the electrode was more “filled” compared to the first fiber observed. Though, for Cathode C no clear understanding of the different locations was found as changes depending on the position on the edge or the center were not visible. More importantly, even on the same GDL fiber (Cathode D) large spheres were side by side with thin film. This led to significant complexification of the results interpretation.

Still, previous observations could in part explain the variation of the morphology. As already mentioned, GDLs suffered from compression and thus their performances could be largely impacted as the number of contact point and so the electronic conduction could change significantly. This was validated by the lower capacities and large discrepancy of the results noticed in the case of GDLs compared to the ones of flexible bi-porous electrodes. Variation of the morphologies on same side of an electrode or within same fiber could be due to modification of the local current density experienced by the GDL compressed. Still, morphology variations could not be certainly attributed only to compression issues. One piece of the puzzle was still lacking to be sure of it. As LABs are based on surface reactions, it was required to check that local modification of the surface was not also responsible for various discharge product morphologies. Then, pretreated GDLs were also tested to evaluate the impact of the GDL surface.

### V.3. LABs high sensitivity toward electrode surface

It was demonstrated that LABs performances were significantly impacted by the nucleation step. So, maybe LABs were so sensitive to the surface that slight defects could lead to the diverse results. In the literature, it was already highlighted that LABs performances depended on carbon surface group.<sup>252</sup> Then, perhaps GDLs surface were not completely homogeneous or might contained some surface defects responsible for the results variations.

To see if it was the case, a special heat treatment was applied to some GDL discs to remove the potential defects. The heat treatment consisted in heating progressively the sample until 400°C (taking two hours) and then the samples remained at 400°C for one hour. All the heat treatment procedure was applied while a constant argon flow was imposed. The treated electrodes were then cycled leading to the discharge profiles in Figure V. 28.

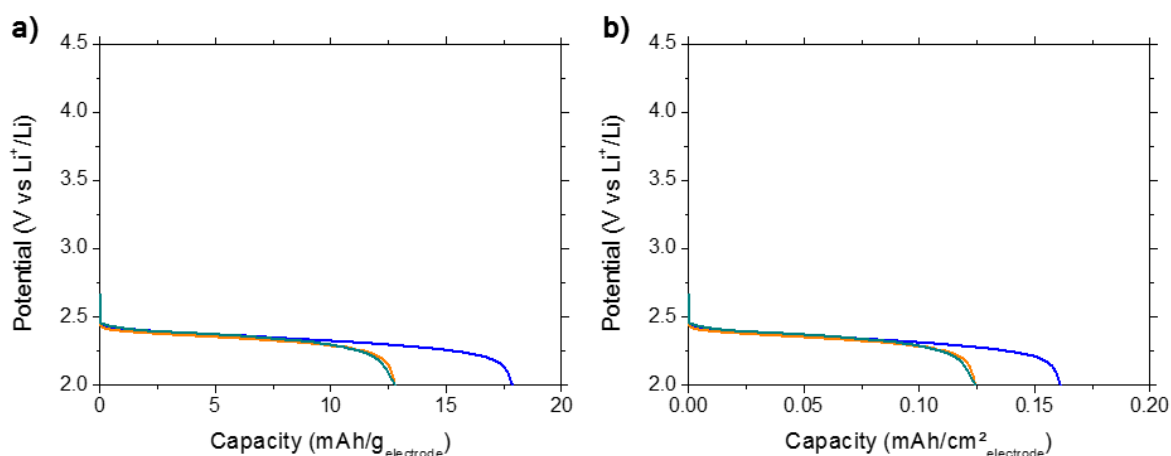


Figure V. 28: First discharges at 27.5 °C of cells made of GDLs pretreated at 400 °C and cycled in dried TriGDME + 0.5 M LiTFSI at 50  $\mu$ A between 2 to 4.5 V. Capacities expressed in a) mAh/g<sub>electrode</sub> and b) mAh/cm<sup>2</sup><sub>electrode</sub>.

Thanks to the heating treatment, the three GDLs had the same overpotential values and so superposed plateau. Also, decrease of the mean discharge capacity was noticed as 14.5 mAh/g<sub>electrode</sub> were achieved compared 40.3 mAh/g<sub>electrode</sub> with not treated GDLs electrodes in same conditions. To see if this diminution was linked to a morphology modification, the electrode corresponding to the orange curve was analyzed by SEM.

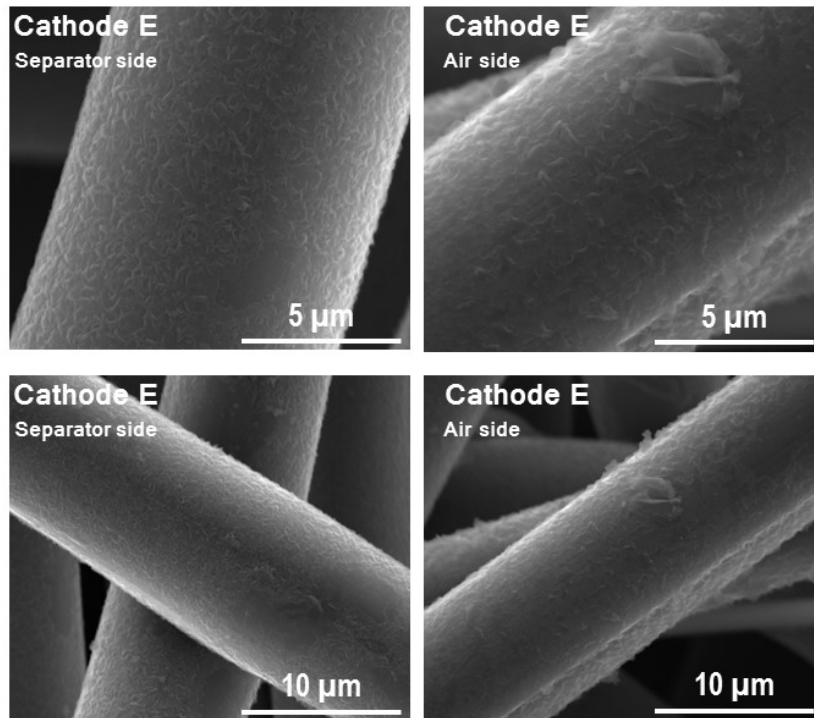


Figure V. 29: Several SEM pictures of the cathode E after cycling five times a GDL pretreated at 400 °C at 50  $\mu$ A and 27 °C.

In both side a film made of needles was observed. While at the separator side the needles were more defined, at the air side less needles were noticed. Except that, a clear homogenization of discharge product over the cell was observed highlighting that cathode surface is a key parameter in LABs. To quantify the influence of the cathode surface modification on the cells performances, the mean value of the discharge capacities was compared to previous results Figure V. 30.

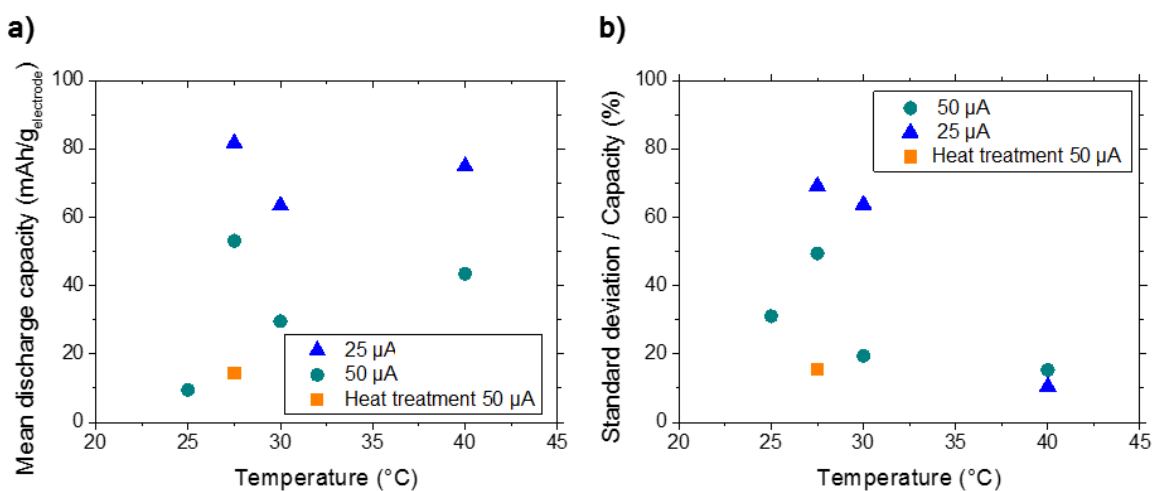


Figure V. 30: Comparison of the GDLs pretreated at 400 °C a) mean capacity and b) the standard deviation ratio in opposition to previous GDLs cells.

It was observed that the mean value capacity in the same conditions (27.5 °C and 50 μA) for the non-treated cell was three times higher than the one for the pretreated GDL. The discharge capacity reduction could have been also triggered by a modification of the electrode wettability. Still, as a homogeneous production of the discharge product was observed such hypothesis was discarded. However the observed reduction of capacity was corroborated by the findings of Wong *et al.* who linked the removal of cathode defect to a decrease of capacity due to carbon surface group modification.<sup>252</sup> Such group modification was obviously occurring during the pretreated GDLs and could then explained the values decrease.

Even though the discharge capacity evolution was damageable, at least, a clear diminution of the standard deviation ratio was observed while using pretreated GDLs. All these observations comforted the idea that LABs are extremely sensitive to the cathode surface. Mastering perfectly the cathode surface is then of major importance. This is in agreement with the nucleation study implemented by Yin *et al.* at LRCS.<sup>233</sup> Nucleation barrier which governs LABs behavior is defined by the following equation

$$\Delta G_{Nu} = \frac{8BV_m^2\sigma^3}{27(n_e e\eta)^2} \left(1 + \frac{E_b}{2\sigma A_i}\right) \quad \text{Eq. 18}$$

Nucleation is then strongly impacted by  $E_b$  which corresponds to the binding energy between  $\text{Li}_2\text{O}_2$  and the electrode material and so depends strongly on the surface. For this reason, avoiding any surface defect and slight contamination which could modified locally the surface is a crucial step on the way to LABs development.



## V.4. Conclusions on LABs reproducibility issues

LABs reproducibility issues have been clearly identified in case of flexible bi-porous electrodes for DBP<sub>40</sub>, DBP<sub>60</sub> and DBP<sub>80</sub>. Several leads have been followed to see if reproducibility problematic could be solved. Controlled electrolyte-filling step, flushing time, operating temperature and removal of water contamination were identified as relevant parameters to reduce reproducibility. Among them, temperature appeared as a crucial one as only 2 °C of difference implied voltage variation. Still, reproducibility issues remained and were considered to be in part explained by the electrodes deformation. Diverse irreversible deformations were noted while comparing several electrodes most probably due to the variation of the pressure applied while closing the Swagelok.

To validate that deformations were responsible for it, other electrodes (GDLs) were used as they can be reversible deformed. It ends up, that GDLs also suffer from reproducibility issues and led to lower capacity values. This at least highlighted the importance of mastering the electrode texture. Even though flexible bi-porous electrodes and GDLs had comparable porosity overall value and so theoretical capacity values, GDLs performed far less than texturized electrodes (due to lower electronic conductivity and developed surface in addition to not improved texture). GDLs non-reproducibility were also triggered by the less efficient electron conduction percolating network strongly impacted by compression.

Finally, combined effects of current and temperature were scrutinized. As both parameters acted in opposite ways on the kinetics, their influences were not deccorelate. Above all, it was recorded that temperature rise improved the repeatability of the experiments no matter which current was applied. Also, another parameter impacting the kinetics and more precisely the nucleation step was the electrode surface. Defect removal tends to reduce again the performances but enhanced the reproducibility. For these reasons, not only electrode texture and operating conditions but also surface state should be managed to design efficient and reproducible LABs electrodes. Still, Torayev *et al.* demonstrated that part of the reproducibility issues can be assigned to the inherent operation principles of LABs. Indeed, they pointed out based on tomography data that even though some electrodes have same overall porosity, depending on how the pores are connected, slight to significant variations of the simulated discharge capacities are induced depending on the current applied to the system.<sup>253</sup> If so, removing completely the reproducibility issues would be tricky or at least will imply high manufacturing cost (to master until exact pore connectivity).



# **CHAPTER VI: GENERAL CONCLUSIONS AND PERSPECTIVES**

Nowadays, one of the main challenge facing the aircraft manufacturers is to reach the development of eco-friendlier airships. Even if feasibility of MEA or fully electrical aircraft have already been demonstrated at the prototyping level, once it comes to commercial aircraft a technological barrier needs to be overcome. To replace kerosene combustion by electrical energy source, the latter should be first stored. To do so, efficient energy storage systems are required. Going toward fully electric propulsion implies that the aircraft design should be revisited from scratch to remove the kerosene tank and to welcome instead energy storage devices and propulsion system (for instance multi-propeller or electric engine). For these reasons, MEA appeared to be a more achievable target within the future years less significant modifications need to be implemented. Still, to pretend to replace a part of the kerosene loaded onboard, the energy storage systems selected for tomorrow MEA need to have high gravimetric and volumetric energy densities.

Even though LIBs are mature, their characteristics in terms of energy densities are low compared to new systems. Among the Post Li-ion technologies, LABs emerged as a potential solution due to their high gravimetric and volumetric theoretical energy densities. Still, as shown previously, LABs encountered many limitations from anode, electrolyte, to cathode. Due to all these limitations, the practical energy densities of these systems are for now far from theoretical ones. As LABs are based on surface reactions, their performances are defined by the cathode properties, more precisely, by the cathode surface and porosity.

Then, as cathode is a key component of LABs, a strong focus was made in an attempt to enhance the practical performances. To repel capacity fading due to the cathode limitations, these ones should be first understood in order to be avoided later. LABs cathodes are subject to three main limitations: oxygen diffusion through the electrode, surface passivation and pore clogging. Occurrence of each phenomenon will be triggered differently by the electrode texture. Indeed, depending on the material used, the surface developed and thus the passivation risk would be modified. Also, the porosity will strongly impact the pathways available for oxygen diffusion. It will also influence the facility for pore clogging to happen.

For these reasons, electrode texture was identified as a crucial step toward development of performant LABs. Carbon-based electrodes were then examined as various textures could be easily achieved using them. To load higher amount of energy per cell, thick electrodes have been explored. This way, most part of the mass and volume of the battery would be due to the electrode materials and not to the battery casing or current collector. However, limitations such

as diffusion are strengthened while using thick electrodes. To overcome the reinforcement of the limitations with enlargement of the cathode thickness, a special electrode design was proposed: bi-porous electrodes. Bi-porosity enabled to have two domains :1) a first meso-porous domain which corresponded to the electrode material domain and acted as the reaction surface provider and 2) a second macro-porous domain which was inserted on purpose to facilitate oxygen diffusion through the electrode.

To develop these bi-porous electrodes, a first theoretical approach was implemented. As the proportion of each domain impacted obviously the limitation phenomena, their respective impacts were analyzed on the basis of multi-scale modeling. A continuum model describing the three phenomena was then built. To be closed to the experimental electrodes developed in parallel, the model also took into account the cathode properties like developed surface, porosity, thickness and formulation (carbon versus binder amounts). Thanks to modeling, it was identified that Carbon SP was more likely to fade due to surface passivation, while Ketjen Black electrode sudden death was linked to oxygen diffusion limitation. Impacts of the formulation and thickness were also scrutinized by comparing the first discharge capacities values and overpotentials. The thickness strongly impacted the efficiency of the electrode utilization. The beneficial impact of adding a macro-porous domain was highlighted thanks to the model and depended on the electrode formulation selected. Indeed, at a certain point adding macro-porosity did not help anymore to enhance the performances and thus no more than 40 % of macro-porous volume should be targeted for all the carbon contents tested. In conclusion, the model exhibited the interest of using bi-porous electrodes. Still, theoretical findings needed to be confirmed by experimental results as several parameters, like the modification of the pore size or the electrode real tortuosity, were not taken into account. Though, a strong experimental study was implemented in parallel.

At experimental level, production of thick highly porous electrodes was accomplished using an electrode fabrication process initially developed for LIBs and known as the Bellcore process. It allowed to fabricate porous self-standing electrodes by dissolution of a porogen agent. The facility to create a macro-porous domain via this process led to select it, this time for LABs electrode fabrication. Still, due to the use of highly divided carbons (to promote high surface for reaction) and the porosity requirement stronger than in LIB field, the formulation had to be reviewed accordingly. In addition, to realize highly porous electrodes the amount of the porogen agent (DBP) was significantly augmented. To make sure that the rise of DBP content directly produced the expected macro-porosity, porosity creation was studied along the

fabrication process. While the efficiency of DBP removal was assessed, some variations highlighted the chemical inhomogeneity of the film especially for higher DBP contents. Demonstration of meso-porous and macro-porous domains creation was made. Although, production of closed porosity was noticed in each case and was probably due to electrode reorganization during DBP removal steps. Contrary to initial thoughts, high initial porogen agent content ( $> 60$  w%) was finally not relevant to obtain homogeneous and highly porous electrodes. On the reverse, a middle range DBP content (40 w%) permitted to design bi-porous electrodes for LABs with high porosity (50 v%) and significant carbon surface developed ( $50 \text{ m}^2 \cdot \text{g}_{\text{electrode}}$ ). Once released from the porogen agent, electrolyte filling of the electrode was proven. Also, the electrodes could bear until  $80^\circ\text{C}$ . Moreover, the achieved electrode efficiencies were interesting as more than 70 % of the theoretical capacity for both DBP<sub>60</sub> and DBP<sub>80</sub> was reached while operating the cell at  $50 \mu\text{A}$ .

Flexible bi-porous electrodes were also compared to GDLs electrode as they have comparable overall porosity. Still, GDLs reached less than 5 % of the theoretical capacity while discharged in the same conditions. This highlighted the necessity to texturize the electrode. Also, it pointed out one drawback: electrode deformation due to compression. Even if GDLs were reversibly deformed they might suffer more than home-made electrodes as they have a less spread percolating network. Indeed, even deformed, flexible bi-porous electrodes percolation is always ensured by the highly divided carbon particles (as many contact points as carbon particles are in contact). On the contrary, depending on the compression the number of contact points between the fibers of a GDL would be more impacted as they are less numerous. These compression issues could explain in part the LABs reproducibility lack. In both cases, to overcome deformation issues, the cell compression should be controlled to enable electrolyte intake and good percolation, while also impeding the electrode deformation because of too tight celling.

In an attempt to solve the reproducibility issues, the testing conditions have been more and more controlled. Initially, various initial discharge curve shapes were observed. While the initial dips observed highlighted the fact that nucleation step was taking place, understanding the underpinning causes was difficult. It ends up that by progressively removing the parameters impacting the nucleation step, reproducibility was improved even though it was not always the case of the performances. For instance, water traces conducted to an extension of the discharge capacity, as well as, higher results discrepancy. LABs high sensitivity toward temperature was also spotted and its impact on performances correlated to the current applied. Temperature and

current influences had to be studied in parallel as they act in opposite ways on kinetics. It was also concluded that temperature should be strictly controlled while operating the cell, to get rid of potential oscillations with temperature variations. Once water traces removed and temperature controlled, higher reproducibility was achieved while incrementing the operating temperature. To check if the enhance reproducibility was linked to better controlled nucleation step the cells were observed post-mortem. Finally, far more various morphologies than the typical toroids described in literature were observed. The formation of distinct morphologies in same conditions or even on same GDL fiber was difficult to apprehend. This spotlighted the strong impact of nucleation mechanism as morphologies strongly changed depending on the electrode location. This was confirmed by the more homogeneous results found while using pyrolyzed GDLs which means GDLs with surface freed from defects.

Finally, extreme sensitivity of LABs was unveiled and the observed reproducibility issues could find their roots in several parameters: reproducibility of the electrode texture, compression of the electrode in the cell, temperature and current applied and obviously surface state.

Unfortunately, perfect control of the operating condition is in opposition with the targeted application which requires to handle significant temperature changes. Moreover, until then only Li-oxygen and not Li-air batteries have been tested. Real LABs would involve atmosphere with higher water contents. Some tests carried on in contact with wet-oxygen (using a bubbler filled with water) or with a mix of oxygen and nitrogen (50/50) led to unstable electrochemical responses. Fast electrolyte decomposition, surface modification, production of lithium carbonates or two less oxygen available could explained the cells failure. To understand the complexity of LABs versus LOBs, a model based on previous nucleation work<sup>233</sup> is currently under development to take into account more complex mechanisms due to air and not oxygen supply. This involved reduction of the oxygen available, water and carbon dioxide contamination and so  $\text{Li}_2\text{O}_2$  transformation in  $\text{LiOH}$  and  $\text{Li}_2\text{CO}_3$  (see Annex). As the model is still under development, no clear conclusions are already available. Still, the number of reactions taken into account to describe the several contaminations highlights the many limitations that need to be overcome prior to performed LABs in contact of air.

More than anything, operation of LABs should be improved at lab scale and their cycling performances improved thanks to the development of a stable electrolyte which should be resistant toward oxygen like species, temperature and water degradation and in a meantime

should enable to solubilize high amount of oxygen. This is of paramount importance and yet is still lacking, no matter the number of publications already released highlighting the complexity of designing such an electrolyte. Still, once the electrolyte technical hindrance would be overcome, utilization of bi-porous electrodes would enable to improve significantly the practical performances of LABs and might permit their utilization, most probably only in stationary applications. Contrary to aeronautical applications, stationary ones enable to easily control the operating conditions, without paying attention to the temperature control device and the oxygen providing systems masses, as there are less demanding on energy gravimetric and volumetric density.

In the light of the current results and literature, LABs application in aeronautical field may never happen due to their sensitivity to operating conditions even though electrolyte stability issue would be solved. However, the study of this system enables to question the electrochemical mechanisms taking place and the chemistry fundamentals. It also permitted here to develop highly-porous and flexible electrodes with a mastered texture that can be transposed to different technologies such as other types of metal-air batteries.

## Bibliography

1. Ashcraft, S. W., Padron, A. S., Pascioni, K. A., Stout Jr., G. W. & Huff, D. L. Review of Propulsion Technologies for N+3 Subsonic Vehicle Concepts. *Nasa* **217239**, 1–38 (2011).
2. Darecki, M. *et al.* *Flightpath 2050. Flightpath 2050 Europe's Vision for Aviation* (2011).
3. Jones, R. I. The more electric aircraft - assessing the benefits. *J. Aerosp. Eng.* **216**, 259–269 (2002).
4. Zhao, W., Guerrero, J. M. & Xiaohua, W. Review of aircraft electric power systems and architectures. in *2014 IEEE International Energy Conference (ENERGYCON)* 949–953 (2014).
5. Dawoud, B., Amer, E. & Gross, D. Experimental investigation of an adsorptive thermal energy storage. *Int. J. energy Res.* **31**, 135–147 (2007).
6. Jay Carmel. *The Quiet Revolution: Aviation Prepares to Go From Jet Age to Electric Era of Flight. Avascent White Paper* (2017).
7. Tomažič, T. *et al.* Pipistrel taurus G4: On creation and evolution of the winning aeroplane of NASA green flight challenge 2011. *J. Mech. Eng.* **57**, 869–878 (2011).
8. Wang, Y. Modeling discharge deposit formation and its effect on lithium-air battery performance. *Electrochim. Acta* **75**, 239–246 (2012).
9. Stoll, A. M., Bevirt, J., Moore, M. D., Fredericks, W. J. & Borer, N. K. Drag Reduction Through Distributed Electric Propulsion. in *14th AIAA Aviation Technology, Integration, and Operations Conference* 16–20 (2014).
10. Clarke, S., Lin, W. Y., Papathakis, K. & Samuel, A. LEAPTech HEIST Power Architecture and Testing Roadmap Power Level for Electrical Propulsion. in *2015 AIAA Aviation Technology, Integration, and Operations Conference*, (2015).
11. Thomson, R., Sachdeva, N., Nazukin, M. & Martinez, N. *Aircraft Electrical Propulsion – The Next Chapter of Aviation? Think: Act* (2017).
12. Robert, F. Lithium-sulfur batteries poised for leap. *Science* **359**, 1080–1081 (2018).
13. Nazar, L. F., Cuisinier, M. & Pang, Q. Lithium-sulfur batteries. *MRS Bull.* **39**, 436–442 (2014).

14. Zhu, X., Guo, Z. & Hou, Z. Solar-powered airplanes: A historical perspective and future challenges. *Prog. Aerosp. Sci.* **71**, 36–53 (2014).
15. Peng, H. J., Huang, J. Q., Cheng, X. B. & Zhang, Q. Review on High-Loading and High-Energy Lithium–Sulfur Batteries. *Adv. Energy Mater.* **7**, 1–54 (2017).
16. Ross, P. E. Boeing ’ s Battery Blues become more dependent on electricity and batteries. *IEEE Spectrum - North American* 11–12 (2013).
17. Williard, N., He, W., Hendricks, C. & Pecht, M. Lessons learned from the 787 dreamliner issue on Lithium-Ion Battery reliability. *Energies* **6**, 4682–4695 (2013).
18. Irfan, U. How Lithium Ion Batteries Grounded the Dreamliner. *Scientific American* 1–6 (2014). Available at: <https://www.scientificamerican.com/article/how-lithium-ion-batteries-grounded-the-dreamliner/>.
19. NTBS - Office of Aviation Safety. *Interim Factual Report- Boeing 787-8, JA829J, Japan Airlines.* (2013).
20. Dyantyi, N., Parsons, A., Sita, C. & Pasupathi, S. PEMFC for aeronautic applications: A review on the durability aspects. *Open Eng.* **7**, 287–302 (2017).
21. Guida, D. & Minutillo, M. Design methodology for a PEM fuel cell power system in a more electrical aircraft. *Appl. Energy* **192**, 446–456 (2017).
22. Nishizawa, A., Kallo, J., Garrot, O. & Weiss-Ungethüm, J. W. Fuel cell and Li-ion battery direct hybridization system for aircraft applications. *J. Power Sources* **222**, 294–300 (2013).
23. Kallo, J. Fuel cells power first takeoff for DLR’s Antares aircraft. *Fuel Cells Bulletin* 3 (2009).
24. Kallo, J. Antares DLR-H2. *Fuel Cells Bulletin* 4 (2008).
25. Rahman, M. A., Wang, X. & Wen, C. A review of high energy density lithium-air battery technology. *J. Appl. Electrochem.* **44**, 5–22 (2014).
26. Girishkumar, G., McCloskey, B., Luntz, A. C., Swanson, S. & Wilcke, W. Lithium-air battery: Promise and challenges. *J. Phys. Chem. Lett.* **1**, 2193–2203 (2010).
27. Scrosati, B. History of lithium batteries. *J. Solid State Electrochem.* **15**, 1623–1630 (2011).



28. Kurzweil, P. Gaston Planté and his invention of the lead-acid battery-The genesis of the first practical rechargeable battery. *J. Power Sources* **195**, 4424–4434 (2010).
29. Armand, M. & Tarascon, J. M. Building better batteries. *Nature* **451**, 652–657 (2008).
30. Ngô, C. *Stockage de l'énergie. Techniques de l'ingénieur* (2016).
31. Placke, T., Kloepsch, R., Dühnen, S. & Winter, M. Lithium ion, lithium metal, and alternative rechargeable battery technologies: the odyssey for high energy density. *J. Solid State Electrochem.* **21**, 1939–1964 (2017).
32. Opitz, A., Badami, P., Shen, L., Vignarooban, K. & Kannan, A. M. Can Li-Ion batteries be the panacea for automotive applications? *Renew. Sustain. Energy Rev.* **68**, 685–692 (2017).
33. Conte, F. V. Battery and battery management for hybrid electric vehicles: A review. *Elektrotechnik und Informationstechnik* **123**, 424–431 (2006).
34. Schipper, F. & Aurbach, D. A brief review: Past, present and future of lithium ion batteries. *Russ. J. Electrochem.* **52**, 1095–1121 (2016).
35. Diouf, B. & Pode, R. Potential of lithium-ion batteries in renewable energy. *Renew. Energy* **76**, 375–380 (2015).
36. Whittingham, M. S. & Gamble, F. R. The lithium intercalates of the transition metal dichalcogenides. *Mater. Res. Bull.* **10**, 363–371 (1975).
37. RECHARGE aisbl. *Safety of lithium-ion batteries*. (2013).
38. Wang, Q., Jiang, B., Li, B. & Yan, Y. A critical review of thermal management models and solutions of lithium-ion batteries for the development of pure electric vehicles. *Renew. Sustain. Energy Rev.* **64**, 106–128 (2016).
39. Berg, E. J., Villevieille, C., Streich, D., Trabesinger, S. & Novák, P. Rechargeable Batteries: Grasping for the Limits of Chemistry. *J. Electrochem. Soc.* **162**, A2468–A2475 (2015).
40. Nitta, N., Wu, F., Lee, J. T. & Yushin, G. Li-ion battery materials: Present and future. *Mater. Today* **18**, 252–264 (2015).
41. Nishi, Y. Lithium ion secondary batteries; past 10 years and the future. *J. Power Sources* **100**, 101–106 (2001).

42. <https://starkpower.com/understanding-lithium-ion-batteries>. lithiumion-charts-01.
43. Hannan, M. A., Lipu, M. S. H., Hussain, A. & Mohamed, A. A review of lithium-ion battery state of charge estimation and management system in electric vehicle applications: Challenges and recommendations. *Renew. Sustain. Energy Rev.* **78**, 834–854 (2017).
44. Tao, H., Feng, Z., Liu, H., Kan, X. & Chen, P. Reality and Future of Rechargeable Lithium Batteries. *Open Mater. Sci. J.* **5**, 204–214 (2011).
45. Lewis, H. *Lithium-ion battery consultation report*. (2016).
46. Sathiya, M. *et al.* Origin of voltage decay in high-capacity layered oxide electrodes. *Nat. Mater.* **14**, 230–238 (2015).
47. Tarascon, J.-M. Key challenges in future Li-battery research. *Philos. Trans. R. Soc. A Math. Phys. Eng. Sci.* **368**, 3227–3241 (2010).
48. Lebedeva, N., Di Persio, F. & Boon-Brett, L. *Lithium ion battery value chain and related opportunities for Europe*. European Commission, Petten, (2016).
49. Pillot, C. *Battery Market Development for Consumer Electronics, Automotive, and Industrial: Materials Requirements and Trends*. Qinghai EV Rally 2015 (2015).
50. Tiamat. (2018). Available at: <http://www.tiamat-energy.com/>.
51. Abraham, K. M. & Jiang, Z. A Polymer Electrolyte-Based Rechargeable lithium / Oxygen Battery. *J. Electrochem. Sci. Technol.* **143**, 1–5 (1996).
52. Bruce, P. G., Freunberger, S. a., Hardwick, L. J. & Tarascon, J.-M. Li–O<sub>2</sub> and Li–S batteries with high energy storage. *Nat. Mater.* **11**, 172–172 (2011).
53. Grande, L. *et al.* The Lithium/Air Battery: Still an Emerging System or a Practical Reality? *Adv. Mater* **27**, 784–800 (2015).
54. Christensen, J. *et al.* A Critical Review of Li/Air Batteries. *J. Electrochem. Soc* **159**, 1–30 (2012).
55. Ottakam Thotiyl, M. M. *et al.* A stable cathode for the aprotic Li-O<sub>2</sub> battery. *Nat. Mater.* **12**, 1050–6 (2013).
56. Peng, Z., Freunberger, S. A., Chen, Y. & Bruce, P. G. A reversible and higher-rate Li-

- O<sub>2</sub> battery. *Science*. **337**, 563–566 (2012).
57. Zhang, S. S., Foster, D. & Read, J. The effect of quaternary ammonium on discharge characteristic of a non-aqueous electrolyte Li/O<sub>2</sub> battery. *Electrochim. Acta* **56**, 1283–1287 (2011).
  58. Gasteiger, H. A. *et al.* Electrocatalytic Activity Studies of Select Metal Surfaces and Implications in Li-Air Batteries. *J. Electrochem. Soc.* **157**, A1016–A1025 (2016).
  59. McCloskey, B. D., Scheffler, R., Speidel, A., Girishkumar, G. & Luntz, A. C. On the mechanism of nonaqueous Li-O<sub>2</sub> electrochemistry on C and its kinetic overpotentials: Some implications for Li-air batteries. *J. Phys. Chem. C* **116**, 23897–23905 (2012).
  60. Padbury, R. & Zhang, X. Lithium–oxygen batteries—Limiting factors that affect performance. *J. Power Sources* **196**, 4436–4444 (2011).
  61. Giordani, V., Freunberger, S. A., Bruce, P. G., Tarascon, J.-M. & Larcher, D. H<sub>2</sub>O<sub>2</sub> Decomposition Reaction as Selecting Tool for Catalysts in Li–O<sub>2</sub> Cells. *Clin. Chem.* **38**, A180–A183 (2010).
  62. Lee, J. S. *et al.* Metal-air batteries with high energy density: Li-air versus Zn-air. *Adv. Energy Mater.* **1**, 34–50 (2011).
  63. Yang, J. *et al.* Atomic layer deposition of amorphous oxygen-deficient TiO<sub>2-x</sub> on carbon nanotubes as cathode materials for lithium-air batteries. *J. Power Sources* **360**, 215–220 (2017).
  64. Torres, W. R., Davia, F., del Pozo, M., Tesio, A. Y. & Calvo, E. J. EQCM and RDE/RRDE Study of Soluble Iron Phthalocyanine Bifunctional Catalyst for the Lithium-Oxygen Battery. *J. Electrochem. Soc.* **164**, A3785–A3792 (2017).
  65. Trahey, L. *et al.* Activated Lithium-Metal-Oxides as Catalytic Electrodes for Li–O<sub>2</sub> Cells. *Electrochem. Solid-State Lett.* **14**, A64–A66 (2011).
  66. Akgül, F. S., Farsak, M., Kardaş, G. & Dehri, İ. Comparison of nonaqueous electrolytes on oxygen reduction in Li-air batteries. *J. Mol. Liq.* **223**, 343–349 (2016).
  67. Roberts, M. *et al.* Increased Cycling Efficiency of Lithium Anodes in Dimethyl Sulfoxide Electrolytes For Use in Li-O<sub>2</sub> Batteries. *ECS Electrochem. Lett.* **3**, A62–A65 (2014).

68. Chen, Y., Freunberger, S. A., Peng, Z., Fontaine, O. & Bruce, P. G. Charging a Li–O<sub>2</sub> battery using a redox mediator. *Nat. Chem.* **5**, 489–494 (2013).
69. Cohen, Y. S., Cohen, Y. & Aurbach, D. Micromorphological Studies of Lithium Electrodes in Alkyl Carbonate Solutions Using in Situ Atomic Force Microscopy. *J. Phys. Chem. B* **104**, 12282–12291 (2000).
70. Gittleson, F. S., Jones, R. E., Ward, D. K. & Foster, M. E. Oxygen solubility and transport in Li-air battery electrolytes: Establishing criteria and strategies for electrolyte design. *Energy Environ. Sci.* **10**, 1167–1179 (2017).
71. Lu, J. *et al.* Aprotic and aqueous Li-O<sub>2</sub> batteries. *Chem. Rev.* **114**, 5611–5640 (2014).
72. Freunberger, S. A. *et al.* Reactions in the Rechargeable Lithium-O<sub>2</sub> Battery with Alkyl Carbonate Electrolytes. *J. Am. Chem. Soc.* *2011*, **133**, 8040–8047 (2011).
73. McCloskey, B. D., Bethune, D. S., Shelby, R. M., Girishkumar, G. & Luntz, A. C. Solvents' Critical Role in Nonaqueous Lithium–Oxygen Battery Electrochemistry. *J. Phys. Chem. Lett.* **2**, 1161–1166 (2011).
74. Aurbach, D., Daroux, M., Faguy, P. & Yeager, E. The electrochemistry of noble metal electrodes in aprotic organic solvents containing lithium salts. *J. Electroanal. Chem.* **297**, 225–244 (1991).
75. Laoire, C. O., Mukerjee, S., Plichta, E. J., Hendrickson, M. A. & Abraham, K. M. Rechargeable Lithium/TEGDME-LiPF<sub>6</sub>/O<sub>2</sub> Battery. *J. Electrochem. Soc.* **158**, A302 (2011).
76. Freunberger, S. A. *et al.* The Lithium-Oxygen Battery with Ether-Based Electrolytes. *Angew. Chemie - Int. Ed.* **50**, 8609–8613 (2011).
77. Mitchell, R. R., Gallant, B. M., Thompson, C. V. & Shao-Horn, Y. All-carbon-nanofiber electrodes for high-energy rechargeable Li–O<sub>2</sub> batteries. *Energy Environ. Sci.* **4**, 2952 (2011).
78. Freunberger, S. A. *et al.* The lithium-oxygen battery with ether-based electrolytes. *Angew. Chemie - Int. Ed.* **50**, 8609–8613 (2011).
79. Laoire, C. O., Mukerjee, S., Abraham, K. M., Plichta, E. J. & Hendrickson, M. A. Influence of Nonaqueous Solvents on the Electrochemistry of Oxygen in the

- Rechargeable Lithium-Air Battery. *J. Phys. Chem. C* **114**, 9178–9186 (2010).
80. Abraham, K. M. Electrolyte-Directed Reactions of the Oxygen Electrode in Lithium-Air Batteries. *J. Electrochem. Soc.* **162**, A3021–A3031 (2015).
  81. Aurbach, D., McCloskey, B. D., Nazar, L. F. & Bruce, P. G. Advances in understanding mechanisms underpinning lithium-air batteries. *Nat. Energy* **1**, 1–11 (2016).
  82. Xue, K.-H., McTurk, E., Johnson, L., Bruce, P. G. & Franco, A. A. A Comprehensive Model for Non-Aqueous Lithium Air Batteries Involving Different Reaction Mechanisms. *J. Electrochem. Soc.* **162**, A614–A621 (2015).
  83. Gao, X., Chen, Y., Johnson, L. & Bruce, P. G. Promoting solution phase discharge in Li–O<sub>2</sub> batteries containing weakly solvating electrolyte solutions. *Nat. Mater.* **15**, 882–888 (2016).
  84. Yang, S., He, P. & Zhou, H. Research progresses on materials and electrode design towards key challenges of Li-air batteries. *Energy Storage Mater.* **13**, 29–48 (2018).
  85. Johnson, L. *et al.* The role of LiO<sub>2</sub> solubility in O<sub>2</sub> reduction in aprotic solvents and its consequences for Li-O<sub>2</sub> batteries. *Nat. Chem.* **6**, 1091–1099 (2014).
  86. Xue, K.-H., McTurk, E., Johnson, L., Bruce, P. G. & Franco, A. A. A Comprehensive Model for Non-Aqueous Lithium Air Batteries Involving Different Reaction Mechanisms. *J. Electrochem. Soc.* **162**, A614–A621 (2015).
  87. Meini, S., Solchenbach, S., Piana, M. & Gasteiger, H. A. The Role of Electrolyte Solvent Stability and Electrolyte Impurities in the Electrooxidation of Li<sub>2</sub>O<sub>2</sub> in Li-O<sub>2</sub> Batteries. *J. Electrochem. Soc.* **161**, A1306–A1314 (2014).
  88. Huang, J. & Faghri, A. Analysis of electrolyte level change in a lithium air battery. *J. Power Sources* **307**, 45–55 (2016).
  89. Albertus, P. *et al.* Identifying Capacity Limitations in the Li/Oxygen Battery Using Experiments and Modeling. *J. Electrochem. Soc.* **158**, A343 (2011).
  90. Wang, Y. & Cho, S. C. Analysis of Air Cathode Performance for Lithium-Air Batteries. *J. Electrochem. Soc.* **160**, A1847–A1855 (2013).
  91. Liu, B. *et al.* Stabilization of Li Metal Anode in DMSO-Based Electrolytes via Optimization of Salt-Solvent Coordination for Li-O<sub>2</sub> Batteries. *Adv. Energy Mater.* **7**,

- 1602605 (2017).
92. Sharon, D. *et al.* Oxidation of dimethyl sulfoxide solutions by electrochemical reduction of oxygen. *J. Phys. Chem. Lett.* **4**, 3115–3119 (2013).
  93. Kwabi, D. G. *et al.* Chemical instability of dimethyl sulfoxide in lithium-air batteries. *J. Phys. Chem. Lett.* **5**, 2850–2856 (2014).
  94. Younesi, R., Norby, P. & Vegge, T. A New Look at the Stability of Dimethyl Sulfoxide and Acetonitrile in Li-O<sub>2</sub> Batteries. *ECS Electrochem. Lett.* **3**, A15–A18 (2014).
  95. Mozhzhukhina, N. *et al.* Insights into dimethyl sulfoxide decomposition in Li-O<sub>2</sub> battery: Understanding carbon dioxide evolution. *Electrochem. commun.* **80**, 16–19 (2017).
  96. Capsoni, D., Bini, M., Ferrari, S., Quartarone, E. & Mustarelli, P. Recent advances in the development of Li-air batteries. *J. Power Sources* **220**, 253–263 (2012).
  97. Akbulut Uludağ, A. *et al.* Stability effect of some organic and inorganic additions in the EMITFSI–LiTFSI nanocomposite electrolytes for lithium-air batteries. *Microsyst. Technol.* **22**, 953–963 (2016).
  98. Yoo, K., Dive, A. M., Kazemiabnavi, S., Banerjee, S. & Dutta, P. Effects of Operating Temperature on the Electrical Performance of a Li-air Battery operated with Ionic Liquid Electrolyte. *Electrochim. Acta* **194**, 317–329 (2016).
  99. Read, J. *et al.* Oxygen Transport Properties of Organic Electrolytes and Performance of Lithium/Oxygen Battery. *J. Electrochem. Soc.* **150**, A1351 (2003).
  100. Yang, S., He, P. & Zhou, H. Research progresses on materials and electrode design towards key challenges of Li-air batteries. *Energy Storage Mater.* **13**, 29–48 (2018).
  101. Henderson, W. A. Glyme-lithium salt phase behavior. *J. Phys. Chem. B* **110**, 13177–13183 (2006).
  102. Kerner, M., Plylahan, N., Scheers, J. & Johansson, P. Thermal stability and decomposition of lithium bis(fluorosulfonyl)imide (LiFSI) salts. *RSC Adv.* **6**, 23327–23334 (2016).
  103. Lim, H. D. *et al.* Superior rechargeability and efficiency of lithium-oxygen batteries: Hierarchical air electrode architecture combined with a soluble catalyst. *Angew. Chemie - Int. Ed.* **53**, 3926–3931 (2014).

104. Kwak, W. J. *et al.* Understanding the behavior of Li-oxygen cells containing LiI. *J. Mater. Chem. A* **3**, 8855–8864 (2015).
105. Nakanishi, A. *et al.* Electrolyte Composition in Li/O<sub>2</sub> Batteries with LiI Redox Mediators: Solvation Effects on Redox Potentials and Implications for Redox Shuttling. *J. Phys. Chem. C* **122**, 1522–1534 (2018).
106. Kim, D. S. & Park, Y. J. Effect of multi-catalysts on rechargeable Li-air batteries. *J. Alloys Compd.* **591**, 164–169 (2014).
107. Yoon, T. H. & Park, Y. J. New strategy toward enhanced air electrode for Li-air batteries: Apply a polydopamine coating and dissolved catalyst. *RSC Adv.* **4**, 17434–17442 (2014).
108. Yu, M., Ren, X., Ma, L. & Wu, Y. Integrating a redox-coupled dye-sensitized photoelectrode into a lithium–oxygen battery for photoassisted charging. *Nat. Commun.* **5**, 5111 (2014).
109. Liu, T. *et al.* Cycling Li-O<sub>2</sub> batteries via LiOH formation and decomposition. *Encycl. Soils Environ.* **350**, 170–175 (2005).
110. Park, J.-B., Lee, S. H., Jung, H.-G., Aurbach, D. & Sun, Y.-K. Redox Mediators for Li-O<sub>2</sub> Batteries: Status and Perspectives. *Adv. Mater.* **30**, 1704162 (2018).
111. Blake, A. J. Synthesis and Characterization of Graphene Oxide/Sulfur Nanocomposite for Lithium-Ion Batteries. 135 (2013).
112. Lepoivre, F. Study and improvement via the development of a silicon-based anode. (2017).
113. Giordani, V. *et al.* Synergistic Effect of Oxygen and LiNO<sub>3</sub> on the Interfacial Stability of Lithium Metal in a Li/O<sub>2</sub> Battery. *J. Electrochem. Soc.* **160**, A1544–A1550 (2013).
114. Uddin, J. *et al.* Lithium nitrate as regenerable SEI stabilizing agent for rechargeable Li/O<sub>2</sub> batteries. *J. Phys. Chem. Lett.* **4**, 3760–3765 (2013).
115. Sharon, D. *et al.* Catalytic Behavior of Lithium Nitrate in Li-O<sub>2</sub> Cells. *ACS Appl. Mater. Interfaces* **7**, 16590–16600 (2015).
116. Radin, M. D. & Siegel, D. J. *Rechargeable Batteries*. (Springer International Publishing, 2015).
117. Yin, Y., Gaya, C., Torayev, A., Thangavel, V. & Franco, A. A. Impact of Li<sub>2</sub>O<sub>2</sub> Particle

- Size on Li–O<sub>2</sub> Battery Charge Process: Insights from a Multiscale Modeling Perspective. *J. Phys. Chem. Lett.* **7**, 3897–3902 (2016).
118. Choi, J. W. & Aurbach, D. Promise and reality of post-lithium-ion batteries with high energy densities. *Nat. Rev. Mater.* **1**, 16013 (2016).
  119. Andrei, P., Zheng, J. P., Hendrickson, M. & Plichta, E. J. Some Possible Approaches for Improving the Energy Density of Li-Air Batteries. *J. Electrochem. Soc.* **157**, A1287–A1295 (2010).
  120. Read, J. *et al.* Oxygen Transport Properties of Organic Electrolytes and Performance of Lithium/Oxygen Battery. *J. Electrochem. Soc.* **150**, A1351–A1356 (2003).
  121. Ye, L. *et al.* A new insight into the oxygen diffusion in porous cathodes of lithium-air batteries. *Energy* **83**, 669–673 (2015).
  122. Bardenhagen, I. *et al.* In situ investigation of pore clogging during discharge of a Li/O<sub>2</sub> battery by electrochemical impedance spectroscopy. *J. Power Sources* **278**, 255–264 (2015).
  123. Bardenhagen, I., Fenske, M., Fenske, D., Wittstock, A. & Bäumer, M. Distribution of discharge products inside of the lithium/oxygen battery cathode. *J. Power Sources* **299**, 162–169 (2015).
  124. Song, M., Park, S., Alamgir, F. M., Cho, J. & Liu, M. Nanostructured electrodes for lithium-ion and lithium-air batteries: the latest developments, challenges, and perspectives. *Mater. Sci. Eng. R* **72**, 203–252 (2011).
  125. Sandhu, S. S., Fellner, J. P. & Brutchon, G. W. Diffusion-limited model for a lithium/air battery with an organic electrolyte. *J. Power Sources* **164**, 365–371 (2007).
  126. Andrei, P., Zheng, J. P., Hendrickson, M. & Plichta, E. J. Some Possible Approaches for Improving the Energy Density of Li-Air Batteries. *J. Electrochem. Soc.* **157**, A1287–A1295 (2010).
  127. Franco, A. A. & Xue, K.-H. Carbon-Based Electrodes for Lithium Air Batteries: Scientific and Technological Challenges from a Modeling Perspective. *ECS J. Solid State Sci. Technol.* **2**, M3084–M3100 (2013).
  128. Xue, K.-H. H., Nguyen, T.-K. K. & Franco, A. A. Impact of the Cathode Microstructure



- on the Discharge Performance of Lithium Air Batteries: A Multiscale Model. *J. Electrochem. Soc.* **161**, E3028–E3035 (2014).
129. Chen, X. J. *et al.* Combined Effects of Oxygen Diffusion and Electronic Resistance in Li-Air Batteries with Carbon Nanofiber Cathodes. *J. Electrochem. Soc.* **161**, 1877–1883 (2014).
  130. Bevara, V. & Andrei, P. Changing the Cathode Microstructure to Improve the Capacity of Li-Air Batteries : Theoretical Predictions. *J. Electrochem. Soc.* **161**, 2068–2079 (2014).
  131. Xue, K.-H. & Franco, A. A. Optimization of the cathode microstructure in lithium air batteries through multiscale physical modeling. in *225th ECS Meeting, Orlando, FL, USA* (2014).
  132. Sergeev, A. V, Chertovich, A. V & Itkis, D. M. Modeling of the lithium-air battery cathodes with broad pore size distribution. *Chem. Phys. Lett.* **660**, 149–154 (2016).
  133. Sergeev, A. V., Chertovich, A. V., Itkis, D. M., Goodilin, E. A. & Khokhlov, A. R. Effects of cathode and electrolyte properties on lithium–air battery performance: Computational study. *J. Power Sources* **279**, 707–712 (2015).
  134. Gaillard, C., Despois, J. F. & Mortensen, A. Processing of NaCl powders of controlled size and shape for the microstructural tailoring of aluminium foams. *Mater. Sci. Eng. A* **374**, 250–262 (2004).
  135. Elango, R., Demortière, A., De Andrade, V., Morcrette, M. & Seznec, V. Thick Binder-Free Electrodes for Li-Ion Battery Fabricated Using Templating Approach and Spark Plasma Sintering Reveals High Areal Capacity. *Adv. Energy Mater.* **8**, 1703031 (2018).
  136. Tarascon, J. M., Gozdz, A. S., Schmutz, C., Shokoohi, F. & Warren, P. C. Performance of Bellcore’s plastic rechargeable Li-ion batteries. *Solid State Ionics* **86–88**, 49–54 (1996).
  137. Gozdz, A. S., Tarascon, J. M. & Schmutz, C. N. Rechargeable lithium intercalation battery hybrid polymeric electrolyte. (1994).
  138. Gozdz, A. S., Schmutz, C. N., Tarascon, J. M. & Warren, P. C. Method of Making an Electrolyte activatable Lithium-ion Rechargeable Battery Cell. (1995).

139. Gozdz, A. S., Schumtz, C. N., Tarascon, J. M. & Warren, P. C. Lithium Secondary Battery Extraction Method. (1996).
140. Du Pasquier, A. *et al.* Plastic PVDF-HFP electrolyte laminates prepared by a phase-inversion process. *Solid State Ionics* **135**, 249–257 (2000).
141. Prosini, P. P., Villano, P. & Carewska, M. A novel intrinsically porous separator for self-standing lithium-ion batteries. *Electrochim. Acta* **48**, 227–233 (2002).
142. Richard, M. N., Koetschau, I. & Dahn, J. R. A Cell for In Situ X-Ray Diffraction Based on Coin Cell Hardware and Bellcore Plastic Electrode Technology. *J. Electrochem. Soc* **144**, 554–557 (1997).
143. Scrosati, B. & Garche, J. Lithium batteries: Status, prospects and future. *J. Power Sources* **195**, 2419–2430 (2010).
144. Tarascon, J. M. & Armand, M. Issues and challenges facing rechargeable lithium batteries. *Nature* **414**, 359–67 (2001).
145. Blyr, A., Sigala, C., Amatucci, G. & Tarascon, J. M. Self-Discharge of LMO/C Li-ion cells in their discharge state. *J. Electrochem. Soc.* **145**, (1998).
146. Morcrette, M. *et al.* In situ X-ray diffraction techniques as a powerful tool to study battery electrode materials. *Electrochim. Acta* **47**, 3137–3149 (2002).
147. Allen, G. *et al.* Atmospheric composition and thermodynamic retrievals from the ARIES airborne TIR-FTS system - Part 2: Validation and results from aircraft campaigns. *Atmos. Meas. Tech.* **7**, 4401–4416 (2014).
148. Salmon, S. R., De Lange, K. M. & Lane, J. R. Structure and Abundance of Nitrous Oxide Complexes in Earth's Atmosphere. *J. Phys. Chem. A* **120**, 2096–2105 (2016).
149. Marengo, A. *et al.* Measurement of ozone and water vapor by Airbus in-service aircraft: The MOZAIC airborne program, an overview. *J. Geophys. Res.* **103**, 25631 (1998).
150. Nédélec, P. P. *et al.* Instrumentation on commercial aircraft for monitoring the atmospheric composition on a global scale : The IAGOS system, technical overview of ozone and carbon monoxide measurements. *Tellus B* **67**, 27791 (2015).
151. Allen, G. *et al.* South East Pacific atmospheric composition and variability sampled along 20° S during VOCALS-REx. *Atmos. Chem. Phys.* **11**, 5237–5262 (2011).

152. Dessler, A. E., Hints, E. J., Weinstock, E. M., Anderson, J. G. & Chan, K. R. Mechanisms controlling water vapor in the lower stratosphere: ‘A tale of two stratospheres’. *J. Geophys. Res.* **100**, 167–172 (1995).
153. Froidevaux, L. *et al.* Global Ozone Chemistry and Related trace gas Data records for the Stratosphere (GOZCARDS): Methodology and sample results with a focus on HCl, H<sub>2</sub>O, and O<sub>3</sub>. *Atmos. Chem. Phys.* **15**, 10471–10507 (2015).
154. Hart, M. H. The evolution of the atmosphere of the earth. *Icarus* **33**, 23–39 (1978).
155. Fegley, B. & Schaefer, L. K. in *Treatise on Geochemistry* **6**, 71–90 (Elsevier, 2014).
156. Peacock, A. J. ABC of oxygen: Oxygen at high altitude. *BMJ* **317**, 1063–1066 (1998).
157. Schlatter, T. W. Atmospheric Composition and Vertical Structure. *Natl. Ocean. Atmos. Adm.* **6**, 1–54 (2009).
158. Lawrence, M. G. The Relationship between Relative Humidity and the Dewpoint Temperature in Moist Air: A Simple Conversion and Applications. *Bull. Am. Meteorol. Soc.* **86**, 225–234 (2005).
159. Newton, R. *et al.* Ozonesonde profiles from the West Pacific Warm Pool. *Atmos. Chem. Phys.* **16**, 619–634 (2016).
160. Huang, S., Cui, Z., Zhao, N., Sun, J. & Guo, X. Influence of Ambient Air on Cell Reactions of Li-air Batteries. *Electrochim. Acta* **191**, 473–478 (2016).
161. Gallagher, K. G. *et al.* Quantifying the promise of lithium–air batteries for electric vehicles. *Energy Environ. Sci.* **7**, 1555 (2014).
162. Wen, Z., Shen, C. & Lu, Y. Air Electrode for the Lithium–Air Batteries: Materials and Structure Designs. *Chempluschem* **80**, 270–287 (2015).
163. Park, M., Sun, H., Lee, H., Lee, J. & Cho, J. Lithium-air batteries: Survey on the current status and perspectives towards automotive applications from a Battery Industry Standpoint. *Adv. Energy Mater.* **2**, 780–800 (2012).
164. Tan, P. *et al.* Advances and challenges in lithium-air batteries. *Appl. Energy* **204**, 780–806 (2017).
165. Vegh, J. M., Alonso, J. J., Orra, T. H. & Ilario da Silva, C. Flight Path and Wing Optimization of Lithium-Air Battery Powered Passenger Aircraft. in *53rd AIAA*

- Aerospace Sciences Meeting* 1–13 (2015).
166. Stückl, S., van Toor, J. & Lobentanzer, H. VOLTAIR - The All Electric Propulsion Concept Platform – A Vision For Atmospheric Friendly Flight. in *28th Congress of the International Council of the Aeronautical Sciences* 1–11 (2012).
  167. Reid, C. M., Doble, A. & Seymour, F. W. *Lithium - Air Cell Development*. American Institute of Aeronautics and Astronautics (2018).
  168. Thielmann, A., Isenmann, R. & Wietschel, M. *Technologie-Roadmap Vorwort*. Fraunhofer ISI (2010).
  169. Tan, P., Shyy, W., Zhao, T. S., Wei, Z. H. & An, L. Discharge product morphology versus operating temperature in non-aqueous lithium-air batteries. *J. Power Sources* **278**, 133–140 (2015).
  170. Yang, X. H. & Xia, Y. Y. The effect of oxygen pressures on the electrochemical profile of lithium/oxygen battery. *J. Solid State Electrochem.* **14**, 109–114 (2010).
  171. Griffith, L. D., Sleightholme, A. E. S., Mansfield, J. F., Siegel, D. J. & Monroe, C. W. Correlating Li/O<sub>2</sub> cell capacity and product morphology with discharge current. *ACS Appl. Mater. Interfaces* **7**, 7670–7678 (2015).
  172. Adams, B. D., Radtke, C., Black, R., Trudeau, M. & Zaghbi, K. Current Density Dependence of Peroxide Formation in the Li-O<sub>2</sub> Battery and its Effect on Charge. *Energy Environ. Sci.* **6**, 1772 (2010).
  173. Wang, F. & Li, X. Discharge Li-O<sub>2</sub> batteries with intermittent current. *J. Power Sources* **394**, 50–56 (2018).
  174. Zhai, D. *et al.* Disproportionation in Li-O<sub>2</sub> Batteries Based on a Large Surface Area Carbon Cathode. *J. Am. Chem. Soc.* **135**, 15364–15372 (2013).
  175. Meini, S., Piana, M., Tsiouvaras, N., Garsuch, A. & Gasteiger, H. A. The Effect of Water on the Discharge Capacity of a Non-Catalyzed Carbon Cathode for Li-O<sub>2</sub> Batteries. *Electrochem. Solid-State Lett.* **15**, A45 (2012).
  176. Cho, M. H. *et al.* The effects of moisture contamination in the Li-O<sub>2</sub> battery. *J. Power Sources* **268**, 565–574 (2014).
  177. Guo, Z., Dong, X., Yuan, S., Wang, Y. & Xia, Y. Humidity effect on electrochemical

- performance of Li–O<sub>2</sub> batteries. *J. Power Sources* **264**, 1–7 (2014).
178. Luntz, A. C. & McCloskey, B. D. Nonaqueous Li–Air Batteries: A Status Report. *Chem. Rev.* **114**, 11721–11750 (2014).
179. Schwenke, K. U., Metzger, M., Restle, T., Piana, M. & Gasteiger, H. A. The Influence of Water and Protons on Li<sub>2</sub>O<sub>2</sub> Crystal Growth in Aprotic Li–O<sub>2</sub> Cells. *J. Electrochem. Soc.* **162**, A573–A584 (2015).
180. Adams, J., Karulkar, M. & Anandan, V. Evaluation and electrochemical analyses of cathodes for lithium-air batteries. *J. Power Sources* **239**, 132–143 (2013).
181. Takechi, K., Shiga, T. & Asaoka, T. A Li–O<sub>2</sub>/CO<sub>2</sub> battery. *Chem. Commun.* **47**, 3463 (2011).
182. Beyer, H., Meini, S., Tsiouvaras, N., Piana, M. & Gasteiger, H. A. Thermal and electrochemical decomposition of lithium peroxide in non-catalyzed carbon cathodes for Li–air batteries. *Phys. Chem. Chem. Phys.* **15**, 11025 (2013).
183. Black, R. *et al.* The Nature and Impact of Side Reactions in Glyme-based Sodium – Oxygen Batteries. *ChemSusChem.* **9**, 1–10 (2016).
184. Meini, S. *et al.* Rechargeability of Li-air cathodes pre-filled with discharge products using an ether-based electrolyte solution: implications for cycle-life of Li-air cells. *Phys. Chem. Chem. Phys.* **15**, 11478–93 (2013).
185. Thotiyl, M. M. O., Freunberger, S. A., Peng, Z. & Bruce, P. G. The Carbon Electrode in Nonaqueous Li–O<sub>2</sub> Cells. *J. Am. Chem. Soc.* **135**, 494–500 (2013).
186. Zhang, J. G., Wang, D., Xu, W., Xiao, J. & Williford, R. E. Ambient operation of Li/Air batteries. *J. Power Sources* **195**, 4332–4337 (2010).
187. Yoo, K., Banerjee, S. & Dutta, P. Modeling of volume change phenomena in a Li-air battery. *J. Power Sources* **258**, 340–350 (2014).
188. Zhang, S. S., Xu, K. & Read, J. A non-aqueous electrolyte for the operation of Li/air battery in ambient environment. *J. Power Sources* **196**, 3906–3910 (2011).
189. Park, J. *et al.* Influence of Temperature on Lithium–Oxygen Battery Behavior. *Nano Lett.* **13**, 2971–2975 (2013).
190. Zhang, Y. *et al.* Amorphous Li<sub>2</sub>O<sub>2</sub>: Chemical Synthesis and Electrochemical Properties.

- Angew. Chemie Int. Ed.* **55**, 10717–10721 (2016).
191. Song, M. *et al.* Discharging temperature dependence of Li<sub>2</sub>O<sub>2</sub> formation and its effect on charging polarization for Li-O<sub>2</sub> battery. *Mater. Res. Bull.* **68**, 75–79 (2015).
  192. Joseph Nemanick, E. & Hickey, R. P. The effects of O<sub>2</sub> pressure on Li-O<sub>2</sub> secondary battery discharge capacity and rate capability. *J. Power Sources* **252**, 248–251 (2014).
  193. Shibata, K., Uemura, S., Tsushima, S. & Hirai, S. Reaction and Mass Transport Simulations by LBM in Electrolyte of Aqueous Lithium-Air Battery. *ECS Trans.* **64**, 39–46 (2015).
  194. Lepoivre, F., Grimaud, A., Larcher, D. & Tarascon, J.-M. Long-Time and Reliable Gas Monitoring in Li-O<sub>2</sub> Batteries via a Swagelok Derived Electrochemical Cell. *J. Electrochem. Soc.* **163**, A923–A929 (2016).
  195. Kwon, H. J. *et al.* Effects of oxygen partial pressure on Li-air battery performance. *J. Power Sources* **364**, 280–287 (2017).
  196. Kwak, K.-H., Kim, D. W., Kang, Y. & Suk, J. Hierarchical Ru- and RuO<sub>2</sub>-foams as high performance electrocatalysts for rechargeable lithium–oxygen batteries. *J. Mater. Chem. A* **4**, 16356–16367 (2016).
  197. Kwak, K. H., Kim, D. W., Kang, Y., Suk, J. & Division, A. M. Supporting Information: Hierarchical Ru- and RuO<sub>2</sub>-foams as high performance cathodes for rechargeable lithium-oxygen batteries. *ournal Mater. Chem. A* **4**, 16356–16367 (2016).
  198. Choi, J. W. & Aurbach, D. Promise and reality of post-lithium-ion batteries with high energy densities. *Nat. Rev. Mater.* **1**, (2016).
  199. Beattie, S. D., Manolescu, D. M. & Blair, S. L. High-Capacity Lithium–Air Cathodes. *J. Electrochem. Soc.* **156**, A44 (2009).
  200. Shen, Y. *et al.* A high-capacity lithium–air battery with Pd modified carbon nanotube sponge cathode working in regular air. *Carbon.* **62**, 288–295 (2013).
  201. Zhou, W. *et al.* Hierarchical Micron-Sized Mesoporous/Macroporous Graphene with Well-Tuned Surface Oxygen Chemistry for High Capacity and Cycling Stability Li–O<sub>2</sub> Battery. *ACS Appl. Mater. Interfaces* **7**, 3389–3397 (2015).
  202. Black, R. *et al.* Screening for Superoxide Reactivity in Li-O<sub>2</sub> Batteries : Effect on

- Li<sub>2</sub>O<sub>2</sub>/LiOH crystallization. *J. Am. Chem. Soc.* **134**, 2902–2905 (2012).
203. Li, M. *et al.* Controlling the microstructure of poly(vinylidene-fluoride) (PVDF) thin films for microelectronics. *J. Mater. Chem. C* **1**, 7695–7702 (2013).
204. Karabelli, D. Séparateurs Macroporeux Innovants à base de Poly(Fluorure de vinildène) (PVdF) pour Supercondensateurs. (2012).
205. Du Pasquier, A. *et al.* Differential Scanning Calorimetry Study of the Reactivity of Carbon Anodes in Plastic Li-Ion Batteries. *J. Electrochem. Soc.* **145**, 472–477 (1998).
206. Lozano, A., Yip, B. & Hanson, R. K. Acetone: a tracer for concentration measurements in gaseous flows by planar laser-induced fluorescence. *Exp. Fluids* **13**, 369–376 (1992).
207. Wood, D. L. *et al.* Technical and economic analysis of solvent-based lithium-ion electrode drying with water and NMP. *Dry. Technol.* **36**, 234–244 (2018).
208. M., Doyle, J., Newman, A.S., Gozdz, C.N., Schumtz, J.M, T. Comparison of Modeling Predictions with Experimental Data from Plastic Lithium Ion Cells. *J. Electrochem. Soc.* **143**, 1890 (1996).
209. Yin, Y. A coupled Modeling/Experimental Study of Li-air Batteries. (2018).
210. Brunauer, S., Emmett, P. H. & Teller, E. Adsorption of Gases in Multimolecular Layers. *J. Am. Chem. Soc.* **60**, 309–319 (1938).
211. Barrett, E. P., Joyner, L. G. & Halenda, P. P. The Determination of Pore Volume and Area Distributions in Porous Substances. I. Computations from Nitrogen Isotherms. *J. Am. Chem. Soc.* **73**, 373–380 (1951).
212. Ishak, H. *et al.* Aqueous solubility, vapor pressure and octanol-water partition coefficient of two phthalate isomers dibutyl phthalate and di-isobutyl phthalate contaminants of recycled food packages. *Fluid Phase Equilib.* **427**, 362–370 (2016).
213. David Linden & Thomas Reddy. in *Handbook of Batteries* (ed. Mc Graw Hill Professional) 74 (R. R. Donelley & Sons Coompany, 2001).
214. Day, Z. Preliminary studies in using X-ray diffraction for analyzing the atomic structure of Central Plains tradition constituents. (2016).
215. Yoo, K., Banerjee, S., Kim, J. & Dutta, P. A Review of Lithium-Air Battery Modeling Studies. *Energies* **10**, 1748 (2017).

216. Tan, P., Kong, W., Shao, Z., Liu, M. & Ni, M. Advances in modeling and simulation of Li-air batteries. *Prog. Energy Combust. Sci.* **62**, 155–189 (2017).
217. Yuan, J., Yu, J.-S. & Sundén, B. Review on mechanisms and continuum models of multi-phase transport phenomena in porous structures of non-aqueous Li-Air batteries. *J. Power Sources* **278**, 352–369 (2015).
218. Cazeaux, P. *Autour de la modélisation du poumon*. (2012).
219. Luntz, A. C. *et al.* Tunneling and polaron charge transport through Li<sub>2</sub>O<sub>2</sub> in Li-O<sub>2</sub> batteries. *J. Phys. Chem. Lett.* **4**, 3494–3499 (2013).
220. Tjaden, B., Cooper, S. J., Brett, D. J., Kramer, D. & Shearing, P. R. On the origin and application of the Bruggeman correlation for analysing transport phenomena in electrochemical systems. *Curr. Opin. Chem. Eng.* **12**, 44–51 (2016).
221. Bruggeman, D. A. G. Berechnung verschiedener physikalischer Konstanten von heterogenen Substanzen. *Ann. Phys.* **421**, 160–178 (1937).
222. Langtangen, H. P. *Finite difference methods for diffusion processes*. (2016).
223. Lu, J. & Amine, K. Recent research progress on non-aqueous lithium-air batteries from Argonne National Laboratory. *Energies* **6**, 6016–6044 (2013).
224. Balaish, M., Kraytsberg, A. & Ein-Eli, Y. A critical review on lithium-air battery electrolytes. *Phys. Chem. Chem. Phys.* **16**, 2801–2822 (2014).
225. Xu, K. Nonaqueous Liquid Electrolytes for Lithium-Based Rechargeable Batteries. *Chem. Rev.* **104**, 4303–4417 (2004).
226. Aurbach, D. *et al.* Design of electrolyte solutions for Li and Li-ion batteries: a review. *Electrochim. Acta* **50**, 247–254 (2004).
227. Younesi, R., Veith, G. M., Johansson, P., Edström, K. & Vegge, T. Lithium salts for advanced lithium batteries: Li-metal, Li-O<sub>2</sub>, and Li-S. *Energy Environ. Sci.* **8**, 1905–1922 (2015).
228. Biotechnology, S. C. *Triglyme Material Safety Data Sheet*. (2009).
229. Biotechnology, S. C. *Diglyme Material Data Sheet*. (2011).



230. Hawash, Z., Ono, L. K. & Qi, Y. Photovoltaics: Moisture and Oxygen Enhance Conductivity of LiTFSI-Doped Spiro-MeOTAD Hole Transport Layer in Perovskite Solar Cells. *Adv. Mater. Interfaces* **3**, 1600117 (2016).
231. Xia, C., Kwok, C. Y. & Nazar, L. F. A High Energy Density Lithium-Oxygen Battery Based on a Reversible Four Electron Conversion to Lithium Oxide. **781**, 777–781 (2018).
232. Tian, F., Radin, M. D. & Siegel, D. J. Enhanced charge transport in amorphous  $\text{Li}_2\text{O}_2$ . *Chem. Mater.* **26**, 2952–2959 (2014).
233. Yin, Y., Torayev, A., Gaya, C., Mammeri, Y. & Franco, A. A. Linking the Performances of Li-O<sub>2</sub> Batteries to Discharge Rate and Electrode and Electrolyte Properties through the Nucleation Mechanism of  $\text{Li}_2\text{O}_2$ . *J. Phys. Chem. C* **121**, 19577–19585 (2017).
234. Köhler, H. The Nucleus in and the Growth Of Hygroscopic Droplets. *Trans. Faraday Soc.* 1152–1161 (1936).
235. Polte, J. Fundamental growth principles of colloidal metal nanoparticles - a new perspective. *CrystEngComm* **17**, 6809–6830 (2015).
236. Molaeimanesh, G. R. & Nazemian, M. Investigation of GDL compression effects on the performance of a PEM fuel cell cathode by lattice Boltzmann method. *J. Power Sources* **359**, 494–506 (2017).
237. Radhakrishnan, V. & Haridoss, P. Effect of GDL compression on pressure drop and pressure distribution in PEMFC flow field. *Int. J. Hydrogen Energy* **36**, 14823–14828 (2011).
238. Ge, J., Higier, A. & Liu, H. Effect of gas diffusion layer compression on PEM fuel cell performance. *J. Power Sources* **159**, 922–927 (2006).
239. Kartal, M., Alp, A. & Akbulut, H. Electrical Conductivity, Viscosity and Thermal Properties of TEGDME-Based Composite Electrolytes for Lithium-Air Batteries. *Acta Phys. Pol. A* **129**, 816–818 (2016).
240. Lau, S. & Archer, L. A. Nucleation and Growth of Lithium Peroxide in the Li-O<sub>2</sub> Battery. *Nano Lett.* **15**, 5995–6002 (2015).
241. Lee, J.-H. *et al.* The role of vacancies and defects in  $\text{Na}_{0.44}\text{MnO}_2$  nanowire catalysts for

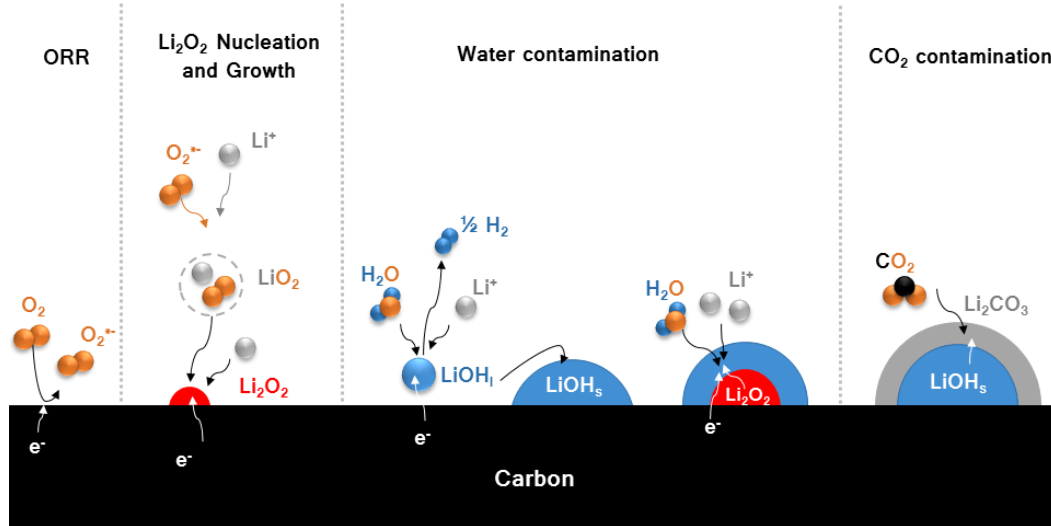
- lithium–oxygen batteries. *Energy Environ. Sci.* **5**, 9558 (2012).
242. Lu, Y.-C. *et al.* Lithium-oxygen batteries: bridging mechanistic understanding and battery performance. *Energy Environ. Sci.* **6**, 750–768 (2013).
243. Aetukuri, N. B. *et al.* Solvating additives drive solution-mediated electrochemistry and enhance toroid growth in non-aqueous Li-O<sub>2</sub> batteries. *Nat. Chem.* **7**, 50–56 (2015).
244. Canham, P. B. The minimum energy of bending as a possible explanation of the biconcave shape of the human red blood cell. *J. Theor. Biol.* **26**, 61–81 (1970).
245. Deuling, H. J. & Helfrich, W. Red blood cell shapes as explained on the basis of curvature elasticity. *Biophys. J.* **16**, 861–868 (1976).
246. Berezina, T. L. *et al.* Influence of storage on red blood cell rheological properties. *J. Surg. Res.* **102**, 6–12 (2002).
247. Mitchell, R. R., Gallant, B. M., Shao-Horn, Y. & Thompson, C. V. Mechanisms of Morphological Evolution of Li<sub>2</sub>O<sub>2</sub> Particles during Electrochemical Growth. *J. Phys. Chem. Lett.* **4**, 1060–1064 (2013).
248. Ganapathy, S. *et al.* Nature of Li<sub>2</sub>O<sub>2</sub> Oxidation in a Li–O<sub>2</sub> Battery Revealed by Operando X-ray Diffraction. *J. Am. Chem. Soc.* **136**, 16335–16344 (2014).
249. Zhang, G. Q. *et al.* Lithium–Air Batteries Using SWNT/CNF Buckypapers as Air Electrodes. *J. Electrochem. Soc.* **157**, A953–A956 (2010).
250. Nanda, J. *et al.* Anomalous discharge product distribution in lithium-air cathodes. *J. Phys. Chem. C* **116**, 8401–8408 (2012).
251. Ren, X., Zhang, S. S., Tran, D. T. & Read, J. Oxygen reduction reaction catalyst on lithium/air battery discharge performance. *J. Mater. Chem.* **21**, 10118–10125 (2011).
252. Wong, R. A. *et al.* Structurally Tuning Li<sub>2</sub>O<sub>2</sub> by Controlling the Surface Properties of Carbon Electrodes: Implications for Li–O<sub>2</sub> Batteries. *Chem. Mater.* **28**, 8006–8015 (2016).
253. Torayev, A. *et al.* Stochasticity of Pores Interconnectivity in Li–O<sub>2</sub> Batteries and its Impact on the Variations in Electrochemical Performance. *J. Phys. Chem. Lett.* **9**, 791–797 (2018).
254. Sahapatombut, U., Cheng, H. & Scott, K. Modelling of operation of a lithium-air battery

with ambient air and oxygen-selective membrane. *J. Power Sources* **249**, 418–430 (2014).



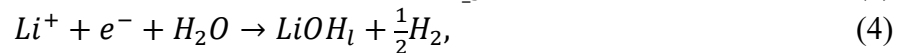
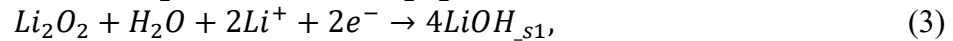
# ANNEX: MODEL CONTAMINATION

## Presentation of model

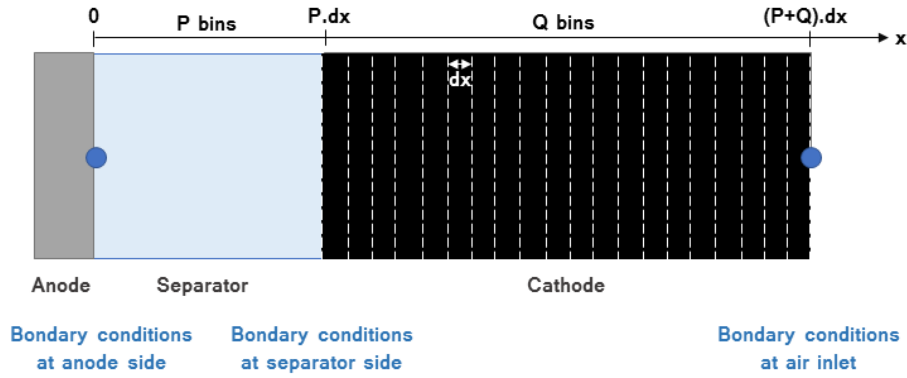


*Annex Figure 1: Schematic of the reactions considered in the contamination model.*

This model was built in order to highlight the possible impacts of air versus pure oxygen supply. The aim was not to focus on the electrode or electrolyte degradation in presence of air. Here, a stable system based on GDLs electrodes was assumed. The model was built in order to take into account the effect of water and carbon dioxide contamination (Annex Figure 1). Then, relative humidity should be easily tuned to see its influence. The reactions simulated were based on the several contaminations mechanisms proposed in literature. To ease the code development, formation of two types of particles was assumed. Rather the particles were based on  $\text{Li}_2\text{O}_2$  nuclei (particles 1) or formed from  $\text{LiOH}$  nucleation (particles 2). Also, ORR reaction was presupposed fast enough to not explicitly describing it. Finally, the previous assumption led to the following list of reactions for the model (nucleation reactions excluded):



The model was then describing the system presented in Annex Figure 2.



Annex Figure 2: Schematic of the model described.

Similarly, as in the previous code, species diffusion was determined along the system (separator + cathode) by the Fick's law:

$$\frac{\partial(\varepsilon \cdot c^X)}{\partial t} = -\nabla J_X^{Diff} - R_X \quad 1.1.$$

with  $\varepsilon$  the cathode porosity,  $c^X$  the concentration of specie X,  $J_X^{Diff}$  the diffusion flux of specie X and  $R_X$  the source term for X due to the reactions (consumption or production). Lithium cations, water, carbon dioxide and oxygen diffusion were solved along the electrode thickness as well as the produced species such as LiOH and LiO<sub>2</sub>. The diffusion flux was defined by the following equation:

$$J_X^{Diff} = -D_X \frac{\partial c^X}{\partial x} \quad 1.2.$$

where  $D_X$  is the effective diffusion coefficient of species X calculated from Bruggeman relation based on :

$$D_X = D_0 \cdot \varepsilon^{1.5} \quad 1.3.$$

with  $D_0$  the oxygen diffusion coefficient of the electrolyte solvent (TetraGDME as TriGDME value was not available)<sup>79</sup> and the Bruggeman coefficient equal to 1.5. For the sake of simplicity and as the values were not available in literature, water and carbon dioxide effective diffusion coefficient were assumed to be equal to the oxygen one.

The equation was then discretized using the volume finite method as presented in discretization part.

### Discretization of the Fick's law

Combination of equation I.1., I.2 and I.3. led for specie X to:

$$\frac{\partial(\varepsilon.c)}{\partial t} = \frac{\partial}{\partial x} \left( D_0 \varepsilon^\beta \frac{\partial c}{\partial x} \right) - R_X. \quad I.4.$$

As  $D_0$  is a constant, the equation could be rewrite as:

$$\frac{\partial(\varepsilon.c)}{\partial t} = D_0 \frac{\partial}{\partial x} \left( \varepsilon^\beta \frac{\partial c}{\partial x} \right) - R_X. \quad I.5.$$

Once discretized by the finite volume method, the diffusion in the bin  $i$  at time  $t$  was obtained according to:

$$\left( \frac{\varepsilon_i^{t+1} c_i^{t+1} - \varepsilon_i^t c_i^t}{\Delta t} \right) = D_0 \frac{\left[ (\varepsilon^\beta)^t_{i+\frac{1}{2}} \left( \frac{\partial c}{\partial x} \right)_{i+\frac{1}{2}} - (\varepsilon^\beta)^t_{i-\frac{1}{2}} \left( \frac{\partial c}{\partial x} \right)_{i-\frac{1}{2}} \right]}{\Delta x} - R_X. \quad I.6.$$

Then several adjustments were implemented:

$$\left( \frac{\varepsilon_i^{t+1} c_i^{t+1} - \varepsilon_i^t c_i^t}{\Delta t} \right) = D_0 \frac{\left[ (\varepsilon^\beta)^t_{i+\frac{1}{2}} \left( \frac{c_{i+1}^t - c_i^t}{\Delta x} \right) - (\varepsilon^\beta)^t_{i-\frac{1}{2}} \left( \frac{c_i^t - c_{i-1}^t}{\Delta x} \right) \right]}{\Delta x} - R_x^i, \quad I.7.$$

$$\left( \frac{\varepsilon_i^{t+1} c_i^{t+1} - \varepsilon_i^t c_i^t}{\Delta t} \right) = D_0 \frac{\left[ \frac{(\varepsilon^\beta)^t_{i+\frac{1}{2}} c_{i+1}^t}{\Delta x} - \frac{(\varepsilon^\beta)^t_{i+\frac{1}{2}} c_i^t}{\Delta x} - \frac{(\varepsilon^\beta)^t_{i-\frac{1}{2}} c_i^t}{\Delta x} + \frac{(\varepsilon^\beta)^t_{i-\frac{1}{2}} c_{i-1}^t}{\Delta x} \right]}{\Delta x} - R_x^i, \quad I.8.$$

$$\left( \frac{\varepsilon_i^{t+1} c_i^{t+1} - \varepsilon_i^t c_i^t}{\Delta t} \right) = D_0 \frac{\left[ (\varepsilon^\beta)^t_{i+\frac{1}{2}} c_{i+1}^t - \left( (\varepsilon^\beta)^t_{i+\frac{1}{2}} + (\varepsilon^\beta)^t_{i-\frac{1}{2}} \right) c_i^t + (\varepsilon^\beta)^t_{i-\frac{1}{2}} c_{i-1}^t \right]}{\Delta x^2} - R_x^i, \quad I.9.$$

Introducing that  $(\varepsilon^\beta)^t_{i+\frac{1}{2}} = \frac{(\varepsilon^\beta)^t_{i+1} + (\varepsilon^\beta)^t_i}{2}$  and  $(\varepsilon^\beta)^t_{i-\frac{1}{2}} = \frac{(\varepsilon^\beta)^t_i + (\varepsilon^\beta)^t_{i-1}}{2}$ , a new equation was reached:

$$\left( \frac{\varepsilon_i^{t+1} c_i^{t+1} - \varepsilon_i^t c_i^t}{\Delta t} \right) = D_0 \frac{\left[ \left( \frac{(\varepsilon^\beta)^t_{i+1} + (\varepsilon^\beta)^t_i}{2} \right) c_{i+1}^t - \left( \frac{(\varepsilon^\beta)^t_{i+1} + (\varepsilon^\beta)^t_i}{2} + \frac{(\varepsilon^\beta)^t_i + (\varepsilon^\beta)^t_{i-1}}{2} \right) c_i^t + \left( \frac{(\varepsilon^\beta)^t_i + (\varepsilon^\beta)^t_{i-1}}{2} \right) c_{i-1}^t \right]}{\Delta x^2} - R_x^i, \quad I.10.$$

$$\left( \frac{\varepsilon_i^{t+1} c_i^{t+1} - \varepsilon_i^t c_i^t}{\Delta t} \right) = D_0 \frac{\left[ \left( \frac{(\varepsilon^\beta)^t_{i+1} + (\varepsilon^\beta)^t_i}{2} \right) c_{i+1}^t - \left( \frac{(\varepsilon^\beta)^t_{i+1} + 2(\varepsilon^\beta)^t_i + (\varepsilon^\beta)^t_{i-1}}{2} \right) c_i^t + \left( \frac{(\varepsilon^\beta)^t_i + (\varepsilon^\beta)^t_{i-1}}{2} \right) c_{i-1}^t \right]}{\Delta x^2} - R_x^i, \quad I.11.$$

this leading to:

$$\varepsilon_i^{t+1} c_i^{t+1} = \varepsilon_i^t c_i^t + \frac{D_0 \Delta t}{\Delta x^2} \left[ \left( \frac{(\varepsilon^\beta)_{i+1}^t + (\varepsilon^\beta)_i^t}{2} \right) c_{i+1}^t - \left( \frac{(\varepsilon^\beta)_{i+1}^t + 2(\varepsilon^\beta)_i^t + (\varepsilon^\beta)_{i-1}^t}{2} \right) c_i^t + \left( \frac{(\varepsilon^\beta)_i^t + (\varepsilon^\beta)_{i-1}^t}{2} \right) c_{i-1}^t \right] - R_x^i \cdot \Delta t. \quad I.12.$$

To simplify, a new annotation was taken,  $z = \varepsilon c$ , permitting to write :

$$z_i^{t+1} = z_i^t + \frac{D_0 \Delta t}{\Delta x^2} \left[ \left( \frac{(\varepsilon^\beta)_{i+1}^t + (\varepsilon^\beta)_i^t}{2} \right) c_{i+1}^t - \left( \frac{(\varepsilon^\beta)_{i+1}^t + 2(\varepsilon^\beta)_i^t + (\varepsilon^\beta)_{i-1}^t}{2} \right) c_i^t + \left( \frac{(\varepsilon^\beta)_i^t + (\varepsilon^\beta)_{i-1}^t}{2} \right) c_{i-1}^t \right] - R_x^i \cdot \Delta t, \quad I.13.$$

giving finally:

$$z_i^{t+1} = z_i^t + \frac{D_0 \Delta t}{2 \Delta x^2} \left[ ((\varepsilon^\beta)_{i+1}^t + (\varepsilon^\beta)_i^t) c_{i+1}^t - ((\varepsilon^\beta)_{i+1}^t + 2(\varepsilon^\beta)_i^t + (\varepsilon^\beta)_{i-1}^t) c_i^t + ((\varepsilon^\beta)_i^t + (\varepsilon^\beta)_{i-1}^t) c_{i-1}^t \right] - R_x^i \cdot \Delta t. \quad I.14.$$

### **Boundary conditions**

#### **Air inlet**

The model was created to easily recreate the air supply and to tune the relative humidity applied. At the air inlet, the diffusive species concentrations in this bin P+Q depends on the ones in P+Q+1. Concentrations in P+Q+1 were linked to the species dissolution in the electrolyte and so were determined using Henry's law<sup>254</sup>:

$$c_{P+Q+1}^X = H_X \cdot p_X \quad I.15.$$

with  $c^X$  concentration of the gas X,  $H_X$  Henry's law constant for the gas X depending on temperature and electrolyte selected and  $p_X$  the partial pressure of the gas X in the atmosphere. Knowing  $c_{P+Q+1}^X$  for all the gas permitted in combination to equation I.14 to calculate their concentrations in the last bin P+Q.

For the other diffusive species not gaseous, diffusion was impeded at P+Q and so a flux equal to zero was considered

$$\left( \frac{\partial c^X}{\partial x} \right)_{air \ inlet} = \frac{c_{P+Q+1}^X - c_{P+Q}^X}{\Delta x} = 0, \quad I.16.$$

leading to

$$c_{P+Q+1}^X = c_{P+Q}^X. \quad I.17.$$



### Anode inlet

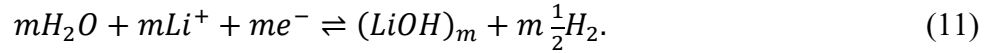
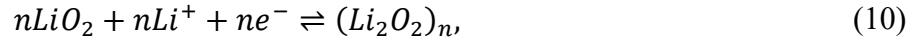
At the anode side except for lithium, all the boundary conditions were solved using the same way a flux equal to zero. Application of a zero flux equal to zero enabled to implement in the equation I.14. that

$$c_{P+Q-1}^X = c_{P+Q}^X. \quad I.18.$$

For the lithium, an extra bin at the maximal concentration was assumed as done in previous model ( $c_{P+Q-1}^{Li^+} = 1 M$ ).

### Nucleation

As in Yin *et al.* paper, heterogeneous nucleation of hemispherical particles was considered.<sup>233</sup> Still, here two competing nucleation mechanism were imagined and described: one for  $Li_2O_2$  nucleation and one for  $LiOH$  (n and m correspond to the numbers of units included in one nuclei of  $Li_2O_2$  or  $LiOH$  respectively).



For each nucleation reaction, a Gibbs formation energy was calculated based on:

$$\Delta G_{critic} = \frac{4B\sigma^3V_m^2}{27(z e \|\eta\|)^2} \quad I.19.$$

with B the geometrical parameter (equal to 18 in case of hemisphere),  $\sigma$  the specific surface energy of  $Li_2O_2$  or  $LiOH$  in contact to the electrolyte,  $V_m$  the volume molar of  $Li_2O_2$  or  $LiOH$ , z the number of electrons transferred, and  $\eta$  the overpotential associated to the nucleation reaction.

Thanks to the Gibbs formation energy, the nucleation reaction kinetics was calculated using:

$$v_{nucleation} = k_{nu} \cdot A_c \cdot e^{\left(-\frac{\Delta G_{critic}}{k_b \cdot T}\right)} \quad I.19.$$

with  $k_{nu}$  the kinetic constant (adjusted) and  $A_c$  the active carbon surface (surface of carbon uncovered from particles).

After the nucleation step, growth was able started. To save the evolution of the particle size distribution, the following equation was implemented:

$$\frac{\partial f(L, t)}{\partial t} + \frac{\partial}{\partial L} \left( f(L, t) \frac{\partial L}{\partial t} \right) = S_{nucleation} \quad I.19.$$

with  $S_{nucleation}$  the nucleation source term and  $f(L, t)$  the number of particles with a size  $L$  at time  $t$ .

Particles formation and growth were assumed to occur within the range of 0-300 nm and the radius step to store them selected was fixed at 2 nm leading to 150 particle classes.

### Kinetics

Depending on the reaction (electrochemical, chemical or as aforementioned nucleation), the kinetics was calculated differently. The following table sums up the kinetics calculations for all reactions (except nucleation).

1	$Li^+ + e^- + O_2 \rightarrow LiO_2,$	$v_1 = k_{f1} \cdot A_c \cdot a_{Li^+} \cdot a_{O_2} \cdot e^{\left(\frac{-\alpha n_1 F(U-E_1^0)}{R.T}\right)} - k_{b1} \cdot a_{LiO_2} \cdot e^{\left(\frac{-(1-\alpha)n_1 F(U-E_1^0)}{R.T}\right)}$
2	$LiO_2 + Li^+ + e^- \rightarrow Li_2O_2,$	$v_2 = k_{f2} \cdot \zeta^{tunneling} \cdot \theta_{s1} \cdot a_{LiO_2} \cdot a_{Li^+} \cdot e^{\left(\frac{-\alpha n_2 F(U-E_2^0)}{R.T}\right)} - k_{b2} \cdot \theta_{s1} \cdot \gamma_{Li_2O_2} \cdot e^{\left(\frac{-(1-\alpha)n_2 F(U-E_2^0)}{R.T}\right)}$
3	$Li_2O_2 + H_2O + 2Li^+ + 2e^- \rightarrow 4LiOH_{s1},$	$v_3 = k_{f3} \cdot \zeta^{tunneling} \cdot \theta_{s1} \cdot \gamma_{Li_2O_2} \cdot a_{H_2O} \cdot a_{Li^+}^{1/2} \cdot e^{\left(\frac{-\alpha n_3 F(U-E_3^0)}{R.T}\right)} - k_{b3} \cdot \theta_{s1} \cdot \gamma_{LiOH_{s1}} \cdot e^{\left(\frac{-(1-\alpha)n_3 F(U-E_3^0)}{R.T}\right)}$
4	$Li^+ + e^- + H_2O \rightarrow LiOH_l + \frac{1}{2}H_2,$	$v_4 = k_{f4} \cdot A_c \cdot a_{Li^+} \cdot a_{H_2O} \cdot e^{\left(\frac{-\alpha n_4 F(U-E_4^0)}{R.T}\right)} - k_{b4} \cdot a_{LiOH_l} \cdot e^{\left(\frac{-(1-\alpha)n_4 F(U-E_4^0)}{R.T}\right)}$
5	$2LiO_2 \rightarrow Li_2O_2,$	$v_5 = k_{ads5} \cdot \theta_{s1} \cdot a_{LiO_2} - k_{des5} \cdot \theta_{s1} \cdot \gamma_{Li_2O_2}$
6	$2LiOH_{s1} + CO_2 \rightarrow Li_2CO_{3,s1},$	$v_6 = k_{f6} \cdot \theta_{s1} \cdot \gamma_{LiOH_{s1}} \cdot a_{CO_2} \cdot e^{\left(\frac{-\alpha n_6 F(U-E_6^0)}{R.T}\right)} - k_{b6} \cdot \theta_{s1} \cdot \gamma_{Li_2CO_{3,s1}} \cdot e^{\left(\frac{-(1-\alpha)n_6 F(U-E_6^0)}{R.T}\right)}$
7	$2LiOH_{s2} + CO_2 \rightarrow Li_2CO_{3,s2},$	$v_7 = k_{f7} \cdot \theta_{s2} \cdot \gamma_{LiOH_{s2}} \cdot a_{CO_2} \cdot e^{\left(\frac{-\alpha n_7 F(U-E_7^0)}{R.T}\right)} - k_{b7} \cdot \theta_{s2} \cdot \gamma_{Li_2CO_{3,s2}} \cdot e^{\left(\frac{-(1-\alpha)n_7 F(U-E_7^0)}{R.T}\right)}$
8	$LiOH_l \rightarrow LiOH_{s1},$	$v_8 = k_{ads8} \cdot \theta_{s1} \cdot a_{LiOH_l} - k_{des8} \cdot \theta_{s1} \cdot \gamma_{LiOH_{s1}}$
9	$LiOH_l \rightarrow LiOH_{s2}.$	$v_9 = k_{ads9} \cdot \theta_{s2} \cdot a_{LiOH_l} - k_{des9} \cdot \theta_{s2} \cdot \gamma_{LiOH_{s2}}$

As two types of particles coexist (1 or 2), the kinetics take into account the surface and composition of the particles depending of the class. Here,  $\theta_{s1}$  stands for the surface developed by the particle based on  $Li_2O_2$  nucleation and  $\gamma_{j,s1}$  corresponds to the molar fraction of component  $j$  in this particle. Both were calculated for each particle class. Same way, for the particles based on  $LiOH$  nucleation  $\theta_{s2}$  and  $\gamma_{j,s2}$  were estimated.

Storing composition for all the particles existing within the same class is too heavy. For this reason, in each class, an overall molar fraction is estimated for each particle class (1 or 2).

For simplicity, and due to the significant unknown parameters (all the kinetics constant  $k$ ), it was assumed that for all electrochemical reactions,  $\alpha$  was the same and equal to 0.5.

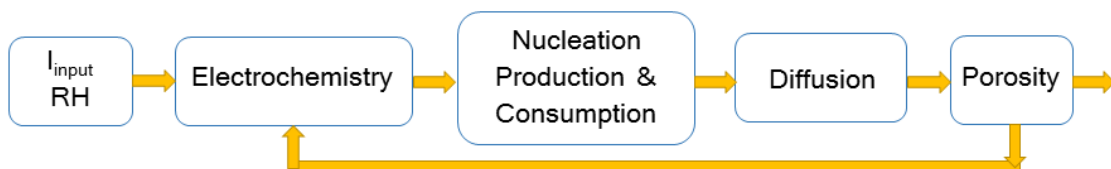
### Electrochemistry

Each local faradic current associated to one of the electrochemical reactions described above ( $j = 1,2,3,4$ ) is then estimated according to:

$$i_j^{Faradic} = n_j F v_j. \quad I.20.$$

The sum of all the local faradic current should then correspond to the overall current applied to the system  $I_{input}$ .

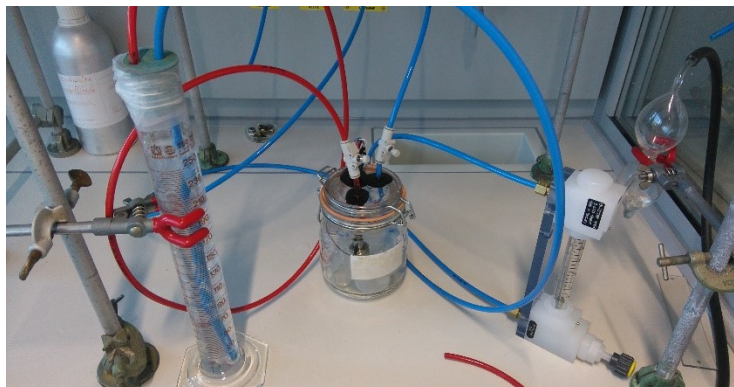
### Code chart flow





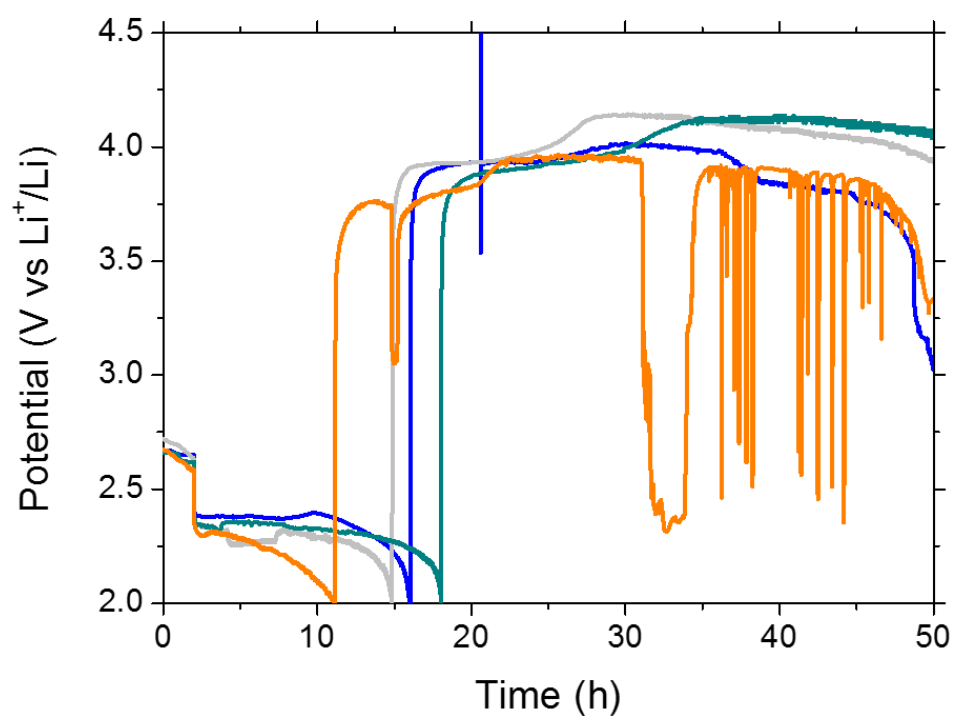
## ANNEX: AIR FLUSHING TEST

The following set-up was used to enrich the pure dry oxygen flow with water.



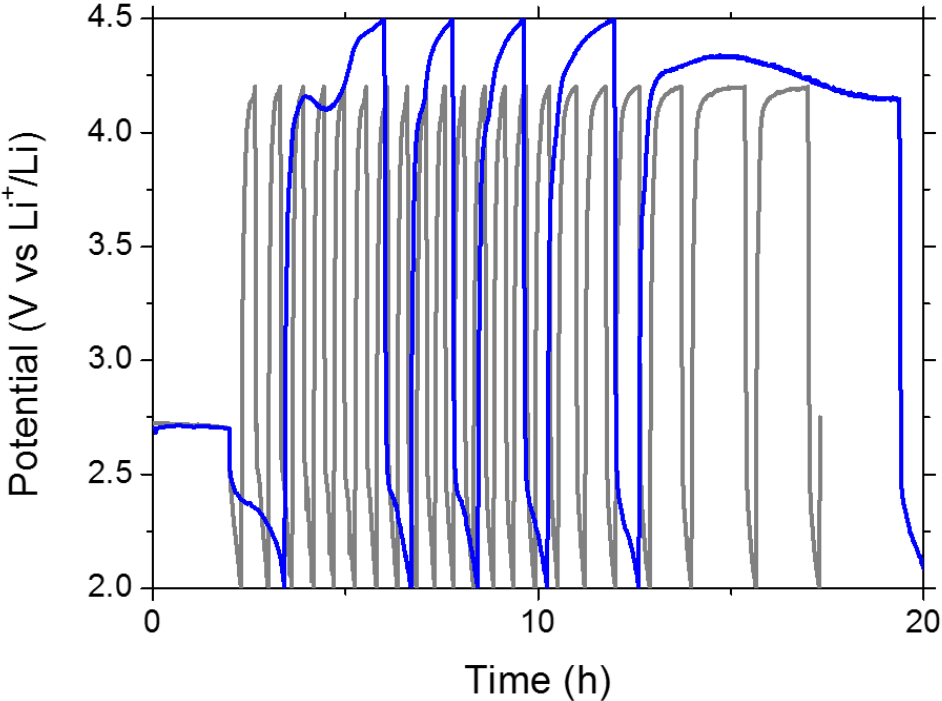
*Annex Figure 3: Schematic of the set-up to let oxygen flow bubble in water.*

Finally, the cells voltage was oscillating a lot and the cells were unable to bear the charge step most probably due to degradation mechanisms (cathode and electrolyte).



*Annex Figure 4: GDLs flushed with wet oxygen then cycled at  $\pm 50 \mu\text{A}$  after two hours of OCV.*

As the charge cutoff at 4.5 V was never reached for the test with a mix of oxygen and azote (50-50), the cutoff was later extended until 4 V. In any case the discharge was not possible with this ratio maybe due to too low oxygen supply.



*Annex Figure 5: GDLs flushed with a mix 50-50 of nitrogen and oxygen then cycled at  $\pm 50 \mu A$  after two hours of OCV.*

## ANNEX: FRENCH DESCRIPTION

Un des plus grands défis que rencontrent les avionneurs de nos jours est le développement d'appareils plus respectueux de l'environnement. Pour ce faire, il est essentiel de diminuer les nuisances sonores et surtout la consommation de kérosène. Le passage au tout électrique apparaît donc comme une solution de choix. Bien que sa faisabilité a déjà été démontrée avec des prototypes pouvant embarquer jusqu'à quatre passagers, sa mise en place sur des avions commerciaux est bien plus délicate. En effet, les avions tout électrique nécessitent de revoir complètement le design de l'avion (suppression des turboréacteurs, modification du fuselage, etc.). Pour cette raison, les avionneurs se focalisent sur le développement d'avions plus électriques (A+E) dont la mise en application est envisagée à plus court terme. Dans un avion, deux systèmes d'alimentation coexistent, le système de propulsion et le système secondaire qui alimente les équipements de bord (ex : lumière, dégivrage, système électronique). Le principe des avions A+E est de remplacer les sources d'énergies du système secondaire, habituellement électriques et hydrauliques/pneumatiques, par une source uniquement électrique. Seulement afin de fournir cette énergie électrique, des systèmes de stockage électrochimique présentant de fortes densités d'énergie gravimétrique et volumétrique doivent être utilisés.

Actuellement, les batteries Li-ion sont les plus matures et envahissent d'ores et déjà le marché des dispositifs portables. Leur utilisation se répand jusqu'à la production de voitures tout électrique. Cependant, d'un point de vue de la densité d'énergie gravimétrique ou volumétrique, les batteries Li-ion ont des performances inférieures à celles annoncées pour certaines nouvelles technologies comme les batteries Li-souffre ou Li-air.

L'étude décrite ici a été dédiée à l'étude des batteries Li-air pour des applications à visée aéronautique. Même si d'un point de vue théorique cette technologie est très prometteuse, de nombreux verrous technologiques demeurent, limitant drastiquement les performances réelles par rapport aux théoriques. Les phénomènes limitant rencontrés existent à tous les niveaux de la batterie : la cathode, l'anode, l'électrolyte et l'approvisionnement en oxygène. Parmi ces éléments, comme le principe de fonctionnement de ces batteries repose sur la production de produit de décharge en surface de la cathode après diffusion de l'oxygène, la cathode a été identifiée comme un élément clef pour améliorer les performances et a donc été dûment étudiée.

Cette étude s'est initialement focalisée sur le développement de cathodes poreuses réalisées à partir de carbone, matériau conducteur, abordable et existant sous de nombreuses formes. Afin de promouvoir les réactions de surface, l'utilisation de carbone très divisé a été sélectionnée. Pour pouvoir améliorer la densité d'énergie, l'étude a été orientée vers le design et la production d'électrodes épaisses. De cette façon, la plupart de la masse de la batterie est attribuée à la cathode et non au collecteur de courant ou encore au boîtier. Cependant, utiliser des électrodes épaisses induit une plus grande sensibilité du système face au problème de diffusion de l'oxygène à travers la cathode. Outre la diffusion de l'oxygène, deux autres phénomènes impactent les performances de la cathode : la passivation de la surface par la formation d'un produit de décharge isolant et la fermeture de la porosité par la formation même de ce produit, empêchant d'autant plus la diffusion des espèces.

Pour outrepasser ou tout du moins limiter l'occurrence de ces phénomènes, les électrodes doivent être texturées. Dans cette étude, le développement d'électrodes bi-poreuses a été proposé pour palier à ces problèmes. Le concept proposé a été de considérer des électrodes avec un domaine mesoporeux correspondant au domaine carbone/liant et un domaine macroporeux remplie d'électrolyte. Ce dernier domaine est ajouté sciemment afin de faciliter la diffusion de l'oxygène à travers l'électrode.

Afin d'étudier théoriquement le bénéfice de la texturisation des électrodes, un modèle continuum a été créé. Pour ce faire, le modèle crée prend en compte deux modèles de diffusion 1D (un pour chaque domaine de porosité) et un flux nommé « intraflux » permettant de traduire la diffusion de l'oxygène existant entre ces deux domaines. Comme l'approche développée ici repose sur une intrication de la modélisation et de l'expérience, afin de déterminer l'intérêt d'une telle architecture et de permettre la réalisation pratique des textures simulées, le modèle a été nourri de nombreuses valeurs expérimentales. Pour comprendre quel phénomène limitant été impliqué dans la chute de capacité selon les cas simulés, les trois phénomènes prépondérants à savoir la passivation de l'électrode, le remplissage des pores et les problèmes de diffusion de l'oxygène ont été modélisés. De plus, il a été supposé que le mécanisme de formation du produit de décharge correspondait à la formation d'une fine couche de produits de décharge. Grâce à la modélisation, il a été alors montré que dans le cas d'électrodes à base de Ketjen Black le phénomène majoritairement limitant était la diffusion de l'oxygène ce qui implique donc d'autant plus la nécessité de texturer les électrodes pour la limiter. Le modèle a aussi souligné qu'il n'est pas nécessaire d'ajouter plus 40 % de macroporosité pour améliorer la capacité de décharge.



En parallèle, la réalisation pratique de ces électrodes a été démontrée grâce à l'utilisation d'un procédé usuellement répandu pour les batteries Li-ion : le procédé Bellcore. Il permet la mise en forme d'électrodes flexibles dont la porosité est créée grâce à l'extraction de l'agent porogène, le DBP, par lavages successifs à l'éther. Habituellement réalisés à partir de graphite, l'utilisation de carbone très divisé a nécessité de revoir les ratios utilisés dans la formulation afin de créer des films cohésifs. Une fois le ratio carbone/liant déterminé, il a été conservé pour pouvoir étudier l'impact du taux DBP sur la création de la porosité. L'objectif étant de créer des électrodes très poreuses, une attention particulière a été apportée aux films contenant 40 à 80 m% de DBP. La porosité créée selon les formulations a alors été évaluée. Premièrement, l'efficacité de l'extraction du DBP a été confirmée lorsque trois étapes successives de lavage dans l'éther étaient appliquées (chacune durant 15 min). Cependant quelques inhomogénéités de répartition des composés chimiques au sein du film ont été observées, et ce d'autant plus pour les films avec des taux élevés de DBP. Une fois extraite les électrodes présentaient une porosité à la fois macro et meso. De plus, sûrement du fait de la réorganisation du film lors de l'étape d'extraction, une partie de la porosité demeure inaccessible. Contrairement à ce qui avait été supposé initialement, des taux de DBP supérieurs à 60 m% ne sont pas nécessaires pour obtenir des films très poreux et de surcroit homogènes. En revanche, un taux de DBP moyen (40 m%) permet d'obtenir des électrodes très poreuses (50 v%) avec une importante surface développée (50 m<sup>2</sup>.gelectrode-1). Une fois libérées de l'agent poreux, les électrodes peuvent aisément accueillir l'électrolyte qui remplit alors la porosité accessible. De surcroit, les électrodes supportent des températures jusqu'à 80 °C (gamme requise pour des applications aéronautiques). Pour finir, l'utilisation de telles électrodes comme cathode de batteries Li-air semble tout à fait intéressant puisque 70 % de la capacité théorique ont été atteints avec les films DBP60 et DBP80 déchargés à 50μA.

Les performances des électrodes flexibles bi-poreuses ont été comparées à celles d'électrodes GDL (enchevêtrement de fibres de carbone) ayant une porosité globale comparable (mais uniquement macro). Pourtant à même valeur de courant, seuls 5 % de la capacité théorique ont été obtenus soulignant la nécessité de texturiser les électrodes. De plus, l'importance de la percolation au sein de l'électrode et l'influence de la compression ont pu être mis en avant. Les électrodes GDL bien que réversiblement déformées par rapport aux électrodes flexibles, sont plus impactées par la compression imposée dans la Swagelok car leur réseau de percolation électronique est moins bien étendu que celui des électrodes flexibles. Selon la compression, le nombre de points de contact entre les fibres de carbone peut être modifié et la

percolation plus ou moins modifiée. Au contraire les électrodes flexibles créées avec du carbone très divisé sont capables de maintenir leur réseau de percolation même après déformation. Dans tous les cas, les légères variations de compression appliquées aux électrodes peuvent expliquer une partie des problèmes de reproductibilité observés. Ces problèmes reposaient sur une variation des capacités de décharge obtenues pourtant dans des conditions similaires. De plus, les courbes de décharges présentaient des profils initiaux différents avec présence ou non d'un rapide décrochage du potentiel (chute puis remontée brusques) associé au phénomène de nucléation lié à la formation du peroxyde de lithium.

Afin de limiter la non-reproductibilité des expériences, une étude a été mise en place pour contrôler au fur et à mesure tous les paramètres pouvant jouer un rôle comme le flux d'oxygène appliqué avant la décharge ou encore le taux d'électrolyte précisément ajouté dans la cellule. Aussi, il a été noté que le contrôle des paramètres influençant ou modifiant la nucléation permettait de réduire les fluctuations de capacité, même si en parallèle une diminution des performances pouvait aussi être observée. Par exemple, lorsque les traces d'eau présentes dans l'électrolyte ont été retirées, une nette diminution de la capacité s'est dessinée bien que la gamme de valeurs des capacités était moins étendue. La sensibilité des batteries Li-air face aux traces d'eau était déjà connue cependant, son impact sur la reproductibilité des expériences n'avait à notre connaissance pas encore été démontrée.

Un autre paramètre influençant fortement la décharge est la température puisqu'une variation de deux degrés entraîne des oscillations significatives du potentiel. Un contrôle de la température a donc été mis en place et l'influence de la température a été observée en parallèle avec celle du courant, en plus des mesures préalablement mises en place (GDL, contrôle volume électrolyte, flux d'oxygène, électrolyte séché). Température et courant ont été étudiés simultanément puisqu'ils influencent de manières opposées la cinétique de réaction du système. Pour les deux courant étudiés, l'augmentation de la température a permis une diminution de la variance des capacités et donc une meilleure reproductibilité.

Afin de savoir si la reproductibilité était due à une nucléation mieux contrôlée, les particules formées à la surface des électrodes ont été analysées post-mortem par Microscopie Electronique à Balayage (MEB). Diverses morphologies ont été déposées à la surface des électrodes observées et, fait singulier, pour la plupart étaient bien loin des particules toroïdales généralement décrites dans la littérature. De plus, dans les mêmes conditions de température et courant, diverses morphologies recouvraient les électrodes. Fait encore plus marquant, sur la

même électrode et même parfois sur la même fibre de GDL, les particules formées pouvaient varier. L'origine de la formation de particules si variées sur une seule fibre est complexe à appréhender. Tout de même, la formation des particules semblait clairement dépendre de la location précise sur la surface de l'électrode. La première hypothèse découlant d'une telle observation est que la surface de l'électrode joue un rôle prépondérant dans les performances des cellules, ce qui se comprend puisque la surface joue un rôle dans la nucléation (la barrière énergétique associée à la nucléation dépend des interactions  $\text{Li}_2\text{O}_2$ /surface). Des tests réalisés sur des GDLs prétraitées à 400 °C sous argon, et donc avec une surface modifiée et supposément plus homogène, ont montrés une meilleure reproductibilité des capacités de décharge. De plus, l'électrode analysée a montré la formation homogène de particules en surface.

Au final, grâce à cette étude, l'extrême sensibilité des batteries Li-air face à la température, la présence d'eau et l'état de surface a été soulignée. De même, les problèmes de reproductibilité ont été en partie attribués à une combinaison des paramètres suivant : reproductibilité de l'électrode, réseau de pores formé, compression de l'électrode, traces d'eau, variation de la température, surface de l'électrode non homogène.

La sensibilité des batteries Li-air pose alors problème puisque l'application envisagée ici est extrêmement demandeuse vis-à-vis des conditions de fonctionnement, notamment par rapport à la température. De surcroit, pour l'instant on parle plus de batterie Li-oxygène que Li-air, or un approvisionnement en air plutôt qu'en oxygène pure implique que d'autres gaz comme de la vapeur d'eau soient en présence de la cellule. Quelques tests menaient avec de l'oxygène humide ont abouti à des courbes de décharges instables (parfois pas de plateau clairement dessiné). Lorsqu'un mélange 50-50 azote-oxygène était utilisé, la capacité de décharge fut drastiquement diminuée probablement à cause du réactif en quantité réduite. Pour pouvoir étudier les batteries Li-air cette fois un modèle de nucléation a commencé à être créé pour appréhender et mettre en avant les divers mécanismes de contamination pouvant prendre place lors de la décharge de la cellule. Ces derniers tests ainsi que le modèle sont brièvement présentés en Annexe et soulignent la complexité de tels systèmes.

Ainsi, la priorité dans la course au développement des batteries Li-air est d'abord d'améliorer leurs performances en laboratoire avec de l'oxygène pur comme source principale avant de s'intéresser aux batteries utilisant l'oxygène de l'air. Par ailleurs, un électrolyte stable face aux espèces oxygénés et aux changements de température ainsi que résistant à de hauts

potentiels manque toujours. Des efforts de recherche doivent donc être mis en place dans ce sens. Une fois cet électrolyte défini les électrodes bi-poreuses développées ici pourront permettre d'atteindre de meilleures performances. Cependant, leur application est plus probable pour du stockage stationnaire car il permet aisément de contrôler les conditions de fonctionnement et aussi d'utiliser de l'oxygène pur sans se soucier du poids et volumes du système d'approvisionnement en gaz.

Pour conclure, la transposition des batteries Li-air au domaine aéronautique semble très peu probable du fait de leur sensibilité vis-à-vis des conditions de fonctionnement, même si l'on suppose le problème de stabilité de l'électrolyte résolu. Pour autant, étudier de tels système permet de se questionner sur les processus électrochimiques et les fondamentaux des batteries. De plus, ici le développement d'électrodes bi-poreuses a été permis et pourra être transposé à d'autres applications par la suite, comme par exemple dans le domaine plus général des batteries métal-air.



# Toward lithium-air batteries for aircraft application: a combined experimental/modeling study

## *Résumé :*

Le développement des avions plus électriques nécessite des systèmes de stockage électrochimique à fortes densité d'énergie, à la fois gravimétrique et volumétrique. Parmi les diverses solutions envisagées, les batteries lithium-air sont apparues comme une solution envisageable du fait de leur densité d'énergie théorique élevée. Cependant, les performances obtenues en pratique sont bien éloignées des théoriques à cause des nombreux verrous technologiques dont souffrent ces batteries.

Afin d'augmenter les performances des batteries une grande partie des travaux a eu pour objectif de créer des électrodes texturées prenant en compte les phénomènes limitant tels que la diffusion de l'oxygène, le remplissage des pores ou encore la passivation de l'électrode afin d'améliorer la capacité de décharge. D'abord étudiées grâce à la modélisation, le développement en laboratoire a ensuite permis de créer des électrodes bi-poreuses pouvant atteindre jusqu'à 70 % de la capacité théorique. Par la suite, en vue d'un manque de reproductibilité certain, l'étude des paramètres pouvant induire une variation des capacités de décharge a été mise en place. Il est alors apparu que les batteries lithium-air sont extrêmement sensibles aux paramètres modifiant sa cinétique et l'étape de nucléation : la température, la densité de courant et l'état de surface de l'électrode.

**Mots-clefs :** batteries Li-air, électrodes poreuses, reproductibilité, modélisation, aéronautique

## *Abstract:*

To develop more electrical aircrafts, energy storage systems with high gravimetric and volumetric energy densities are required. Among the potential solutions, lithium-air batteries appeared as a promising choice due to their high theoretical energy densities. However, such systems suffer from many limitations which induces low practical energy densities.

To enhance the batteries performances, a study on the electrode texture was implemented taking into account the limiting phenomena of passivation, pore clogging and oxygen diffusion. First studied by the help of modeling, development of these electrodes was later achieved at lab scale. The bi-porous electrodes obtained could reached the 70 % of the expected capacity. Later, due to the reproducibility issues observed a second study was settled to limit variation of the discharge capacities. It was noticed that lithium-air batteries were extremely sensitive to the parameters impacting kinetics and more especially the nucleation step. So temperature, current density and electrode surface should be perfectly mastered.

**Keywords:** Li-air batteries, porous electrodes, reproducibility, modeling, aeronautic sector